Turbulence and Ice Nucleation in Mixed-Phase Altocumulus Clouds in the Mid-Latitudes

Paul Alan Barrett

Submitted in accordance with the requirements
for the degree of
Doctor of Philosophy

The University of Leeds
Institute for Climate and Atmospheric Science

March 2017

Intellectual Property Statement

The candidate confirms that the work submitted is his own and that the appropriate credit has been given where reference has been made to the work of others.

Acknowledgements

Most importantly I would to thank my supervisor Alan Blyth. His help by asking vital and challenging questions helped me immensely and kept me thinking. I thank Philip R.A. Brown, my co-supervisor for most of the project until his partial-retirement, for many discussions and I am grateful to my employer the Met Office for supporting me throughout the project. Many others, too numerous to name, have contributed to this work including the aircrew, ground-crew and instrument operators of the FAAM BAe146 research aircraft. In particular I acknowledge Graeme Nott (FAAM), and Ian Crawford and James Dorsey (University of Manchester) who provided quality control aerosol and cloud microphysics data products and Steve Abel (Met Office) for processed WVSS2 data. Thanks to all in Earth and Environment for many useful discussions, especially Ian Brooks, Ben Murray, Jon Marsham, Jenn Brook and also to Michelle Lesnianski and to all in the NCAS office for their hospitality. Joseph Ulanowski offered useful insights into cloud physics probes. The assistance of Mirek Andrejczuk and Adrian Hill is appreciated. I'm very grateful for diligent proof reading undertaken by my mum, Elaine, and also Kate Szpek, Steve Abel and Richard Cotton. Remaining errors are my own.

I would not have got to this stage without the early support of family, including my dad, Alan, for taking me star-gazing when I was nor-but-a-lad and my sister Helen. The subtle encouragement of Bailey and Starks is recognised and in no way underestimated. Dr. Tim Richardson and Prof Richard Jones guided me through my undergraduate degree in the first place. All at *Number 20*, and on *the-wider-green*, served up relaxation with many bbqs along the way and the moral support from Jessica Pearson helped to get me over the line.

Abstract

Mixed-phase layer clouds are common throughout the globe, from the tropics where detrainment from convection forms long-lived altocumulus layers, to the mid-latitudes where humidity is brought to the mid-troposphere by cyclonic activity, and in the Arctic regions where low-level mixed-phase stratocumulus clouds persist. Supercooled water is common in these clouds and so they have a strong impact on the radiative balance of the planet.

Global climate and numerical weather prediction models fail to predict sufficient mid-level cloud and this leads to deficiencies in the representation of incoming solar radiation at the surface and thus large biases in surface temperature, notably in the Southern Ocean. High resolution and cloud resolving models do not perform significantly better, and in part this is due to large uncertainties in the nature of ice nucleation and the phase transition from liquid to ice.

This study exploits new observations of mixed-phase cloud to attempt to better understand the processes that control their evolution. Observations of altocumulus clouds from an instrumented aircraft are presented that probe the nature of liquid and ice cloud particles, and the underlying aerosol population. The performance of cloud microphysics probes in measuring ice particles smaller than 100 μm when liquid cloud drops are present is assessed. New characterisation of SID2 (Small Ice Detector 2) and CIP15 (Cloud Imaging Probe, 15 μm) is presented. Calculations are performed that assess the ice nucleating particle budget in altocumulus, and the ice production rate in mixed-phase altocumulus and cumulus clouds.

Contents

List of Figures

List of Tables

Abbreviations

2DC 2 Dimensional Cloud Probe

2DS 2 Dimensional Stereo Cloud Probe

2D 2 Dimensional

3D 3 Dimensional

AoA Angle of Attack

AoSS Angle of Sideslip

AVHRR Advanced Very High Resolution Radiometer

B668 FAAM Research Flight 23^{rd} January 2012

B674 FAAM Research Flight 2^{nd} February 2012

B816 FAAM Research Flight 24^{th} November 2013

BADC British Atmospheric Data Centre

BAe146 British Aerospace Engineering 146 Large Research Aircraft

BL Boundary Layer

CALIPSO Cloud Aerosol Lidar and Infrared Pathfinder Satellite

CCD Charge Coupled Device

CCN Cloud Condensation Nuclei

CDP Cloud Droplet Probe

CEDA Centre for Environmental Data Analysis

CFDC Continuous Flow Diffusion Chamber

CIP100 Cloud Imaging Probe (100 μm Resolution)

CIP15 Cloud Imaging Probe (15 μm Resolution)

CIRCREX CIRrus Coupled Radiation EXperiment

CloudSat Cloud Satellite

CNIO Contact Nucleation Inside Out

CPI Cloud Particle Imager

CPI_col Column (CPI category)

CPI_bud Budding (CPI category)

CPI_bir Budding Irregular (CPI category)

CPI_plt Plate (CPI category)

CPI_ros Rosette (CPI category)

CPI_sir Small Irregular (CPI category)

CPI_sph Sphere (CPI category)

CTH Cloud Top Height

CTT Cloud Top Temperature

CSD Cumulative Size Distribution

CWC Condensed Water Content

DMA Differential Mobility Analyser

DMT Droplet Measurement Technologies

DoF Depth of Field

DRC Detector Response Correction

ECMWF European Centre for Medium Range Weather Forecasting

FAAM Facility for Airborne Atmospheric Measurement

FFT Fast Fourier Transform

FoV Field of View

FSSP Forward Scattering Spectrometer Probe

ft foot (imperial unit of distance)

GCM General Circulation Model

GIN GPS-aided Inertial Navigation System

GPS Global Positioning System

HHC87 Harris-Hobbs and Cooper (1987)

HL Higher Level

HM Hallett Mossop secondary ice Production via rime-splintering

IAS Indicated Airspeed

IAT Inter-Arrival Time

INC Ice Nucleus Counter

INP Ice Nucleating Particle

INR Ice Nucleation Rate

Int 1. Intermediate 1

Int 2. Intermediate 2

ISCCP International Satellite Cloud Climatology Project

IWC Ice Water Content

JAR Joint Airworthiness Regulations

kft kilofoot (imperial unit of distance)

kn Knot

Lat Latitude

LES Large Eddy Simulator

Lim. Limit

LoD Limit of Detection

Lon Longitude

LWC Liquid Water Content

LWP Liquid Water Path

LWRC Long Wave Radiative Cooling

Max. Maximum

MetUM Met Office Unified Model

MEVALI Microwave Emission Validation over sub-Arctic Lake Ice Project

min minute

Min. Minimum

ML Mixed Layer

MSG Meteosat Second Generation

NAME Numerical Atmospheric-dispersion Modelling Environment

NaN Not-A-Number

NCAR National Centre for Atmospheric Research

NWP Numerical Weather Prediction

OAP Optical Array Probe

OASIS Optical Array Probes Shadow Imaging Software

OPC Optical Particle Counter

$\mathbf{P}_0$ Ice Production Rate

PCASP Passive Cavity Aerosol Spectrometer Probe

PDF Probability Density Function

PIKNMIX Prestwick Mixed-Sorties Flight Campaign

PIKNMIX-C Third Prestwick Mixed-Sorties Flight Campaign

PIP Primary Ice Production

PMS Particle Measuring Systems

Pro Slant Profile (aircraft)

PSD Particle Size Distribution

$\boldsymbol{r}$ SID2 individual detector element response

Res. Resolution

RVSM Reduced Vertical Separation Minimum

SID Small Ice Detector

SID2 Small Ice Detector Mk. 2

SID3 Small Ice Detector Mk 3.

SIP Secondary Ice Production

SL Stable Layer

SODA2 System for OAP Data Analysis version 2

SLR Straight and Level Run (aircraft)

SPEC Stratton Park Engineering Company

SPIN Spectrometer for Ice Nuclei

STP Standard Temperature and Pressure

TAS True Airspeed

TDL Tunable Diode Laser

TKE Turbulence Kinetic Energy

TWC Total Water Content (Condensed)

U. Herts. University of Hertfordshire

U. Man. The University of Manchester

UL Upper Layer

UTC Coordinated Universal Time

WBF Wegener-Bergeron-Findeisen

WGS84 A Particular Reference Geoid

WMO World Meteorological Organisation

WVSS2 Water Vapour Sensing Systems Mk 2. Near Infrared TDL Absolute Humidity Spectrometer

Nomenclature

$\boldsymbol{A}$ Asphericity

$\boldsymbol{cf}_{ice}$ $\boldsymbol{cf}_{liq}$ $\boldsymbol{cf}_{mixed}$ Cloud fraction (ice, liquid, mixed phase)

$\boldsymbol{d}$ Diameter

$\boldsymbol{D}$ SID2 geometric equivalent diameter

$\overline{d}$ Geometric mean diameter of log-normal distribution

$\boldsymbol{d}_l$ Diameter of liquid cloud particle

$\boldsymbol{d}_{eff}$ Effective cloud drop diameter

$\boldsymbol{d}_i$ Diameter of ice particle

$\boldsymbol{Dz}_{CTH}$ Vertical altitude w.r.t. cloud top height

$\boldsymbol{Dz}_{inv.}$ Vertical altitude w.r.t. inversion altitude

$\boldsymbol{F}$ Flow rate

$\boldsymbol{N}_a$ Aerosol particle number concentration

$\boldsymbol{N}_d$ Cloud droplet number concentration

$\boldsymbol{N}_i$ Ice particle number concentration

$\boldsymbol{N}_0$ Number concentration of log-normal distribution

$\boldsymbol{P}_0$ Ice production rate

$\boldsymbol{q}$ Specific humidity

$\boldsymbol{q}_t$ Total water content (vapour + liquid + ice)

$\boldsymbol{r}$ Humidity mixing ratio

$\boldsymbol{RH}$ Relative Humidity

$\boldsymbol{RH}_I$ Relative Humidity w.r.t. ice

$\boldsymbol{RH}_L$ Relative Humidity w.r.t. liquid

$\boldsymbol{SA}$ Sample Area

$\boldsymbol{SA}_E$ Extended Sample area

$\boldsymbol{SA}_Q$ Qualified Sample Area

$\boldsymbol{u}_{bulk}$ Easterly wind component from aircraft-motion vectors

$\boldsymbol{u}_{turb}$ Easterly wind component from 5-port probe

$\boldsymbol{u}'$ Fluctuation of easterly wind component from 5-port probe

$\boldsymbol{u}_z^*$ Vertical velocity required to short-cut WBF process (Korolev, 2007a)

$\boldsymbol{v}_{bulk}$ Northerly wind component from aircraft-motion vectors

$\boldsymbol{V}_{sample}$ Sample volume

$\boldsymbol{v}_{turb}$ Northerly wind Component from 5-port probe

$\boldsymbol{v}'$ Fluctuation of northerly wind component from 5-port probe

$\boldsymbol{v}_{max}$ Size dependent particle fall speed

$\boldsymbol{vmr}$ Humidity volume mixing ratio

$\boldsymbol{wa}_{bulk}$ Horizontal wind angle from aircraft-motion vectors

$\boldsymbol{ws}_{bulk}$ Horizontal wind speed from aircraft-motion vectors

$\boldsymbol{w}_{turb}$ Vertical wind component from 5-port probe

$\boldsymbol{u}'$ Fluctuation of vertical wind component from 5-port probe

$\boldsymbol{z}_{fall}$ Particle fall distance

θ Potential temperature

σ Standard deviation

τ_{gl} Cloud glaciation time

Φ_{INP} INP Reservoir depletion time

Constants

$\boldsymbol{c_p}$ = 1005.7 J Kg^{-1} K^{-1} Specific heat capacity of air at constant pressure

$\boldsymbol{e_0}$ = 6.113 hPa Reference vapour pressure

$\epsilon = {}^{R_d}/_{R_w} = 0.621$ Ratio of gas constants

$\boldsymbol{Lv_l}$ = 2501 kJ kg^{-1} Latent heat of vapourisation (liquid)

$\boldsymbol{Lv_i}$ = 2835 kJ kg^{-1} Latent heat of vapourisation (ice)

$\boldsymbol{P_{ref}}$ = 1000 hPa Reference pressure

$\boldsymbol{R_d}$ = 287.5 J Kg^{-1} K^{-1} Gas constant of dry air

$\boldsymbol{R_w}$ = 461.5 J Kg^{-1} K^{-1} Gas constant of water vapour

T_0 = 273.15 K Melting temperature

Chapter 1

Introduction

1.1 Altocumulus Clouds

The clouds studied in the research are Altocumulus Stratiformis: mid-tropospheric layer clouds that often reside at altitudes above the zero degree isotherm. Liquid water may therefore be supercooled and ice may form and precipitate from the clouds in the form of virga. *Alto-* clouds are found in the middle layers of the troposphere. *Cumuliform* clouds are those which possess some turbulent activity and vertical motion. *Stratiform* clouds extend spatially over a wide area. These categories are determined by the World Meteorological Organisation (2008) for synoptic observations purposes, and are based on altitude and appearance of clouds. The physical processes and phase composition are considered a "less formal" way to classify a cloud, and so nomenclature is often a source of confusion when discussing cloud types. It has been suggested in the literature that alto-stratocumulus be used as a synonym since this better describes the physical mechanisms at work in these clouds (Larson et al., 2006). This term may seldom be used but does

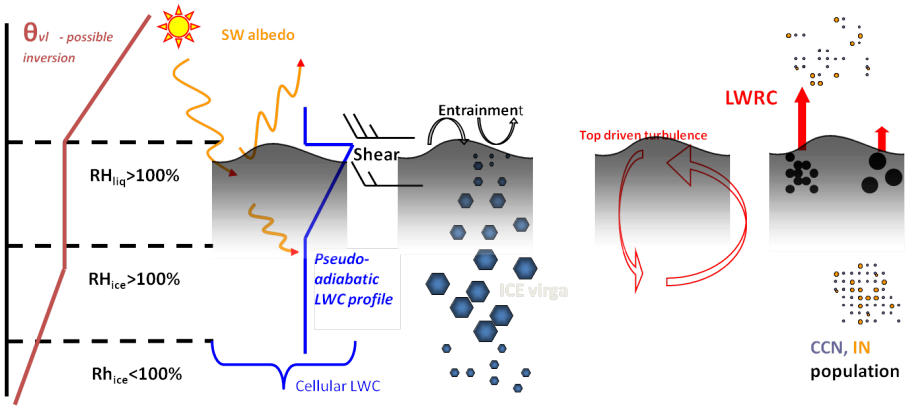

Figure 1.1: Illustration of the processes that maintain and evolve altocumulus clouds (after Morrison et al. (2012)).

accurately describe the mid-level layer clouds in this study. The term altocumulus will be used throughout this work.

The maintenance of altocumulus clouds is the result of a complex network of processes relating supercooled water to ice through turbulence, radiative effects, underlying aerosol properties and entrainment. Morrison et al. (2012) describes a network of interactions for Arctic boundary layer clouds and the non-surface related processes are relevant to mid-latitude mid-level layer clouds. The processes that are pertinent to altocumulus evolution are illustrated in Figure 1.1. Altocumulus clouds share many characteristics with low level Arctic mixed-phase clouds (Smith et al., 2009). The clouds may be formed through large scale ascent or wind shear at a stable interface as well as outflow from convection when it reaches a stable layer (Rauber and Tokay, 1991) or through upwards air-motion associated with gravity-waves (Hogan et al., 2003a). The clouds have turbulent structure imparted through Long Wave Radiative Cooling (LWRC) from the liquid cloud top which results in a cellular structure. The cooling may result in the development of a temperature inversion above, and a thermodynamically well-mixed layer beneath. As the clouds are often supercooled there is the potential for ice nucleation and ice

production that could precipitate from the liquid layer and grow if the sub-cloud layer is super-saturated with respect to ice. Ice Nucleating Particles (INP) may be found within the layer or above.

An altocumulus life-cycle might be as follows:

- Wind shear or some other processes instigates positive vertical velocity that produces supersaturation and initiates liquid cloud.
- LWRC (Long Wave Radiative Cooling) from cloud top causes some cloud parcels to descend, in narrow strong downdraughts, then
- conservation of mass results in some weaker, broader updraughts.
- The induced TKE (Turbulence Kinetic Energy) structure maintains the liquid layer, and at some stage
- Ice nucleation take place through an immersion freezing, or other exotic heterogeneous freezing mechanism. The exact location is unknown.
- During updraughts, once ice saturation is reached, there may be ice formation through deposition nucleation
- Ice particles would then grow and precipitate out from below the liquid cloud. The cloud may fully glaciate, dissipate, or develop a multi-layered structure.

1.1.1 Motivation

Altocumulus clouds are much less frequently studied than other clouds such as their boundary layer equivalent stratocumulus, for example. In part, this is because the clouds themselves are not responsible for severe weather and rarely produce precipitation that reaches the ground (Fleishauer et al., 2002).

However, altocumulus clouds have been implicated in the enhancement of surface precipitation via ice precipitation seeding supercooled cloud below (Crosier et al., 2011). Additionally, supercooled water in these clouds may present a hazard to air traffic (JAR, 2007) (Joint Airworthiness Regulations).

In situ aircraft measurements are difficult in these environments as the cloud layers are typically less than 500 m thick (Korolev et al., 2007). Many of the existing studies took place before the impact of shattering of ice on cloud physics instrumentation was fully appreciated (Korolev et al., 2011) and so there is some doubt cast on the quality of the measurements. New instruments with higher resolution than those in the existing studies are now available, and so the focus has developed from observing the large scale properties of the clouds, to closing in on the physical processes controlling their evolution. Therefore it is timely to return to study these mixed-phase clouds, with a focus on the measurement of small ice with a view to disentangling the problem of ice nucleation in mixed-phase clouds. Better in situ measurement of the turbulent environment which these clouds generate will place the microphysical observations in context.

1.1.2 Aims

This research aims to exploit cloud and aerosol microphysics and turbulence observations in order to better understand mixed-phase altocumulus clouds in the mid-latitudes, in particular in terms of the properties of small ice. In situ data collected with the FAAM (Facility for Airborne Atmospheric Measurements) BAe146 Atmospheric Research Aircraft were used to observe aerosol and cloud microphysical properties and to measure thermodynamics and turbulence. Observations are presented here of three mixed-phase clouds: altocumulus, stratocumulus and cumulus. Along with calculations performed on the data using published

techniques, these observations were used to determine the ice production rate in an altocumulus and cumulus cloud, and the ice nuclei budget based on aerosol observations. Observations of small ice particles with d $\geq$ 45 μm are presented from within regions where liquid cloud drops are present and this represents a step forward in exploitation of the current generation of cloud physics probes.

The measurements and observations were made so as to further the understanding of this type of cloud, and of the physical processes at work. These processes may be applicable to other cloud types, and the aim is to present the observations such that the output from numerical models for both weather and climate forecasting may be tested and improved.

1.2 Literature Review

1.2.1 Climatology and Simulation of Altocumulus Clouds

Supercooled water is common in the atmosphere with altocumulus and altostratus clouds present throughout the globe in all seasons to a varying extent (Warren et al., 1988). Zhang et al. (2010) use CALIPSO (Cloud-Aerosol Lidar and Infrared Pathfinder Satellite Observations) and CloudSat data to show that the global mean occurrence of altocumulus is 7.8 % and that mixed-phase layer clouds represent 33.6 % of all mid-level clouds. A higher incidence of mixed-phase layer cloud was found at night, in the tropics, and more so over land. In the northern hemisphere, away from the tropics, almost all liquid topped layer clouds are mixed-phase when Cloud Top Temperature (CTT) is less than -13° C. Ground based observations from the mid-latitudes show that liquid water layers are found above ice clouds in the majority of cases warmer than -27° C (Westbrook and Illingworth, 2011).

Stein et al. (2011) reported on the use of remote sensing to find significant amounts of altocumulus in tropical regions in the west of Africa, associated with the outflow from deep convective systems, above the zero degree isotherm, between 600 hPa and 500 hPa. These clouds are shown to contain supercooled liquid and occur up to 20 % of the time between 5 N and 30 N, covering the Sahara to some extent, which will be crucial for the radiative balance of the region.

Ground-based remote sensing from the island of Cape Verde allowed Ansmann et al. (2009) to observe more than 200 oceanic tropical altocumulus clouds and found them to have similar structure to those clouds mentioned above. Layers were 262 m $\pm$ 137 m deep, and as cold as T = -37° C, with the ice phase being correlated with cloud top temperature indicating that the ice nucleation in these clouds is temperature dependent. Liquid was required before any ice was observed, and the conclusion was that ice nucleation occurs first at cloud top through freezing of drops and that deposition and condensation nucleation are unimportant in the initial, crucial, ice formation phase. However, no evidence is presented for ice formation at cloud top, but evidence is presented for ice formation in updraughts prior to water saturation being reached. Deposition nucleation is suggested as the mechanism as this occurs below the liquid cloud base. No ice was observed prior to this and so the conclusion is questioned here. An alternative explanation could be that the ice only formed once any potential Ice Nucleating Particles (INP) had undergone some form of processing through the cloud drops, and hence no ice was observed until after the liquid was present.

Detailed ground based remotely sensed observations and a theoretical model of altocumulus was presented by Schmidt et al. (2014). The structure of altocumulus clouds were resolved on an unprecedented scale with features of the order 100 m depicted. Figure 1.2 is reproduced here from Schmidt et al. (2014) and shows

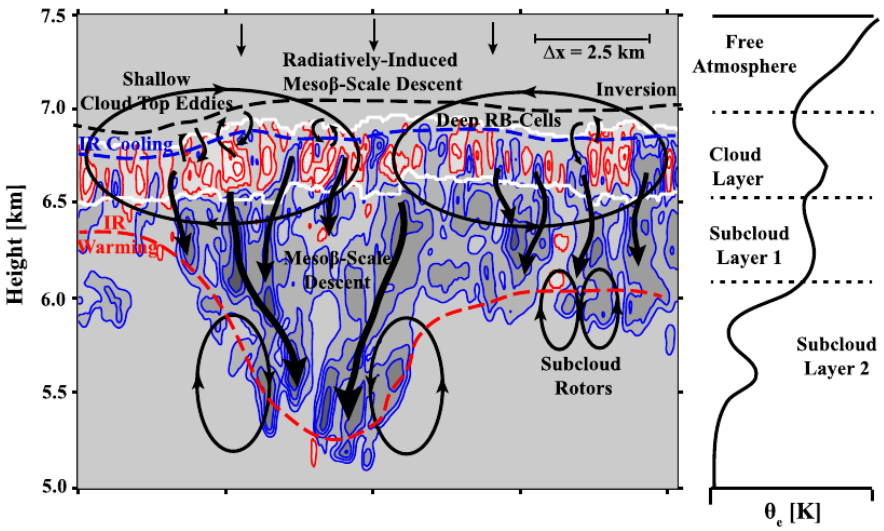

Figure 1.2: Schematic of the turbulence structure in observed altocumulus clouds as presented in Schmidt et al. (2014). Dark grey shading and blue countour outlines show downdraughts (at -0.3, -0.6, -0.9, -1.2 m s^{-1}). Updraughts in red contours (0.1, 0.2, 0.3 m s^{-1}). Cloud layer depicted by white contours contains Rayleigh-Bérnard (RB) type convective circulations. Shallower eddies were observed near cloud top (smaller black arrows). Longer thick black arrows show narrow small-scale downdraughts from various levels in cloud. Subcloud rotors associated with downdraughts are shown as vertically oriented ellipses. Simplified static stability profile shown on right of figure.

a summary of the observed features of the turbulence structure of the clouds that they observed. As expected the liquid cloud layer contains Rayleigh-Bérnard type convective circulations, driven by LWRC from cloud top, with strong narrow downdraughts driving weaker, broader updraughts. Smaller circulations were observed within the cloud top layer. Connection between the liquid cloud layer and below was observed by the presence of strong downdraughts penetrating through the virga layer. In turn, these downdraughts result in weak updraughts and small sub-cloud rotors. Distinction between the turbulence within the liquid cloud layer and the sub-cloud virga systems were clear. Small scale structures such as eddies at cloud top and small sub-cloud rotors were shown to contribute to the overall

turbulence spectra.

Supercooled altocumulus clouds will often produce ice phase precipitation in the form of sub-cloud virga. The glaciation of a liquid cloud has significant consequences for fractional cloud coverage and albedo. A supercooled liquid cloud may have large areal coverage and significant optical depth, although the amount of condensed water is relatively low with with 50% of clouds having LWP $\leq$ 100 gm^{-2} (Korolev et al., 2007). Once glaciated the coverage can be much reduced and the optical depth of the ice cloud much lower and so understanding the phase partitioning is crucial in understanding the radiative balance of the global climate system (Sun and Shine, 1995). Altocumulus clouds have important radiative properties as they may be optically thick especially if the cloud has significant Liquid Water Path (LWP). Radiative transfer calculations performed by Hogan et al. (2003b) suggest that the radiative impact of the liquid layer is extremely significant. Climate models generally parametrise Ice Water Content, IWC = $Fn(\mathrm{T}^{-1})$ which is in disagreement with observations for mixed-phase layer clouds (Carey et al., 2008) which show that ice mass is present in greater concentrations in the lower part of the cloud system.

Westbrook and Illingworth (2011) found that the supercooled water in mid-level clouds is drastically underestimated in GCMs (General Circulation Models) and NWP (Numerical Weather Prediction). Large scale GCMs in NWP mode do not produce realistic simulations of these mid-level mixed-phase clouds. A comparison by Hogan et al. (2003b) found that both ECMWF (European Centre for Medium Range Weather Forecasting) and MetUM (Met Office Unified Model), in forecast mode, had difficulty in predicting the frequency of supercooled water layers over the Chilbolton radar station. Both models had too much supercooled water between 0° C and -20° C and little, if any, supercooled water at T $\leq$ -20° C. Systematic

GCM deficiencies are attributed to low vertical resolution in the mid-levels, poor mixed-phase microphysics, and a lack of subgrid-scale processes such as cellular convection (Hogan et al., 2003a; Bodas-Salcedo et al., 2008). The problem of resolution is compounded at higher altitudes, where model levels are more widely spaced, as thinner clouds are correlated with lower temperatures (Korolev et al., 2007).

Climate simulations are found to have too little cloud in the mid-levels which results in a warm bias in sea surface temperatures, one of the largest of which is found in the Southern Ocean (Bodas-Salcedo et al., 2014). Previous work by Bodas-Salcedo et al. (2012) found that the bias in solar downwelling short-wave radiation can be as large as 35 Wm^{-2} in the Southern Ocean and attributed the cause to missing, or misrepresented, mid-level cloud on the cold side of a composite southern-hemisphere cyclone. The impact is felt most strongly to the south of 55° S, so much so that it dominates the climatological signal over the range 40° S to 70° S (Bodas-Salcedo et al., 2014). Stratocumulus clouds are also implicated and the poor representation of these clouds in part being restricted by the poor vertical resolution in the current generation of numerical models. Cumulus congestus and mid-level stratiform clouds are not understood to the same level of detail in these studies.

Mason et al. (2014) has gone some way to rectifying this uncertainty in the source of the bias by defining four new "high-latitude Southern Ocean cloud regimes". By combining passive sensors with active radar and lidar data and with the meteorological state parameters, they applied a k-means clustering algorithm to present new insights into the dynamics and cloud properties associated with these mid-level clouds. Polar-Lows, small meso-scale features that are not resolved in the 280 km scale of ISCCP (International Satellite Cloud Climatology Project), are

contributors to deep, high optical depth midtopped cloud. Sub-categorisation of the low-level broken cumulus and stratiform regimes is shown. Further segregation of the occurrence of shallow and deep mid-level layers, and cloud occurring in warm-conveyor belt and subsidence cold-air regimes was presented. The in situ details of the microphysical processes that control these features remain elusive.

Turbulence in mixed-phase clouds has been explored by Marsham et al. (2006) by interrogating a cloud resolving model with ground based observations. Accurate representation of the vertical velocities was found to be important in maintaining the LWP and ice nucleation and in particular the INP budget was identified as a control on LWP. GCMs typically have a treatment of weakly forced turbulent mixing in the boundary layer (e.g. The Lock et al. (2000) Boundary Layer Scheme) but there is no such representation of turbulence in isolated mid-level layers, meaning that models will continue to struggle to have large enough LWP. There is also evidence that the ice production process is too efficient (Abel et al., 2017).

1.2.2 In Situ Observations of Altocumulus Clouds

A number of studies of altocumulus have been made previously with instrumented aircraft, predominantly in the mid-latitudes. Heymsfield et al. (1991) found two highly-supercooled clouds with cloud top temperatures of -30° C, with low droplet number concentrations of a few 10s cm^{-3}, and LWC (Liquid Water Content) of 0.05 gm^{-3} and 0.02 gm^{-3}. Only the higher LWC cloud was found to precipitate ice.

Fleishauer et al. (2002) find, for altocumulus in mid-latitudes, that cloud systems can consist of single and multiple layers and span depths of typically 500 m. Similar values of liquid water were found, typically with 0.01 $gm^{-3} \leq$ LWC $\leq$ 0.15 gm^{-3},

peaking at LWC = 0.39 gm^{-3}. Vertical wind velocity data showed a standard deviation range of 0.15 ms^{-1} to 0.75 ms^{-1}. IWC did not correlate with colder temperature but showed a maximum in the range -8° C $\leq$ T $\leq$ -20° C, where the largest difference in saturation vapour pressure between liquid and ice surfaces occurs, in support of Carey et al. (2008).

Korolev and Field (2008) use in situ data from five field campaigns and find that there are distinct types of supercooled LWC profile, with shallow, slightly sub-adiabatic type layers where a linear increase with altitude is observed. Many clouds have more complex layered structures and can have highest LWC at, or towards, cloud base. The median peak-LWC value was found to be 0.32 gm^{-3} at the 100 m averaging scale, with an absolute maximum of 1.0 gm^{-3}. These LWC values were relatively independent of depth for clouds deeper than 500 m, and the average in-cloud LWC was 0.14 gm^{-3}. More than half of the clouds were in fact shallower than 500 m, with thinner clouds being well correlated with colder layer-averaged temperatures. Where temperatures were colder than -25° C the cloud depths were less than 100 m. Deeper clouds were found, at low frequency of occurrence, up to 4 km thick, and these deep-stratiform clouds were more likely to have many local LWC maxima.

Carey et al. (2008) observed that mid-latitude altocumulus layer clouds were of mixed-phase composition on more than two-thirds of occasions and that mixed-phase conditions began within a few tens of metres of observable cloud top. Peak LWC was found at cloud top, and IWC (Ice Water Content) precipitated as virga from the liquid layer to reach a maximum in the lower half of the cloud or below. The similarity to Arctic boundary layer mixed-phase stratocumulus was noted. Many clouds were between 100 m and 300 m thick, ranging from 80 m to 1000 m and had cloud top temperatures from the warmest at -13° C to the

coldest at -26° C. No association between temperature and peak LWC was found, whereas peak IWC did occur at warmer temperatures, although the trend was weak. Long-lived clouds of up to 9 hours were identified and some mixed-phase clouds appeared to "de-glaciate" and return to being liquid-phase only. Perhaps this cloud underwent large scale descent to a level where the temperature increased above the ice nucleation temperature, leaving the remaining liquid cloud in place.

The mixed-phase stratocumulus in the Arctic is well studied (Verlinde et al., 2007; McFarquhar et al., 2011; Lloyd et al., 2015), and those clouds are found to share many properties with altocumulus. Hobbs and Rangno (1998) found a wide range of liquid and ice properties in Arctic altocumulus clouds, with cloud drop numbers ranging from less than 105 cm^{-3} up to 450 cm^{-3} with 0.02 $gm^{-3} \leq$ LWC $\leq$ 0.14 gm^{-3} and 11.8 μm $\leq d_{eff} \leq$ 17.8 μm. The liquid cloud droplet spectra in altocumulus often looked similar to those found in stratocumulus clouds. The maximum size of cloud particles was generally smaller than 25 μm. Clouds were 30 m to 800 m deep, and did not appear well mixed, and so no variation of LWC with height was observed. Ice precipitation occurred at T $\leq$ -10° C. Rangno and Hobbs (2001), amongst others, studied the properties of Arctic mixed-phase clouds and determined a number of sub-types based on the partition between ice and liquid, the amount of turbulence, etc.

Hobbs and Rangno (1985) observed ice concentration enhancement close to the tops of supercooled stratiform clouds when a proportion of the liquid cloud particles were larger than $\approx$ 20 μm and postulated that the ice may have been formed during partial evaporation of cloud droplets during mixing of dry air from aloft. The observations required only $\approx$ 0.1 % of the larger drops to freeze to explain the ice concentrations. Given the probable over estimation of ice concentrations the actual fraction is likely to be orders of magnitude lower. The observational studies

made at this time are likely to have suffered from shattering on cloud physics probes (e.g. Korolev et al. (2011)) and so the presented ice concentrations may not be reliable.

1.2.3 Ice Nucleation in Altocumulus

One remaining big question in cloud physics is the precise nature of the ice formation process in the atmosphere. Much of the uncertainty revolves around understanding the nature of the heterogeneous phase transition between liquid and ice. Homogeneous ice nucleation is only important at T $\leq$ -33° C (Cantrell and Heymsfield, 2005) and very little liquid cloud is observed below this (Illingworth et al., 2007), although there is a small, but finite, homogeneous nucleation rate (Herbert et al., 2015) for T $\leq \approx$ -30° C.

Supercooled water has been observed in Arctic stratus clouds at T = -31° C (Hobbs and Rangno, 1998). There are observations of altocumulus clouds persisting in an almost equilibrium state for upwards of twenty-four hours (Westbrook and Illingworth, 2013), long after traditional ice nuclei parametrisations would suggest is possible (e.g. DeMott et al. (2015)). The lifetime and albedo of the clouds are found to be extremely sensitive to the properties of aerosols and ice nucleation processes in climate models (Storelvmo et al., 2011).

Observations (Westbrook and Illingworth, 2011) supported by modelling (Fridlind et al., 2007) show that water saturation is required before these clouds produce ice and so it is likely that the ice are produced via a variant of immersion freezing (see Vali (2014) and references therein), whereby an INP immersed in a cloud drop becomes active either once a particular temperature is reached, or as a result of some stochastic process. Laboratory studies are beginning to shed light on the

stochastic process of immersion freezing of supercooled drops via heterogeneous ice nucleation in the presence of an INP (Broadley et al., 2012).

A number of instruments exist that are able to measure the number concentrations of INP in the atmosphere using Continuous Flow Diffusion Chamber (CFDC) Ice Nucleus Counters (INC), as described initially by Rogers (1988). More recently a commercial instrument produced by Droplet Measurement Technologies (DMT, 2016) based on a research instrument developed by Stetzer et al. (2008) has been available to the airborne atmospheric research community. Such instruments offer a method of quantifying the number of ice nucleating particles across a part of the temperature-humidity-time phase space. The instruments are able to prescribe certain combinations of temperature and humidity. Residence time is limited by the narrow range of flow rates that can be selected.

Experiments undertaken with airborne INC do not typically explore immersion freezing mechanism, since operation at water saturation is difficult, and the short residence time in the freezing section of the chamber is restrictive. This topic is in the early stages of being researched using ground based equipment (ETH Zurich, 2016). As the parametrisations if INP concentrations as a function of temperature in numerical models are developed from the observations they necessarily share the same limitations. Recent work by DeMott et al. (2015), using ground based instrumentation, introduced a correction factor to be applied to CDFC data to account for this systematic underestimation. The measured number concentrations of INP may be lower by a factor of two or three, when compared against immersion freezing in general.

Traditional heterogeneous ice nucleation mechanisms, contact, immersion, deposition and condensation freezing cannot explain the production of ice in weakly forced supercooled liquid clouds whereas an evaporation freezing mechanism was

shown to replicate the observed liquid and ice properties of mixed-phase Arctic stratocumulus with some degree of success by Fridlind et al. (2007). A second evaporation mechanism, where a small fraction of the CCN (Cloud Condensation Nuclei) from evaporated cloud drops become effective INP was postulated to account for the excess of ice crystals concentrations over available traditional INP. In the evaporation region around a cloud the air is likely to be still supersaturated with respect to ice. The study proposes that if an INP were released/produced when a cloud drop evaporated then it would be able to immediately form an ice crystal.

Contact Nucleation Inside Out (CNIO) (Durrant and Shaw, 2005) is similar to INP production through evaporation but does not require the cloud drop to be fully evaporated. A particular INP is typically active at a warmer temperature as a contact nuclei than an immersion nuclei and so the likelihood that a freezing event takes place is expected to be greater for CNIO than for traditional immersion freezing.

For CNIO to take place a particle must enter a region sub-saturated w.r.t. liquid, where full or partial evaporation of the droplet may result in an embedded INP being exposed to the environment whereupon it may act as a contact nuclei rather than an immersion nuclei. Locations where this is likely include close to cloud top where dry air entrains from aloft, or in downdraughts. Once frozen, the ice crystals may be entrained into eddies that increase their residence time in cloud and permit them to grow to precipitation size particles.

The CNIO mechanism could be responsible for the time dependent nucleation observed in a long-lived altocumulus cloud by Westbrook and Illingworth (2013). The path length in cloud for any given liquid cloud particle will be governed by the particular turbulence spectra and there will be a spread of different lifetimes in

cloud. Droplet lifetimes in turbulent environments have been considered before for warm boundary layer clouds (Nicholls, 1987) and the model developed was capable of producing an appropriate number of drizzle-sized drops. In the supercooled environment in this study the drizzle process is potentially short-circuited by ice production and so the results may be transferable to the production of ice from supercooled liquid layers.

There are many locations where CNIO could become active, including cloud top, through entrainment of dry air from aloft or through lateral mixing of sub-saturated (w.r.t. liquid) air causing contact freezing following evaporation (e.g. Ladino et al. (2013) and references therein). Or else, during a downdraught, once the descending parcel becomes sub-saturated and begins to grow in the ice-super-saturated air. These small ice particles would potentially get re-entrained into updraughts where they could continue to grow as pristine crystals.

Water saturation being required prior to the initiation of the ice phase does not restrict the ice production mechanism to these variants of immersion freezing. Once the turbulence structure is established it may be possible for deposition nucleation to proceed within updraughts that are ice super-saturated but below water saturation. Observations of tropical altocumulus using ground based radar showed evidence of narrow bands of ice nucleation in updraughts just below liquid cloud base (Ansmann et al., 2009). The question as to why the INP did not act as a deposition nuclei during the initial updraughts that formed the liquid altocumulus clouds is not answered. A sudden influx of INP seems unlikely and so perhaps the INP were produced during cloud processing of aerosol.

By invoking a slow stochastic time dependent freezing process of liquid drops in a simple 1-D model Yang et al. (2013) were able to represent the expected properties of a mixed-phase cloud. In the real atmosphere, aircraft measurements of any

stochastic or time dependent processes (Vali, 2014) are difficult due to the long sampling time that is required.

Mechanisms such as freezing of evaporating drops, production of INP from an evaporated drop, of the spontaneous freezing by a stochastic time dependent mechanism require further study and observations of the properties of liquid and ice in mixed-phase clouds are one way to do this. Measurement of the smallest, first-ice particles in mixed-phase clouds is a crucial requirement in the field of cloud physics study in order to assess the nucleation and production of ice directly rather than through the indirect observations of INP.

1.3 Outline

The methods used in the study are presented in Chapter 2. Subsequently there is an overview of each of the clouds under study in Chapter 3, which includes the new method for studying altocumulus in a similar manner to stratocumulus, relative to a derived vertical coordinate. The following results chapter presents an analysis of ice production in a mixed-phase altocumulus cloud and uses aerosol observations to measure Ice Nucleating Particle (INP) concentrations (Chapter 4). Characterisation of asphericity-broadening in SID2 observations is presented, and small ice particles ($\leq$ 100 μm) are observed in mixed-phase altocumulus, using detailed analysis of cloud microphysics probes, in Chapter 5. Conclusions and suggestions for further work are given at the end. Supplementary and supporting materials are presented in appendices at the end of the document.

Chapter 2

Methods

2.1 Introduction

Data were collected from an instrumented aircraft, the FAAM BAe146 Atmospheric Research Aircraft (BAe146) on three research flights, through mixed-phase clouds. Altocumulus clouds were sampled on 2^{nd} February 2012 (Flight B674), cumulus clouds on 24^{th} November 2013 (B816) and stratocumulus clouds on 23^{rd} January 2012 (B668) with details given in Table 2.1. The work concentrates on the analysis of altocumulus clouds from flight B674 and presents these in contrast to stratocumulus and cumulus clouds. Whilst it would be advantageous to include additional cases of altocumulus clouds from different flights this has not been possible. The nature of the clouds themselves means that they are difficult to forecast using numerical models, and so it is consequently difficult to schedule research flights to go and sample them. The often transient nature of the altocumulus cloud systems further complicates the matter. Attempts to sample mixed phase altocumulus clouds have been made at temperatures warmer

Flight	Date	Campaign	Cloud Type	Instruments
B668	23^{rd} January 2012	PIKNMIX	stratocumulus	PCASP CDP 2DC CIP15 CIP100
B674	2^{nd} February 2012	PIKNMIX	altocumulus	PCASP CDP CIP15 CIP100 CPI
B816	24^{th} November 2013	PIKNMIX-C	cumulus	PCASP CDP 2DS

Table 2.1: FAAM BAe146 research sorties from the PIKNMIX and PIKNMIX-C, cloud type and aerosol and cloud microphysics instrumentation (Section 2.6).

than the clouds sampled here, only to be hampered by problems with icing of instrumentation and the airframe. The FAAM BAe146 has sampled similar clouds in a similar temperature range on occasion but generally with a reduced suite of cloud microphysical instrumentation resulting in a weaker dataset, or with less time on-task, or with a less favourable flight pattern.

Data are available from BADC (2017) (British Atmospheric Data Centre, part of CEDA - Centre for Environmental Data Analysis). Instrumentation and the data processing methods employed to analyse the data are presented in this chapter.

2.2 BAe146 Atmospheric Research Aircraft

The BAe146 is a four-engined jet aircraft that is fully equipped to measure the meteorological and thermodynamic conditions encountered during cloud physics research flights (FAAM, 2017). It carries a scientific payload capable of making measurements of a wide range of atmospheric parameters across a wide range of environmental conditions on research sorties of up to 6 hours. Sampling can take place between 50 ft (30 m) above the ocean surface and 35 kft (10 km). During sampling the aircraft typically flies at "science speed" which is an Indicated Airspeed (IAS) of 210 kn (approximately 100 m s^{-1} in the planetary boundary

layer). The particular payload varies according to the type of science that is being investigated, described in part by Mirza et al. (2016) and Allen et al. (2014). There are facilities to record the basic state parameters and positional coordinates along with specialist cloud and aerosol sampling probes. The information that follows is a comprehensive list of each of the instruments that feature in this research but not all were present on each flight. An overview of the data processing and limitations for each instrument is given but some specific details are covered in the chapters that follow.

2.2.1 Coordinates and Aircraft Attitude

Three dimensional geographical coordinates were determined using an Applanix POS AV 510 GPS (Global Positioning System) -aided Inertial Navigation (GIN) unit and data processing system, which reports at 32 Hz (Woolley, 2009a). Occasionally the data record showed spurious data where Latitude=Longitude=[0, 0] and these data points were removed from the data stream. GPS altitude data were corrected to the WGS84 reference geoid using a look-up table method. Aircraft attitude parameters such as True Airspeed (TAS), IAS, pitch, yaw and roll, along with derived Angle Of Attack (AoA) and Angle of Sideslip (AoSS) were also reported at 32 Hz. Time was provided by synchronisation with a remote time server and reported as Universal Coordinated Time (UTC).

2.2.2 Defining Slant Profiles and Straight and Level Runs

A research sortie is constructed from individual elements and the two that are relevant to science sampling are the Straight and Level Run (SLR) and the Slant Profile (Pro). Data from some instruments, such as those fed with an inlet, only

Segment Type	Parameter	Units	Limit
SLR / Pro	$^{d}/_{dt}$ Heading	$^{\circ}$ s^{-1}	$\pm$ 1.0
SLR / Pro	Roll	$^{\circ}$	$\pm$ 3.0
SLR	$^{d}/_{dt}$ Altitude	ft min^{-1}	$\leq \pm \approx 100$
Pro	$^{d}/_{dt}$ Altitude	ft min^{-1}	$\approx \pm$ 1000

Table 2.2: Parameters and limits used in determining when aircraft is in a Straight and Level Run (SLR) and a Slant Profile (Pro) on B674.

provide reliable data when the aircraft is sampling with wings level, and where the altitude does not vary. Other instruments can accept a moderate change in altitude. Data were selected from times when the aircraft was flying a constant heading using the limits for rate of change of heading and roll in Table 2.2. No strict limits were placed on the rate of change of altitude, but an SLR typically has a rate of change of altitude less than 100 ft min^{-1}. A standard boundary layer profile is flown at a rate of change of altitude of 500 ft min^{-1}. A faster rate was flown for the altocumulus sampling, of 1000 ft min^{-1} which does reduce the resolution in the vertical on a second-by-second basis, but improves the negative impact of horizontal variability on the profile data. As will be shown later (Chapter 3), the determination of the thermodynamic position within the cloud system was not determined to better than 25 m and increased vertical resolution from a slower ascent/descent rate was not the limiting factor.

Derived Spatial Coordinates

Aircraft position data from flight B674 were combined with wind, cloud physics and thermodynamic data to generate an *air-relative* horizontal coordinate and two new vertical coordinates. These being the vertical position of the aircraft relative to i) Cloud Top Height (CTH): $\mathrm{Dz}_{(CTH)}$ and ii) the inversion altitude: $\mathrm{Dz}_{(inv.)}$. Details and the results of this process are presented subsequently in Chapter 3.

2.3 3D and 2D Wind Components

2.3.1 5-Port Turbulence Probe Winds

Three dimensional wind components were sampled at 32 Hz using a 5-port turbulence probe (Brown et al., 1983; Brown, 2009) located on the nose of the aircraft. The probe has a centre port, and two pairs of ports, one in the horizontal, and one in the vertical plane between which differential pressure is measured. Impact pressure, equal to static plus dynamic pressure, is theoretically measured by the centre port. The 5-port probe pressure-fluctuations and supporting data were all recorded at 32 Hz which allows for the generation of high frequency turbulent fluctuations. In truth, the readings at each port depend on both the local turbulent wind speed and direction, and on the attitude of the aircraft. Pressure fluctuations at these ports along with a measure of static pressure were combined with the output of the GIN allowing resolution into northwards: v_{turb}, eastwards: u_{turb}, and vertical: w_{turb}, wind components.

Data drop-outs occurred infrequently in one or more of the components (≤ 0.01 %). Large excursions from the mean occurred with a similar frequency. It is thought that the cause is related to the aircraft positioning data, but the occurrence is low and the cause was not investigated. Spurious large excursions from the mean were determined by assessing the standard deviation calculated over 3200 records (100 s). A point was marked as "bad" if it was found to be more than three standard deviations away from the mean for horizontal wind components, and more than 5 standard deviations for the vertical wind component. An unbroken data record is necessary for making turbulence measurements and so where missing data, or bad data, were found in the 32 Hz record they were replaced with a simple nearest-neighbour interpolation. These points occur at such low frequency that

the impact was assumed to be negligible.

The aircraft *AoA* and *AoSS* parameters (Woolley, 2009a) were determined from this wind vector and the previously computed aircraft attitude variables. Along-heading mean wind errors were found to be present in the turbulence probe data on flight B674. Errors could be further minimised by an improved TAS calibration, but this it not essential for turbulence measurement since the mean is removed. No problems due to icing of the turbulence probe pressure ports were observed during B674.

2.3.2 2D Horizontal "Bulk" Wind Components

Along-heading wind errors were present in the turbulence probe data from 2^{nd} February 2012 (B674) and so low resolution (1 Hz) horizontal wind data were taken from "bulk winds", calculated as the resultant vector between aircraft ground speed and airspeed vectors (Woolley, 2017). Data from the science GPS system and the aircraft RVSM (Reduced Vertical Separation Minima) system were combined and the wind vector resolved into eastwards: u_{bulk}, and northwards: v_{bulk}, wind components. Wind speed: ws_{bulk}, and wind angle: wa_{bulk}, were then resolved. Bulk wind components were only calculated when the aircraft was in straight and level flight. An offset of 0.35° was first applied to the aircraft heading measurements to account for slight offsets within the system (*pers. comm.* A. Wellpot, FAAM).

2.3.3 Turbulent Fluctuations and TKE

Turbulent flux profiles are typically calculated using Reynolds decomposition (e.g. French et al. (2007), Petersen and Renfrew (2009)) from a vertical stack of level

flight legs. The flight pattern from the altocumulus flight on 2^{nd} February 2012 did not result in segments suitable for Reynolds decomposition, and so by removal of a low-pass Butterworth-filtered time-series the high frequency time-series of fluctuations of horizontal: u', v' and vertical: w' wind fluctuations were generated. Lenschow et al. (1988) is perhaps the first to have done this and others have used this method for analysis of stable boundary layers (e.g. Mahrt (1985), Brooks et al. (2003)). This is the first example of the technique being employed in the mid-troposphere in altocumulus clouds, and it was applied to both slant profiles and level flight segments.

A suite of 4-Pole low-pass Butterworth filters were constructed with filter lengths that ranged from 1.5 km to 16 km to investigate the impact on the derived fluctuations of thermodynamic parameters (Table 2.3). It was assumed that TAS = 140 m s^{-1} throughout the measurement period as the true value varied by less than 5%. The theoretical vertical offset was calculated using the nominal vertical rate of change of 1000 ft min^{-1}. The literature reports that the Butterworth filter should be applied in both directions in order to not phase shift the data (e.g. Petersen and Renfrew (2009), (Brooks et al., 2003)). The implications of this omission are not thought to be important for magnitudes of calculated fluctuations of wind components.

Once the low-frequency variations in wind components are removed an estimate of Turbulence Kinetic Energy (TKE) was computed from the residual high-frequency fluctuations were for each filter length using

$$TKE = \frac{1}{2}\sqrt{u'^2 + v'^2 + w'^2}. \tag{2.1}$$

The impact of filter length is considered in Chapter 3.

Filter Lengths [km]	1.5	3.0	5.0	6.0	9.0	12.0	14.0	16.0
Filter Frequency [Hz]	0.093	0.046	0.028	0.023	0.015	0.011	0.010	0.0088
Vertical Offset [m]	54	109	181	217	326	435	508	580

Table 2.3: Butterworth Filter Lengths and Frequencies, used to investigate turbulence, including the minimum and maximum, along with selected intermediate values.

2.4 Thermodynamics and Humidity

2.4.1 Temperature

Two Goodrich Type 102 platinum-resistance thermometers were fitted to measure temperature, one within a de-iced Rosemount housing and one with an ambient temperature (non-de-iced) Rosemount housing and recorded at 32 Hz (Woolley, 2009b). The instruments typically measure to within 1° C of each other. The non-de-iced probe data was selected for use on flight B674 (2^{nd} February 2012) as no evidence of contamination by LWC on the non-de-iced probe was apparent and the de-iced probe suffered from spurious excursions at high frequency. The non-de-iced sensor was used on B668, (23^{rd} January 2012) as no impact of supercooled water was observed on this sensor and the de-iced sensor had excessive noise on the signal of over 6 K. The de-iced sensor was used on the cumulus cloud sampling during B816 (24^{th} November 2013) because the higher liquid water contents and larger cloud particle sizes would be expected to contaminate the data from the non-de-iced probe.

Potential temperature, θ, is calculated using the approximation from (Bolton,

1980):

$$\theta = T_K \left(\frac{P_{ref}}{P} \right)^{R_d/c_p}. \tag{2.2}$$

2.4.2 Humidity

Humidity data, at 0.4 Hz, were provided by a WVSS2 (Water Vapour Sensing System Mk. 2) near-infrared Tunable Diode Laser (TDL) absolute humidity spectrometer which was fitted to a flush mounted inlet (Vance et al., 2014). The instrument reports humidity volume mixing-ratio, *vmr*, by measuring the absorption of light by the optical depth of water vapour molecules in the path length of the sensing chamber. The benefit of using a TDL hygrometer is the fast response to sharp changes in humidity as compared to the slower response of a chilled mirror hygrometer, as discussed by Stevens et al. (2003).

High frequency measurements of total water content, q_t were made using an evaporative technique to measure the combined humidity from vapour, liquid and ice phases. The Total Water Probe (Nicholls et al., 1990) has a set of heaters that evaporate any condensed water and a Lyman-Alpha lamp and detection system to measure the total amount of humidity in the atmosphere. The instrument is fast (64 Hz), but the calibration drifts over time, and so the data are referenced to the more stable WVSS2.

Dew point temperature, T_d, was calculated by converting the humidity volume mixing ratio, *vmr*, from WVSS2 into specific humidity, q, using

$$q = vmr \times {}^{R_d}/_{R_w} \tag{2.3}$$

and converting to mixing ratio, r,

$$r = \frac{q}{1-q} \tag{2.4}$$

and then computing dew point temperature using Equation 4.15b from Stull (2015)

$$T_d = \left[\frac{1}{T_0} - \frac{R_v}{L}\ln\left(\frac{r \cdot P}{e_0 \cdot (r+\epsilon)}\right)\right]^{-1}. \tag{2.5}$$

The measured humidity was converted to Relative Humidity w.r.t. liquid, RH_{liq}, and ice, RH_{ice}, using saturation vapour pressure formulations, for liquid from (Wexler, 1983), and for ice from (Goff and Gratch, 1946) as reported by Murphy and Koop (2005). The exact form of saturation vapour pressure formulation does not have a huge impact at the temperature ranges in this current study.

2.5 Bulk Cloud Properties

2.5.1 Cloud Top Height: Lidar

When the aircraft was above cloud, a nadir-pointing Leosphere ALS450 355 nm elastic backscatter and depolarisation aerosol lidar enabled the measurement of cloud top height. Processing details for aerosol observations are given in Marenco et al. (2011). The return from liquid cloud is strong and so averaging time is reduced from that study to 2 s (*pers. comm.* - Franco Marenco) and thresholds on the backscatter profile are applied as stipulated by Allen et al. (2014). This resulted in a spatial horizontal resolution of between 200 m and 300 m and the range gate resolution of 1.5 m is taken to be the location error in the vertical. Altitude bias introduced by the GPS system is not accounted for, since data are

considered relative to one another and so this is not necessary.

2.5.2 Condensed Water Content: Nevzorov Probe

A Nevzorov hot-wire probe (Korolev et al., 2008) with a deep-cone total-water content sensor and a liquid-water content sensor were used to provide bulk measurements of Liquid Water Content (LWC) and Total (condensed) Water Content (TWC) at 32 Hz. The probe operates by measuring the increase in power required to evaporate impinging cloud particles and maintain a constant wire set-point temperature. The magnitude of the power is related to the mass of the impinging condensed water by the latent heat of vapourisation of either liquid, Lv_l or ice, Lv_i. The TWC sensor responds to both liquid- and ice-phase condensed water. The LWC sensor is designed to only respond to liquid water, because ice particles should bounce off the sensor before being evaporated, although there is some residual sensitivity to ice, of the order 10 % of the total IWC.

The processing of hot-wire type bulk water probes requires removal of the dry-air baseline drift in order to achieve the best possible accuracy of the measurement (Abel et al., 2014). The baseline of a bulk water probe varies with atmospheric conditions and if mounted on an aircraft will also depend on parameters such as the aircraft airspeed and potentially attitude. Essentially the baseline drift is a function of the magnitude of the cooling of the heated wire due to aspiration by the airflow over it. Where bulk water measurements are used the baseline was removed according to the scheme presented by Abel et al. (2014) resulting in a sensitivity $\pm$ 0.002 gm^{-3} on Condensed Water Content (CWC) measurements.

Additionally, the Nevzorov TWC probe was used to derive a clear-flag (cloud-free) (Section 4.7.2) and, for this purpose, only the raw power is considered, without

conversion to physical units of condensed water mass. The method exploits the fact that variability in-cloud is very different from that out-of-cloud. A 1 Hz time series of the standard deviation of power was computed from the 32 Hz data record of power, and thresholds placed on this parameter to partition the data into cloud-contaminated and clear-sky time periods. A "safety window" of either 2 s or 5 s was applied to the derived clear-sky flag to account for in-cloud variability, potential timing offsets between individual logging system clocks, and cloud edges where the CWC may fall below the sensitivity of the probe. The impact of different threshold values was investigated.

2.6 Cloud And Aerosol Microphysics Instrumentation

Cloud microphysics instrumentation was fitted to the aircraft in wing-mounted pods known as PMS (Particle Measuring Systems) Canisters. These instruments use a laser light source to illuminate a sample volume. Particles that are intercepted break the beam and are detected by some method and properties of the particle can be inferred by the detection system. A range of detection techniques are necessary in order to sample the full size range expected, from aerosol particles as small as 0.1 μm up to precipitation sized particles larger than 1 mm.

The cloud and aerosol microphysics probes that were used in this study are presented in Table 2.4, although not all were flown on each flight. Liquid cloud properties were measured using an Optical Particle Counter (OPC), the CDP (Cloud Droplet Probe) (Section 2.6.4) (DMT, 2016). Precipitation size particles were measured with a suite of Optical Array Probes (OAP) (Section 2.6.5): the 2DC (Two-Dimensional Cloud Probe); CIP15 and CIP100 (Cloud Imaging Probe, 15 μm and 100 μm) (all DMT (2016)), and 2DS (Two-dimensional Stereo Probe)

(SPEC, 2017). Cloud particles were imaged using a Cloud Particle Imager (CPI) (Section 2.6.6) (SPEC, 2017). Aerosol particles were sampled with a Passive Cavity Aerosol Spectrometer Probe (PCASP) (Section 2.6.2) (DMT, 2016) with supporting measurements from CDP. SID2 (Small Ice Detector 2) (U. Herts.) was used to measure small liquid and ice particles (Section 2.6.7)

2.6.1 Particle Shattering

Previous measurements from aircraft of the number and size of small atmospheric ice particles have been hampered by shattering of ice particles on probe leading edges. Recent developments, such as the addition of anti-shatter tips to the leading edges of probes, have begun to address this particular problem (Korolev et al., 2011). Where applicable all probes had anti-shatter tips fitted, including CDP, 2DC, CIP15, CIP100 and 2DS. Algorithms, based on the interarrival times of particles, were applied to CIP15 and CIP100 data using SODA2 (System for OAP Data Analysis version 2 (Bansemar, 2016)), in order to identify shattering artefacts (Field et al., 2003, 2006). Maximum observed ice crystal diameters were often less than 1 mm in this study and so the impact of shattered ice fragments on microphysical measurements is expected to be low. Careful inspection of particle imagery from the OAP probes supports this. SID2 is relatively immune to shattering due to the open path design and the lack of shattering surfaces. CPI is liable to shattering as the probe is fed by an inlet.

2.6.2 PCASP

In the Passive Cavity Aerosol Spectrometer Probe (PCASP), ambient aerosol particles are drawn into a sampling cavity through an aspirated needle which

Name	D_{min} [μm]	D_{max} [μm]	Res. [μm]	# Bins	SA_Q [mm^2]	SA_E [mm^2]	Phase	Technique*	Reference	Manufacturer
PCASP	0.1	3.0	≈ 0.1	30	n/a	n/a	no	*S*		DMT
CDP	5.0	50.0	≈ 1	30	0.30 ± 0.04	2.7 ± 0.04	no	*FS*	Lance et al. (2010)	DMT
SID2	1	100	≤ 1	arbitrary	0.88	60.0×0.88	yes	*FS*	Cotton et al. (2010)	U. Herts.
2DS	10	1280	10	128			only $\geq 40\mu$m	*OAP*	Lawson et al. (2006)	SPEC
CIP15	15	960	15	64			only $\geq 60\mu$m	*OAP*	Cotton et al. (2013)	DMT
2DC	25	800	25	32			only $\geq 100\mu$m	*OAP*	Knollenberg (1970)	PMS
CIP100	100	6400	100	64			only $\geq 400\mu$m	*OAP*	Cotton et al. (2013)	DMT
CPI	4	1000	≈ 4	arbitrary			only $\geq 50\mu$m	*HSI*	Connolly et al. (2007)	SPEC

Table 2.4: Cloud Physics Instrumentation. Comparison of size range, Resolution (Res.), Sample Area (SA) - Qualified (Q) and Extended (E), and technique for the cloud physics and aerosol probes. *Technique: *S*: scattering, *FS*: forward scattering, *OAP*: OAP Shadow Imaging, *HSI*: high-speed imaging.

directs the particle flow through a laser beam protected by a dry sheath flow (Knollenberg, 1970). Aerosol particles with dimensions between 0.1 μm and 3.0 μm are detected as they intercept the beam, by collecting the scattered laser light using parabolic mirrors over a wide forwards and backwards angular range.

The intensity of the detected light pulse is related to the particle size by Mie-Lorentz Theory, using the refractive index of the material and assuming a spherical particle. The PCASP was calibrated at FAAM (Nott, 2013) using di(2-ethylhexyl)sebacate (DEHS) which had been size segregated using a DMA (Differential Mobility Analyser) and the method of Rosenberg et al. (2012). The calibration that is relevant to the PCASP data from flight B674 is the "pre-MEVALI" campaign calibration, performed at FAAM on 23^{rd} February 2012.

PCASP aerosol data are only valid when out of cloud. Contamination due to break up of cloud and precipitation particles contaminates the in-cloud data. A cloud-free "flag" was generated using data from the Nevzorov TWC probe (Section 4.7.2) to segregate the data.

Aerosol Number Concentration

Aerosol Number concentration, N_A, is given by

$$N_A = count_A / F_{pcasp} \tag{2.6}$$

where the sample flow rate, F_{pcasp}, is the measured flow rate, typically 1.0 ± 10 % cm^{-3} at STP (Standard Temperature and Pressure). There is no information regarding the particle shape, and so, particularly for non-spherical particles such as mineral dust, the optical size may not be strictly related to the particle geometric size.

2.6.3 Particle Size Distribution

The individual particle sizes from PCASP can be composited over a fixed time period, by default 1 s, and were placed initially into 30 size bins with calibrated dimensions. The procedure is analogous for the CDP, 2DC, CIP15, CIP100, and 2DS. Following Ryder et al. (2013) the data from bins adjacent to gain-stage cross-overs in the PCASP were summed into a single, wider, bin, namely bins 4 and 5, and bins 15 and 16. The lowest size channel was rejected as the lower bound is unknown. The calibrated bin dimensions for PCASP (and other probes) are presented in Appendix A.

Particle Size Distribution Errors

The relationship between scattering cross-section and geometric size is non-monotonic and so there is uncertainty in the method. For this reason, and to account for potential step-changes in the calibration and misalignment of the probe, a sizing error of at least plus or minus one bin was assumed.

With all particle probes there is a counting uncertainty, assumed to obey Poisson counting statistics, where the magnitude of the uncertainty is the square root of the numbers of counts in the bin.

A composite error was calculated by combining fractional errors from each contributor: bin size, counts and flow rate. It is apparent that, even for low bin counts, the major contribution to the uncertainty in PCASP was from the sizing.

Absolute minimum Limit-of-Detection (LoD) per bin was calculated for aerosol data from PCASP by assuming that a single particle falls in to the bin in the averaging period time. When concentrations are low the counts from adjacent

bins can be combined to make a new wider bin. A new set of bin dimensions was defined by combining two adjacent bins (or three bins in the case of the largest 9 bins, and where gain-stage cross-overs are present), to produce a 12-bin size distribution. This reduces the counting statistics errors as there are greater numbers of counts-per-bin and LoD is reduced by up to an order of magnitude. Determination of the bin dimensions is also improved because the uncertainty of the bin edge locations is the same as at full-resolution, but is a much smaller fractional error.

Log-normal fitting

Log-normal curves were fitted to the PCASP aerosol particle size distribution using a similar method to Ryder et al. (2013), in part to verify the aerosol observations and to validate the clear-flag (Chapter 3). Initially, three log-normal curves were fitted to the full resolution data using

$$\frac{dN}{d\log D} = \sum_{mode=1}^{3} \frac{N_0}{\sqrt{2\Pi}} \frac{1}{\log \sigma d_p} \exp\left(-\frac{\left(\log d_p - \log \overline{d_p}\right)^2}{2\log^2 \sigma}\right) \tag{2.7}$$

to account for two accumulation modes and a large particle mode where d_p is the particle mode-diameter, N_0 is number concentration, and σ is the standard deviation (Seinfeld and Pandis, 2006). These values were then used to initialise a two-mode log-normal fit to the downgraded resolution data, for a single (the larger) accumulation mode, and a large mode. The cumulative sum in the large mode was then used to infer the numbers of large aerosol for input into Ice Nucleating Particle (INP) parametrisations. Start parameters, intermediate values and final parameters are presented in Appendix B.

2.6.4 CDP

Liquid cloud particles between sizes 5 μm and 50.0 μm were counted and sized using forward scattering over a narrow angular range of 4° to 12° using the Cloud Droplet Probe (CDP) (Lance et al., 2010). The sized particles data were composited at a frequency of 1 Hz into 30 calibrated size channels (as per the PCASP, Section 2.6.3). The performance of the probe was monitored using glass spheres of known diameter using the method presented in Rosenberg et al. (2012). The CDP was calibrated prior to PIKNMIX and additional glass bead checks were routinely performed throughout the field-campaign to ensure that there was no drift in the performance. Bin dimensions are given in Appendix A. Sizing uncertainty due to non-monotonic Mie-Lorentz scattering occurs in this instrument.

CDP does not give information regarding particle shape and so in cloud all particles are treated as spheres. Forward scattering probes are known to suffer from artefacts when determining particle diameter in the presence of ice in liquid clouds and interpretation of the droplet spectra requires caution in these conditions (Gardiner and Hallet, 1985), where FSSP (Forward Scattering Spectrometer Probe) signals were inconclusive. Both CDP and FSSP operate in a similar manner, by detection of forward scattered light from cloud particles. Further study on this problem by Gayet and Febvre (1996) revealed that FSSP responded well to spherical ice particles such as those in contrail cirrus clouds but not to those ice particles in natural cirrus, which narrows down the source of the problem in Gardiner and Hallet (1985) to one of poor response to non-spherical particles. This may in part be due to the signal qualifier (also present on a CDP), or that the Depth of Field (DoF) is wider for a non-spherical particle. The probe is sensitive to ice particles but uncertainty in the scattering phase function of an ice crystal means that accurate sizing is impossible (Chen et al., 2006).

The cloud drop number concentration, N_d, was calculated from the number of counts divided by the sample volume, V_{sample},

$$N_d = count_d / V_{sample} \tag{2.8}$$

where sample volume was determined from the sample area, SA, and TAS using

$$V_{sample} = TAS \times SA. \tag{2.9}$$

Table 2.4 gives probe specific sample areas for SA_E: Extended Sample Area and SA_Q: Qualified Sample Area.

When out of cloud, on flight B674, the CDP data were used to measure the number concentration of large aerosol particles. Number concentrations were expected to be low, and so adjacent bins were combined as for the PCASP in order to reduce statistical errors (see Appendix A). Particle shape and complex refractive index were unknown and un-knowable, leading to uncertainty in the scattering phase function and hence size.

2.6.5 Optical Array Probes (OAPs)

Larger particles, be they liquid or ice, were counted and sized with Optical Array Probes (OAPs), also known as shadow imaging probes. OAPs detect and size particles by recording the shadow cast by the object particle on a previously illuminated linear detector array as it is moved through the sample volume with aircraft motion. Four different OAPs were flown in various combinations across the three flights in order to sample the full size range of ice particles from 40 μm up to and larger than 1 mm. The 2DS (Two Dimensional Stereo Probe) (Lawson

et al., 2006) has a pixel resolution of 10 μm with 128 elements. The CIP15 (Cloud Imaging Probe 15 μm) and CIP100 (Cloud Imaging Probe 100 μm) each have 64 elements and pixel size of 15 μm and 100 μm respectively (DMT, 2016). The 2DC (Two Dimensional Cloud Probe) (Knollenberg, 1970) has 32 pixels at 25 μm pitch. Bin width in these probes is constant and thus, determination of the bin dimensions is trivial and is not reproduced here.

Particle sizing is complex even for spherical liquid drops, in part because the size of the projected imaged particle is partly related to its position within the DoF, but is well described by Fresnel diffraction for spherical liquid particles (Korolev et al., 1991). Number concentration and the measurement of the particle size distribution is also hampered by the particle size-dependent DoF (Knollenberg, 1970). Discretisation of the shadow image and non-zero instrument response time lead to losses of particles smaller than $\approx$ 4 pixels (100 μm for 2DC) (Korolev et al., 1998b). The finite time response also leads to uncertainty in sizing for sub-500 μm particles and particularly sub-100 μm particles (Strapp et al., 2001). Accurate sizing of ice is even more complex.

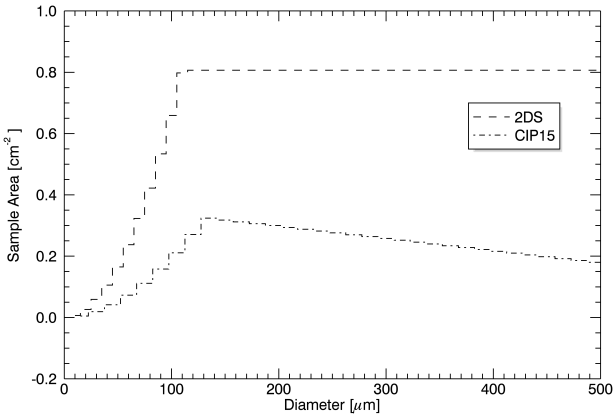

Figure 2.1: Size dependent sample area from CIP15 and 2DS

Figure 2.1 shows a representation of the particle size-dependent sample area for

CIP15 and 2DS, up to 500 μm (Korolev et al., 1991; Lawson et al., 2006). The sample area in 2DS reduces at sizes $\leq$ 100 μm and for CIP15 $\leq$ 125 μm. At larger sizes the effective sample area reduces also, because larger particles begin to extend beyond the width of the detector array. Sample Volume (Equation 2.9) is calculated from these sample area measurements and TAS. Assuming an error of 3 % on TAS, the total error in sample volume is calculated, shown in Figure 2.2a for the CIP15 as an illustrative example. The errors in sample volume can be up to 100 % for the smallest size bins Figure 2.2b, represented by the interior (smaller) error bar, showing it contributes the majority of the uncertainty.

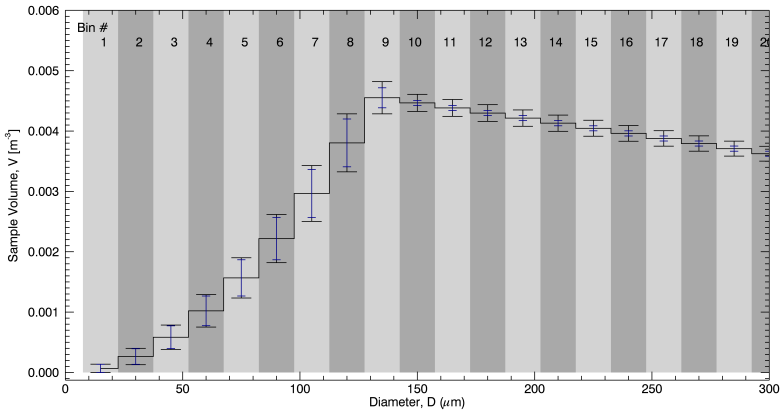

(a) CIP15 Sample Volume

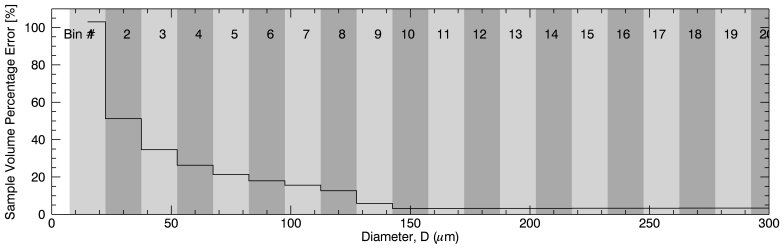

(b) CIP15 Sample Volume Errors

Figure 2.2: Size dependent sample volume for CIP15 assuming True Airspeed of 140 ms^{-1} (upper panel) and percentage error (lower panel).

The CIP15 and CIP100 data were processed using the SODA2 package (Bansemar, 2016) from NCAR (National Centre for Atmospheric Research). The specific

settings used here were i) to not reconstruct particles that are at the edge of the diode array, and ii) not apply corrections for out-of-focus liquid drops. The assumption was that the particles were not all liquid. However, CDP data do show on flight B674 that some liquid particles were present that were large enough to be detected by the CIP15 probe (considered more completely in Chapter 5). OAP probes occasionally suffer from "stuck bits" where one pixel remains constantly "on". Inspection of the imagery did not indicate that this problem occurred for any of the pixels and so the option to correct for "stuck bits" was turned off. 2DC data were processed at FAAM using the core processing (Nott, 2017) with variable DoF (Depth of Field) as given by Heymsfield and Parrish (1978). 2DS data were supplied by *I. Crawford* (U. Man.) following processing using the OASIS Optical Array Shadow Imaging Software package as described by Crosier et al. (2014); Taylor et al. (2016). Specifically (Taylor et al., 2016, Appendix A), the Heymsfield and Parrish (1978) variable DoF, and rejection of particles with short interarrival times ≤ 1 μs (Field et al., 2006). Poorly imaged particles with fewer than 80 % imaged pixels were rejected as were particles with an aspect ratio larger than 5:1 (streakers). The OASIS software allows for categorisation of particles by phase (specifically degree of irregularity). Particles are given a status of low, medium of high irregularity, which can be used to assess the occurrence of ice and liquid particles in a sample.

Counts per bin were corrected for variable DoF and ice particle number concentration, N_i was calculated using

$$N_i = \left(\frac{\sum_{bin=1}^{n_{chn}} count(bin)}{DoF(Fn(bin))} \right) / (SA \times TAS) \tag{2.10}$$

by summation of the counts across all size channels and using sample area as

shown in Table 2.4. For the 2DC probe, and CIP15 and CIP100, the IWC was calculated from the integrated size distribution and from 2DS using the maximum ice particle dimension (Crosier et al., 2011), all using the mass-dimensional relation from Brown and Francis (1995).

OAP probes are able to distinguish between phases by assessing the shape of a particular shadow image, but only for particles larger than a certain minimum size which is dependent on the number of pixels in the image (Korolev, 2007b). Probes require more than 5 shadowed pixels for an assessment of the particle size and habit to be made. Data processing for 2DS categorises particles based on their degree of irregularity from spherical. These data have been processed using the method in Crosier et al. (2011) and the same limits as presented in Taylor et al. (2016, Appendix A1).

A major aim of this study is to identify and size the ice particles that are embedded within liquid cloud regions where liquid drops are smaller than 50 μm but that is not straightforward with the current generation of probes. All OAPs are unable to identify the phase or habit of a particle with such small size. The best probe with which to identify the smallest ice is the 2DS, which flew on B816; the cumulus cloud flight. On the altocumulus flight only the CIP15 and 2DC were fitted, giving a minimum phase-distinguishable particle size of the order 75 μm. Careful analysis of the data and combination with the CDP measurements and CPI observations may permit reduction of this minimum size.

2.6.6 Cloud Particle Imager (CPI)

The CPI (Cloud Particle Imager - SPEC (2017); Connolly et al. (2007)) provides imagery of individual cloud particles with sizes between 10 μm and 1 mm at an

optical resolution of ≈ 3 μm. Data are binned into 10 μm wide size bins between the extremes. For subsequent analysis of habit resolved size distributions, for this work the data from five adjacent bins are combined to make 50 μm wide bins. Habit and phase classification are possible to some extent, for particles larger than 50 μm. Bin dimensions are trivial to obtain and are not reproduced here.

The temporal resolution is not as fast as for scattering and shadow imaging probes as the data rate is limited by the length of time taken to read out the data buffer from the CCD (Charge Coupled Device) chip. The CCD camera results in the CPI having a relatively slow response and so sampling of low concentration particles is not reliable, in fact the sampling is biased towards those particles that are at the mode of the size distribution. The slow read-out time, combined with the small sample volume and uncertainties resulting from the flow field through the inlet, limits the utility for making statistically robust estimates of particle size distributions from this probe.

2.6.7 SID2: Small Ice Detector 2

The SID2 Small Ice Detector (Cotton et al., 2010) is an OPC that records forward scattered light from a single particle in the angular range 9° to 22° in a set of 28 azimuthally arranged sectors. The peak intensity measured by each element is recorded, once a dark-current background has been subtracted (Ulanowski, 2005). The probe can detect particles with spherical equivalent size ≈ 1 μm $\geq d \geq 100$ μm. The additional information recorded by the SID probes compared to CDP allows for determination of particle sphericity and phase and, in some cases, habit. In SID2, each particle is individually time stamped (much faster than 32 Hz), and it takes ≈ 50 μs for the probe electronics to recover from a sampling event (Johnson et al., 2014).

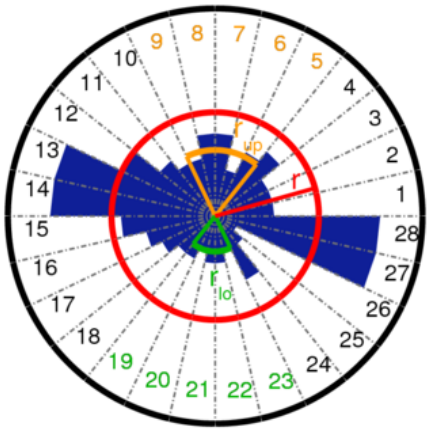

Figure 2.3: Simulated SID2 response to a synthetic non-spherical particle, showing the individual response, r, of 28 azimuthally arranged detectors (blue shading), mean response from all segment is shown in red. Super-sectors (see text for details): Upper, r_{up} (5 to 9): Orange, Lower: r_{lo} (12 to 23): green.

The sample volume is defined as being where the Field Of View (FoV) of a pair of photomultiplier tubes overlap. The pair of trigger-detectors activate the detection system when a particle breaks the laser beam by crossing into the sample volume. SID2 has a relatively large sample volume (Table 2.4) and has been successfully used in airborne field campaigns to make measurements of small, low concentration, ice particles (Cotton et al., 2010). The higher particle number concentrations often found within liquid and mixed-phase clouds are responsible for a large number of coincidence artefacts in SID2 data (Johnson et al., 2014). A new method for identifying and removing coincidence events is presented in this research.

SID2 Scattering Patterns

The scattering patterns from SID2 can be interrogated and the properties used to size the particle, and, in some situations, determine the phase (Section 2.6.7). A graphical representation of a scattering pattern from a synthetic non-spherical

particle is shown in Figure 2.3. The radius in each of the 28 sectors corresponds to the measured peak intensity in the detector element: the Sector Response, r, with the mean shown in red. New for this study, super-sectors are defined by segments 5 to 9 (upper, r_{up}) in orange and segments 19 to 23 (lower, r_{lo}) in green. These are defined for use in a coincidence-finding algorithm (Section 2.6.8). The scattering pattern from a perfectly spherical particle should have identical radius in each sector.

SID2 Scattering Pattern Rejections

Particles were rejected if the scattering patterns failed certain quality tests. Those tests follow those found in Johnson et al. (2014):

i) 9 or more detector elements are blank

ii) 10, or more, detector elements are saturated

iii) inter-arrival times are less than 50 μs, indicative of shattering

iv) negative signals occur on any detector: a result of digitisation errors within the probe electronics.

Using data from B674 it was found that blank detectors occurred on 1.4 % of recorded scattering patterns, possibly resulting from the poor sampling of larger aerosol, and were removed from the dataset. Negative detector values were screened for, to identify possible digitisation errors, but none were found. There were no rejections based on saturated detectors, probably because the incidence of large ice particles was low. For similar reasons, particle shattering incidence is expected to be low, and no evidence was found when interrogating the interarrival times. Unlike in Johnson et al. (2014), asymmetric pattern rejection using the strong

mode-1 in the particle FFT (Fast Fourier Transform) is not undertaken here. These off-axis/out-of-focus particles should be rejected by the coincidence rejection algorithm that is developed below (Section 2.6.8).

SID2 Particle Properties: Diameter and Asphericity

Particle water-equivalent geometric diameter, D, was calculated from the mean of individual detector element responses, $\overline{r}$, using

$$D = 2.15\overline{r}^{0.53} \tag{2.11}$$

which has the same functional form as in Cotton et al. (2010).

The pre-factor of 2.15 and the exponent of 0.53 are valid from the time of the CIRCREX campaign (CIRrus Coupled Cloud-Radiation EXperiment) onwards (*pers. comm.* J Ulanowski), and have likely drifted over time as a result of changing sensitivity of the photomultiplier tubes.

These data were manually binned into 40 size channels with 5 μm $\leq D <$ 100 μm, with details given in Appendix A. Ice is likely to be undersized using this method (Ulanowski, 2005) because there is insufficient information regarding the scattering phase function of an ice particle (e.g. Chen et al. (2006)). Size defined here is an expression of the relative size of similarly shaped particles, and may not apply directly to any observable geometric dimension. For this current study the main focus of the SID2 observations is on phase discrimination and number concentration and not absolute size.

The second SID2 parameter, the asphericity factor, A, (Cotton et al., 2010), was calculated from the sum of the individual detector elements deviation from the

mean using

$$A = \frac{k \sqrt{\sum_{i=1}^{n} (\bar{r} - r_i)^2}}{\bar{r}} \tag{2.12}$$

where the scaling factor

$$k = {}^{100}/\sqrt{n^2 - n} \tag{2.13}$$

maps the asphericity values to a scale between 0 and 100 for a detector with n elements. It will be shown later that this scale is misleading (Chapter 5).

Spherical particles return lower asphericity values, whilst ice particles have higher asphericity, which allows for some level of phase discrimination although there is no distinct boundary. A liquid cloud drop is expected to have A = 0.0, whilst non-spherical ice will have non-zero asphericity values. In practice, noise and measurement artefacts result in non-zero asphericity factors even for spherical liquid cloud drops. The impact of noise and off-axis sampling on the measured asphericity is large. Analysis of SID2 scattering patterns collected in warm liquid-only stratocumulus cloud show that asphericity can be even greater than 10.0 (Cotton et al., 2010). The source of this asphericity is explored in Chapter 5.

Detector Response Corrections

A modified Detector Response Correction (DRC) algorithm (Cotton et al., 2010) was applied to account for differences between individual amplifiers for each detector, and other instrumental artefacts. To locate the most spherical particles in the clouds on B674 a region was defined where the CDP reported liquid drop concentrations between 1 cm^{-3} and 10 cm^{-3} in order to minimise the probability of coincident particles producing non-spherical scattering patterns. Scattering patterns were then selected based on the first-pass diameter being larger than

5 μm and smaller than 25 μm and with the reported asphericity less than 1.2. This scheme resulted in a collection of nearly 14000 particles containing the most spherical particles encountered during the flight. Mean detector element response was calculated from these quasi-spherical particles and the DRC generated from the inverse of this response, resulting in individual detector element scaling factors between 95 % and 105 %. Scattering patterns were then reprocessed, resulting in updated diameter and asphericity values. Particle diameters remained unchanged at the significance quoted (0.01 μm) as expected because the mean of the DRC is very close to 1.0 and so the total magnitude of the scattering is constant. Asphericity values tended to show a 25% reduction indicating that the particles now have a more spherical representation.

2.6.8 Coincidence in SID2

The detector of a SID probe is sensitive to light that comes from a wider area than the well-defined trigger regions. Particles that are outside of the well-defined sample area may still have an impact on the scattering pattern recorded by the detector if they are present in the extended sensing volume when the probe is triggered (Ulanowski, 2005). These events can happen when an object particle passes into the sample volume and triggers the probe whilst a second particle is present in the extended sensing volume, and is defined as a "Coincidence Event". The extended sensing volume is poorly constrained, and is a major limitation of the technique. It is defined by (Cotton et al., 2010) to be 12.3 mm^3.

Coincidence events between two spherical particles occur increasingly often as cloud particle concentration increases and lead to errors in sizing, and result in an asphericity which is higher than would be expected. This results in the artificial-broadening of the asphericity distribution. Ice-liquid coincidences will

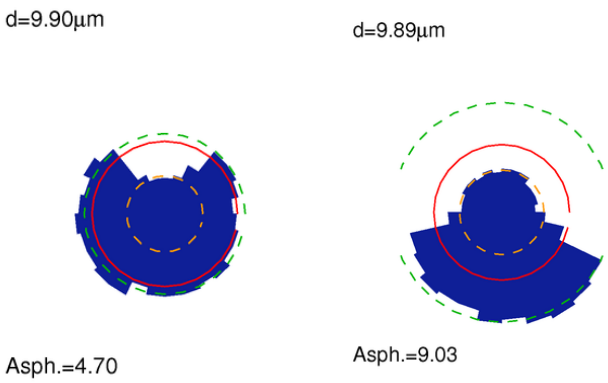

Figure 2.4: Examples of SID2 Scattering Patterns generated by coincidence events. The axis of alignment of the sample volume is vertical, Left: "upper" Coincidence, Right: "lower" Coincidence.

occur too infrequently to trouble the measurements.

The frequency of coincidence is predictable assuming that the cloud particle events occur randomly and thus follow Poissonion statistics (Johnson et al., 2014). Cotton et al. (2010) suggested that an upper limit for concentration before coincidence errors become unacceptable is 30 cm^{-3} which results in a coincidence frequency of $\approx$ 5 %, or 1.5 cm^{-3}. A limit of this magnitude may be acceptable when the focus is on liquid cloud particles, however, ice particle concentration is of a much lower order of magnitude and so these errors are unacceptable when attempting to quantify the small ice concentration in mixed-phase cloud.

An algorithm was defined to attempt to identify and remove coincidence events. The SID2 sensing volume is elliptical in shape and so any coincidences between two particles will be preferentially aligned along the major axis, resulting in two types of coincidence, with canonical examples for "upper" and "lower" coincidences shown in Figure 2.4. The two super-sectors are aligned with the major features of these scattering patterns.

The mean super-sector response can be calculated from the 5 bins in each sector,

sr_{up} and sr_{lo}, and the range calculated using

$$Range = \left| sr_{up(5)} - sr_{lo(5)} \right|, \tag{2.14}$$

which can also be presented as a percentage of the derived diameter. The intra-segment variability was calculated as the sum of the absolute deviation of each element from the mean super-sector response, Δ_{up} and Δ_{lo}. This measure is not statistically robust but indicative of similarity of detector response within the super-sectors.

Coincidence was identified if the particle scattering pattern satisfied the following two tests:

- Difference between r_{up} and $\mathrm{r}_{lo} \leq 20$ %
- Low intra-segment variability, Δ_{up} and Δ_{lo}.

It can be seen in the scattering patterns from coincidence events in Figure 2.4 that there is very low fractional variability between the detector element responses in each super-sector, something that is attributed to the spherical nature of the particles involved in the coincidence event, and assumed to be general. Limits were chosen to be $\Delta_i \leq 0.150$ and $\Delta_{ii} \leq 0.450$. The limit for both super-sectors was initially set to the more strict value of 0.150. However, this resulted in many manually identified coincidence events being undetected. Subjective optimisation by manual inspection of the scattering patterns resulted in the increase in value of one (either) sector to 0.450. The reason for the need to have different limits for the upper and lower super-sectors is not understood. The algorithm is also expected to positively flag for removal any highly asymmetric scattering patterns that Johnson et al. (2014) may have identified using FFT analysis.

2.6.9 Particle Concentrations from SID2

Particle number concentration for ice and liquid is calculated as in Cotton et al. (2010), using

$$N_{l,i} = \frac{f_{l,i}}{\gamma V_{sample}} \tag{2.15}$$

where the sample volume scaling factor

$$\gamma = 1.0 - 50e^{-6} \times (f_{rej} + f_{dead}) \tag{2.16}$$

was applied to account for probe-dead time due to rejected scattering patterns, f_{rej} (including coincidence, blank detectors, saturated detectors, IAT), and for read out of accepted particles, f_{dead}. The sample area for SID2 is also size-dependent as seen for the OAP probes (Section 2.6.5). The correction factor only becomes significantly different from 1.0 for ice and liquid particles smaller than 10 μm and is not considered here (Ulanowski, 2005).

Both CDP and SID2 provided very similar estimates of concentrations of liquid cloud particles indicating that both probes worked similarly. Low concentrations of ice particles would not impact this comparison.

2.7 NAME Model

Observations of aerosol are put into context by using the Met Office NAME (Numerical Atmospheric Dispersion Model) model (Jones et al., 2007) to run back trajectories that are used to investigate the source regions for the airmasses. Meteorological data is from the MetUM global model, which at the time was running at a nominal horizontal resolution of 25 km (in the mid-latitudes) and

with 70 vertical levels between the surface and model top at 80 km. At a vertical level of 6000 m the model level is approximately 400 m deep, varying by around 10% between 5000 m and 8000 m. Processes such as turbulence and wet and dry deposition are not present in the model, it is simply a way of tracking where an air parcel has travelled from. The history of the airmasses over the few days represented here is likely to be complex, and involve various weather systems, cloud and precipitation formation, and uplift of aerosol and potentially wet and dry deposition. These are limitations of the back trajectory technique, and so the trajectories presented in Chapter 4 are only interpreted as a guide to the choice of which INP parametrisation might be appropriate.

Chapter 3

Observations of Aircraft Case Studies

Flight data were collected using the FAAM BAe146 Atmospheric Research Aircraft on three days, in three different types of mixed-phase cloud, altocumulus, stratocumulus and cumulus. These flights took place in the mid-latitudes, in a region around the UK and North Atlantic. The research concentrates on analysis of mixed-phase altocumulus cloud data collected during flight B674, on 2^{nd} February 2012. Supporting data from a boundary layer mixed-phase stratocumulus cloud were collected during flight B668 on 23^{rd} January 2012 and from a mixed-phase cumulus cloud encountered on flight B816 on 24^{th} November 2013. This chapter presents the data collected during those flights and describes the relevant properties of the clouds and the thermodynamic environment in which they were found.

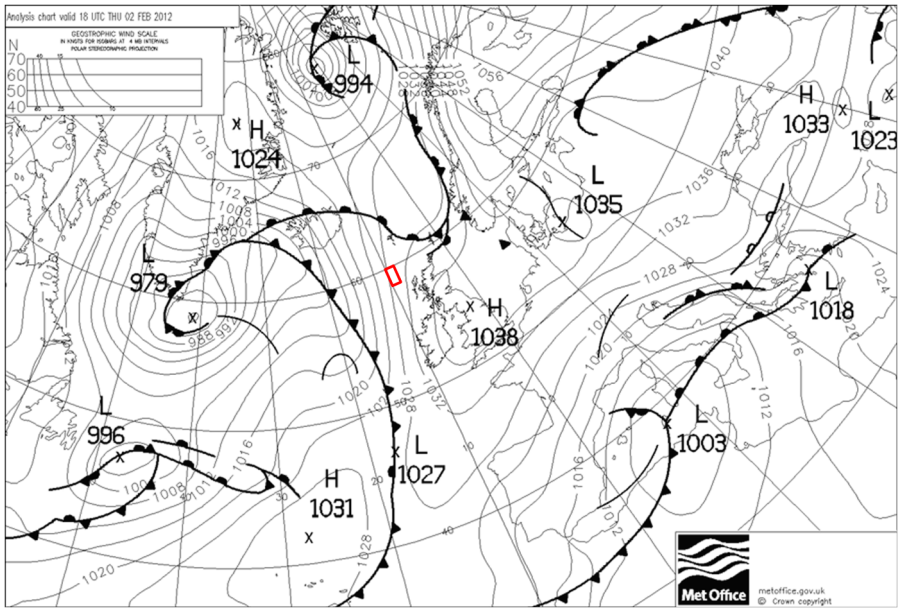

Figure 3.1: Means Sea Level Pressure Analysis chart valid for 1800 UTC on 2^{nd} February 2012 from UK Met Office for North Atlantic . The measurements were made in the warm sector to the north-west of Scotland, red box indicates the location of the airborne sampling.

3.1 Altocumulus Case, 2^{nd} February 2012

A mid-latitude cyclone was centred off the southern tip of Greenland on 2^{nd} February 2012. The warm front extended eastwards across Iceland towards Scandinavia, whilst the cold front extended roughly north-south over the Atlantic Ocean a few hundred kilometres west of Ireland (Figure 3.1). The broad warm sector covered the north-west of the UK with high pressure to the south and east. Measurements were made of a mixed-phase altocumulus layer cloud with precipitating ice virga in the warm-sector of a mid-latitude cyclone at 9.8 W along a track orientated north-south between 58 N and 60 N between 1600 UTC and 1900 UTC. The data collection began in the early afternoon, and the end of the measurement period was flown in twilight conditions.

Figure 3.2 shows 10.8 μm infra-red satellite images of (a) the North Atlantic region from AVHRR (Advanced Very High Resolution Radiometer) and (b) MSG (Meteosat Second Generation) for the northern half of the UK. Extensive layer cloud was observed within the warm sector. Close to the low pressure centre, west of 10 W, the cloud top temperature was colder than -50° C and away from here to the south-east the cloud top temperature was between -18° C and -29° C as estimated using Met Office products derived from MSG and NWP output (Figure 3.3). Discussion regarding this technique is in Hamann et al. (2014). Supercooled stratocumulus was present beneath the mid- and high-level cloud observed both visually from the flight deck and by satellite products through breaks in the higher level cloud.

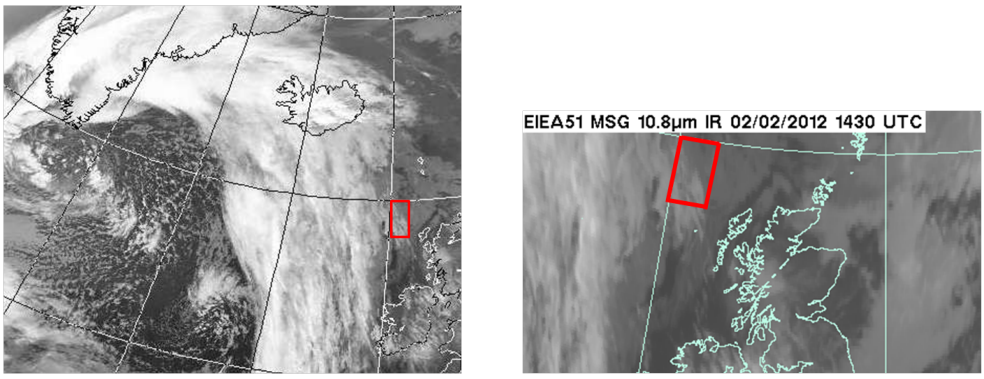

Figure 3.2: Infra-red satellite imagery (10.8 μm) on 2^{nd} February 2012 from (a) AVHRR (Advanced Very High Resolution Radiometer) at 1440 UTC and (b) MSG (Meteosat Second Generation) Satellite at 1430 UTC (© EUMETSAT/Met Office). Layer cloud associated with the warm sector is visible to the west of the UK. Red box indicates the location of the airborne sampling.

The aircraft measurements took place at the south eastern edge of the high cloud band to the north-west of Scotland. Constant altitude legs interspersed with slant profiles were flown between 4500 m and 7500 m. A layer of mixed-phase altocumulus with precipitating ice virga falling from a liquid layer was observed from the flight deck upon arrival into the area with the features visible in the

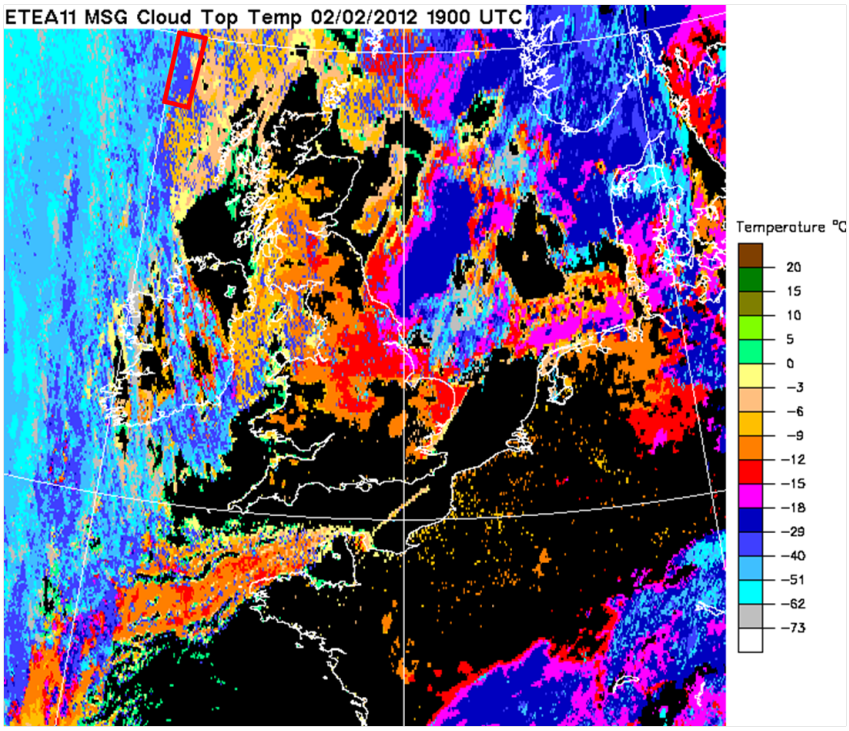

Figure 3.3: Cloud Top Temperature derived from MSG for 1900 UTC on 2^{nd} February 2012 (Hamann et al., 2014). Red box indicates the location of the airborne sampling

photograph in Figure 3.4. The choice of flight track was restricted by air traffic considerations and so it was impossible to advect with the cloud in a Lagrangian sampling strategy. Fortunately the north-south flight track was closely aligned to the direction of the mean wind.

Figure 3.5 shows the flight profile, in black, plotted on a latitude-altitude cross section. The potential temperature measurements, although not uniformly distributed throughout the section, were interpolated across the latitude-altitude space to give an overview of the thermodynamic environment in which the cloud was found. A freely-available software package was used to interpolate the data (Fanning (2017)). The liquid water content from CDP, in blue circles, and ice number concentration from CIP15 in red stars, were over plotted.

Figure 3.4: Photograph of the Altocumulus layer with precipitating ice virga, taken on arrival in the operating area at 1617 UTC, 2^{nd} February 2012. The broken cellular structure of the liquid layer cloud is visible. Ice virga can be seen below the liquid cloud, being advected with the mean wind from right to left. Boundary layer stratocumulus cloud is visible below. *Photo: S Abel.*

Visual observation from the flight deck, real-time inspection of in situ data and Figure 3.5 revealed that the cloud structure was typified by a thermodynamically well-mixed layer (hereafter the "mixed layer"), capped by a weak temperature inversion ($\approx$ 1 K). An optically thick liquid cloud was present below the inversion with a cellular structure and an estimated areal coverage of between 6 and 7 Oktas. Cloud top sloped from 5800 m and -31° C at the southern extent of the sampling region, to 5400 m and -27° C at the northern end. Wind was predominantly from the south and strongest in the north. Slant profiles were flown and indicated a pseudo-adiabatic liquid water structure with larger liquid water content towards cloud tops, similar to observations by Korolev et al. (2007). Cloud top temperatures in altocumulus are typically between -31° C $\leq$ T $\leq$ 0° C (Fleishauer et al., 2002) and so this cloud is one of the coldest expected.

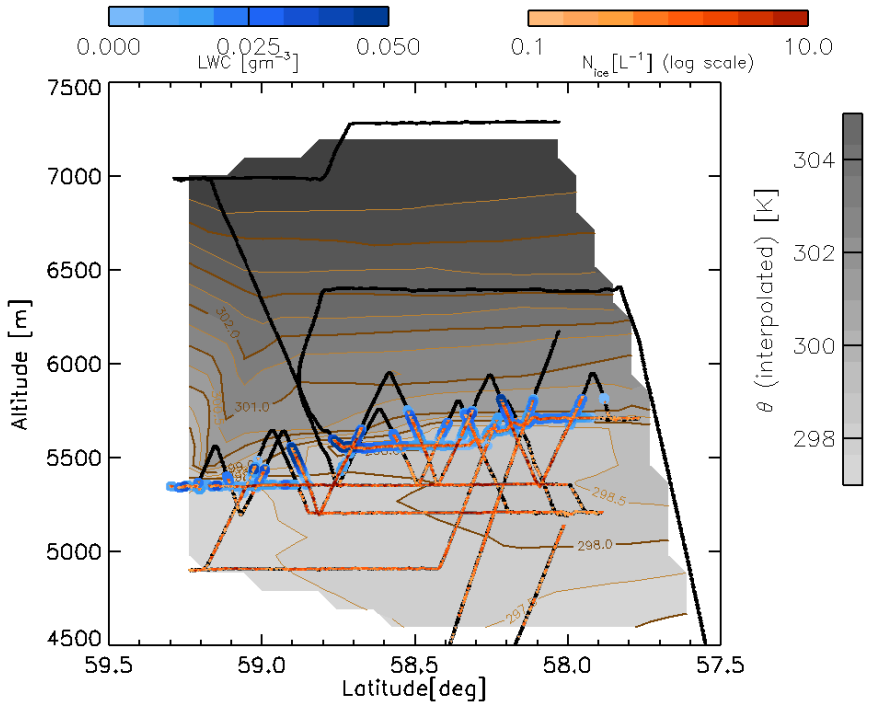

Figure 3.5: Aircraft altitude as a function of latitude from flight B674, 2^{nd} February 2012: black line, LWC from CDP: blue circles and N_i from CIP15: red stars. θ observations, interpolated in altitude-latitude: grey-scale contours.

3.1.1 Coordinate System

The structural similarity to stratocumulus permits analysis of the data relative to the inversion or cloud top altitude. In the free troposphere however the cloud systems are not constrained by a fixed surface at the bottom and are free to move along thermodynamically similar surfaces: isentropes. The sloping cloud top in this case resulted in an analysis challenge and so, to simplify, the variables were analysed in a new coordinate system that permitted comparison of thermodynamic and cloud and aerosol microphysical variables in the vertical.

Air traffic and airspace restrictions limited the flight pattern, and so the measure-

ments were made as the clouds moved through the sampling region. Horizontal coordinates were therefore converted to an air-relative position in the mixed layer to account for this advection. The altitude of the inversion capping the cloud topped mixed layer varied by 400 m across the sampling region, shown in Figure 3.5. It was practically impossible to fly at a constant altitude from inversion/cloud top. Given the slope, an aircraft would have to fly a constant ascent/descent rate of 100 ft min^{-1}. But, the minimum rate-of-change of altitude of the BAe146 is probably closer to 500 ft min^{-1} (*I. Ramsay-Rea*, Direct Flight Limited *pers. comm.*). The cloud top height information from the preliminary lidar leg would not be have been able to assist, since the limiting factor was aircraft performance. A cloud radar would not offer any benefit, because the liquid cloud layer was much thinner than the insensitive region of a cloud radar, close to the airframe, which is likely to be of the order 100 m up and down (Wang et al., 2012).

The new vertical coordinate was therefore specified in relation to a derived time series of inversion altitude or cloud top altitude, based on the individual spot measurements, and the air-relative horizontal coordinate. Mean wind speed as a function of latitude (Lat.) in the mixed layer was determined and then by accounting for this and the aircraft passage though the air volume, the air-relative coordinate was determined. It was assumed that wind speed and direction as a function of latitude remained constant throughout the sampling period and that the variation of wind speed with height was minimal. There was some degree of wind shear between the mixed layer and the free atmosphere above (not shown) and so only those data from below the inversion were used. Because the flight track was north-south the longitude (Lon.) was considered to be constant.

The mixed layer was humid compared to the relatively dry-air in the free-troposphere above and was identified by using total water content, q_t, as a tracer.

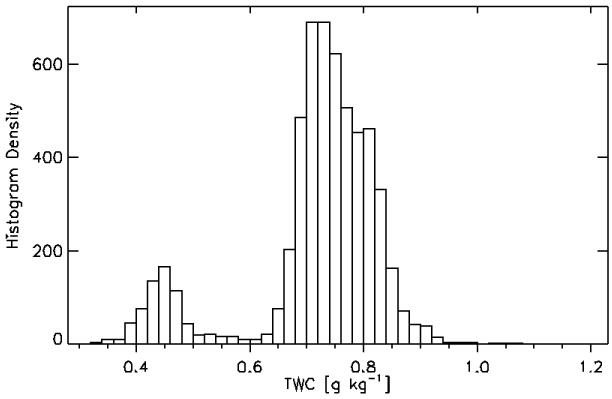

Figure 3.6: Total water content, q_t, distribution from 2^{nd} February 2012, B674. Bi-modal structure was used to determine the mixed layer data, which have $q_t \geq 0.62$.

Data at 1 Hz were considered between 1700 UTC and 1900 UTC in a region bounded by 58 N, 9.7 W and 60 N, 9.9 W in the altitude range 4.5 km to 6.0 km. In this volume the distribution of q_t was observed to be bi-modal (Figure 3.6). The mode of the dry layer was close to 0.45 gm^{-3} and the mode of the moist layer was close to 0.725 gm^{-3}. Data were defined as within the mixed layer if $q_t \geq 0.62$ gm^{-3} where a distinct minima was found between the two populations. Northerly bulk wind component data (v_{bulk}) were selected from this mixed layer and put in six equally spaced latitude bins, and the mean and standard deviation were calculated (Figure 3.7). Wind speed was lower in the south (6 ms^{-1}) than the north (8 ms^{-1}). Easterly bulk wind component (u_{bulk}) was $\leq 15\%$ of the northwards component, and was therefore considered to be negligible. Wind speed as a function of latitude was calculated from these observations using a linear fit, valid for the sampling period for the mixed layer.

Air-relative latitude coordinate was then calculated for each point along the flight track by modulating each location by the total amount of airmass advection

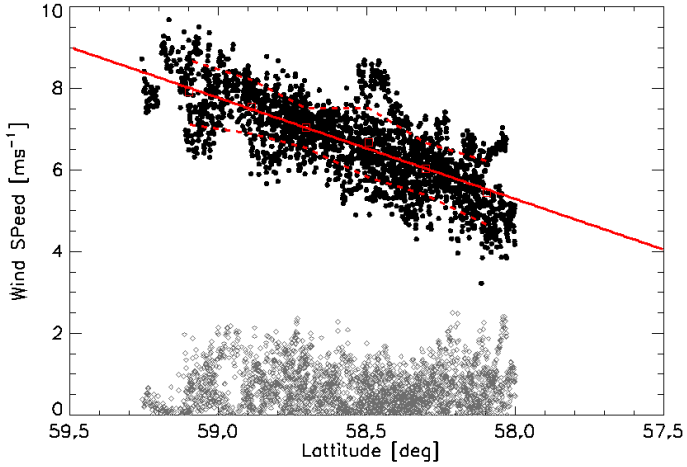

Figure 3.7: Wind speed as a function of latitude from B674 mixed layer observations (northwards component *(v_{bulk})* in black filled circles, eastwards component *(u_{bulk})* (absolute value) in empty grey diamonds). Linear fit to the data: solid red line. Empty red squares: latitude bin mean, and red dashed lines, one latitude bin standard deviations.

during the time since the start of the measurement period. Once the horizontal coordinate was specified, the vertical coordinate could be derived from observations of inversion altitude and cloud top altitude.

In total there were 19 inversion crossings and on 16 occasions there was cloud at the top of the layer (Figure 3.8). The temperature inversions at the top of the mixed layer were weak, typically 1 K, and the slant profiles of the aircraft through the inversion introduced some horizontal variability into the sampling. The variability made it difficult for an automated scheme to identify features of the inversion and so a manual graphical approach was used to locate the inversion base and top from the slant profiles of temperature at 1 Hz. When lower resolution data (0.2 Hz and 0.5 Hz) were subjected to this method the inversions were represented as being higher and weaker as might be expected from lower resolution data. Higher resolution data contained more natural variability which did not aid the process.

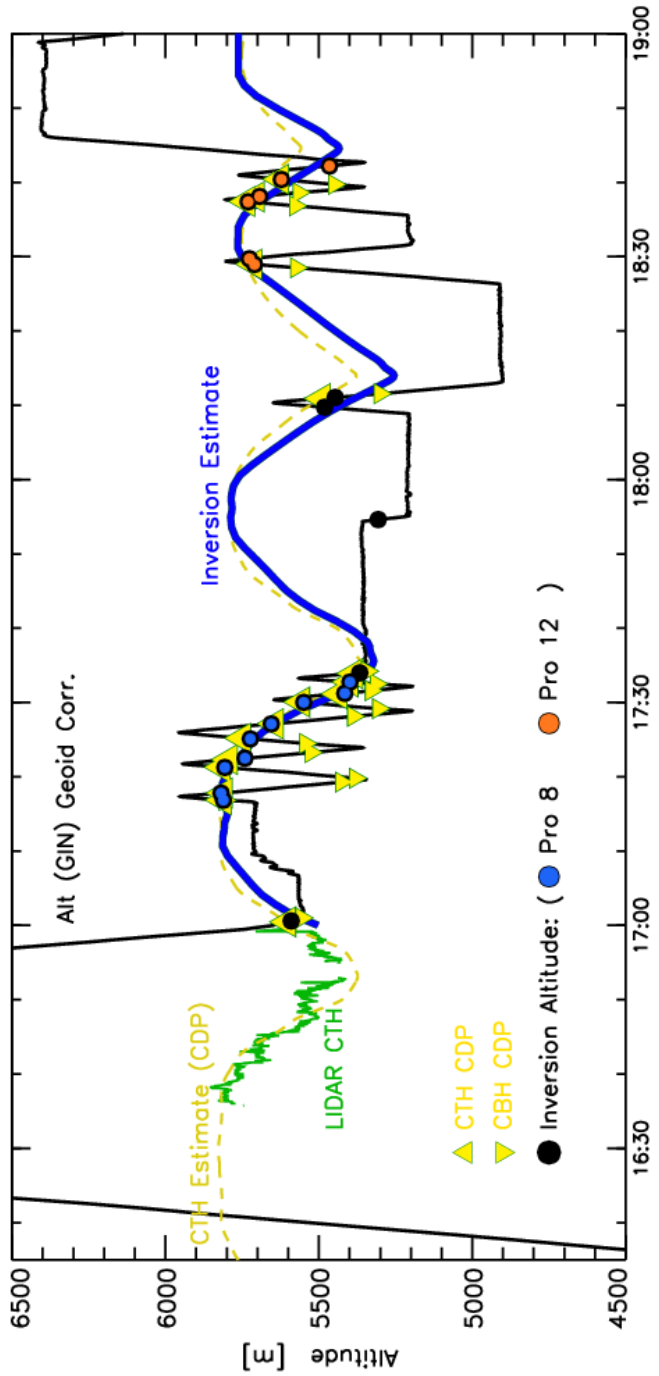

Figure 3.8: Aircraft flight profile time series (black). Circles: Inversion top location (Profile 8: orange, Profile 12: blue, others: black) - one spurious measurement rejected (at 1754 UTC). Yellow Triangles: Cloud base: "down", Cloud top: "up", from CDP measurements. Yellow dashed line: Cloud top height time series estimate. Blue Solid Line: Derived Inversion top estimate, Green: Lidar Cloud Top Height.

Aircraft altitude during the sampling period was taken from the GIN instrument, and corrected to the WGS84 geoid, shown in Figure 3.8 with a solid black line. Inversion crossings are plotted in filled circles, for *Profile-8* these are blue, for *Profile-12* these are orange (Figure 3.8). Others are plotted in black.

Cloud boundaries were estimated using CDP cloud droplet number concentration data (1 Hz), and are shown in yellow triangles; upwards for cloud top, and downwards for cloud base. An initial above-cloud lidar-leg was flown and the CTH values from this instrument are shown as a solid green line.

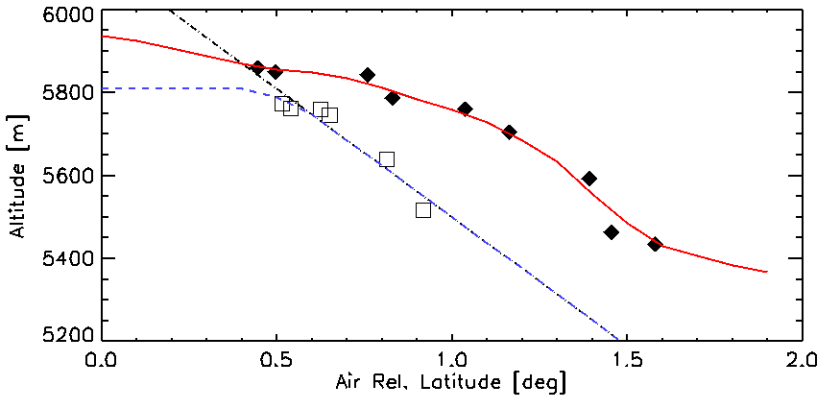

Figure 3.9: Inversion altitude from *"Profile-8"* (black diamonds) and *"Profile-12"* (empty squares) plotted against air-relative coordinate. Red line is interpolated and smoothed *"Profile-8"*. Black dot-dashed line is linear fit to *"Profile-12"*. Blue dashed line is modified linear fit to fix altitude for air-relative coordinate less than 0.5.

The inversion was well sampled between 1710 UTC and 1735 UTC: *"Profile-8"* - provides nine individual inversion crossings. Between 1825 UTC and 1840 UTC the inversion was sampled six times in the southern half of the region *("Profile-12")*. Data from *"Profile-8"* were interpolated in air-relative space and smoothed to give an estimate of inversion altitude as a function of air-relative latitude. Figure 3.9 shows the altitudes of the inversion crossing plotted against air-relative latitude.

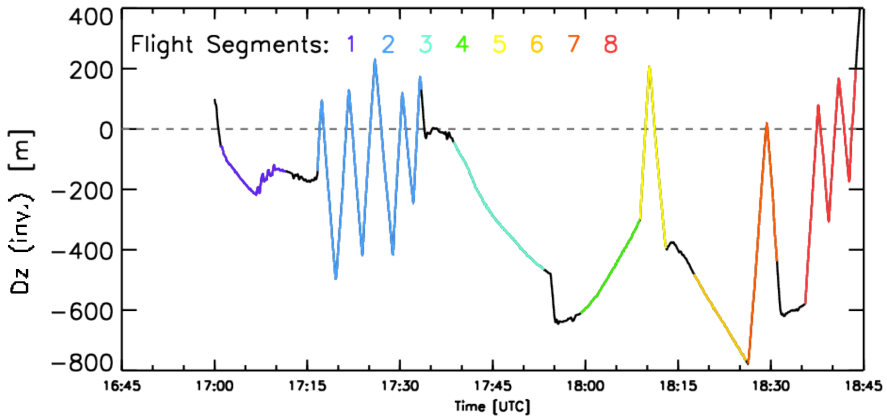

Figure 3.10: Aircraft altitude relative to derived inversion top, $Dz_{(inv.)}$. A total of 8 flight segments are defined. Even geometrically level flight sections (1,3,4,6) are slant profiles w.r.t. the inversion altitude.

Inversion altitude was observed to fall by up to 200 m between these two times. Only the northern half of the region is sampled during *"Profile-12"*. The inversion altitude estimate was therefore fixed at the southern-most value for air-relative coordinate less than 0.5 (blue dashed line). A linear fit applied to the six inversion crossings valid for air-relative coordinate greater than 0.5 (black dot-dashed line) gives the inversion altitude estimate as a function of longitude valid for this profile.

It was assumed that the inversion altitude falls uniformly in time, allowing the inversion altitude estimates from Profile-8 and Profile-12 to be linearly interpolated in time at 1 Hz (and uprated to 32 Hz) across the range of air-relative latitudes. The derived time-series of inversion altitude (Figure 3.8, solid blue line) is well constrained by the observations of inversion altitude. The time series of Cloud Top Height (CTH) was derived using a similar method (yellow dashed line) and is also well constrained. Furthermore, by extrapolation backwards in time, the derived CTH compares well with the lidar observations.

Parameter	Mean [m]	Std. Dev. [m]	Range [m]
Cloud Top	5656	150	432
Inv. Top	5666	146	439
Inv. Top Diff.	30	25	112

Table 3.1: Cloud Top Height (CDP LWC) and inversion altitude (temperature profiles) and difference (residual) between the measured inversion altitude and the derived inversion altitude: mean, standard deviation and range.

Once the inversion altitude time series estimate exists the derivation of a time series of the vertical position of the aircraft relative to the inversion was trivial, as shown in Figure 3.10 with individual flight segments coloured. Start and end times for 8 flight segments (different colours in Figure 3.10) were chosen by manual determination of when the aircraft was in wings-level constant heading flight. Whilst some segments were flown geometrically level (1, 3, 4, 7) others were slant profiles (2, 5, 6, 8). It can be seen that all flight segments were effectively slant profiles through the thermodynamically mixed layer, even the four that were flown geometrically level.

Figure 3.11 shows temperature profile data plotted against (top left) altitude and (top right) the derived inversion altitude, and cloud LWC (Liquid Water Content) profiles against derived inversion altitude: $\mathrm{Dz}_{(Inv.)}$ (bottom left) and CTH: $\mathrm{Dz}_{(CTH)}$ (bottom right). The range of inversion and cloud top height altitudes (left panels), was greatly reduced from more than 400 m, to closer to 50 m (right panels) by plotting against the derived inversion and CTH altitude.

The residual differences between the derived time series of inversion altitude or CTH and the observations was typically less than 50 m and in all cases less than $\approx$ 100 m (see Table 3.1). Lidar CTH data histograms in Figure 3.12 suggest that the actual variability was of this order. The trend was first removed over both 30 km and 3 km to demonstrate that the variation of CTH was horizontal-scale

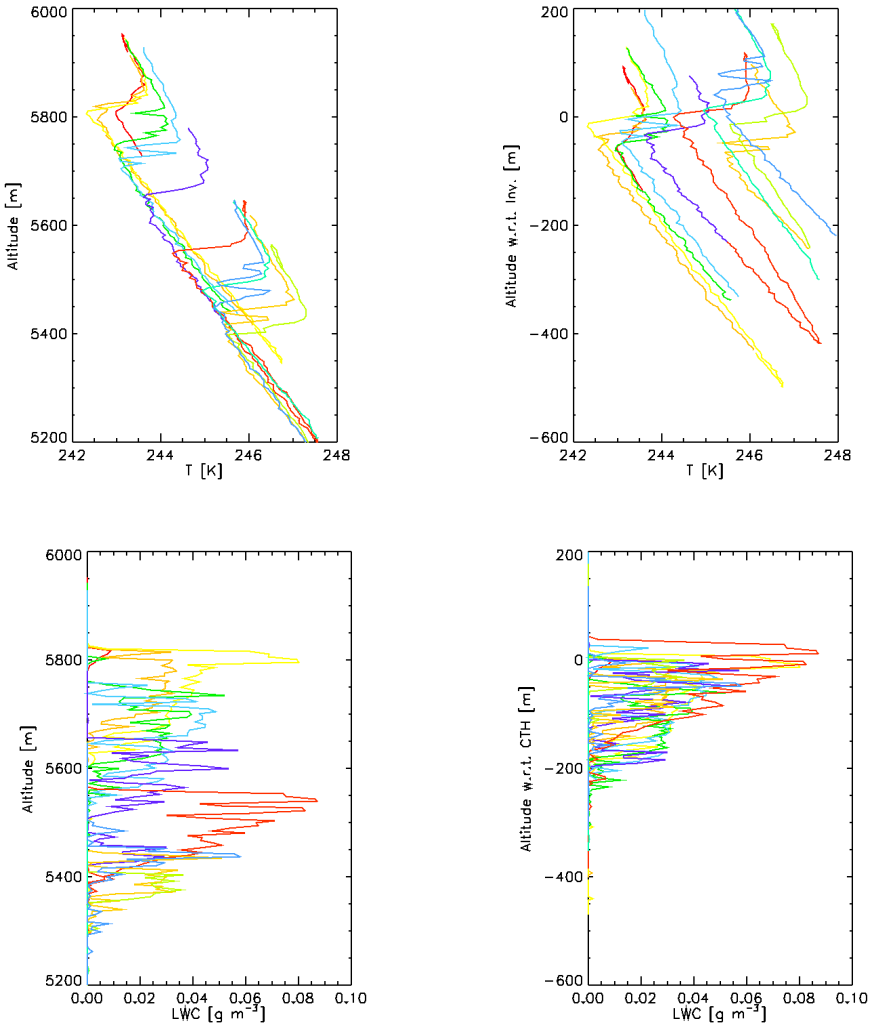

Figure 3.11: Top Left: Temperature profiles w.r.t. altitude, Top Right: Temperature Profiles w.r.t. derived inversion altitude, $Dz_{(inv.)}$. Bottom Left: LWC profiles w.r.t. altitude and Bottom Right: LWC w.r.t. derived CTH altitude, $Dz_{(CTH)}$, on 2^{nd} February 2012 (Vertical depth is the same for all figures). Colours represent individual profiles and are consistent between panels.

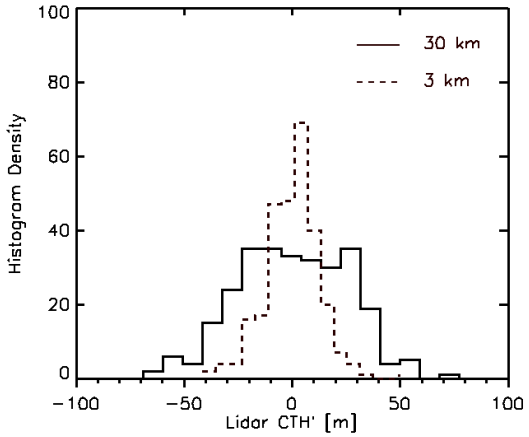

Figure 3.12: Histogram of cloud top height deviation from the mean, as measured by downward facing lidar, on two different length scales; 30 km in black solid line and 3 km in black dashed line.

dependent. The standard deviation of CTH at 30 km was of the order 25 m and at 3 km was close to 13 m. The uncertainty from the inversion altitude and CTH derived time series is only two or three times larger than the observed lidar variability.

The method of estimating the inversion and CTH altitude throughout the measurement period allowed the data from both geometrically level flight segments and slant profiles to be used together to build up a picture of the structure of the cloud system with as much detail as possible. By applying this new coordinate system the problem was reduced to a single vertical dimension. This simplification resulted in a dataset similar to that obtained from a ground-based mast, but for mid-tropospheric features, with the additional benefit of measurements at all vertical points and approximately doubles the quantity of data available. Application of this method could also be applied to the airborne study of boundary layers.

3.1.2 Vertical Profiles of Thermodynamics and Cloud Properties

Data were analysed statistically with respect to the vertical coordinate by taking all data in a given time period and generating percentiles and Gaussian statistics. Both dimensions were considered; the vertical coordinate and the *parameter* under test. For B674, the parameters were analysed w.r.t. the previously derived inversion or cloud top altitude. The data were sorted by altitude and segregated into a number of vertical categories, each with an equal number of data points. By definition then, the statistics from each vertical level are equally significant but the vertical depth of each bin is not the same. The number of bins is a balance between i) a sufficient number of points in each bin on which to perform statistical calculations, ii) vertical resolution and iii) clarity of figures. For thermodynamic parameters, 15 vertical categories gave layer depths between 30 m and 100 m. Between 4 and 7 vertical layers were generated for liquid and ice particle statistics profiles.

Plots throughout this work make use of the following plotting scheme, but not all values are displayed on each figure: The 50^{th} percentile of *parameter* and altitude coordinate is shown with an empty-diamond; The box-outline indicates 25^{th} and 75^{th} percentile in both directions; bar-and-whisker in *parameter* space are the 5^{th} and 95^{th} percentiles; 1^{st} and 99^{th} are filled-triangles, and 0.1^{th} and 99.9^{th}, when plotted, are down-empty-triangles; The mean and standard deviation of parameters are occasionally plotted as a filled circle and solid bar.

Thermodynamic data were sorted by distance from inversion altitude and binned into 15 altitude bands each having more than 250 data points. The deepest layer was of the order 100 m (Figure 3.13) and the separation between the shallowest layers was on a similar scale to the standard deviation in the inversion top estimate,

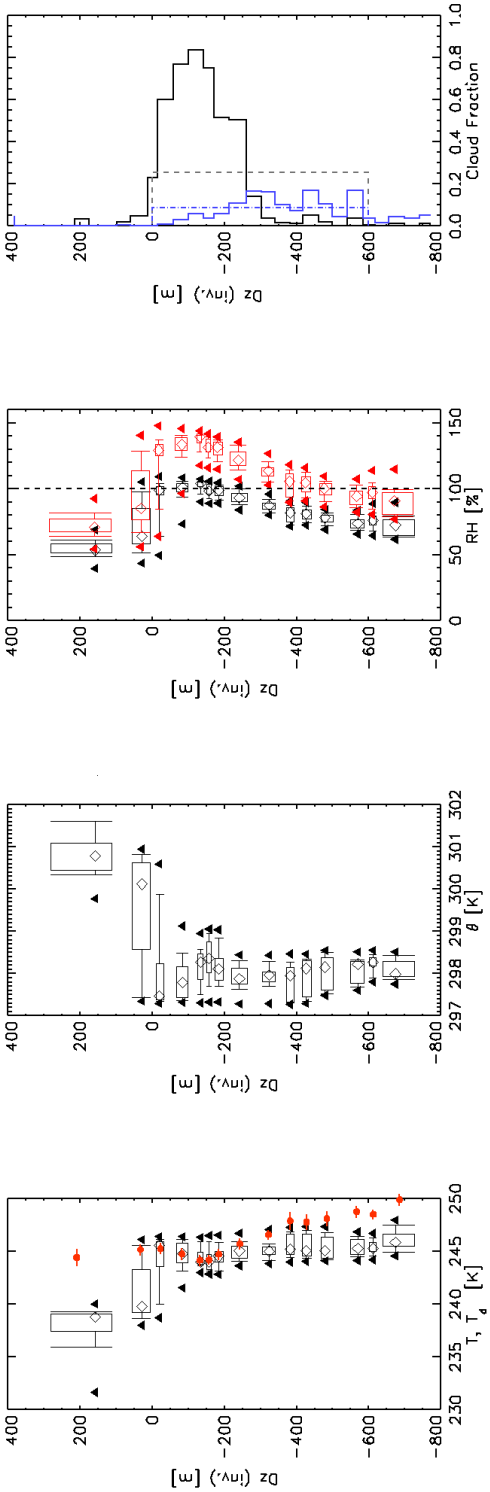

Figure 3.13: Vertical profiles of statistics w.r.t. inversion altitude, $Dz_{(inv.)}$, for (a) dew point (black), and mean and standard deviation of temperature (red), (b) potential temperature and (c) Relative Humidity w.r.t Ice (red) and Liquid (black). (d) Areal cloud fraction calculated from number concentration of liquid (CDP) (black solid) and ice (2DC) (blue solid) particles over 40 m altitude bins with dashed lines showing the volume mean over a 600 m deep layer.

$\approx$ 30 m. Results were not particularly sensitive to the number of bins chosen. Statistics of cloud microphysics (Section 3.1.4) were calculated over 4 altitude bins for liquid cloud and 6 altitude bins for ice particles. Cloud fraction (Figure 3.13d) was calculated over the full depth of the profile in 40 m intervals relative to the inversion altitude estimate using the ratio of cloudy to cloud free data points using CDP number concentrations. Here, the layers are not comparable in terms of statistical significance but the results are instructive nonetheless. For the LWC comparison between calibrated CDP values and Nevzorov data 7 altitude bins were specified (Figure 3.14).

There was an inversion in potential temperature of the order 3° C which extended over less than 100 m, giving confidence to the estimate of the inversion altitude time series (Figure 3.13). A layer below the inversion was found to be well mixed in terms of temperature (buoyancy) and humidity and will be referred to as the mixed layer. The air was much drier above the inversion (Figure 3.13a) where relative humidity w.r.t. liquid fell from saturation at the top of the mixed layer to $\approx$ 50 % above (Figure 3.13c).

The liquid cloud at the top of the mixed layer had a depth of just over 200 m with a maximum coverage of 80 % just below the inversion (Figure 3.13d). Ice cloud fraction was much lower, close to 10 %, found in the lower part of the mixed layer. Ice supersaturation extended down through the top 500 m of the mixed layer (Figure 3.13c). The CDP showed a small response to the ice cloud below the liquid layer. Mean cloud fraction was calculated for the mixed layer depth (assumed for this purpose to be = 600 m) for ice and liquid cloud, shown in dashed lines. The depth of this layer is comparable to the vertical resolution of a typical NWP model (Walters et al., 2017), which is a few hundred metres deep in the mid troposphere. Simplistically this is one way that a model simulation could treat

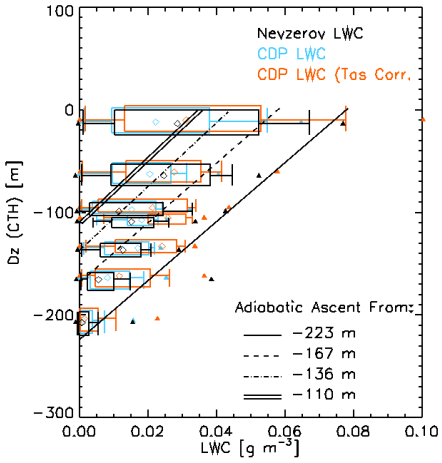

Figure 3.14: LWC statistics profile for the mixed-phase cloud layer with data from: Nevzorov LWC sensor in black, CDP with TAS corrected sample volume in blue (offset in vertical for clarity), and TAS corrected and calibrated bins in red (offset double in vertical). Four theoretical profiles showing adiabatic ascent of a saturated air parcel from four start altitudes are shown in black lines. See text for details.

the clouds.

A more sophisticated numerical model might represent the liquid part of the cloud as having greater horizontal extent and reduced vertical extent in a grid box. By considering the top 200 m of this cloud, the mean liquid cloud fraction can be assumed to be $cf_{liq} = 0.75$ and the mean ice cloud fraction to be $cf_{ice} = 0.05$. Making a not unreasonable assumption of full overlap between the two phases gives a maximum mixed phase cloud fraction in the top 200 m of $cf_{mixed} \leq 0.06$. If this values were to be scaled by the full depth of the mixed layer (or grid box) then $cf^{grid}_{mixed} \leq 0.02$. These observations may be useful in the parametrisation of ice process rates in mixed-phase clouds in large scale numerical models. A similar type of scaling was applied by Abel et al. (2017) when investigating cold-air outbreak clouds using numerical model simulations to attempt to reduce the liquid to ice conversion rate.

A comparison between the CDP size spectra integrated LWC and Nevzorov LWC probe is shown in Figure 3.14 with statistics data plotted with respect to $\mathrm{Dz}_{(CTH)}$. The CDP LWC with calibrated bin dimensions show that the magnitudes are not vastly different, although, as expected, the TAS and calibrated bins data show slightly higher mean and peak values. Correlations are high (≥ 0.96) for all combinations. The slope of a linear fit between CDP and Nevzorov improved (closer to unity) with i) calibrated bins, from 0.71 to 0.81, and ii) with TAS corrected sample volume, where the slope is 1.12. Being the closest to the expected value of unity, this calibration was accepted, although, it does introduce artefacts, including a non-physical looking shoulder to the data on B674.

Theoretical adiabatic LWC profiles were calculated by assuming an ascent of a saturated air parcel from four different initial altitudes (*pers. comm. Philip R.A. Brown*). The first, from the minimum cloud base at -227 m show that peak observed values compare well with this theoretical estimate to within 20%, for all calculated LWC values. An ascent from -167 m peaks close to the 75^{th} percentile. The third ascent from -130 m, and the fourth ascent, beginning at -110 m, have peak cloud top LWC near the 66^{th} and 50^{th} percentiles respectively. These observations and theoretical calculations demonstrate that the non-uniform cloud base probably contributed to the in-cloud variability in LWC at a given level, implying that there must be a range of turbulent eddies and updraught depths that contribute to the overall spectrum. It may not be necessary to invoke entrainment either at cloud top or cloud element edges in order to explain the variability of in-cloud LWC values.

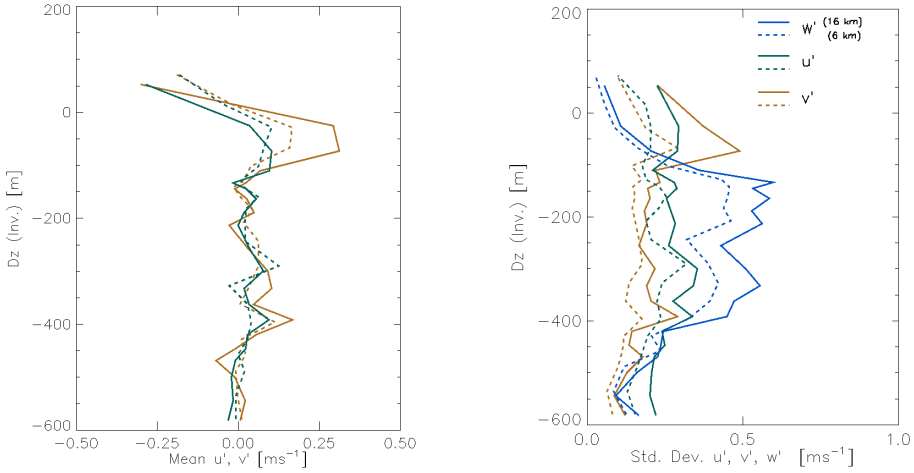

Figure 3.15: Profiles of Butterworth high-pass filtered data for wind fluctuation components u′ (green), v′ (brown), w′ (blue), relative to estimated inversion altitude for Left: residual mean value for u′ and v′ and Right: standard deviation of u′, v′, w′. Filter length of 16 km in solid line, and 6 km in dashed line.

3.1.3 Turbulence Structure

Impact of Butterworth Filter Length

Mean values of horizontal wind fluctuations are plotted in Figure 3.15 (left) against the derived inversion altitude, for u' and v', with the 6 km filter and the 16 km (Section 2.3.3, Table 2.3). Assuming that the synoptic and turbulence scales are spectrally distinct, a perfect high-pass filter would result in the mean of the parameter in question being equal to zero at all locations. Throughout the depth of the layer residual mean is close to zero, but towards the inversion this is not the case. The situation is worse for the longer, 16 km filter, probably a result of smoothing of the vertical wind shear across the inversion, thus contaminating the turbulence fluctuations. The vertical wind fluctuations do not show this behaviour.

The shorter filter length of 6 km (dashed lines) acts to suppress variance at all levels, as can be seen in the profiles of standard deviation of u', v' and w' in

Figure 3.15 (right). The longer 16 km filter allows more variance to pass. Vertical wind fluctuations contribute more to the turbulence variance than either of the horizontal wind components. Close to the inversion it can be seen that the spurious contribution from the long filter length horizontal wind data is larger than the vertical velocity variance, which is not likely to be physical. The well-mixed layer was $\approx$ 600 m in depth, although unbounded at the base, and so could be viewed as being deeper. A perfectly sharp 6 km filter would allow wavelengths of ten times this depth to pass. Significant loss of variance (TKE) occurs at filters up to 9 km in length (not shown). The resolved TKE falls below 90 % of the maximum value for filter lengths shorter than 9 km, below 75 % at 6 km, and then below 50 % at 2.5 km. The reduction in overall TKE indicates that scales of this order were contributing to the turbulent fluxes in the vicinity which means that there was some energy at length scales that are a factor of 10 greater than this depth.

No filter can be perfect, and ringing would occur for a perfectly sharp filter, and so the roll-off could account for some of this loss, close to the filter length. There will also be spurious removal of some real variance on those scales by the filter which implies that there are fluctuations on scales many times greater than the layer depth. Such scales were not found to be present in altocumulus observed by Schmidt et al. (2014), who presented a power spectra showing energy containing scales up to three times the depth of the layer. The observations of those large scales of motion presented here may be related to gravity waves on top of the layer at the interface between the mixed layer and the dry layer aloft. The ideal filter is situation-dependent, and care must be taken when interpreting the results in the vicinity of sharp gradients such as near the temperature inversion.

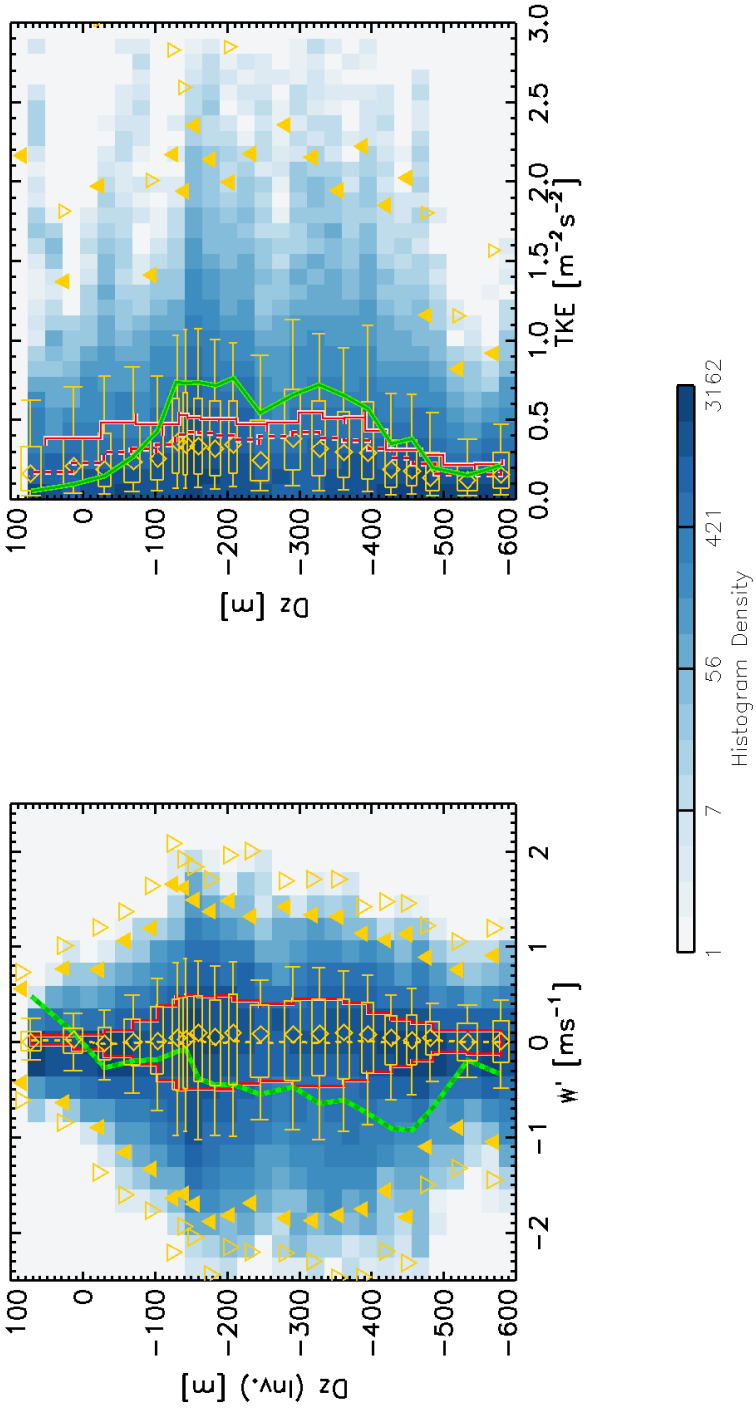

Figure 3.16: 2 dimensional histograms for 9 km filtered data, against vertical altitude coordinate, for Left Panel: vertical velocity fluctuations, w′ and Right Panel: TKE from 2^{nd} February 2012. Bother panels: 32 Hz data: Blue histogram with legend in lower panel. Percentiles including extremes: yellow statistics boxes and triangle symbols. Left panel: Mean value of w′ (9 km): yellow dashed line. Standard deviation of w′: red solid outline. Skewness of w′: green dashed line. Right Panel: Mean value of TKE, 6 km filtered data: Dashed red line and 16 km filtered data: solid red line. Mean TKE caculated by replacing u′ and v′ with $2 \times$ w′: solid green line.

Vertical Profiles of TKE and Vertical Velocity Distribution

Figure 3.16 shows profiles of vertical wind fluctuations, w′ (left) and TKE (right), with the raw data shown in black, for the Butterworth filtered data (9 km filter length). The percentiles are shown in 20 vertical levels, each containing 5876 data points. Extreme values shown as filled upwards triangles for 1^{st} and 99^{th} (58 data points), and empty downwards triangles for 0.1^{th} and 99.9^{th} (5 data points), in orange.

Vertical velocity fluctuations (Figure 3.16, left) ranged between -3 ms^{-1} and +2 ms^{-1}, with the 9 km filter returning a mean value close to zero, as expected. The variability characterised by the standard deviation of w′ increased from inversion top, to a maximum of 0.5 ms^{-1} at -150 m, and remained reasonably constant to -400 m. Magnitudes of vertical velocity variance were similar when a Canberra aircraft was flown through altocumulus clouds by Watson (1967). The skewness of the vertical velocity distribution was observed to be increasingly negative with depth through the cloud system, indicating that the turbulence in this cloud was generated through Long Wave Radiative Cooling (LWRC) from cloud top (e.g. Hogan et al. (2009)). The extreme values show stronger negative fluctuations than positive below -150 m. Similar observations in a mixed-phase cloud system were presented by Simmel et al. (2015), using lidar to measure the cloud base w′ spectra and radar to return the spectra within the ice virga. The range, maxima and skewness of the vertical velocity distribution were all similar in magnitude to these in situ observations.

The TKE profile (Figure 3.16, right) show data computed from the same parameters with the addition of the mean TKE from 6 km filtered data which is of lower magnitude than the same parameter as calculated from 16 km filtered data, showing

that some of the variance was removed by the shorter filter length. Median values were close to 0.5 m^2s^{-2} from -150 m to -400 m, whereupon they reduced. The theoretical TKE that results if the horizontal wind components, u', v' are each replaced with the vertical velocity fluctuations, w' is also shown. This artificial calculation was performed to explore the impact of the contamination of horizontal variability, and to minimise the impact of the filtering removing some variance associated with this. The parameter appears to show a more physically reasonable profile with a steady increase in TKE from inversion top, to a value of 0.8 m^2s^{-2} at -100 m, then constant throughout the well mixed layer to -400 m. The implication here is that the filtering does introduce contamination into the time-series of fluctuations, but that the impact is understood, and so the observations can still be useful. The profile is very similar to that observed in stratocumulus in terms of structure and magnitude (Ghate et al., 2014).

At the top of the mixed layer the TKE tended towards zero. It is likely that some of the contribution to the TKE in the region -100 m to +100 m is due to the data processing smoothing the structure across the inversion. Non-uniformities in inversion altitude could also be generated by updraughts penetrating to different depths into the inversion due to the distribution of updraught magnitudes and hence relative buoyancy. A summary of the vertical velocity fluctuations as a function of distance from inversion altitude is presented in Figure 3.17 for five vertical ranges. Each PDF contains the same number of 32 Hz data-points, one-fifth of the total: $\geq$ 30000. The depth of each level is consequently not identical, but the standard deviation of depth below inversion altitude range from 15 m to 50 m. The highest level, within cloud-tops, centred on $Dz_{(inv.)}$ = -55 m, had a narrow w' distribution, with minimal skewness and a range that was predominantly between -1 ms^{-1} and +1 ms^{-1}. Within the bulk of the liquid cloud, centred on -151 m

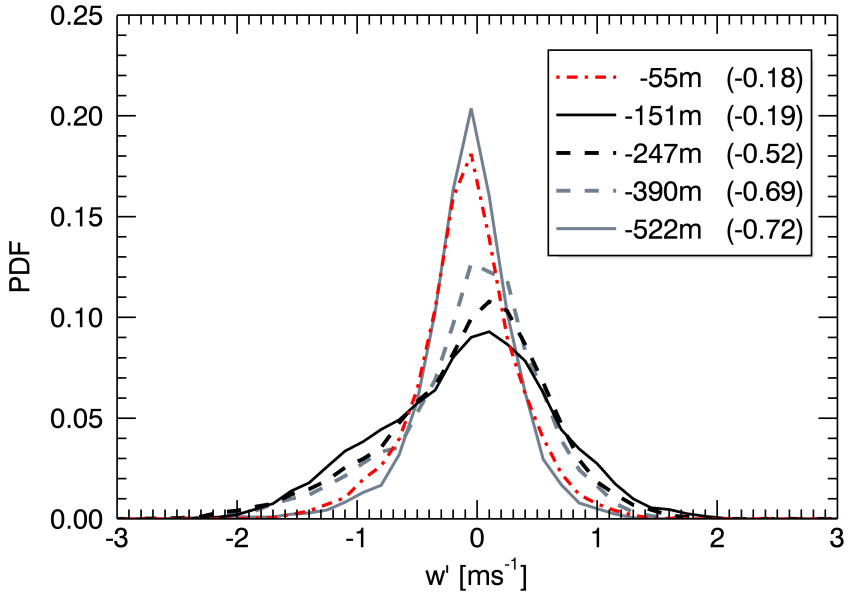

Figure 3.17: Vertical velocity fluctuations PDFs from 5 altitudes below inversion altitude with levels given in the legend. First value gives the centre altitude of the level, with the second number giving skewness of the vertical velocity distribution. Standard deviations of depth in each level was between 15 m and 50 m.

the range was larger with peak updraughts of 1.5 ms^{-1} and stronger maximum downdraughts of -2.0 ms^{-1}, although skewness was only slightly greater than the level above. There were more weak updraughts ($\leq$ 0.5 ms^{-1}) than downdraughts. Peak updraughts were weaker in the next vertical level down, centred on -247 m and roughly corresponding to the cloud base layer and start of sub-cloud virga. Here the skewness was much larger and it is clear from the PDF that strong downdraughts were present at -2 ms^{-1}, whereas similar numbers of updraughts were only observed for +1.5 ms^{-1}. Deeper into the virga layer the skewness increased further, to -0.69 at -390 m, and -0.72 at -552 m. The PDF at the lowest level showed most fluctuations in the range $\pm$ 0.5 ms^{-1}, but that occasional strong

downdraughts up to -1.5 ms^{-1} were present.

Observations presented by Schmidt et al. (2014) from high-resolution ground based active remote sensing of mixed-phase altocumulus cloud showed variability of turbulent motions on a range of scales as a function of depth through a mixed layer containing altocumulus. Their observations model is reproduced in Figure 1.2. Cloud top and cloud base rotors were resolved along with circulations spanning the depth of the liquid cloud and others that penetrated deeper into the mixed layer. Such a structure could be created by, and maintain, the features of LWC structures described above and the PDFs of vertical velocity fluctuation observed here. The PDF of w′ from $Dz_{(inc.)}$ = -151m shows positive and negative fluctuations of almost equal magnitude and roughly corresponds to the "cloud-layer" where Rayleigh-Bérnard type-cells were observed (Figure 1.2). At the top of the cloud system there are shallow cloud top eddies resolved by the remote sensing observations of Schmidt et al. (2014) which is best represented by the PDF found at $Dz_{(inc.)}$ =-55m. At the level, close to the inversion, the broader-deeper circulations do not have space to develop. The "Subcloud Layer 1" is represented here by the PDF from $Dz_{(inc.)}$ =-247m and -390 m. The "Subcloud Layer 2" shares properties with the PDF from $Dz_{(inc.)}$ =-552m.

3.1.4 Cloud Microphysical Observations

Liquid cloud particle size distributions for the five vertical ranges (Table 3.2) are plotted in Figure 3.18 by compositing data from the CDP within the altitude band. The CDP records at 1 Hz and cloud cover is lower than 100%, so the layers were chosen to be 80 m deep (except the lowest level: 60 m deep) in order to increase the number of particles in each distribution and improve counting statistics whilst still allowing for probing of the vertical structure of the cloud.

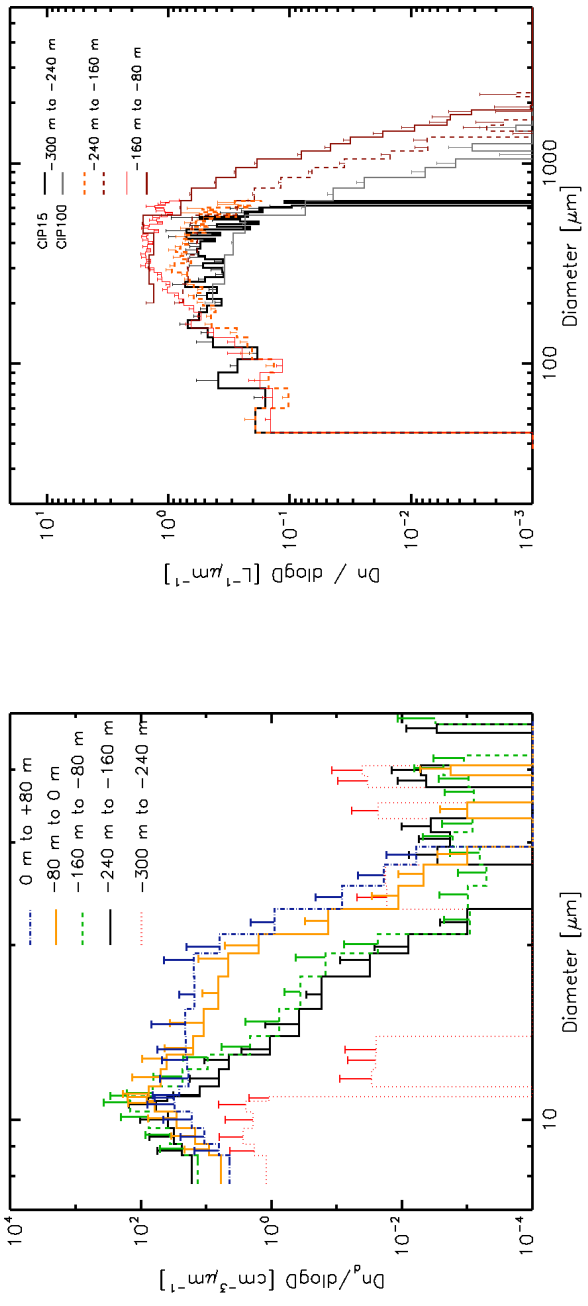

Figure 3.18: PSD, $dN/D \log D_p$ as a function of depth through the cloud layer (Table 3.2) for Left Panel: CDP and Right Panel: CIP15 and CIP100. Vertical layers are not the same for both panels (see Legends).

A very small number of cloudy data-points (21) were found at the "lower" level between 300 m and 240 m below mean cloud top height. All the cloud particles were smaller than 11 μm, and in very low concentrations. The CDP also responded to low concentrations of ice particles at this level, as can be seen for the occasional particle at diameters larger than 11 μm, and for other levels at sizes large than the liquid cloud population. Similar to previous FSSP observations by Gardiner and Hallet (1985), this was deemed to be a spurious response by the CDP to non-spherical ice particles with unknown scattering phase function.

Significant cloud was encountered between -240 m and -160 m ("Intermediate 1" (Int. 1)) with a mode diameter close to 10.6 μm and a sharp fall in number at sizes larger than this. On this occasion the probe was seen to respond to ice, at sizes larger than 30 μm. Concentrations were somewhat greater in the level above and the mode size was similar (10.8 μm) but with more particles larger than the mode, up to a similar maximum size of 19 μm ("Intermediate 2" (Int. 2)). Differences larger than the uncertainties occur mainly for the larger sized bins.

By the "Upper" layer, the mode increased further towards 11 μm and a broad shoulder of particles as large as 25 μm was present, as expected from an adiabatic uplift. Particles smaller than the mode were reduced in concentration relative to other layers, perhaps as some grow out of the size range and possibly, as the smallest were completely evaporated during mixing with drier air from above. Data which were occasionally collected from above the estimated cloud top height, were found with similar properties to the cloud top regime, although the distribution was broader, with fewer cloud particles at small sizes and around the mode ("Above"). Mixing of dry air from aloft would result in modification of the size spectra, through partial or complete evaporation of drops. A limitation of the compositing technique is that the location and timing information is lost.

Name	CDP			CIP			
	Altitude [m]			Altitude [m]		CIP15	CIP100
	Base	Top	n	Base	Top	n	
Above	+80	0	79	-	-	-	-
Upper	0	-80	485	0	-100	499	563
Int. 2	-80	-160	723	-100	-200	817	1116
Int. 1	-160	-240	327	-200	-400	866	1132
Lower	-240	-300	21	-	-	-	-

Table 3.2: Vertical level (w.r.t. CTH) ranges for CDP PSD and CIP PSD with number of data points, n

Following a similar method, the PSD from the two CIP probes are plotted in Figure 3.18 for three vertical levels, as detailed in Table 3.2. These levels share some vertical overlap with the liquid cloud layer. CIP15 data are truncated for d $\geq$ 600 μm to improve plot clarity at the data sparse sizes. The "upper" level CIP15 data and the CIP100 data are shown to agree well where the sizes overlap. The mode of the ice particle size distribution was larger than 100 μm but was not well defined. The maximum size of ice particles at this level was $\approx$ 1 mm. There are large concentrations in the smallest bin of CIP15, and a composite CDP distribution is shown for all data between -300 m and 0 m with to show that it is clear that the CDP responded to some particles, presumed to be ice, with d $\geq$ 30 μm.

Data from the next layer down in the cloud system: "Intermediate 2"; showed higher concentrations of particles greater than 200 μm in diameter. The mode diameter for CIP15 observations is between 250 μm and 300 μm and $d_{max} \approx$ 1.5 mm. There were an order of magnitude fewer particles in the smallest CIP15 channel than in the upper layer. Data from CIP15 show the mode the ice particle distribution at the "Intermediate 1" level was between 300 μm and 400 μm and $d_{max} \approx$ 2.0 mm. Ice particles were seen to increase in number and grow in size with increasing

distance below cloud top.

Statistics were calculated for the in-cloud number concentration (Figure 3.19, left) and in-cloud CWC profiles (Figure 3.19, right). Cloud drop numbers were constant in-cloud at $\approx 30\ cm^{-3}$. Cloud drops were found to be larger at cloud top, as expected because the largest LWC values were also at cloud top. CIP15 was sensitive to the liquid cloud population (more discussion in Chapter 5) in the smallest size channels, as shown by number concentration data for *all* size channels.

The number concentration data from CIP15 were plotted excluding the smallest size channel, bin 1 as a proxy for ice concentrations. Median number concentrations were of the order 0.5 L^{-1} to 5 L^{-1}, from CIP15, peaking just below the liquid cloud base. The concentration reduces by a factor of two further up into the liquid cloud, and there were very few instances of ice observations within the top 100 m of the cloud. Ice number concentration percentiles from the CIP100 probe are plotted, showing that the concentration of these particles followed a similar trend, again peaking in concentration just below cloud base at 0.5 L^{-1} (50^{th} percentile), and being a factor of two lower in the middle of the liquid cloud, 0.24 L^{-1} (50^{th} percentile). Concentrations of these larger ice particles were found to be between 2 and 10 times lower than those measurements from CIP15 with the smallest bin excluded. The ratio of the mid-cloud to lower-cloud concentrations is constant with depth, perhaps implying that ice particles were nucleated uniformly throughout the cloud depth. The smallest particles at cloud top would not be detectable in this scenario.

Peak IWC was greater than peak LWC (Figure 3.19, right panel) but the mean values were comparable in magnitude. Ice was not found at the top of the liquid layer and, in general, peaked in magnitude below the liquid cloud. Below about

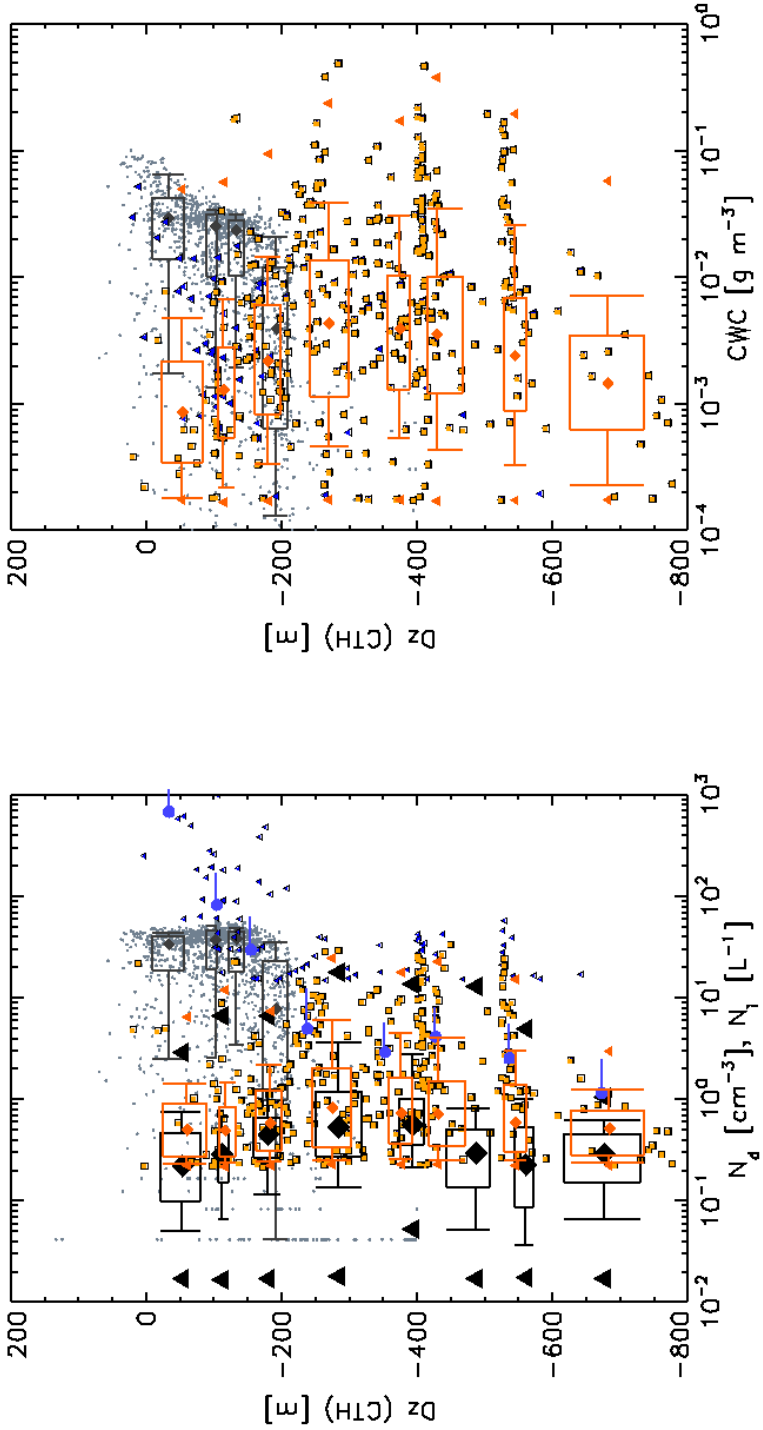

Figure 3.19: Left: Profile of Cloud Particle Number concentrations (liquid - CDP: grey dots, black statistics [cm^{-3}] and ice [L^{-1}] - CIP15: All bins: blue triangles, mean in blue circle, standard deviation in positive error bar, CIP15 excluding bin 1 orange squares and percentiles. and CIP100 percentiles in black) and Right: Profile of CWC (liquid and ice) with same colours.

500 m below CTH the ice water content reduced, assumed to be where the ice crystals fall out of the ice-saturated layer.

Observations of altocumulus clouds by Heymsfield et al. (1991), from a similar altitude and temperature to the 2^{nd} February 2012 case, found the peak vertical velocity values to be $\pm$ 0.75 ms^{-1} in the most turbulent cloud, with peak LWC = 0.05 gm^{-3} and drop number concentration between 20 cm^{-3} and 30 cm^{-3}. The reported IWC values were also similar and had a maximum value slightly larger than the peak LWC with IWC = 0.08 gm^{-3}, this being found low down in the mixed-phase system. A cloud with lower maximum LWC = 0.02 gm^{-3} was found to have lower turbulence, and the IWC is presumed to be negligible as it is not reported. These observations suggest there may be a link between the LWP of a cloud, the turbulence intensity and the production of ice.

3.2 Stratocumulus Case, 23rd January 2012

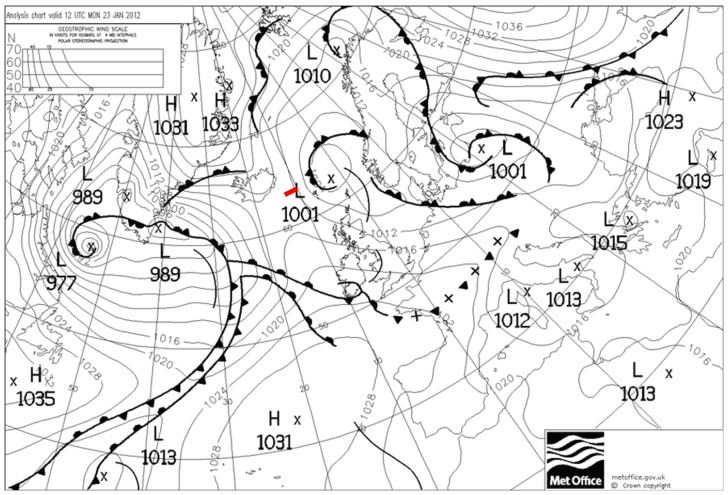

Figure 3.20: Analysis chart from UK Met Office for North Atlantic valid for 1200 UTC on 23rd January 2012. The measurements were made in the stratiform region of the cold air outbreak. Red line indicates airborne sampling region.

Flight B668 took place on 23^{rd} January 2012 over ocean to the north-west of the Faroe Islands, flying along the 63 N parallel between 12 W and 10 W. The general airflow was from the north, during a cold air outbreak set-up as seen in the Met Office surface analysis chart (Figure 3.20). The high resolution MSG satellite image from (Figure 3.21), valid for 1200 UTC on 23^{rd} January 2012, shows the transition between the stratiform region and the convective region that was to the south-west of the Faroe Islands. Measurements of the stratocumulus cloud took place in a region upstream of the break-up into cumuliform clouds, between 1110 UTC and 1255 UTC. The flight pattern was oriented east-west, across wind.

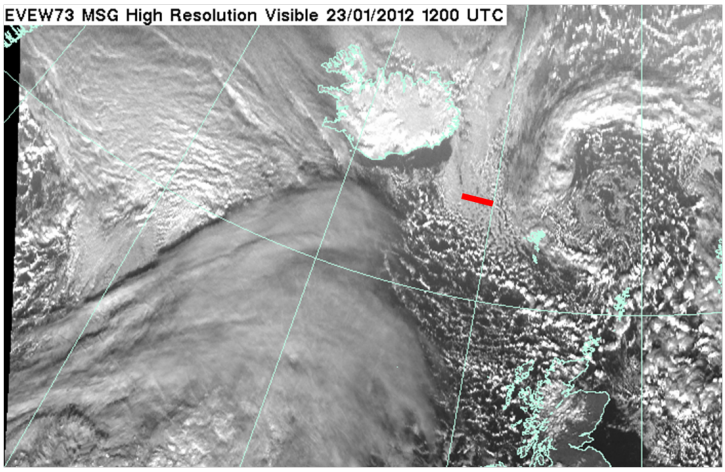

Figure 3.21: High resolution MSG satellite image of North Atlantic region, showing the stratiform cloud sampled during B668, 23^{rd} January 2012, 1200 UTC. Cold air outbreak dominates UK region. Mid-latitude cyclone located to south of Iceland. Red line indicates airborne sampling region.

Mixed-phase stratocumulus cloud from this flight is presented as a comparison against the mixed-phase altocumulus layer cloud. The cloud was similar in the sense that a liquid layer was found atop precipitating ice virga. The cloud top, and the thermodynamic environment, was geometrically level.

Figure 3.22 shows the potential temperature field, interpolated from the flight

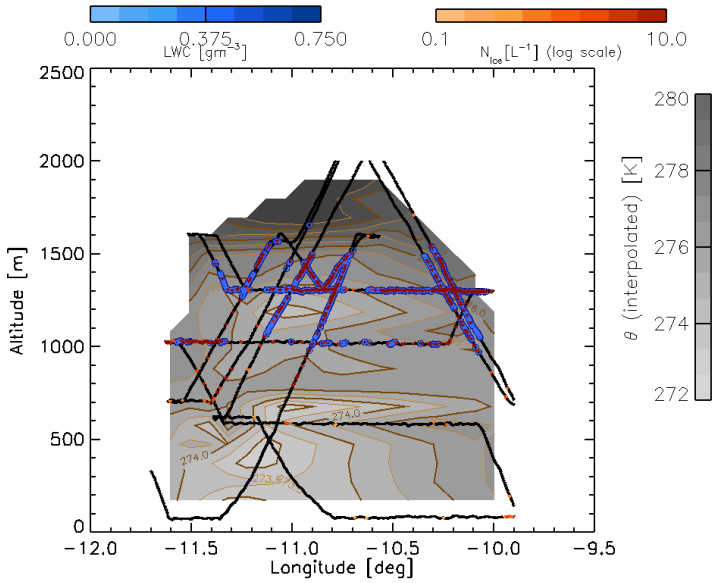

Figure 3.22: Aircraft altitude as a function of longitude (black line) on flight B668, 23^{rd} January 2012, with Thermodynamic cross section (coloured shading) and cloud properties (see text for details (as Figure 3.5)).

level measurements, this time on a longitude altitude cross section (as Figure 3.5). Below 1.5 km the potential temperature data show a reasonably well mixed layer. The vertical structure above this level showed an increase in potential temperature and hence the layer was stable to vertical development, and so stratocumulus cloud could persist. Cloud LWC from the CDP is plotted in blue, showing the level cloud top. Ice concentration from the 2DC probe shows ice throughout the liquid cloud layer, and some precipitation down to the surface.

In this case the flight track was across the mean wind direction, and so the cloud field was advecting through the operating region. Since cloud top/inversion altitude did not vary significantly, either across wind, or along wind, the correction of the horizontal coordinate into air-relative terms was not necessary in this case. There were straight and level flight segments at four levels within the boundary layer

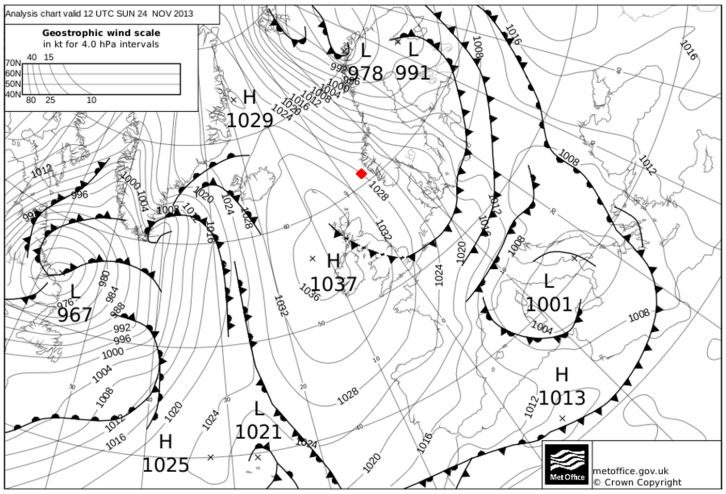

Figure 3.23: Analysis chart from UK Met Office for North Atlantic valid for 1200 UTC on 24^{th} November 2013. Red diamond indicates the location of airborne sampling.

connected by slant profiles.

3.3 Cumulus Case, 24^{th} November 2013

The data from 24^{th} November 2013 come from a profile through a developing convective cloud system that was downstream of the transition from stratocumulus cloud during a cold-air outbreak. The Met Office surface analysis valid at 1200 UTC on 24^{th} November 2013 is shown in Figure 3.23 and a high resolution visible satellite image (MSG) from 1115 UTC is in Figure 3.24.

The BAe146 measurements were taken from a location close to 61 N, 3 E, between Lerwick in Shetland and Bergen in Norway. The aircraft slant profile climbed from close to the surface, to be just below cloud base at 1120 UTC and at cloud top at 1125 UTC. Mixed-phase cloud and precipitation was encountered below 800 hPa. Abel et al. (2017) have used data from this flight to investigate the

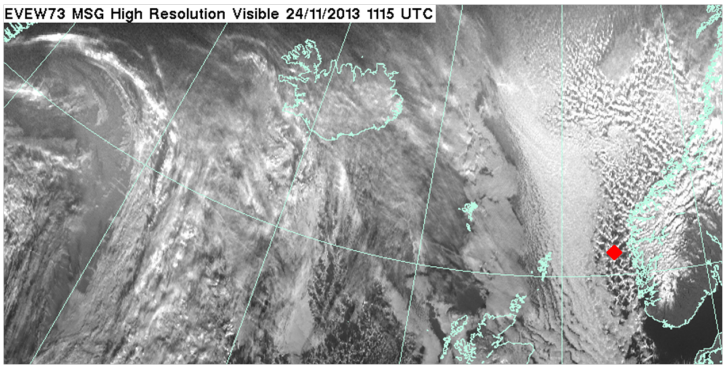

Figure 3.24: High resolution MSG satellite image of North Atlantic region, showing the stratiform cloud sampled during B816, 24^{th} November 2013, 1115 UTC. Red diamond indicates the location of airborne sampling.

cold-air outbreak transition from stratocumulus cloud to cumulus.

The tephigram in Figure 3.25 shows the part of the profile that contained the relevant measurements, with temperature from the de-iced temperature probe and dew point data from the WVSS2 probe (data provided by S. Abel, Met Office). The data from the flush-mounted probe were chosen, as the Rosemount inlet data showed artefacts due to evaporating cloud and precipitation particles when in-cloud (Vance et al., 2014). All of the data from this slant profile were collected at altitudes above the zero degree isotherm. Below 770 hPa the thermodynamic profile was unstable, and conducive to vertical development of cloud. Humidity data showed that the atmosphere was saturated from 930 hPa to 850 hPa, with significant amounts of moisture at levels up to the inversion as compared to the incredibly stable and dry layer above.

Profiles of temperature and condensed water content (LWC, IWC), and ice particle number concentrations are given in Figure 3.26 which also highlights the two temperature ranges which were used to calculate ice production rates in Chapter 4. The condensed water estimates shown in Figure 3.26 (centre panel) were

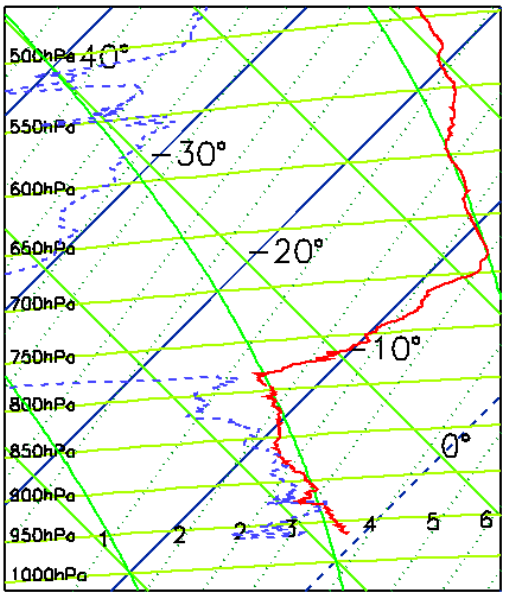

Figure 3.25: B816 tephigram, temperature from de-iced probe and dew point from WVSS2 flush.

made by integrating the droplet (CDP) or ice particle (2DS) spectra. The 2DS data, provided by *I. Crawford* (Univ. Manchester) were processed such that the contribution from different species are resolved. The final panel, Figure 3.26 (right panel), presents the number concentration data, again, from either CDP or 2DS.

Cloud base was close to 930 hPa, at T = -4° C, and predominantly liquid, with a number concentration, N_d = 50 cm^{-3} and LWC = 0.1 gm^{-3} as shown by CDP The data in the "2DS small" category correlated very well with the CDP data throughout most of the profile, with the weakest correlation observed when number concentration was low.

The "low irregular" 2DS category was well correlated with CDP number concentrations and "medium irregular" category followed a similar trend, but had concentrations that were an order of magnitude larger in the -7° C $\leq$ T $\leq$ -9° C

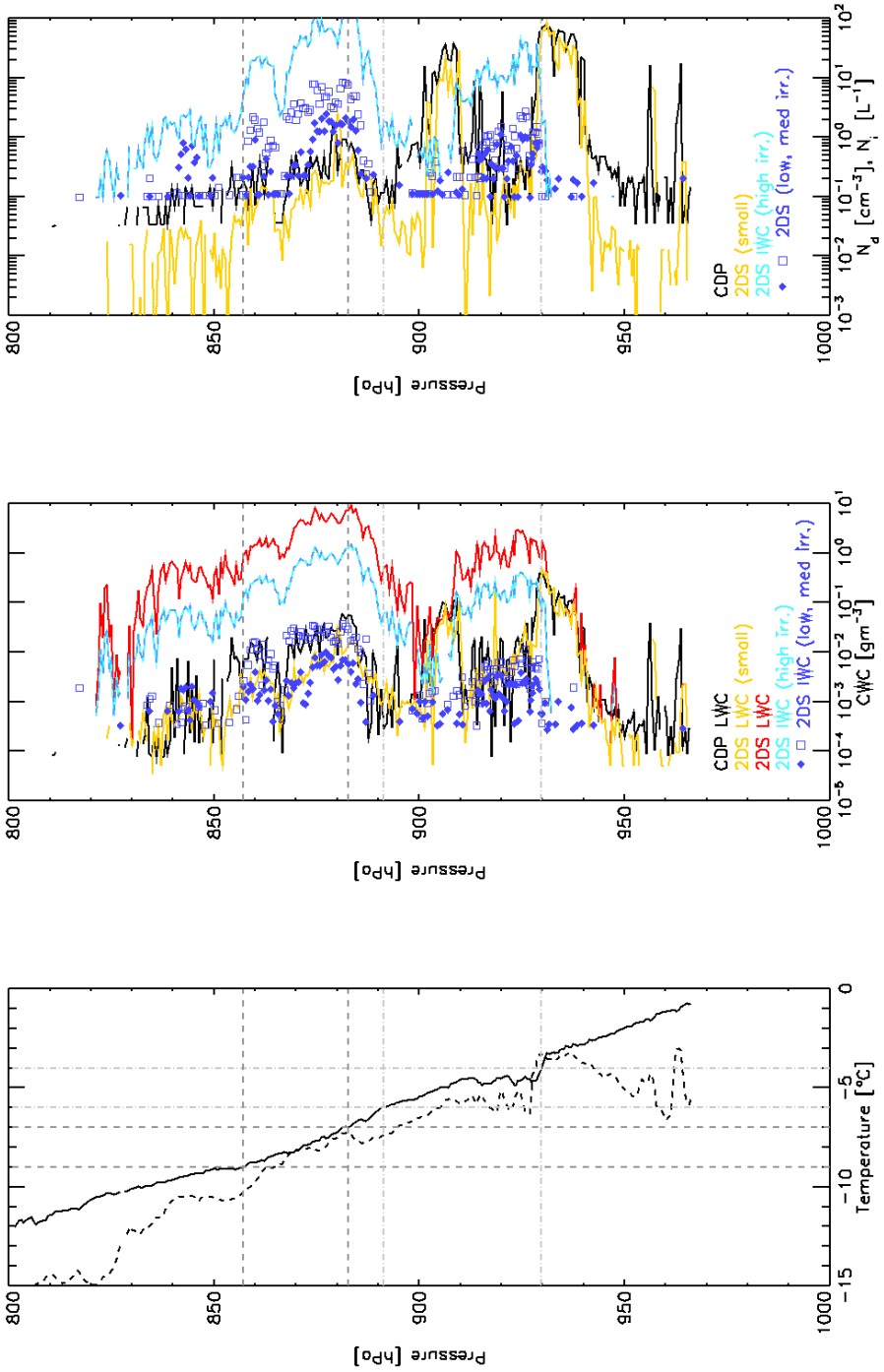

Figure 3.26: Vertical profiles relative to pressure from B816, 24^{th} November 2013 of Left: Temperature (de-iced, solid) and Dew Point (WVSS2 flush, dashed), and cloud properties: Centre: Condensed Water Content and Right: Ice Particle Number Concentration with CDP: Black, 2DS LWC, N_d: red, 2DS Small: Yellow, 2DS Low Irregular, Blue Diamonds, 2DS Medium Irregular, Blue Empty Squares, 2DS Highly Irregular, Dash Blue Line. Ranges -4° C≤T≤-6° C, light grey dash-dot, and -7° C≤T≤-9° C, grey dash.

region. The "high irregular" particles were present in concentrations that were mostly many orders of magnitude higher than other species. It is presumed that these particles were the product of some secondary ice multiplication process (Hallett and Mossop, 1974).

3.4 Conclusion

Observations of a highly supercooled mixed-phase mid-level altocumulus cloud have been presented. Liquid cloud was topped by a weak temperature inversion and precipitating ice virga were observed falling out of the layer. The structure of the cloud was similar to long-wave radiatively-driven boundary layer stratocumulus (e.g. Nicholls (1989)) with liquid cloud underneath an inversion, and precipitating ice virga. Measurements from such a cloud, sampled on flight B668, 24^{th} November 2013, were presented as a brief comparison of the thermodynamic structure. There are few observational studies of this kind as the clouds are often transient in nature.

Cloud top was found to slope significantly which required cloud top and inversion height to be estimated. The problem was reduced to a single vertical dimension and the aircraft data were used as though from a "synthetic mast" observing the cloud advect past. This method allowed for comparison of thermodynamic and cloud microphysics data from both geometrically level flight segments and slant profiles, and increased the quantity of data available. For this reason, application of the same technique to existing flight data in the archive may be useful, and new ways of planning flights also become possible.

Observations of the thermodynamic and cloud properties in the context of this vertical coordinate confirm that it worked as expected. The profiles of the variability

of thermodynamic and cloud parameters in altocumulus with respect to depth below the inversion should be of use to the modelling community.

Liquid water content was larger at cloud top and the profiles followed adiabatic type trajectories, with theoretical calculations suggesting that the saturated air parcels originated from different levels below the inversion altitude. No drizzle was apparent in the observations; the maximum diameter of cloud drops was smaller than 30 μm and the integrated CDP measurements compared well with the Nevzorov values. Ice mass had a maximum just below the liquid cloud base, a feature observed by others (Carey et al., 2008). Ice number concentration also peaked just below cloud base.

When placed in the context of other observational studies (e.g. Heymsfield et al. (1991)) these were typical single-layer highly-supercooled mixed-phase altocumulus clouds. In fact they are some of the coldest expected given ground based climatologies in both the mid-latitudes (Bühl et al., 2016), and the tropics (Ansmann et al., 2009) and also in situ aircraft observations (Fleishauer et al., 2002).

Turbulent wind fluctuations were calculated by generating high-pass Butterworth filtered time series. The turbulence structure showed negative skewness to the vertical velocity fluctuations in the mixed layer, an indication of LWRC top-driven mixing (Nicholls, 1989; Hogan et al., 2003a). These observations are a snapshot in time of a dynamic environment and there is an implicit assumption that the turbulence is frozen in an extension of Taylor's Hypothesis to airborne measurements (Stull, 1997). It is a necessary assumption that the characteristics of the turbulence do not vary in the horizontal or temporal dimensions. A similar assumption must be made when flying a more traditional stack of legs in a turbulent boundary layer study.

The stratocumulus cloud of B668, 23^{rd} January 2012, was presented to demonstrate that the thermodynamic and general cloud structure in the altocumulus and stratocumulus clouds were similar. That is not to suggest that all processes were active in both types of clouds to the same degree. The stratocumulus cloud had a geometrically level cloud top height, adiabatic type LWC profiles and precipitating ice virga.

The flight through glaciating cumulus cloud, B816, 24^{th} November 2013, was presented to contrast and support the altocumulus measurements of ice production rate. The aim of the sortie was to investigate the transition between stratocumulus and cumulus cloud in a cold-air outbreak scenario, and is analysed in detail by Abel et al. (2017). Here the data from a profile climb through a precipitating cumulus cloud is used for the sole purpose of calculating ice production rate in a region where ice multiplication processes were thought to be active.

The mixed-phase altocumulus cloud case study is the basis for the bulk of this work. Observations are used subsequently to estimate the in-cloud ice production rate, P_0, and the INP budget (Chapter 4). Calculated PIP for the altocumulus are compared against measurements of SIP rate from a developing cumulus cloud, sampled on 24^{th} November 2013 (Chapter 4).

Chapter 4

Ice Production in Mixed-Phase Clouds

4.1 Introduction

Measurements are presented here of Primary Ice Production Rate, PIP, with an associated error in mixed-phase altocumulus clouds on 2^{nd} February 2012, flight B674. Ice Production Rate, P_0, and Ice Nucleation Rate (INR) are important quantities that will go some way to explaining the evolution of a mixed-phase cloud system. The two are not necessarily the same, for example in cases where ice multiplication is active, such as Secondary Ice Production (SIP) via rime-splintering, the Hallett-Mossop (HM) process (Hallett and Mossop, 1974). In steady-state conditions, P_0 will be equivalent to INR. It is assumed that all ice in this altocumulus cloud is produced via primary ice production since it is outside the HM temperature zone. Better determination of P_0 in a range of conditions will be very useful in the ongoing development of NWP and climate models.

The PIP mechanism is likely to be a variant of immersion freezing. Upon nucleation the ice particles were assumed to have a minimum size equal to that of one of the liquid particles from which they formed giving a maximum initial size of 30 μm. None of the cloud microphysics probes here were able to distinguish ice from liquid at these sizes including SID2 and CIP15 which are discussed in more detail in Chapter 5 .

An INC did not fly on the BAe146 and so INP concentrations for this study were derived from observations of the aerosol particles. A clear-sky flag was generated from bulk condensed water observations from the Nevzorov TWC probe and aerosol measurements were taken from the PCASP at these locations. Parametrisations for immersion freezing rates are available in the literature and here the work of DeMott et al. (2015) and Tobo et al. (2013) are considered. The technique of measuring INP concentration using the CFDC technique has been shown to underestimate the INP concentration by up to a factor of 3 (DeMott et al., 2015). Uncertainty in the flow field within the CFDC instruments is likely to be the main culprit with values of $2.6 \leq cf \leq 9.5$ found, for a different instrument, the SPIN (Spectrometer for Ice Nuclei) (Garimella et al., 2017).

The motivations for making these observations include:

1. Phase partition in mixed-phase layer clouds strongly impact the radiation budget and hence climate (Sun and Shine, 1995; Hogan et al., 2003a; Morrison et al., 2012),

2. Phase partition is challenging for numerical weather prediction models that try to simulate cloud evolution, cloud lifetime and precipitation processes (Westbrook and Illingworth, 2011, 2013),

3. The liquid to ice phase transition is not well understood (Fridlind et al.,

2007),

4. Better understanding of the initiation of ice in these layer clouds will help to constrain the problem.

The next section introduces the Harris-Hobbs and Cooper (1987) method of calculating ice production rate, followed by the results from altocumulus and cumulus clouds, discussed in the context of previous measurements of this type. Aerosol particle size distribution observations are presented next and INP concentrations are derived. The source region of aerosol was investigated using the NAME dispersion mode (Jones et al., 2007) to assist in interpretation of the ice and ice nucleating particles observations that complete the chapter.

4.2 Calculating In-Cloud Ice Production Rate, P_0

Calculations of ice production rate from observations were first performed by Harris-Hobbs and Cooper (1987) (hereafter HHC87), originally to calculate the rime splintering Secondary Ice Production (SIP) rate in cumulus clouds within the Hallett-Mossop temperature range (Hallett and Mossop, 1974). Those same calculations have been applied to measure primary ice production rate, P_0, in mixed-phase altocumulus layer clouds.

HHC87 calculated P_0 from the difference in the cumulative size distribution of measured ice particles, C, between two size thresholds, L_1 and L_2,

$$P_0 = [C(L_2) - C(L_1)]/t_{21}, \tag{4.1}$$

where the growth time is given by

$$t_{21} = (L_2 - L_1)/G(T). \tag{4.2}$$

The function G(T) is the average ice particle growth rate (see Section 4.2.1).

A number of assumptions must be made in order to apply these calculations. It is essential that the growing particles remained in a water saturated environment so that the entire growth history can be represented by a laboratory derived growth rate, without having to resort to the complex and error-prone task of measuring the in-cloud temperature and ice supersaturation (e.g. Krämer et al. (2009)). There must be no processes such as aggregation, which would modify ice particle number concentration or riming, which would modify particle size. Likewise, the particle must not be a fragment of mechanical breakup, for example of a large dendrite. Any change in size must be the result of diffusional growth only: number must only change via the ice production mechanism.

In HHC87 the ice particles are assumed to have negligible size upon production; the particles were fragments from rime splintering in cumulus clouds. In the altocumulus clouds the ice particles were also assumed to initially have small size since they were formed from the liquid cloud population. In the clouds on 2^{nd} February 2012, the maximum size of cloud drops was ≤ 30 μm.

To ensure these assumptions were satisfied, only ice particles smaller than 137 μm were considered in HHC87. With the current generation of instruments the minimum size where calculations are valid should be smaller, due to the improved resolution of the newer OAP probes. The calculations were performed for all particles larger than the minimum probe size (for CIP15, this is 30 μm), and the implications of doing this are discussed. The same calculations were also performed

for larger size categories, up to 800 μm, to test how far the assumptions hold.

The ice production rate was calculated for adjacent bins using data from the CIP15 (15 μm pixel size) for altocumulus sampling, and 2DS (10 μm pixel size) for the cumulus clouds.

4.2.1 Ice Growth Rates in Mixed-Phase Clouds

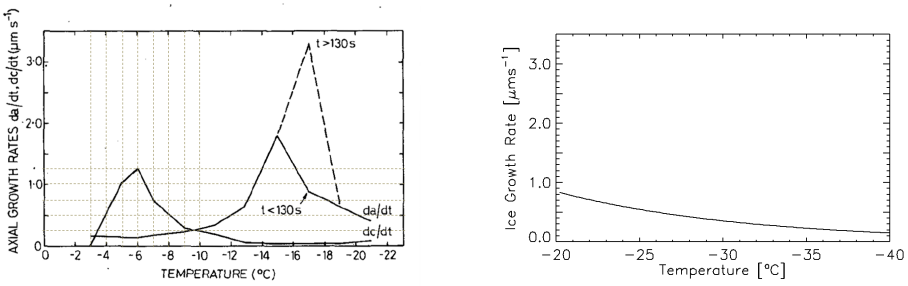

Figure 4.1: Ice particle growth rates as a function of temperature for different temperature ranges left: (Ryan et al., 1976), 0° C $\leq$ T $\leq$ -22° C with construction lines annotated. right: (Bailey and Hallett, 2012) -40° C $\leq$ T $\leq$ -20° C for water saturated "Region A".

The altocumulus clouds sampled on 2^{nd} February 2012 were found with CTT = -30° C. The curve for water saturated "Region A" (Bailey and Hallett, 2012), Figure 4.1 (right panel) was applied which is a temperature dependent growth rate for plate-like particles in the temperature range from -40° C to -20° C. At T = -30° C, the growth rate G(R) = 0.36 μm s^{-1}. The CTT temperature was used as input to the growth rate equation. This implicitly states that ice nucleation had taken place here, at cloud top. Uncertainty in the nucleation location was accounted for by a range in the ice growth rate to account for a possible range in nucleation temperature (vertical location). At temperatures greater than -20° C the most appropriate growth rate is found in Ryan et al. (1976), (Figure 4.1,

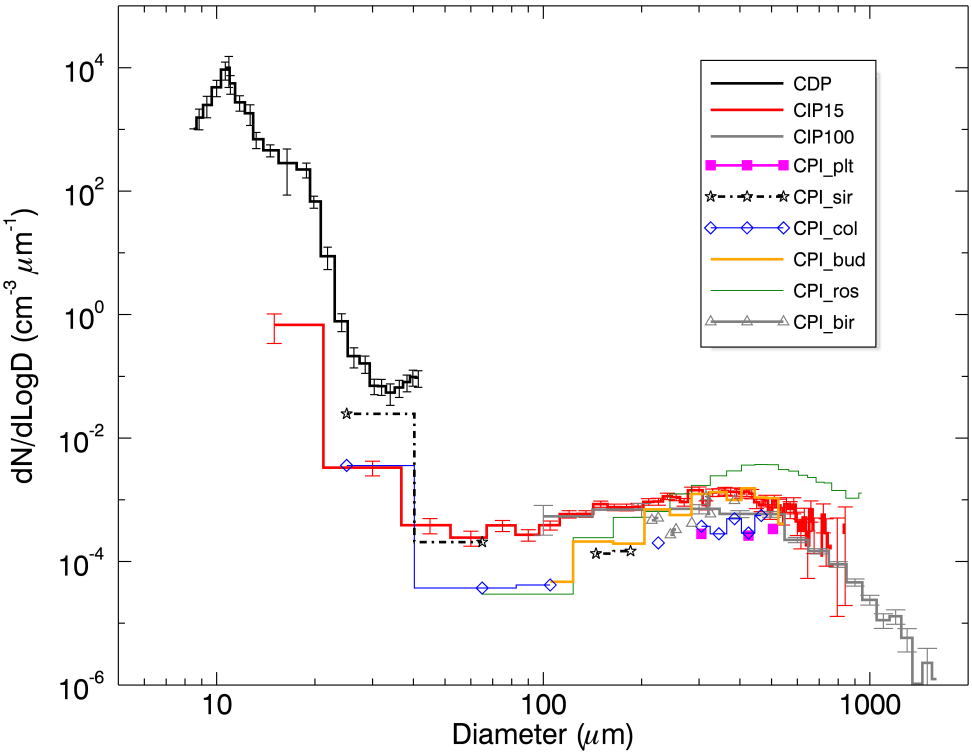

Figure 4.2: Composite cloud particle size distribution on 2^{nd} February 2012, for 636 seconds in mixed-phase altocumulus cloud where N_d(CDP) $\geq$ 2 cm^{-3} and N_i (CIP15) $\geq$ 0.1 L^{-1}. CDP (black), CIP15 (red), CIP100 (grey) and habit segregated CPI data downgraded to 50 μm bin size (Connolly et al., 2007) (see figure legend).

left panel, as per HHC). Construction lines were added to the curve to allow manual extraction of rates from the original figure, for use in the cumulus clouds encountered on 24^{th} November 2013 and show that G(R)$_{(-7^{\circ}\ C)}$ = 0.95 μm s^{-1} and G(R)$_{(-9^{\circ}\ C)}$ = 0.5 μm s^{-1}.

4.3 Observations of Ice Particles in Altocumulus, 2^{nd} February 2012

The general observations were presented in Chapter 3. Figure 4.2 shows a composite size distribution of liquid cloud and ice particles from mixed-phase altocumulus on 2^{nd} February 2012 between 1700 UTC and 1730 UTC. These data were used in the calculations of ice production rate. Mixed-phase cloud was defined where drop concentrations reported by CDP were greater than 2 cm^{-3} and CIP15 data show concentrations greater than 0.1 L^{-1}, resulting in 636 seconds of data with T = 243.9 $\pm$ 0.6 K (242.3 $\leq$ T $\leq$ 246.1 K).

It can be seen in Figure 4.2 that the CDP shows a strong mode at 8.5 μm, and a maximum size close to 25 μm. The smallest two bins of the CIP15 (red line) ($\leq$ 30 μm) show lower concentrations than CDP but have a similar shape, and so this probe is likely to be responding to the liquid cloud population. It is not possible to distinguish the shape or habit of particles on CIP15 at this size.

CPI data were first re-binned by combining data from 5 adjacent bins, so that each are 50 μm in width. Then the sizes distributions are plotted, segregated by a derived habit (Connolly et al., 2007). For the smallest bin the sampled particles predominantly fall into the "spherical (CPI_sph)" category (not shown), with "small irregular (CPI_sir)" (star, and dashed-dotted black) and "columns (CPI_col) (blue diamond, solid)" up to 100 μm. The habit at these small sizes should be treated with caution, although it is clear that qualitatively the CPI responded to the large liquid particles and supports the CDP and CIP15 observations at this size range. The small sample volume also limits the confidence in the reported number concentrations.

There is a minima in the distribution measured by CIP15 between 50 μm and 70 μm which represents a crossover between the liquid cloud at smaller sizes, and the growing ice particles at larger sizes. The CPI did not respond to many particles in this size range, a consequence of the low sample efficiency of the probe. The probe suffers from "dead-time" whilst an image is read-out to disk, and so the triggering is strongly biased to the mode of the size distribution. At all sizes larger than 100 μm both the CIP15 and CIP100 sample the ice population and agree reasonably well. The measurements of the particle size sample volume may also be in error.

From 100 μm and larger there are particles identified by CPI as "budding (CPI_bud)" and "rosettes (CPI_ros)" with concentrations increasing with size up to a mode close to 300 μm and 500 μm respectively. Between sizes of 100 μm and 200 μm are "small irregular (CPI_sir)" that above 200 μm give way to "budding irregular (CPI_bir)", "plates (CPI_plt) and columns, up to 400 μm. Above this size only rosettes are identified, but at much larger concentrations than either CIP15 or CIP100 which agree well at all sizes within error margins.

Figure 4.3: CPI Particle Imagery from 2^{nd} February 2012 to show ice particle habits as expected at this temperature range (Bailey and Hallett, 2004, 2009). The particles are plates and assemblages of plates. There is evidence of riming at sizes larger than 400 μm. The CPI sample rate is too slow for a representative sample and so the mode of the size distribution is sampled preferentially. (*courtesy of I. Crawford, Univ. Manchester*)

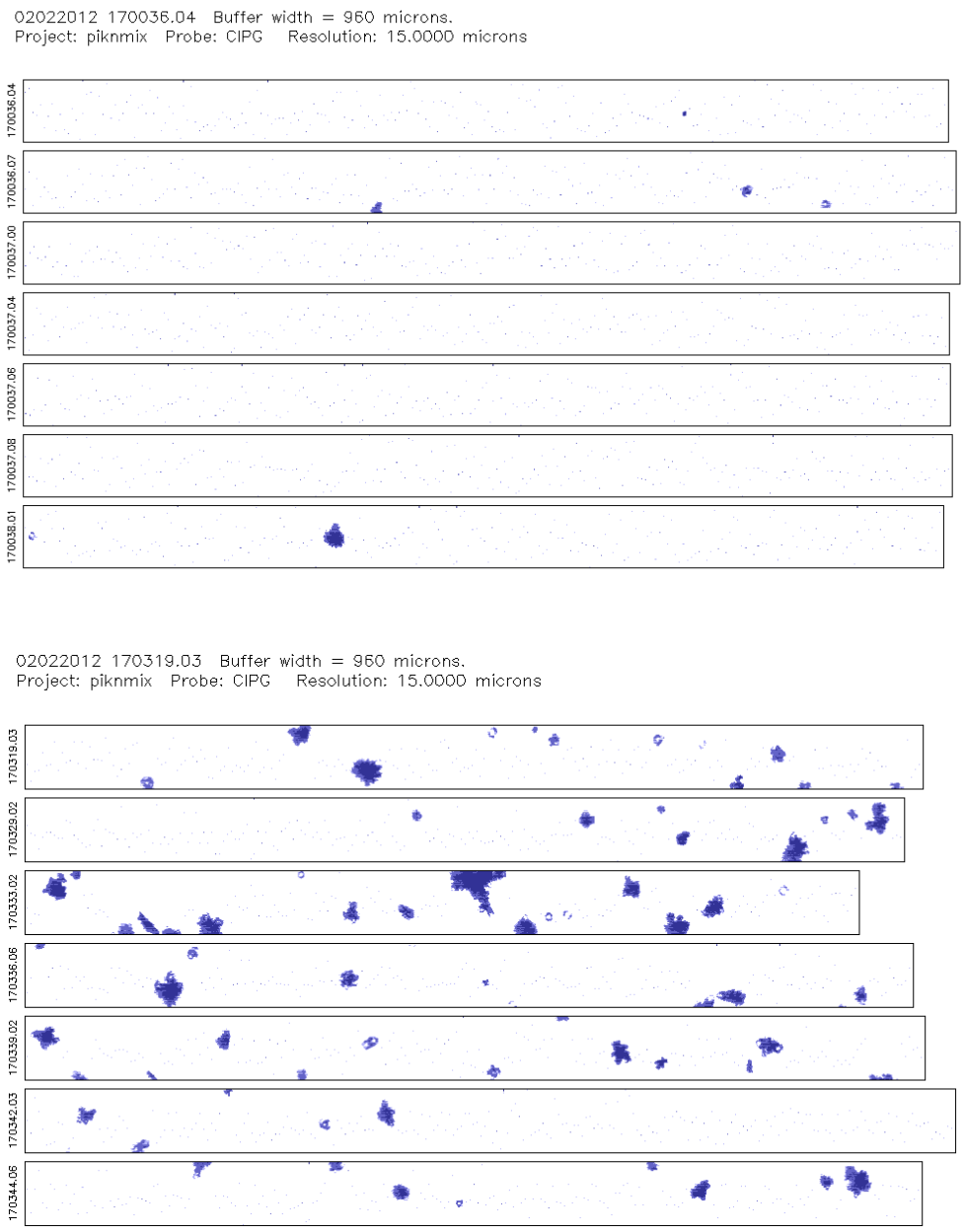

Figure 4.4: CIP15 imagery from 2^{nd} February 2012 mixed-phase region from (a) close to top of liquid layer and (b) close to base of liquid layer. Each panel is 960 μm deep. The probe responds to liquid cloud particles, predominantly at cloud top, where they are largest. Close to cloud top the concentration of ice particles is low. Close to cloud base the ratio is now shifted and ice is the predominant habit.

The dominant ice particle type sampled by CPI (Figure 4.3) in this mixed-phase regime appeared to be complex polycrystalline structures. Many images show particles that are close to 400 μm in size. The particles share many features of "assemblages of large plates" that are shown by Bailey and Hallett (2009, Figure 5) to be present at temperatures close to -30° C above water saturation. In general the particles are complex, also observed by Korolev et al. (2000). But it is thought that they have grown as single crystals, without aggregation, certainly for the smaller sized particles $\leq$ 400 μm. Small pristine particles and columns were not frequently sampled but some particles of less than 20 μm are present. If, though, the observations of columns at sizes smaller than 50 μm are in fact correct then the calculation of primary ice production rate will not be correct. The observations presented here do show some evidence of particle riming, particularly at the larger sizes above 400 μm. However, calculations were performed as if riming was insignificant and the impact of this assumption is discussed below.

There was no evidence of particle shattering on the CIP15 probe when inspecting the imagery. The maximum particle size was smaller than 2 mm and predominantly below 1 mm. Minimisation of particle shattering by physical anti-shatter tips (Korolev et al., 2011) on the probe leading edges coupled with Inter-Arrival-Time (IAT) algorithms in the processing appeared to be successful in this case. It is more difficult to diagnose shattering on the CPI (Connolly et al., 2007) and so the concentrations of small particles $\leq$ 50 μm are more uncertain.

The evidence supports the notion that these ice crystals have a growth history in a water saturated environment. CIP15 data are shown in Figure 4.4 for two short time periods from a location close to the liquid cloud top (Figure 4.4, Top) that shows predominantly small particles, probably liquid, with the occasional larger irregular ice crystal. Lower down, close to the base of the liquid cloud layer

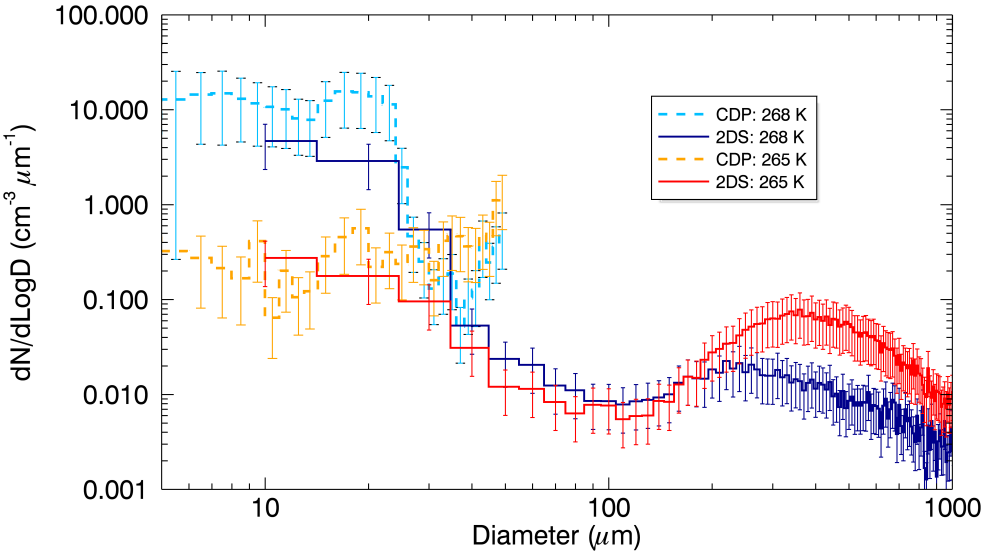

Figure 4.5: Composite cloud and ice particle size distribution for two passages through cumulus cloud during B816, 24^{th} November 2013, Case 268 K: CDP (cyan) and 2DS (blue), 265 K case: CDP (orange) and 2DS (red).

(Figure 4.4, Bottom), the frequency of the small (liquid) cloud particles was lower, and large irregular ice particles were observed in much greater concentrations. Number concentrations of ice particles increased with distance below cloud top, to a maximum at cloud base, and remained constant throughout the mixed layer until $Dz_{(CTH)} \leq$ -400 m (Figure 3.19, left), taken to be further evidence that the ice is growing within the cloud layer and falling through it.

4.4 Observations of Ice Particles in Cumulus, 24^{th} November 2013

The cumulus clouds on 24^{th} November 2013, flight B816, were sampled on a slant profile climbing from liquid cloud base at 930 hPa, and T = -4° C through the mixed-phase region to cloud top colder than -10° C at 850 hPa (Section 3.3). Two

segments through mixed-phase cloud were defined, the first in the temperature range -4° C to -6 ° C, (the 268 K case) and the second between -7° C and -9° C (the 265 K case). Both sections were taken from this single profile, upwards through a mixed-phase cumulus cloud, and are each only a few seconds long. The size distribution data from CDP and 2DS are presented in Figure 4.5. The limited sampling time means that the errors are somewhat larger than for the composite size distributions presented from the altocumulus cloud. The data are adequate for the computation of ice production rate.

The CDP data from the 268 K case show that there were much greater concentrations of liquid cloud drops at the warmer lower altitude level, with a mode at 10.5 μm. The 2DS data showed good crossover at the larger sizes up to 30 μm. Above this size, the CDP bin concentrations increased markedly; possibly indicating spurious data and evidence of CDP responding to large ice, outside the DoF. At the higher, colder altitude of the 265 K case the liquid drops were present in much lower concentrations and showed a more flat distribution with a similar increase at the largest sizes. The cause of this increase is unknown, but may in part be related to the ice production of elongated columns which are not well characterised by the CDP, which assumes liquid spheres in the calibration. The flat distribution is probably the result of ice growth causing drops to both evaporate and reduce in number, implying that the Wegener-Begeron-Findeison (WBF) process (Korolev, 2007a) was active, reducing the size of and even evaporating the smallest drops, and also that riming was occurring causing reduction in concentration of larger particles.

Ice particles with small size were more numerous at the lower level but only slightly, however there were many more particles larger than 200 μm at the upper, colder level. These particles were in the correct temperature regime and of the

appropriate size (Abel et al., 2017) to have been produced by rime-splintering in the Hallett-Mossop process (Hallett and Mossop, 1974), and were likely to be growing whilst they were lofted in the updraught that generated and supported the cumulus cloud, at the expense of the liquid cloud drops.

4.5 Calculation of Observed Ice Production Rate, P_0

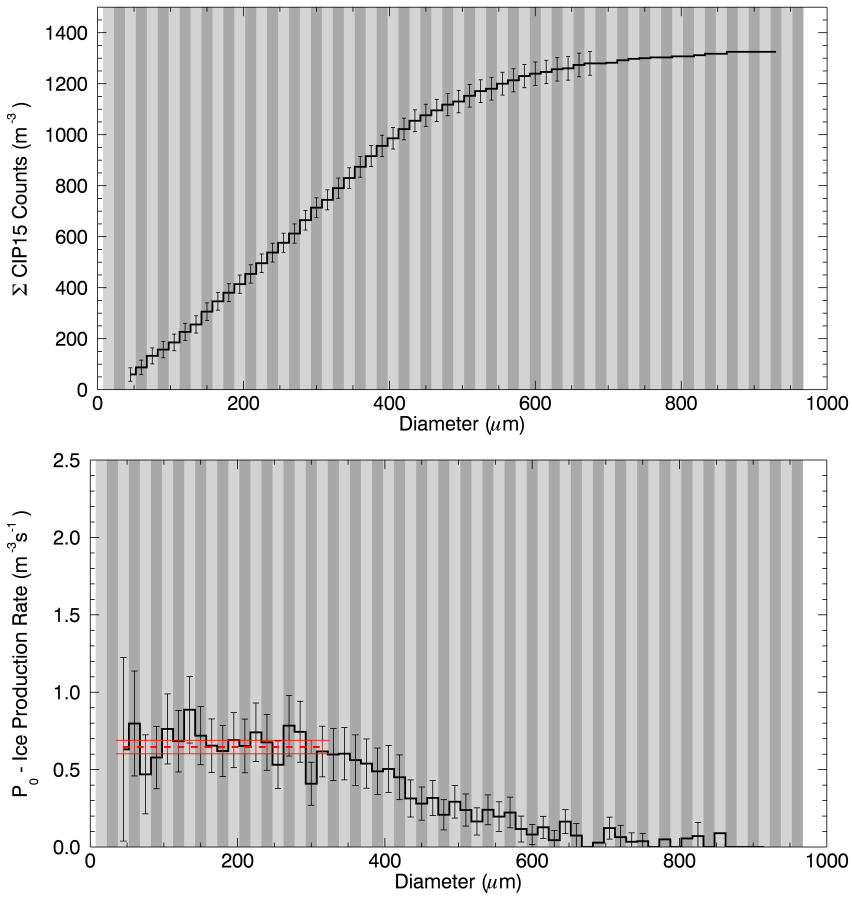

Figure 4.6: Top: CIP15 Cumulative size spectra with errors and Bottom: Calculated ice production rates, P_0, from CIP15 between 50 μm and 800 μm with errors (black), and error weighted mean (red-dashed) and standard deviation (red-solid) between 50 μm and 300 μm, in altocumulus cloud on 2^{nd} February 2012.

The Cumulative Size Distribution (CSD) from the CIP15 for the mixed-phase altocumulus cloud sampled on 2^{nd} February 2012 is plotted in Figure 4.6 (upper panel) for the full range of the instrument. The smallest two bins, which respond to the liquid cloud population, have been excluded. The gradient of the distribution is consistent, considering errors, up to a size of 350 μm. At sizes larger than 400 μm the gradient reduces in steepness, suggesting that a different process was operating, and so the original assumptions become invalid. This large particle region of the cumulative size distribution is possibly evidence for growth through the riming process (see imagery in Figure 4.3) which changes particle size independent of the vapour deposition growth rate. Applying riming calculations to observations is considered to present complexities that are beyond the scope of this work (e.g.)Erfani and Mitchell (2017)).

Ice production rate, P_0, was calculated for all data ($\approx$ 45 μm to 900 μm) by using the difference in counts between a particular bin, and its neighbour below (Figure 4.6, lower panel). The growth rate was prescribed as 0.36 $\pm$ 20% μm s^{-1} (Figure 4.3, Bailey and Hallett (2012)), with the range accounting for uncertainty in the nucleation temperature (i.e. altitude in cloud). The liquid layers were up to 300 m deep, and so the temperature range between top and base is of the order 2 K to 3 K.

Calculated rates are presented as a function of particle size and it is interesting to note that the calculated values vary little across the size range, and this feature is exploited by using all data $\leq$ 300 μm (bins 3 to 20) and calculating a weighted mean P_0, valid below this size, accounting for the error on each measurement. The result is that for this cloud the ice production rate, $P_0 = 0.65 \pm 0.04$ m^{-3}s^{-1}, plotted as a red-dashed-line, with errors in solid-red lines (Figure 4.6).

The same calculations of P_0 were performed for the two glaciated cumulus cloud

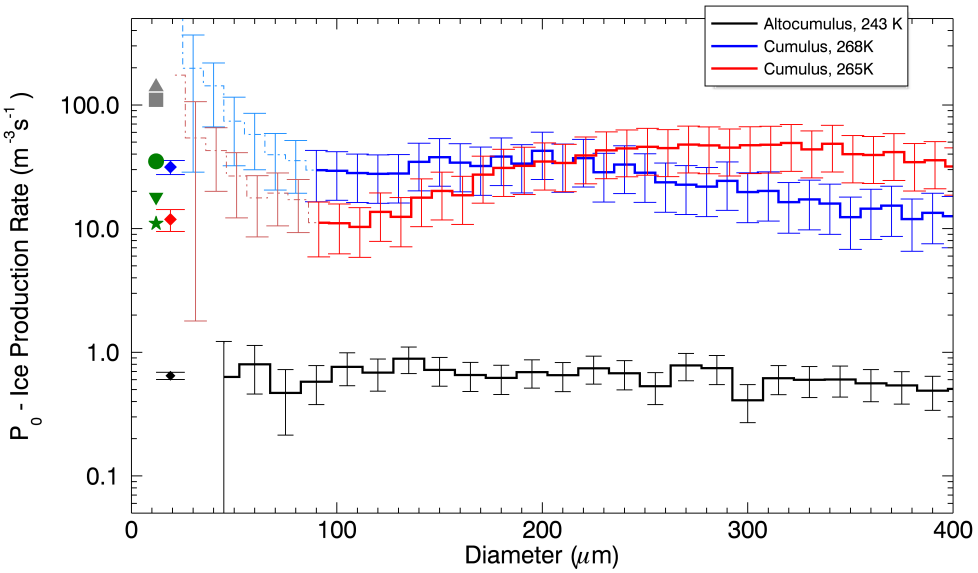

Figure 4.7: Calculated ice production rates for flight in altocumulus cloud at 243 K(black) and in cumulus cloud at 268 K (blue) and 265 K (red), from adjacent bins from CIP15 or 2DS, up to 300 μm. Mean value for appropriate size range shown in diamond and error bar - see text for discussion. Literature reported cases of SIP indicated with green filled shapes (Harris-Hobbs and Cooper, 1987) for three clouds, and grey filled shapes (Taylor et al., 2016) for two clouds (see text for full details).

passages and the final results are presented in Figure 4.7 as a function of particle size, in this case with data from the 2DS probe which benefits from a smaller pixel dimension of 10 μm. The results are from cumulus cloud at a temperature of 268 K and 265 K. The rate of growth for these ice crystals was taken from Ryan et al. (1976) which covers a more appropriate temperature range. For the colder case, 265 K, the applied growth rate is 0.5 $\pm$ 0.2 μm s^{-1} and for the warmer cloud at 268 K is 0.95 $\pm$ 0.38 μm s^{-1}, with the ranges here taken from the variability of growth rate across the temperature range.

At sizes smaller than 100 μm the 2DS probe appears to be sampling the largest of the cloud drops and so these size bins are excluded from the calculations. The data are plotted in muted blue and red colours. The warmer cumulus cloud at 268 K

shows less variability in the ice production rate estimate across a wider range of bin sizes, up to 200 μm. In the colder case, at T = 265 K, the calculated rates begin to increase rapidly for sizes larger than 140 μm something that is attributed to the lofting of ice particles from below into this level.

Particles generated at lower altitudes in an updraught have time to grow to larger sizes before reaching the upper, colder level. Horizontal variability means that it is unlikely that the same updraught was sampled on both segments. Any lofted particles would contaminate attempts to measure the local ice production rate due to rime splintering. Hence, for the cold case (265 K) only particles between 100 μm and 140 μm were used when calculating a weighted mean and error, shown with a red-filled diamond with error bars. For the warmer case data from 100 μm to 200 μm were included in the weighted mean calculation, shown with a blue filled diamond and error bar.

Also on the figure are the data from the original HHC87 work, for a variety of cumulus clouds in the USA within the HM SIP zone. The green star is for Florida clouds, the green downwards-triangle for Montana and the green circle for California. These observations lie within the range of the cumulus SIP rate observations presented here. Other more recent results were presented by Taylor et al. (2016) for observations in cumulus cloud in the UK, shown with a grey-upwards triangle for 286 K and a grey-square for 261 K. These measurements are larger than those in this research or HHC87, but are comparable when the quoted error margin of an order of magnitude is account for.

Flights	Cloud	Temp. [K]	Instrument	Diameter [μm] Min	Diameter [μm] Max	P_0 [$m^{-3}s^{-1}$]
2^{nd} Feb 2012	Altocumulus	243	CIP15	45	300	0.65 ± 0.04
24^{th} Nov. 2013	Cumulus, UK	268	2DS	90	200	31.4 ± 4.0
		265		90	140	11.9 ± 2.4
Harris-Hobbs and Cooper (1987)	Cumulus, Florida	268, 262	2DC	112.5	137.5	18 ± 31
	Cumulus, Montana	265±5				11 ± 29
	Cumulus, Calif.	266±6				35 ± 88
Taylor et al. (2016)	Cumulus, UK	286	2DS	-	150	140 ±
		261		-		110 ±

Table 4.1: Calculated Ice Production Rates, P_0 Harris-Hobbs and Cooper (1987).

4.6 Ice Production Discussion

The observations of the ice particle size distribution were used to compute the ice production rate, P_0, in altocumulus and cumulus clouds. The rates calculated for altocumulus are deemed to be primary ice production rate. The cumulus clouds were in the ideal temperature range for ice production through rime splintering and so the ice production is presumed to have been dominated by a secondary ice production mechanism. The calculated values of ice production rate in altocumulus clouds were found to be at least one or two orders of magnitude lower than those found in cumulus clouds where SIP processes were suspected. An ice production rate could not be calculated for the stratocumulus clouds in this study due to the presence of drizzle in the cloud observations. The drizzle particles fall in the same size range as the smallest ice particles and so contaminate attempts to make the ice production measurements.

Potential under-sizing of columns by up to 50 % due to orientation was a source of error in HHC87, leading to an error in ice production rate of a factor of 2. The same problem is not as large in the altocumulus clouds since the particles are complex shapes rather than columns. The feature may apply to the cumulus clouds on 24^{th} November 2013. The constant slope of the altocumulus CSD up to 300 μm is taken to imply that the same process is responsible for the ice production up to this size. Assuming steady state production and growth: ice production has been operating for a period that is equal to the maximum dimension divided by the growth rate, which assuming the growth rate of 0.36 μm s^{-1} gives an ice-production-time to get to this size of the order 100 s.

4.6.1 Onset of Riming in Altocumulus Case

Erfani and Mitchell (2017) present results from previous observational and modelling studies that indicate a range of minimum riming dimension thresholds, D_{thresh}, for various ice particle habits, between 35 μm for hexagonal columns, and 200 μm for broad-branched plates. Particle imagery in this research shows evidence of riming. The PSD shows a reduction in number concentration of particles larger than a few hundred microns suggesting that the onset of riming occurs at sizes somewhat smaller than 300 μm.

This riming theory could explain the change in PSD gradient *or* the growth rate could have been badly prescribed. Assuming that the only other process that changes the ice particle size is riming then there is information in this gradient that contains the riming growth rate, as a function of ice particle size. Simultaneous determination of both the raw ice production rate and the riming rate would probably require an iterative procedure to find the optimum solution and is not considered in any more detail here.

4.6.2 Ice Nucleation Mechanism

The uncertainty on the growth rate means that, in these thin cloud layers, it is impossible to determine at what vertical level the ice was nucleated. In the altocumulus clouds it is possible to use ice particles as small as 60 μm because, fortuitously, the largest liquid cloud particles do not contaminate the ice observations from CIP15 to the same extent as they do in the cumulus cloud, where the tail of the size distribution of liquid cloud particles extends up to 80 μm. The additional resolution on 2DS is therefore redundant in this situation, although it would be welcome when sampling altocumulus clouds.

The mode of the cloud drop size distribution is of the order 10 μm with a maximum particle size greater than 25 μm. The ice will have an initial size equal to one of the particles in the liquid cloud drop size distribution but it is not known which of the particles freeze during the ice nucleation process. Depending on the immersion freezing mechanism at work, it could be the very smallest drops, during Contact Nucleation Inside Out (CNIO, Durrant and Shaw (2005)) or alternatively a large drop, containing a large INP (de Boer et al., 2010), acting either stochastically (Vali, 2014) or deterministically.

Observational studies from Arctic stratocumulus suggests that large droplets are required before ice formation is observed (Rangno and Hobbs, 2001). Large drops will result in a reduction in the concentration of any contaminants that prohibit freezing (e.g. de Boer et al. (2010)). The implication is also that there is a drizzle process prior to initiation of ice, and there is no evidence for that here.

Despite this, the largest drops are found near cloud top and this would mean that ice crystals are most likely to form close to here where the concentrations of larger drops is greater. The observations are consistent with this happening here, because

the size of ice particles is observed to increase with depth, down through cloud. Confirmation of this is not possible because there is not sufficient information. It could also be the case that ice particles formed uniformly throughout the cloud depth, whereupon they begin to grow and sediment, with the probes then identifying this automatic size sorting.

4.7 Aerosol Particle Measurements

In the absence of an INC, an assessment of the Ice Nucleating Particle (INP) concentration was made by measuring the number concentration of large aerosols with d $\geq$ 0.5 μm and applying empirically based parametrisations from DeMott et al. (2015) and Tobo et al. (2013). The PCASP only makes good aerosol measurements when out of cloud, so clear-sky time periods were identified using data from the Nevzorov Total Water Content probe. Defining a clear-sky flag using a hot-wire probe is beneficial because it is independent of the cloud microphysics probes, meaning that CDP could be used to measure the larger aerosol particles.

4.7.1 Thermodynamic Regimes

Four thermodynamic regimes were defined from the flight data collected on 2^{nd} February 2012 to facilitate the analysis of aerosol observations, as can be seen in the profile of potential temperature, θ, in Figure 4.8a. Details of the layers are summarised in Table 4.2, which has a summary of the mean and standard deviations of temperature and potential temperature within the layers. The Boundary Layer (BL) was defined to extended up to 1000 m. A Stable Layer (SL) was found between 3000 m and 4200 m. The altocumulus clouds were present in the thermodynamically well-Mixed Layer (ML), physically located between

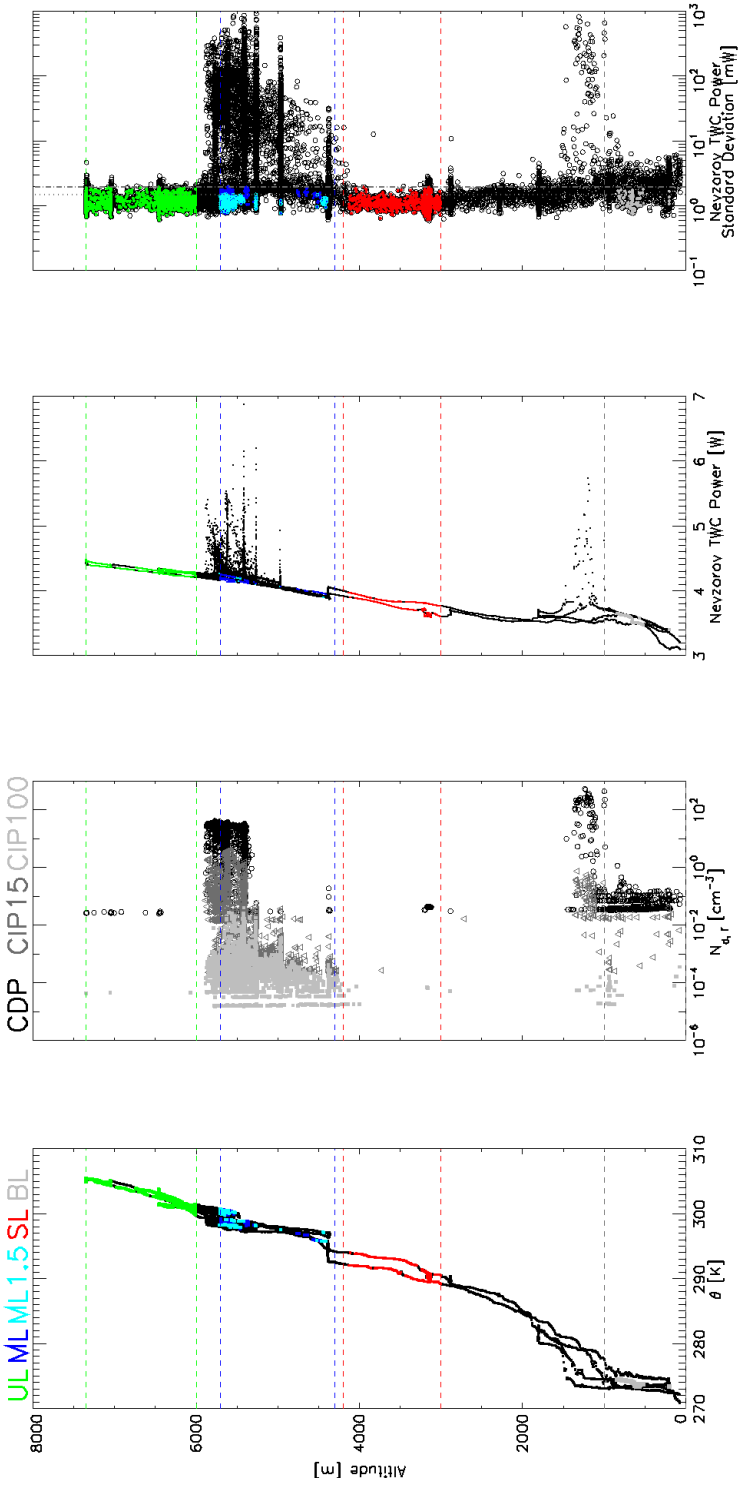

Figure 4.8: Vertical profiles of (a) potential temperature, (b) cloud microphysics from: CDP (black circles), CIP15 (Dark grey triangles) and CIP100 (light grey squares) and (c) Nevzorov TWC power and (d) Nevzorov TWC power standard deviation. Thermodynamics regimes for (a), (b), (c) (see Table 4.2), BL: grey, SL: red, $ML_{2.0}$: blue, $ML_{1.5}$: cyan, UL: green.

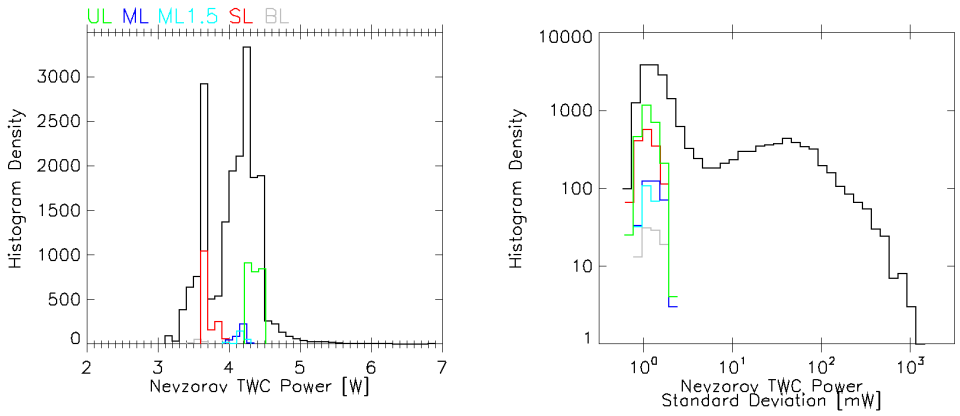

Figure 4.9: Histograms of Left: Nevzorov Total Water Content (NVT) sensor power, and Right: standard deviation of Nevzorov Total Water Content Power for use as a cloud flag. All data: black, Thermodynamics regimes (Table 4.2), BL: grey, SL: red, $ML_{2.0}$: blue, $ML_{1.5}$: cyan, UL: green.

approximately 4300 m and 6000 m. The limit at the top of the layer was actually defined as 50 m below the previously calculated CTH. Two flags were defined, based on different Nevzorov TWC thresholds. Above 6000 m, and above the altocumulus clouds, referred to as the Upper Layer (UL), the air was also vertically stable. For these thermodynamically identified layers the variability of potential temperature was less than 1 K in the boundary layer and stable layer, and between 1 K and 2 K in the mixed and upper layers.

The cloud and precipitation measurements are shown in Figure 4.8b with number concentrations of cloud particles measured by CDP, larger cloud and precipitation sized particles from CIP15 and precipitation particles from CIP100. The vertical profile of Nevzorov TWC Power (Section 2.5) is in Figure 4.8c, and the 1 Hz standard deviation of the 32 Hz record of power is shown in Figure 4.8d.

4.7.2 Clear-Sky Flag from Nevzorov TWC Power Data

Whilst the data from the cloud microphysics probes in Figure 4.8b could be combined to generate a cloud flag, the lower size limit of 5 μm means that CDP will miss some of the smaller cloud particles, especially near cloud boundaries, where nucleation or evaporation occur, and so such a clear-sky flag is prone to failure. The Nevzorov TWC probe can detect particles smaller than 5 μm , albeit with a collection efficiency below unity, close to 0.3 (Korolev et al., 1998a). The probe sensing head was the deep-cone version so the collection efficiency as a function of particle size is expected to be slightly different from that presented in the original work.

The power drawn by the hot-wire probe ranges between 3 W and 7 W, with a general increase in power with altitude when out of cloud (Figure 4.8c). The drift is related to the dry-air baseline which varies as a function of atmospheric and aircraft attitude parameters (Abel et al., 2014). The variability was much larger when sampling in-cloud, as evidenced by comparing observations of standard deviation of Nevzorov TWC power in Figure 4.8d to those of cloud particles in Figure 4.8b. The out-of-cloud regions, in the stable and upper layers, show that typical out-of-cloud variability was between 0.5 mW and 3 mW. When cloud physics probes reported cloud particles the Nevzorov TWC reported orders of magnitude greater variability, of up to 1 W.

In Figure 4.9 (left panel) the histogram of the Nevzorov power for the whole flight is plotted in black. There was no separation between the clear regions and the cloudy regions, based on power alone. The histogram of the standard deviation of Nevzorov TWC power shows that data from the flight fell into a bi-modal distribution (Figure 4.9 (right)). The lower variability mode corresponds to clear

sky, and the larger variability mode is attributed to in-cloud data, on this scale of 32 records per second. There is a crossover between these two distributions somewhere in the region of 8 mW, but the distinction is not clear cut.

The noise, or variability of the signal of the hot-wire probe is assumed to have a source in the electrical signal noise of the instrument and from unrepresented changes to the dry-air cooling baseline term. The mixed layer has a high relative humidity, and below water saturation there will still be some humidification of aerosol due to water molecules that get adsorbed onto the surface of aerosol particles. Evaporation of this moisture on the humidified aerosol could potentially be responsible for some component of the "noise" that is seen on the Nevzorov baseline signal. More exploration would be required, by looking at data from different regions, with a range of humidity and aerosol concentrations.

4.7.3 Clear-Sky Thermodynamic Regimes

Clear-sky regions were defined using the four thermodynamic regions and a threshold on the standard deviation of Nevzorov TWC power of 2.0 mW (Table 4.2). A tolerance window of 5 s either side of any positively-identified cloudy data-point protects against clock differences on probes, different instrument locations on the aircraft, and imprecise determination of cloud edges, including rogue particles, over a length-scale of up to 700 m, at the expense of a reduction in the number of data points. As a check on the standard deviation thresholds, a second mixed layer flag was produced with a 1.5 mW limit.

Flagging in this way resulted in nearly 3000 seconds of data in UL, 1800 s in SL, but only 500 s in ML and less than 100 s in BL. To mitigate against so few data points in the layer of interest, ML, a composite Higher Layer HL=ML+UL was

Code	Layer Type	Altitude [m]		Sample Volume [L]		Temperature [K]		θ [K]		
		Min.	Max.	PCASP	CDP	$\overline{T}$	σ_T	$\overline{\theta}$	σ_θ	n [s]
BL	boundary	0	1000	0.2	5.0	270.9	1.2	274.0	0.3	95
SL	stable	3000	4200	3.1	81.6	261.4	1.8	290.8	0.9	1713
ML	mixed	4300	(-50)	0.6	25.6	246.9	2.6	298.8	1.3	506
UL	upper	6000	(-)	3.9	197.1	237.3	3.2	303.9	1.5	2993
HL	ML and UL	4400	(-)	4.5	222.7	243.4	7.5	300.4	4.3	3499

Table 4.2: Cloud-free flags for different atmospheric layers on 2^{nd} February 2012, Categories are Boundary (BL), Stable (SL), Mixed (ML) and Upper (UL) Layer and a composite flags Higher Level (HL) from ML and UL. See text for details. Mean and standard deviation of temperature, potential temperature and number of seconds of data in each flag are provided.

defined, using a lower tolerance window of 2 s. For this to be successful requires the assumption that the aerosol populations in the two regimes are self-similar. This is not necessarily the case, as the inversion and the humidity distribution are suggestive of different airmasses. This is a major limitation of these airborne observations. The total volume of air sampled during the compositing regions for CDP and PCASP are give in Table 4.2.

Nevzorov TWC power and standard deviation values for these flagged regions are indicated in Figure 4.9 with BL, SL, ML, 1.5 mW, ML, 2.0 mW, and UL. The same regimes are over-plotted on the profiles in Figure 4.8, for Potential Temperature, Nevzorov TWC Power and Standard Deviation.

4.7.4 Aerosol Particle Size Distribution Data

Aerosol Particle Size Distributions (PSDs) observations from the PCASP and CDP data were extracted for the clear-sky regimes in order to verify the performance of the clear flag and to identify the number concentrations of particles larger than 0.5 μm for input into INP parametrisations (see Section 4.7). The data are presented in Figure 4.10 for the Higher Level composite layer. Errors were greatly reduced by using the combined-bin schemes and the measurements were then above the limits-of-detection by up to an order of magnitude.

The data collected from the Mixed Layer (ML) only are shown in hatched-grey lines for comparison against the composite. The data from the mixed layer and upper layer look very similar although data from the mixed layer was truncated at sizes larger than 1 μm and also are absent in the CDP data. Truncation also occurred when other choices were made in the flagging routine: the 1.5 mW mixed layer flag and a flag with a higher power standard deviation of 4.0 mW both

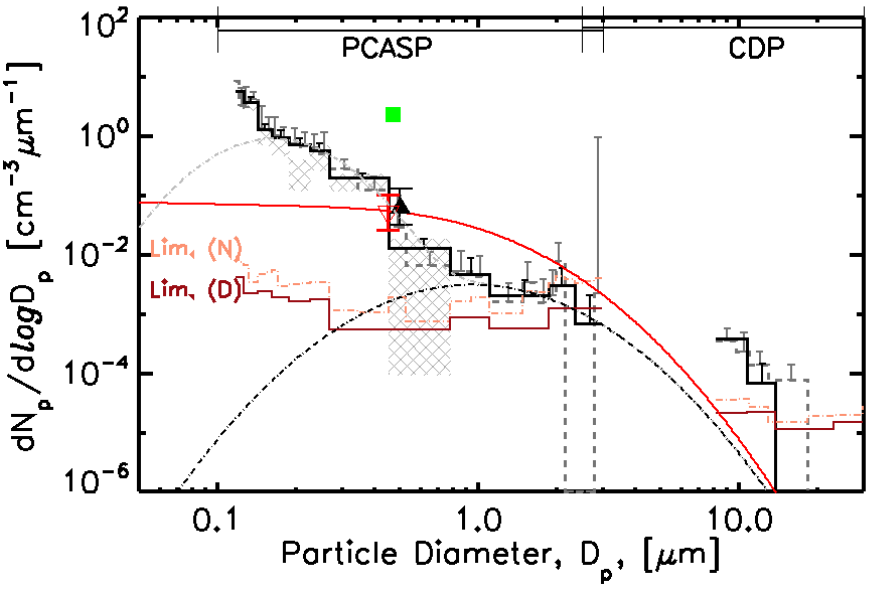

Figure 4.10: Aerosol particle size distribution observations from 2^{nd} February 2012 from PCASP (27 bins - high (native) resolution (dashed grey)), 12 bins low (downgraded) resolution (solid black) and CDP (10 bins - high resolution (dashed grey), 6 bins low (solid black)) for Higher Level (HL) composite. Positive error bars only are shown for clarity. Fitted two-mode log-normal curve, thin-dashed grey (accumulation) and dot-dashed black (large mode) and the LoD (native res. solid red, downgraded res. dashed-orange). CSD (large mode) in solid red curve. Total CSD and error: empty red triangle, sum of observations and error: filled black triangle. Observations assuming dust (approximately doubled size bins): green square.

showed similar truncation (not shown). The reason for the lack of large particles with d $\geq$ 1.0 μm in the mixed layer observations is not clear, it could be a lack of particles due to their removal through ice or cloud processing, or a lack of sensitivity to them with the processing methods adopted.

Large particles that were observed with CDP in the Upper Layer are of unknown type and refractive index. The low number concentrations and consequent large statistical counting uncertainty make the size distribution determination difficult.

The narrow forward scattering angle makes the measurements more uncertain for the large particles, which, being potentially non-spherical, may not scatter in a well known way.

PCASP data from all regimes show that the full size distribution of aerosol particles was not fully sampled - the mode of the distribution was smaller than the PCASP can identify, so was not resolved. There is evidence that more than one sub-micron mode was present with peaks in concentration between 0.2 μm and 0.3 μm, and possibly a smaller mode in the region of 0.12 μm. Composition data, which could potentially shed light on this, were not available. The two modes in the sub-micron range may indicate two different types of aerosol, but there is also the possibility that this is an artefact of the instrument itself, or of the calibration procedure. It is suspicious that a very similar feature is also present in all the data from all different levels.

A freely available package, MPFIT (Bohlender et al., 2009), was employed to generate fit parameters with the errors considered as in Chapter 2. A two-mode log-normal curve (e.g. Seinfeld and Pandis (2006)) was fitted to the PCASP data following the procedure detailed in Appendix B. Initially the data at higher bin resolution were considered, for particles with d $\geq 0.161\mu$m, in order to exclude the smallest particles, which could be the result of instrumental or data processing artefacts. The final curve was generated from the downgraded 12-bin PCASP dataset, using the initial fit parameters as the new starting values and plotted in Figure 4.10 as a double-solid red line with the fit parameters shown in the final column of Table B.1. Higher Level PCASP data look to be reasonably well represented by this fit, implying that different aerosol types, or species, are contributing to the two modes. The particles in the large mode have the potential to be significant for ice nucleation.

When downgraded CDP data (6 bins) were included in the fit, with the errors, the fit parameters were greatly altered, with the mode of the large mode reducing to less than 0.7 μm and the width of the distribution increasing greatly, in a non-physical way. Artificially increasing the uncertainty on the CDP measurements by an order of magnitude did not improve the fit. Whilst CDP may have utility in identifying the presence of large aerosol particles, and counting them, it is not reliable when it comes to reporting size in this case where unknowns such as material (refractive index) and shape are unknown.

Summation of the aerosol PSD, from large sizes to small, allowed an estimate of the number concentration of large aerosol particles with d $\geq$ 0.5 μm. Observations from CDP and PCASP were combined and plotted in Figure 4.10, in black. The black triangle and error-bars show that $N_{A_{(d\geq 0.5)}}^{obs.} = 0.066 \pm 50\%$ cm^{-3}, calculated by generating a weighting function for the contribution by the two channels surrounding the 0.5 μm threshold. A separate value was determined by computing the Cumulative Size Distribution (CSD) of the large-mode log-normal fit (solid red curve), resulting in an estimate of $N_{A_{(d\geq 0.5)}}^{lrg.} = 0.052 \pm 50\%$ cm^{-3} shown with an empty red triangle and error bar. The accumulation-mode log-normal curve, has $N_{d\geq 0.5}^{acc.} = 0.082 \pm 50\%$ cm^{-3} (not plotted). Values from the raw bin concentrations are very similar to those obtained from the large mode log-normal fitted curve.

Aerosol Discussion

The PCASP and CDP composite aerosol particle size distribution confirms that the screening for condensed water by using the standard deviation of Nevzorov TWC power signal is adequate. The aerosol PSD from the PCASP does not look to be contaminated by cloud particles and this is confirmed by observation of very low concentrations from CDP for the same regions. The screening within the

mixed layer is very strict and results in very few data points.

The aerosol size distributions were multi-modal indicating different aerosol types. It is unclear if there were two small accumulation modes or if the smaller was is an artefact of the instrument or the processing. The current work is unaffected by this. Both the PCASP and CDP observed large aerosol particles between 0.5 μm and 3 μm from PCASP, and up 10 μm and larger from CDP. A two-mode log-normal fit to the PCASP data looks reasonable, and supports the notion of a distinct large-aerosol mode. There is no way of ascertaining the material that this mode is composed of and so the refractive index remains unknown, and thus the sizing is also uncertain. Number should be unaffected, other than to say that some particles may have been incorrectly placed into an adjacent bin.

The particle composition, if known, could be used to better constrain the refractive index of the particles and so allow better determination of the scattering properties and hence size determination. The impact can be significant for the PCASP and CDP instruments. Mie scattering calculations (Rosenberg et al., 2012) performed using a refractive index of 1.53 + 0.002i, valid for Saharan dust (Ryder et al., 2013) show that the bin edges in both of these instruments can vary by over 200%. Dust can also be highly irregular in shape, which increases uncertainty in the determination of geometric size from the optical scattering due to uncertainty in the scattering phase function (Chen et al., 2006), more so for the CDP than PCASP due to the narrow collection angle of the optics.

Instrumentation that would provide species information was not fitted and so analysis of back-trajectories from a numerical weather forecast model are one way of narrowing down the source and type of aerosol at a particular location in time.

The NAME Model (Section 2.7) was employed to calculate trajectories of air

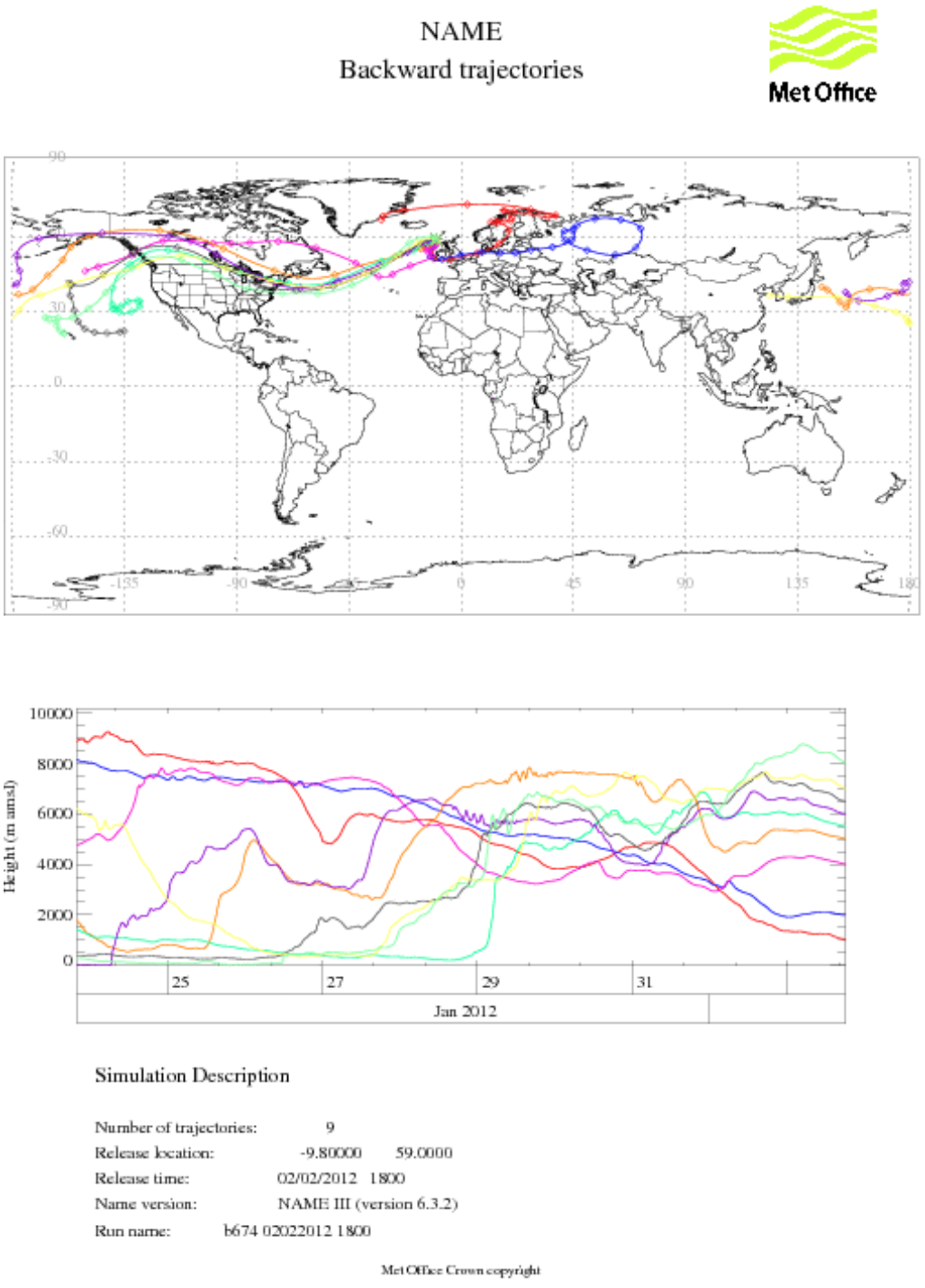

Figure 4.11: "Back Trajectories" from NAME on 2nd February 2012, ending at -9.8 W, 59.0 N, at 1800 z, at altitudes of 1000, 2000, 4000, 5000, 5500, 6000, 6500, 7000 and 8000 m. (Graphics generated by Met Office NAME model).

parcels arriving at a location in the middle of the sampling region, -9.8 W, 59.0 N, on 2^{nd} February 2012 (for flight B674) at 1800 z. The nine trajectories, ending at altitudes between 1000 m and 8000 m, are plotted in the automatically generated Figure 4.11. None of the air parcels that ended above an altitude 1000 m had been in contact with the surface for at least the previous four days. Trajectories relevant to the mixed and upper layers were close to the ground between the 26^{th} and 29^{th} January 2012, over the forested north-western seaboard of North America. It therefore seems unlikely that the aerosol are dust particles but it cannot be ruled out. It is possible that some are uplifted from the boreal forest. If so, then an INP parametrisation which specifically studied the ice nucleating properties of forest emissions, such as Tobo et al. (2013), would be relevant.

4.8 Ice Nucleating Particle Concentrations

The values obtained for the number concentration of large aerosol were input into the INP parametrisations from DeMott et al. (2015) for generic aerosol type, and from Tobo et al. (2013) for forest emissions. Both have a similar functional form. The calculations were performed for a fixed value of 243 K, equal to the altocumulus cloud top temperature and hence this is the maximum possible rate. Deviation from this temperature of ± 1 K is explored with calculations performed using DeMott et al. (2015) at 242 K and 244 K. The results are presented in Table 4.3 for the Upper Level aerosol number concentrations along with extreme values at 248 K and 238 K.

			N_{INP} [L^{-1}]								
			DeMott et al. (2015)			Tobo et al. (2013)			Ratio		
Type	T [°C]	$N_{A(d\geq 0.5)}$ [cm^{-3}]	Low	Mean	High	Low	Mean	High	Tobo:DeMott		
Obs.	-25	0.066	0.013	0.031	0.073	0.0026	0.010	0.039	0.20	0.33	0.52
Obs.	-29	0.066	0.06	0.14	0.34						
Obs.	-30 (CTT)	0.066	0.13	0.31	0.73	0.07	0.21	0.65	0.56	0.71	0.89
Obs.	-31	0.066	0.20	0.48	1.16						
Obs.	-35	0.066	1.29	3.01	7.20	2.03	4.47	10.9	1.51	4.7	10.9
Fit(large)	-30	0.052	0.095	0.23	0.53	0.049	0.14	0.44	0.41	0.65	1.03

Table 4.3: Calculated INP concentrations for Upper Layer aerosol observations, using DeMott et al. (2015) and Tobo et al. (2013), calculated from the aerosol observation, N_A (mean), with 50% error range in Low and High. Correction factor, *cf* not applied.

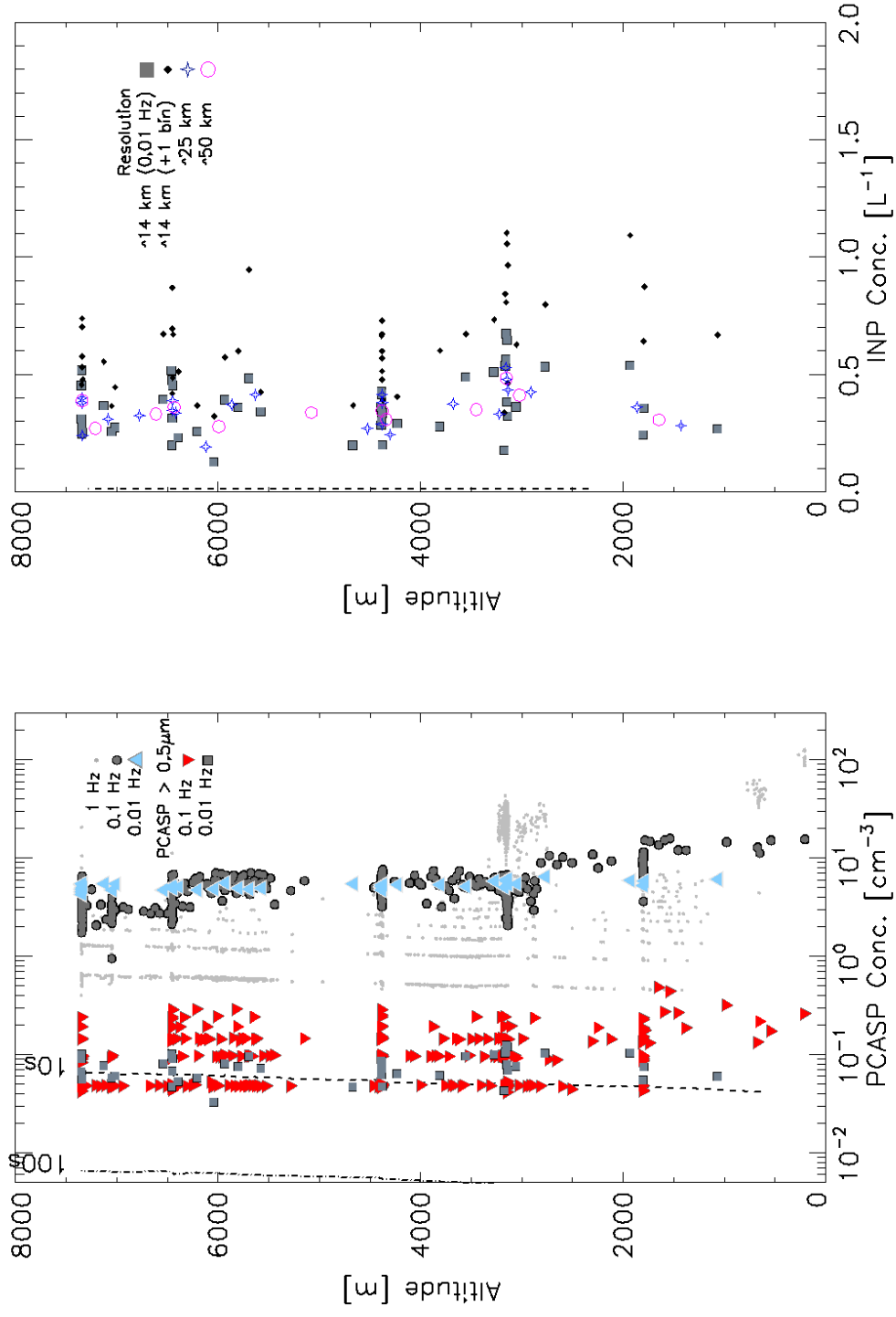

Figure 4.12: Vertical profiles of Left: N_A (PCASP) with LoD of large aerosol ≥ 0.5 μm at 0.1 Hz (dashed-line) and 0.01 Hz (dot-dashed-line). N_A PCASP data at 1 Hz: grey dots, at 0.1 Hz: large dark grey circles, at 0.01 Hz: blue-grey triangles. $N_A^{d \geq 0.5}$ at 0.1 Hz: red down-triangles, at 0.01 Hz, grey-squares, and Right: calculated INP concentrations (DeMott et al. (2015) at 243 K) and LoD (dashed line) and N_{INP} at 0.1 Hz: black diamonds, at 0.01 Hz: grey squares, 0.005 Hz: blue empty stars, 0.0025 Hz: open magenta circles.

4.8.1 Vertical Distribution of Aerosol and Derived INP

Figure 4.12 shows the vertical profile of measured particle number concentration from the PCASP instrument. Grey dots are data at the native 1 Hz resolution and larger dark-grey circles are the same data at 0.1 Hz (10 second averaging). High resolution 1 Hz data, show that close to the surface the $N_A \approx 100$ cm^{-3}, reducing with height to 1 cm$^{-3} \leq N_A \leq 10$ cm^{-3} between 1000 m and 2000 m. Above this altitude the 1 Hz data were close to, or below, the LoD of PCASP, as can be seen from the banding structure in the vertical, except for higher concentrations up to 30 cm^{-3} at 3000 m. Data averaged over 10 s, did not have the same banding structure and show that these data were above the limit of detection at the expense of reduced sampled variability. Further averaging to 100 s (0.01 Hz) show a similar picture with this data plotted in filled-grey triangles.

Aerosol number concentrations of large particles with d $\geq$ 0.5 μm are plotted at 0.1 Hz in red down triangles, showing that many observations were close to the mean LoD. Further averaging to 0.01 Hz (grey-squares) show that there were between 3 L^{-1} and 100 L^{-1} with mean values and variability constant with altitude. The averaging time corresponds to a length scale of the order 14 km, similar to a state-of-the art global NWP model (Table 4.4). The higher resolution data show that the maximum values can be larger, up to 400 L^{-1}, at a length scale of 1.4 km, which is more similar to a high-resolution limited area numerical model (Table 4.4). Longer averaging time results in reduced sensitivity to small scale variability.

Figure 4.12 (right panel) shows the calculated INP number concentration profile using the the large aerosol observations in Figure 4.12 (left panel) with 0.01 Hz data in grey squares. The range of INP concentrations was 0.1 L^{-1} to 0.7 L^{-1} for an activation temperature of 243 K. The limit of detection for INP is shown

Time period [s]	Length Scale [km]	Model Type	Model Resolution
10	1.4	Regional NWP	1.5 km (-)
-	-	Global NWP (current)	10 km (N1280)
100	14	Global NWP	14 km (N768)
-	-	Global NWP (future ensemble)	20 km (N640)
200	28	Global NWP Ensemble, Hi-Res Climate	28 km (N400)
400	56	Global Climate / Climate Ensembles	56 km (N216), 208 Km (N96)

Table 4.4: Sampling averaging scales (assuming TAS = 140 ms^{-1}) compared against Met Office Unified Model (Walters et al., 2017) NWP and Climate modelling scales and resolutions, N, where resolution is half the number of horizontal grid points.

for the DeMott et al. (2015) case at 243 K with a dashed black line, close to 0.02 L^{-1}. Longer temporal averages are calculated for the INP data with blue empty stars representing 200 s averaging and open magenta circles for 400 s of data-per-record, corresponding to spatial length scales of 28 km and 56 km. Each downgrade reduces the sampled variability as would be expected. The data from the 0.1 Hz aerosol record is plotted in black dots, but should be interpreted with caution due to the proximity of aerosol data to the PCASP LoD.

Figure 4.13 shows the histograms of calculated number concentrations of INP using DeMott et al. (2015) and Tobo et al. (2013) with the latter equation producing about 80 % of the INP number concentration that the DeMott et al. (2015) parametrisation does. The impact of applying the correction factor $c_f = 3$ (DeMott et al., 2015) is shown in a red outline. The variation that can be obtained using the two equations and accounting for instrumental uncertainty is large, close to two orders of magnitude.

It is difficult to relate the ice production to the budget of INPs. Large aerosols

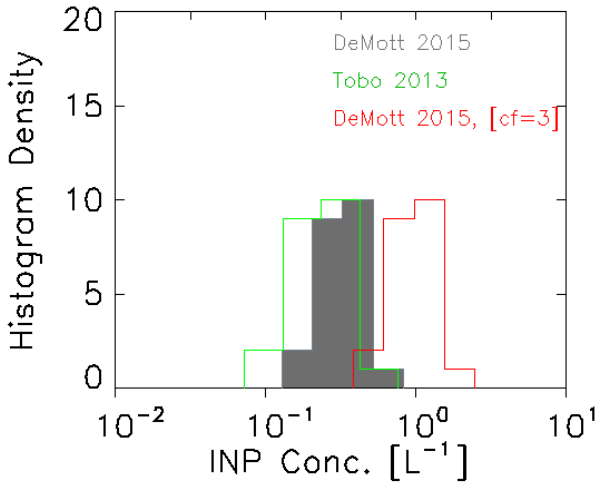

Figure 4.13: Histograms for INP concentration at 243K using Tobo et al. (2013) (green outline), DeMott et al. (2015) (filled grey), and DeMott et al. (2015) with correction factor of 3 applied (red outline).

are typically implicated in the creation of atmospheric ice particles, with much discussion around the reasons and nature of this. Efficacy of a particle as an INP is likely to be material-dependent, and have some relationship to the surface area of those materials, and the initial ice formation might take place on an active site on the material. Cloud processing may be important.

A large amount of sampling time is required to make robust estimates of the INP number concentrations, either using the method here of sampling the aerosol PSD, and then applying a parametrisation, or by direct observation with an INC. When measurements are to be made with an instrumented aircraft the long sampling time requirement is restrictive. As a minimum, in order to have meaningful INP concentrations, data must be collected over much more than ten seconds; here 100 seconds or more are used. If the data were required to provide a measure of sub-grid-scale variability in NWP then many more data points are required.

Table 4.4 gives a summary of the time period and consequent length scale to which the observations are applicable. More than 30 minutes and up to an hour of sampling is required to generate a mean and variability for a length scale of the order of the current generation of global NWP models ($\approx$ 10 km).

The number of observations of particles that it is possible to make in these low concentration regimes is a great limitation, as is not knowing the composition and source region. The life-cycle of aerosol particles in the atmosphere, including the processing of them by weather systems, is a field of study in its own right. The identification of the INP budget and the PSD of aerosols when in cloud in a mixed-phase layer cloud is a major challenge, one that requires a wide range of instrumentation to sample the full size distribution of aerosols with suitable counting statistics, as well as coincident measurement of cloud properties and ideally aerosol mineralogical composition.

4.9 Attempting to Close the INP/Ice Production Budget

INP reservoir depletion time, Φ_{INP}, can be calculated by dividing the number concentration of INP by the ice production rate and assuming steady state. For the observations presented in Figure 4.12 there were 0.1 $L^{-1} \leq$ INP $<$ 1.0 L^{-1}. Taking the ice production rate, $P_0 = 0.65 \pm 0.04$ $m^{-3}s^{-1}$ from Figure 4.7 gives an INP reservoir depletion time of 145 s $\leq \Phi_{INP} <$ 1639 s [$<$ 0.5 hr] for the INP concentrations considered.

Cloud Glaciation Time, τ_{gl}, is a related quantity and can be calculated by making some assumptions of simple ice and liquid cloud microphysics and either zero,

positive or negative vertical velocity (Korolev and Isaac, 2003). The ice production rate concerns only the generation of an ice particle and, if INP limited, can be used to estimate the time taken for all INP to activate. Calculations of cloud glaciation time give the period of time taken to convert all the liquid in a given volume into ice particles, given an ice number concentration.

Taking the same, typical, ice concentrations as above, and the observed cloud top upper-quartile $\mathrm{LWC}_{75^{th}} = 0.05$, and for the case of zero vertical velocity (Korolev and Isaac (2003)) the calculated glaciation times were found to be 2.45 hr [1 L^{-1}] $\leq \tau_{gl} <$ 11.3 hr [0.1 L^{-1}]. Without consideration of the dynamics of the cloud, it is clear that the lifetime of the liquid cloud, is controlled by the transfer of condensed water from the liquid phase to the ice phase, rather than by the ice nucleation rate.

In real clouds, especially this turbulence-driven altocumulus cloud, the dynamics are important. Consideration of positive vertical velocity was shown to both extend and decrease τ_{gl} depending on the magnitude of the updraught (Korolev and Isaac, 2003). A simple model of an oscillating cloud parcel shows that in certain cases a quasi-equilibrium state can be attained where the LWC and IWC vary, out of phase with one another, for longer than 25000 s ($\mathrm{N}_i = 10$ L^{-1}), or 10000 s ($\mathrm{N}_i = 100$ L^{-1}). Much of the real-world physics is missing from this model, including ventilation, habit dependent growth rate etc.

Ice nucleation could occur immediately once a threshold temperature was reached. The longevity of the cloud would then be determined by the dynamics and the rate of uptake of moisture by the ice crystals. This might suggest that there are many small ice particles that reside with the liquid cloud, which would presumably remain spherical, awaiting mass-transfer to become efficient enough to allow them to grow and precipitate.

4.10 Conclusions

The technique of HHC87 has been applied to altocumulus clouds for the first time to calculate the primary ice production rate. An altocumulus cloud with CTT = -30° C was sampled on 2^{nd} February 2012 and the observations were used to calculate the ice production rate, using HHC87, of $P_0 = 0.65 \pm 0.04$ $m^{-3}s^{-1}$.

A contrasting case, in cumulus cloud sampled on 23^{rd} November 2013, found ice production rates several orders of magnitude greater, with $P_0 = 11.9 \pm 2.4$ $m^{-3}s^{-1}$ at 268 K and $P_0 = 31.4 \pm 4.0$ $m^{-3}s^{-1}$ at 265 K. The cumulus observations were assumed to be from SIP and compare well with literature reported values (Harris-Hobbs and Cooper, 1987; Taylor et al., 2016).

Observations of aerosol PSD were made using data from the PCASP and CDP. In order to make this possible it was necessary to determine cloud-free conditions so as to avoid contamination of the observations by liquid and ice particles. A clear-sky flag was produced using the variability on the Nevzorov TWC probe and recognising that the standard deviation of power drawn by the sensor is bi-modal, with one mode generated in-cloud and the other in clear-skies.

The PCASP and CDP aerosol measurements were used to show that at least two distinct modes existed: these were likely to be formed from two different materials. It might be that there were particles smaller than 0.5 μm that are active as INP but these cannot be disentangled from other aerosols. The fitted log-normal distribution is one way to do this, but the width of the distribution was poorly constrained at the larger end of PCASP, and from CDP.

INP concentrations were found to be 0.1 L^{-1} to 0.7 L^{-1} at 243 K using DeMott et al. (2015). Number concentrations as great as 400 L^{-1} may be observed at

high temporal resolution, but with low confidence in the measurement validity. Comparable values calculated with Tobo et al. (2013) were some 80 % of those calculated with DeMott et al. (2015). The uncertainty due to corrections factors associated with the INC technique (of a factor of three or more) is larger than the variation due to an assumed aerosol type, demonstrated here.

The INP reservoir depletion timescale is much smaller than the calculated cloud glaciation time, assuming no dynamical effects. However, the dynamics is important and perhaps more important than the details of the aerosol and INP budget. There is no information here on how the INP act to form ice crystals, but the ice production rate is determined from observations.

Chapter 5

Further Small Ice Observations

5.1 Introduction

Data from the SID2 and CIP15 probes in altocumulus on 2^{nd} February 2012 were further interrogated to attempt to reduce the minimum size of ice particle that can be positively identified as ice and distinguished from liquid. Trying to assess the concentrations of small ice using the SID2 probe is complicated by instrumental artefacts and coincidence events, that are expected to occur at a larger frequency than the small ice events in the altocumulus clouds in this study. Coincidence events in SID2 were identified, explored and interpreted.

Calculation of correlations between individual size channels in CIP15 and with CIP100 were made in order to separate ice and liquid modes. These improved, and better characterised, observations were then used to look at the concentrations of small ice with reference to the vertical coordinate. Finally CIP15 ice particle concentrations data were segregated by size to test the relationship between size resolved ice particle number concentration and the vertical velocity spectra.

5.2 The Performance of SID2 in Mixed-Phase Clouds

5.2.1 Asphericity: Idealised Ice Scattering Patterns

For SID2 scattering patterns, the maximum observable asphericity reduces with increasing particle diameter, a result that was obtained by calculating the asphericity for a range of synthetic ice "columns". The theoretical maximum value of asphericity that can be obtained, will be obtained, for a column which, in the simplest case, will have scattering recorded in only two opposite detectors as plotted in Figure 5.1, top-left. This scattering pattern results in a asphericity of 63.9, up to a particle derived spherical equivalent diameter of 26.6 μm, obtained when digital detector signal is at its maximum value of 2048 counts. The value is obtained for any values of scattering in only two detectors, and in fact they do not have to be opposite one another. In reality, the scattering pattern would be rejected since there are too many black detectors.

Further increase in diameter in SID2 for a "perfect column" can only be achieved by including scattering in additional detectors. This is done for 2, 3, then 4 adjacent detectors, and so on to the maximum, and is shown to consequently reduce the derived asphericity values. Three further examples are shown in Figure 5.1: top-right shows two pairs of two fully illuminated detectors, with $d_{2|2} = 37.6$ μm and $A_{2|2} = 47.1$; bottom-left shows 2 pairs of four detectors, where with $d_{2|4} = 53.2$ μm and $A_{2|4} = 30.4$ and bottom-right shows two pairs of 12 detectors with $d_{2|12} = 92.1$ μm and $A_{2|12} = 7.85$. These calculated diameters are water-sphere equivalent and so because ice is expected to be undersized, the impact on maximum observable asphericity will be larger in reality. For this reason, it is deemed unsatisfactory to remap the asphericity scale between 0 and 63.9 on to the current 0 to 100 scale. A maximum value of A = 63.9 would also never be attained

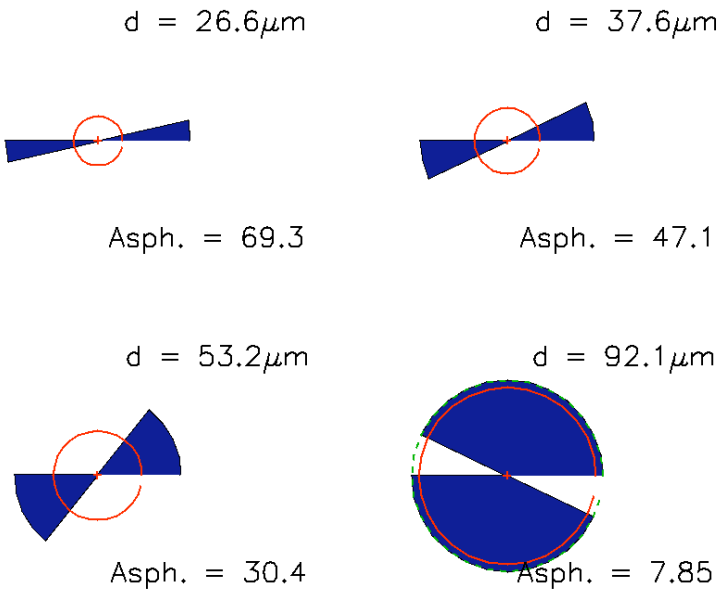

Figure 5.1: SID2 scattering patterns of idealised columns where groups of opposite detectors are illuminated with maximum illumination of 2048, for single opposite detectors (top-left), 2-detectors (top-right) 4-detectors (bottom-left) and 12-detectors (bottom-right). Reported diameter is liquid-sphere equivalent.

in reality, and any consistency between new and old observations would be lost. In summary, the asphericity parameter is not able to offer a size independent method of partitioning scattering patterns into ice- and liquid-phase.

5.2.2 Synthetic Liquid Scattering Patterns

Previous SID2 measurements in warm clouds, where the drops are known to be spherical, show a large tail to the asphericity distribution with values up to and greater than 10 (Cotton et al., 2010). Instrumental artefacts, off-centre or off-axis sampling and detector noise as well as the coincidence of two or more particles in the sensing volume can introduce artificial broadening of the asphericity distribution.

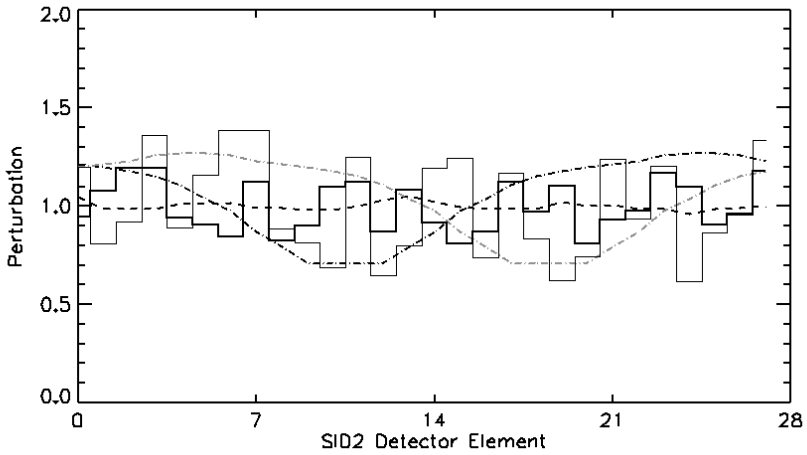

Figure 5.2: Perturbations applied to a perfectly spherical SID2 scattering pattern, used to replicate real world factors that degrade the collected scattering patterns. Detector Response Correction: dashed line, noise: 5 μm: thin black line, 10 μm: thick black line, 30 % offset filter example: black dot-dashed line, rotated 30 % offset filter grey dot-dashed line.

Synthetic scattering patterns of five perfect spheres have been constructed that consist of a uniform detector response in each of the 28 elements. Detector magnitudes of 4, 5, 6, 10 and 25 result in nominal particle diameters of 4.40 μm, 4.81 μm, 5.38 μm, 6.95 μm and 11.0 μm respectively.

Figure 5.2 introduces a collection of perturbations that are functions of detector element. These perturbation functions attempt to replicate some of the real-world sources of asphericity to model the impact they have on SID2 observations. The original work on SID2 suggested that variation of up to 30 % is to be expected due to positioning of the particle within the sample volume (*pers. comm.* J. Ulanowski). The dot-dashed black line shows an example of a function to account for this off-axis sampling, and variation of particle position, within the Field of View (FoV). An additional example is shown, rotated about the detector by a random amount, in a grey dot-dashed line. There will be preferential alignment of

		"Perturbation"		New Properties	
Diameter [μm]	$\overline{r_{det.}}$	Noise	Offset 30%	Diameter [μm]	Asphericity
4.40 to 4.91	5	Y	n	5.06	3.32
6.60 to 6.95	10	Y	n	7.05	1.65
10.7 to 11.0	25	Y	n	11.0	0.67
4.40 to 4.91	5	n	Y	4.82	2.74
4.40 to 4.91	5	Y	Y	4.97	4.86
6.60 to 6.95	10	Y	Y	6.92	3.62
10.7 to 11.0	25	Y	Y	10.8	3.01

Table 5.1: Synthetic SID2 scattering pattern properties using perturbations from Figure 5.2, for three spherical particles with resolved diameter range shown in the first column for the detector magnitude, $\overline{r_{det.}}$, shown in the second column. Modified parameters refer to the upper end of the size range.

this function along the sample volume axis but this is not replicated here since this simple model is not intended to be a statistically robust determination of the sources of uncertainty in SID2, but to demonstrate the sources of the uncertainty.

Random noise was generated, normally distributed, around a magnitude of 3 counts, on a scale of 0 to 2048 so as to mimic real detector noise. Application of this noise to a spherical 5 μm particle is shown in the thin solid line, and to a 10 μm particle in thick solid line. From Section 2.6.7 comes the Detector Response Correction (DRC) which varied by a few percent across the detector, shown in a dashed-line, and is seen to be the lowest of the perturbations, and the only one that can be reliably and deterministically corrected for. Each of the perturbations impacts the representation of sphericity and to a lesser extent diameter, with the interaction between effects causing a spread in the distribution of asphericity.

Table 5.1 shows a summary of the impact of the perturbations in Figure 5.2 for three of the synthetic particles, with uniform detector responses of 5, 10 and 25. Due to digitisation within the detection system the detector responses cover

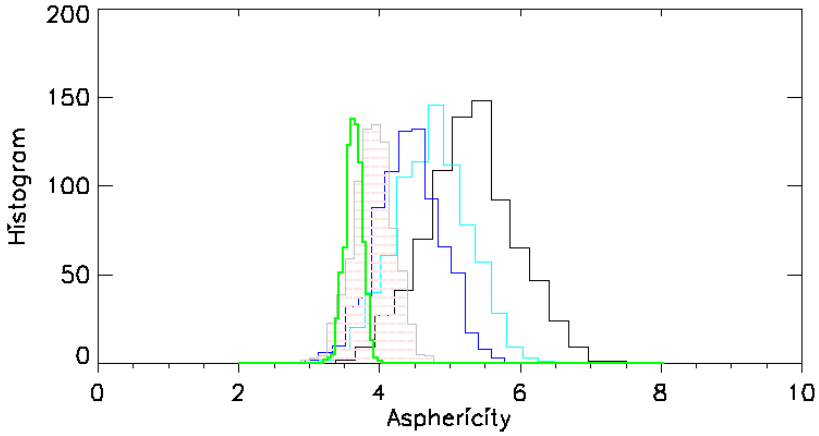

Figure 5.3: Synthetic SID2 asphericity values presented as histograms for individual initial particles: d = 4.40 μm (black line), 4.91 μm (cyan line), 5.38 μm (blue line), 6.95 μm (grey outline, red shading) and 11.0 μm (green outline).

particles within a size range. For this case the ranges are 4.40 μm to 4.91 μm, 6.60 μm to 6.95 μm and 10.7 μm to 11.0 μm respectively.

Noise and offset perturbations were applied in isolation and in concert for a single realisation, with the consequent impact on asphericity shown in the final column. Diameter is affected by less than 1 %. In general noise has a reduced effect on asphericity for larger particles as can be seen in the top section. The impact of the offset perturbation alone is of similar magnitude to noise for the smallest particles. Combined, the two perturbations make for increased asphericity over and above the individual response, but in a non-linear manner.

Histograms of asphericity were generated for each of 5 original synthetic particles by rotating the offset perturbation function and the noise function around the detector ring, resulting in 784 individual realisations . The resulting distribution in Figure 5.3 shows that the magnitude and spread of asphericity decreases with

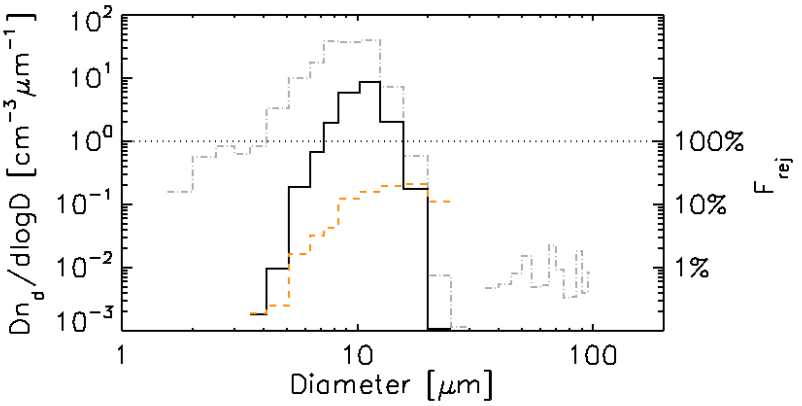

Figure 5.4: SID Coincidence algorithm PSD (solid-black line) for cloud sampled in altitude range -100 $\leq$ $Dz_{(CTH)}$ < -75, with resulting cloud particle PSD (grey dot-dashed line). Coincidence percentage rejections, F_{rej} in orange dashed line on right-hand axis, with black dotted line highlighting 100 %.

increasing size of particle as expected: noise has a reduced impact. Even though these distributions are not statistically robust it is clear to see, even from this simple model, how the large spread of asphericity values can emerge from noise, and offsets within the SID2 detection system. Making a statistically robust model would require detailed laboratory work to better characterise the sample volume and and the impact of off-axis sampling, something which is beyond the scope of this study.

5.2.3 Results of Coincidence Algorithm

Once SID2 particles from the altocumulus clouds flight on 2^{nd} February 2012 were identified as coincidence using the tests in Section 2.6.8 they were removed from the cloud data set, but not before an exploration of their properties and where they occur was undertaken. Diameter data from scattering patterns identified as "coincidence events" were plotted as a PSD in Figure 5.4 from -100 m $\leq$ $Dz_{(CTH)}$ <-

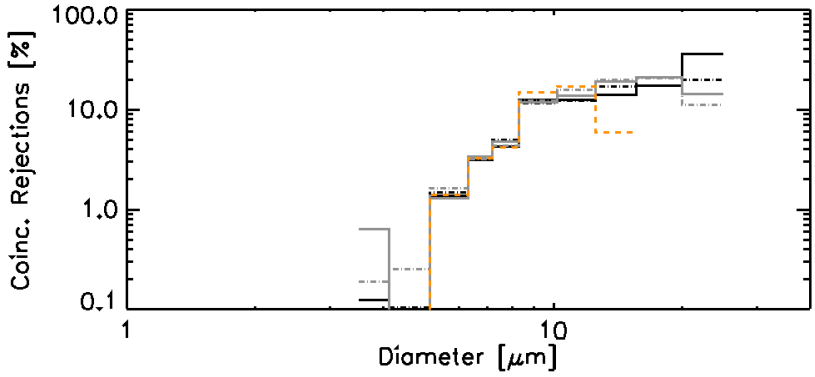

Figure 5.5: Vertically resolved SID2 Coincidence fractions as a function of particle size for various levels. -25 m $\leq$ $Dz_{(CTH)}$ $<$ 0 m: solid black line, -50 m $\leq$ $Dz_{(CTH)}$ $<$ -25 m: black dot-dashed line, -75 m $\leq$ $Dz_{(CTH)}$ $<$ -50 m: grey solid line, grey dashed line: 100 m $\leq$ $Dz_{(CTH)}$ $<$ -75 m and -225 m $\leq$ $Dz_{(CTH)}$ $<$ -200 m: orange dashed line.

75 m and show a modal diameter that is just larger than 10 μm. A PSD of the remaining particles, following removal of these coincidence events, is also shown. the rejected fraction, F_{rej}, was computed as the percentage of actual particles in each size bin. For this level in cloud, the coincident fraction increases from less than 0.01 at a size of 3.5 μm, to is a maximum of just over 0.1 close to 20 μm.

Coincidence frequency as a function of diameter is shown for other levels in cloud in Figure 5.5. For larger particles, d $\geq$ 20 μm, the computed coincidence-fraction increases from 10 % at $Dz_{(CTH)}$ = -100 m, to 40 % at cloud top. Results are similar at all levels for particles with d $\leq$ 12 μm down to a layer at -225 m $\leq$ $Dz_{(CTH)}$ $<$ -200 m. Here there is an slight increase of coincidence-frequency at particle size 8 μm $\leq$ d $<$ 12 μm and a reduction in the bin size above this. There are very few, if any, particles larger than 15 μm at this level.

5.2.4 Coincidence Discussion

Curves show the rejected fractions as a function of particle size were strongly centred on the mode of the size distribution, as expected as frequency of coincidence should be biased to the mode. Increased coincidence frequency at large particle sizes occurs closer to cloud top, where more particles are expected to be larger, again following the statistics of the situation. The "range" criterion will also preferentially select larger particles since the particles have to be large enough so that a 10 % change can be registered on the digital output scale, something that is increasingly more likely for larger particles.

Probability of coincidence was calculated by assuming the process obeys Poisson statistics, using equations given by Johnson et al. (2014). Cloud droplet number concentration observations were taken from the CDP, the extended sample volume from Cotton et al. (2010), and SID2 beam depth from Johnson et al. (2014). The CDP fitted to the BAe146 has the "pin-hole modification" (Lance et al., 2010) resulting in coincidence frequency of much less than 0.1 %. The expected SID2 coincidence frequency for 20 $cm^{-3} \leq N_d < 35$ cm^{-3} is between 2 % and 5 %, with a 30 % error for an uncertainty of 20 % on the sample volume estimate. Results of the algorithm suggest that the observed frequency was twice as large. Particle scattering patterns that Johnson et al. (2014) may have identified using the strong FFT mode 1 may be included in the number here.

The coincidence identification scheme results in an overall coincidence rejection-frequency of almost 10 % of the SID2 scattering patterns. A relatively small error on the sample volume could explain the discrepancy, but, the false positive rate is currently unknown and may contribute to the enhanced frequency.

Concentrations of coincidence events would be 1.5 cm^{-3} assuming the theoretical

calculations to be correct, and were double this, 3.0 cm^{-3}, for the observed results. Both are orders of magnitude larger than the expected ice particle number concentration in the altocumulus clouds.

More refinement of the technique could be performed, and more datasets interrogated in order to get a more well-tuned set of tests to identify coincidence. There are myriad algorithms and tunings that could give similar answers. Without manually assessing the results of such a scheme it would be very difficult to determine if the output was correct or if it simply returned a realistic looking answer for the wrong reasons.

A better strategy might be to apply machine learning algorithms to try to find correlations between the particle scattering properties and the types of particles, be they liquid, ice, coincidence or other class of event that require rejection. For data from altocumulus cloud in the mixed-phase regions there are expected to be many fewer ice particles than liquid and there should be an intermediate number concentration of coincidence events, and "bad" scattering patterns, which should be identified for rejection. There are numerous specific types of machine learning, including simple regression algorithms. Identification of phase in SID2 scattering patterns may be suitable for a clustering algorithm such as hierarchical agglomerative clustering, a technique that has been successfully used in similar circumstances to identify categories of aerosol particles in an optical instrument (Robinson et al., 2013). Hierarchical agglomerative clustering is renowned for being able to handle clusters that are very different in terms of the number of members that each may contain.

5.3 Diameter and Asphericity from SID2, 2^{nd} February 2012

Vertically resolved particle diameter and asphericity distributions are shown for the SID2 data in Figure 5.6. The size distribution plot in Figure 5.6 (upper panel) shows that close to cloud-top, the SID2 data from -50 m $\leq Dz_{(CTH)} <$ -25 m were similar to the CDP data which were interpolated onto SID2 bins. For context, the composite liquid and ice PSD for the mixed phase cloud region can be found in Figure 4.2 where it was shown that the liquid and ice have different properties of size and number. The mode is just larger than 10 μm with a maximum dimension of this mode, close to 20 μm. Larger particles with d $\geq$ 30 μm are presumed to be the response of SID2 to ice particles which, due to unknown scattering phase function, have an uncertain diameter (Chen et al., 2006). Attempts have been made previously to correct for this deviation from pure forward scattering from spherical drops by applying a scaling factor of 1.7 (Cotton et al., 2010). The actual scaling factor will be habit-dependent and no attempt will be made here to apply a correction since many atmospheric ice particles are irregular (Korolev and Field, 2008) and the main focus is on phase-resolved particle number concentration.

The asphericity distribution in Figure 5.6 (lower panel) shows that the vast majority of these SID2 particles have very low asphericity ($\leq$ 2). The phase of all particles is not known but there are asphericity values as large as 25 with very low frequency of occurrence.

At the higher altitude of -25 m $\leq Dz_{(CTH)} <$ 0 m there are fewer particles observed at d = 10 μm. The mode is close to 8 μm and there are more particles at smaller sizes, probably due to entrainment of dry air from aloft causing particle evaporation and a shift in the PSD towards smaller diameters. At this altitude there is also

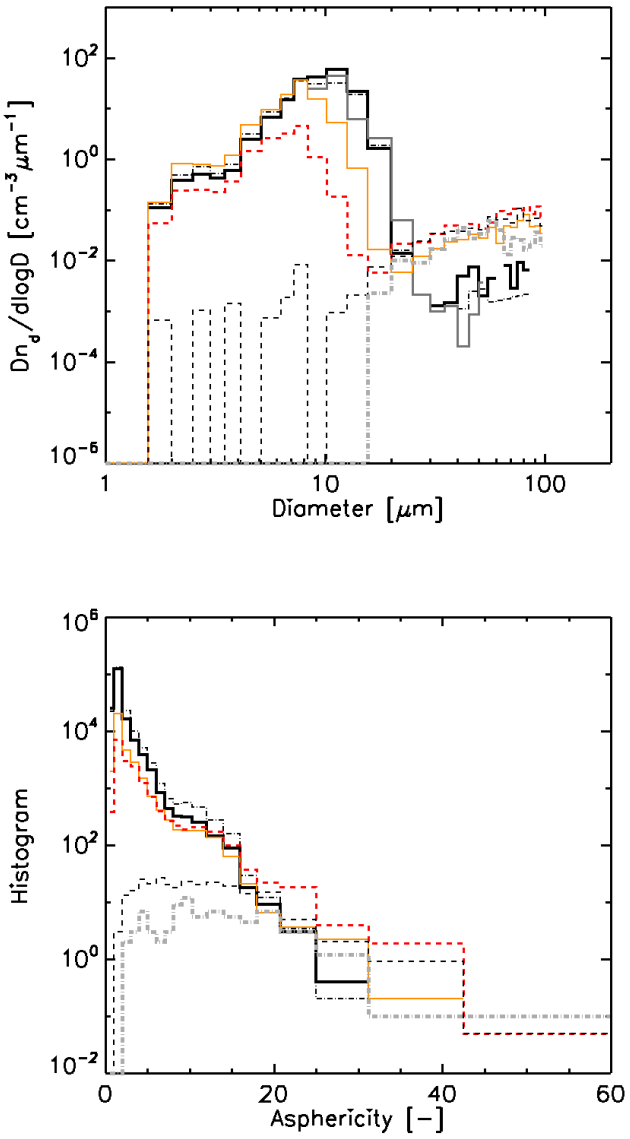

Figure 5.6: Vertically resolved (a) PSDs and (b) Asphericity distribution, relative to derived CTH in altocumulus on 2^{nd} February 2012 from SID2 probe, with CDP PSD for comparison near cloud top. -50 m $\leq$ $Dz_{(CTH)}$ < -25 m: solid black line, (and CDP PSD interpolated to SID2 bins in grey), 25 m $\leq$ $Dz_{(CTH)}$ < 0 m: dot-dashed black line, -200 m $\leq$ $Dz_{(CTH)}$ < -175 m: orange solid line, -300 m $\leq$ $Dz_{(CTH)}$ < -200 m: red dashed line, -400 m $\leq$ $Dz_{(CTH)}$ < -300 m: dashed black line, -600 m $\leq$ $Dz_{(CTH)}$ < -400 m: dot-dashed grey line.

evidence of ice in low concentrations from the response of SID2 at sizes larger than 30 μm. Asphericity is increased markedly for values larger than 8, which must be predominantly from the increased numbers of smaller and evaporating particles. These observations all agree with those presented in previous chapters.

Descending through cloud sees a reduction in the size of the mode, and in the number of particles at sizes larger than the mode. Close to cloud base at -200 m $\leq$ $Dz_{(CTH)}$ < -175 m the particles have 7 μm $\leq$ d^{mode} < 8 μm. The occurrence of particles with d $\geq$ 30 μm is much increased compared to the layers above. There is a corresponding increase in the frequency of asphericity $\geq$ 20, with a broader shoulder to the asphericity distribution at A $\geq$ 30, indicative of ice particles.

Due to reduced numbers of particles in the lower part of the cloud system the depth of the layers is increased (-300 m $\leq$ $Dz_{(CTH)}$ < -200 m). The mode size is still close to 8 μm, but numbers are vastly reduced at sizes larger than this either because cloud particles that have not had sufficient time to grow to the larger sizes, or as evaporating cloud particles embedded within downdraughts. Ice particles with d $\geq$ 20 μm are found in greater numbers when compared with concentrations in the layer above and the corresponding increase in the asphericity frequency of occurrence for A $\geq$ 15 supports this observation. Below the liquid layer at -400 m $\leq$ $Dz_{(CTH)}$ < -300 m the response to ice at sizes larger than 20 μm is similar to the layer above, whilst there is almost no response to particles smaller than this, except in very low concentrations, and with unknown phase. The asphericity distribution is nearly as broad as for the layer above, with the source potentially being both ice and small liquid particles. Deeper in the virga layer (-600 m $\leq$ $Dz_{(CTH)}$ < -400 m) there is no response to particles smaller than 15 μm, and the resulting asphericity distribution is flatter, and extends to values

of 60, close to the theoretical asphericity maximum of 63.9.

5.3.1 Diameter vs. Asphericity Joint-Histograms

The observations presented may well be contaminated with the artefacts of coincidence. Joint-histograms of diameter and asphericity were constructed to investigate this. The method follows the one presented by Cotton et al. (2010) which showed such histograms for various cloud and aerosol types. Here, the data from vertically resolved levels within the mixed-phase altocumulus cloud system are presented in Figures 5.7 and 5.8 along with coincidence events and corrected data. Data from all other cloud levels, in 25 m increments, are plotted and included in Appendix D.

The diameter vs. asphericity raw-data joint-histogram is shown in Figure 5.7a is for the cloud-top level -25 m $\leq \mathrm{Dz}_{(CTH)} < 0$ m. Positively identified coincidence events were used to generate the coincidence-event diameter vs. asphericity joint-histogram in Figure 5.7b. It is possible to remove these coincidences from the raw-data. Figure 5.7c shows the coincidence-corrected joint-histogram. In each panel there is a diagonal-hatched region that corresponds to combinations of diameter and asphericity that are not physically possible in the SID2, as derived above.

In the top 25 m of cloud there were no observations of particles with d ≥ 20 μm, and no highly aspherical particles (A ≥ 20). This data represents the scattering patterns obtained from the liquid cloud population in the very top 25 m of the cloud system. The most common particles were present in the diameter range 8 μm $\leq$ d < 10 μm, with $0.9 \leq$ A < 2. At sizes close to the mode of the size distribution the asphericity distribution took values of $0.4 \leq$ A < 15. Digitisation by the probe detection systems resulted in reported asphericity values for particles

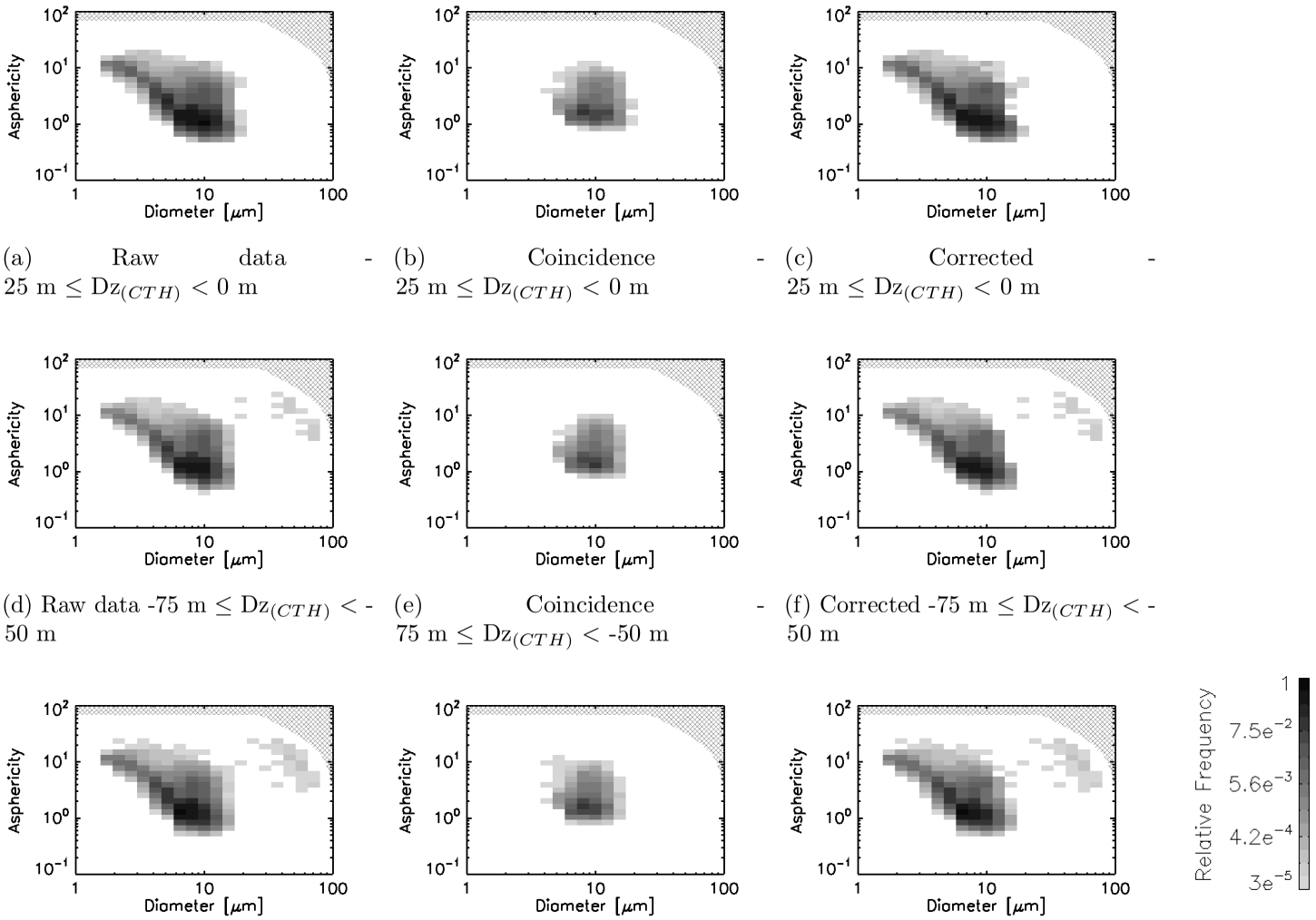

(a) Raw data - 25 m $\leq$ Dz$_{(CTH)}$ < 0 m

(b) Coincidence - 25 m $\leq$ Dz$_{(CTH)}$ < 0 m

(c) Corrected - 25 m $\leq$ Dz$_{(CTH)}$ < 0 m

(d) Raw data -75 m $\leq$ Dz$_{(CTH)}$ < -50 m

(e) Coincidence - 75 m $\leq$ Dz$_{(CTH)}$ < -50 m

(f) Corrected -75 m $\leq$ Dz$_{(CTH)}$ < -50 m

(g) Raw data -125 m $\leq$ Dz$_{(CTH)}$ < -100 m

(h) Coincidence - 125 m $\leq$ Dz$_{(CTH)}$ < -100 m

(i) Corrected -125 m $\leq$ Dz$_{(CTH)}$ < -100 m

Figure 5.7: Vertically resolved diameter vs. asphericity joint-histograms, for three 25 m deep vertical levels between -125 m $\leq$ Dz$_{(CTH)}$ < 0 m (see sub-captions). Left: raw data, centre: coincidence, Right: corrected data. Diagonal-hatching indicates combinations that are physically impossible in the probe. Logarithmic colour scale shown bottom right.

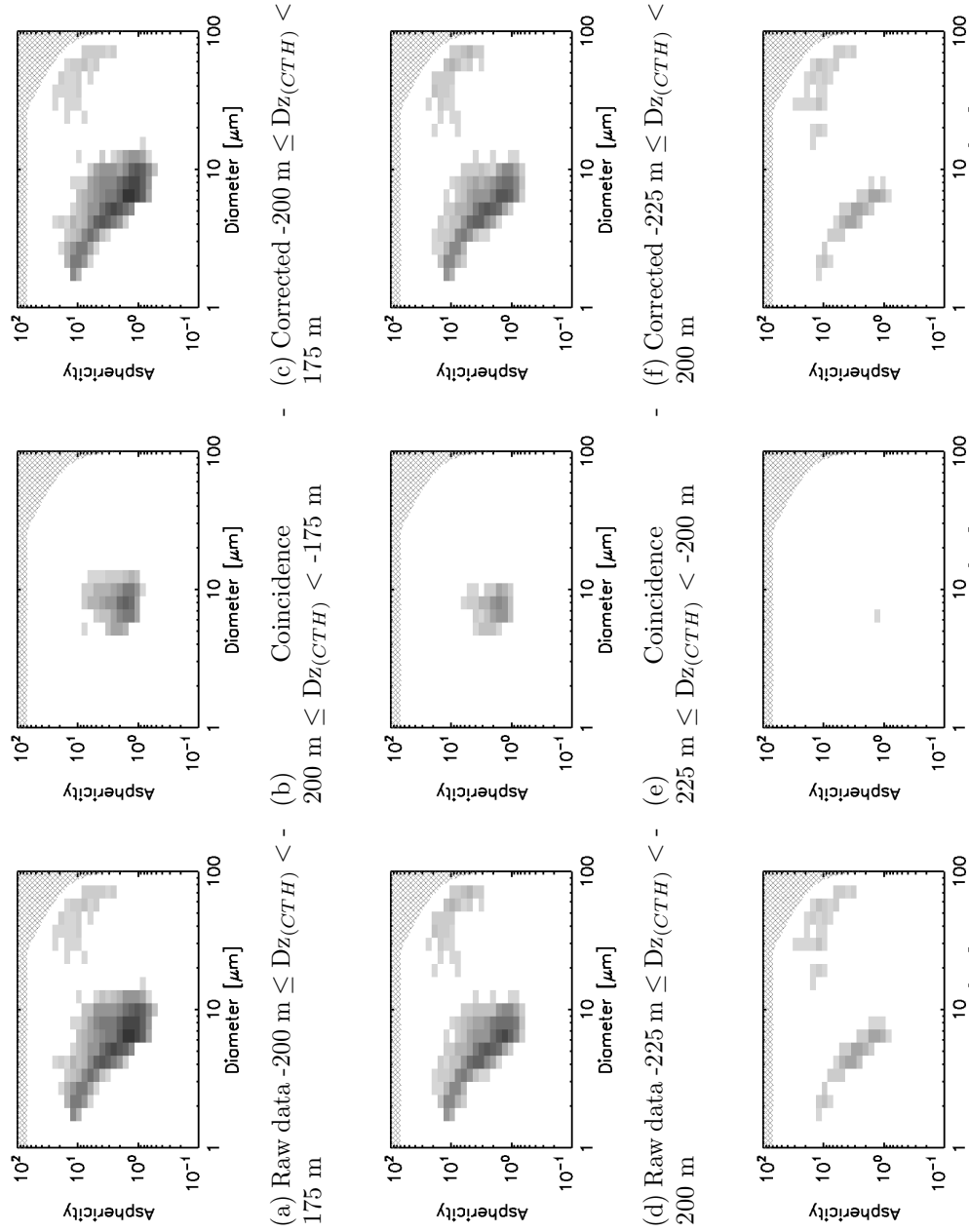

(a) Raw data -200 m $\leq$ $\mathrm{Dz}_{(CTH)}$ < -175 m

(b) Coincidence - 200 m $\leq$ $\mathrm{Dz}_{(CTH)}$ < -175 m

(c) Corrected -200 m $\leq$ $\mathrm{Dz}_{(CTH)}$ < -175 m

(d) Raw data -225 m $\leq$ $\mathrm{Dz}_{(CTH)}$ < -200 m

(e) Coincidence - 225 m $\leq$ $\mathrm{Dz}_{(CTH)}$ < -200 m

(f) Corrected -225 m $\leq$ $\mathrm{Dz}_{(CTH)}$ < -200 m

(g) Raw data -275 m $\leq$ $\mathrm{Dz}_{(CTH)}$ < -250 m

(h) Coincidence - 275 m $\leq$ $\mathrm{Dz}_{(CTH)}$ < -250 m

(i) Corrected -275 m $\leq$ $\mathrm{Dz}_{(CTH)}$ < -250 m

Figure 5.8: Vertically resolved diameter vs. asphericity joint-histograms, for three 25 m deep vertical levels between -275 m $\leq$ $\mathrm{Dz}_{(CTH)}$ < -175 m (see sub-captions), as Figure 5.7. Logarithmic colour scale shown bottom right.

with d $\leq$ 3 μm in the range 5 $\leq$ A $<$ 20. Occasionally the probe would sample particles with diameter larger than 20 μm.

The distribution of asphericity was artificially broadened at all sizes by the physical features of the probe itself. Coincidence is another mechanism for this broadening. The coincidence metric determined above results in the distribution shown in Figure 5.7b for coincidence events in the altitude range -25 m $\leq$ $Dz_{(CTH)}$ $<$ 0 m and these are closely related to the most frequently occurring drops, as expected. There are no instances of coincidence for particle diameter $\leq$ 4 μm. There is a lower chance of this occurring based on the low concentrations at those sizes and the statistical nature of the mechanism. But, there is a limit to the smallest size of particle that could be identified that is implied in the test that stipulates a difference between the upper and lower super-segment variability be larger than 10 % (Section 2.6.8). This range will not be achievable for the smallest of particles.

Larger and more aspherical particles were present in the data from -50 m $\leq$ $Dz_{(CTH)}$ $<$ -25 m, (Appendix D), and the frequency of these particles was further increased at the -75 m $\leq$ $Dz_{(CTH)}$ $<$ -50 m level (Figures 5.7d, 5.7e 5.7f). The particles larger than d = 20 μm with asphericity values 4 $\leq$ A $<$ 20 were very rare in comparison to the smaller cloud particles. These particles are assumed to be the smallest discernible ice particles in this cloud.

Two regimes were apparent in the distribution throughout the depth of the cloud, down to cloud base at -275 m $\leq$ $Dz_{(CTH)}$ $<$ -250 m, (Figures 5.7f to 5.8i): a liquid cloud particle mode with sizes smaller than 10 μm to 20 μm depending on altitude and a larger ice particle population with d $\geq$ 15 μm to d $\geq$ 25 μm. There is no clear distinction between these two populations based on the asphericity alone. Coincidence frequency is lower in magnitude towards cloud base and the diameter and asphericity range are smaller (Figures 5.7e, 5.8h)

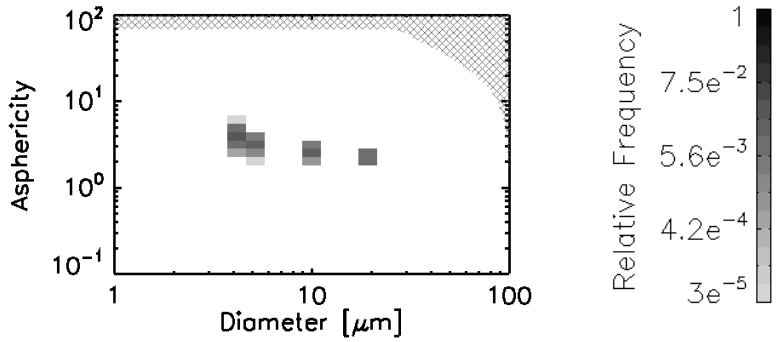

Figure 5.9: Synthetic SID2 Diameter vs. Asphericity joint-histogram using data from Figure 5.3, as Figure 5.7.

Using the previously modelled synthetic scattering patterns it is possible to create the synthetic diameter vs. asphericity plot shown in Figure 5.9. These five particles are not intended to be a statistically robust distribution the figure is merely designed to illustrate the impact of artificial asphericity-broadening in SID2 and similar scattering probes. The particles smaller than 5 μm show asphericity values of $2 \leq A \leq 4$.

5.4 SID2 Conclusions

There is currently no objective way of determining the phase of a particle from the information contained in a SID2 scattering pattern. SID2 can distinguish ice particles as small as 30 μm on the scale of 25 m in the vertical, by using both diameter and asphericity observations in combination with CDP particle size observations, and making an assessment of coincidence events.

A coincidence finding algorithm for SID2 scattering patterns was developed. Identified coincidence events occur from 4 μm $\leq d < 20$ μm, with most found close to the modal diameter at d ≈ 8 μm, with a range of asphericities of $0.8 \leq A < 12$.

These events are more common at the top of the cloud, reducing in frequency with depth in cloud. It is not clear how many of the real coincidence events have been identified, and how many are false positives. CDP and SID2 size distributions agreed well, implying that potential missed coincidence events did not impact the resulting PSD. Liquid cloud observations from CDP were critical in determining the maximum diameter, on a statistical basis, but not on a particle-by-particle basis.

Calculations were performed that show that some combinations of diameter and asphericity are not possible within the SID2. In all cases $A_{SID2} \leq 63.9$. For spherical-equivalent d $\geq$ 26 μm the maximum possible asphericity value begins to fall rapidly.

SID2 suffers from artificial asphericity-distribution broadening. Large asphericity values, typically associated with ice particles, were also found for small liquid particles. Asphericity was greater than 1.0 for *all* particles smaller than 4 μm and the minimum observed asphericity increased at smaller particle diameters. In part, this is due to the nature of the detection system and digitisation levels of the electronics and the gain of the amplifiers (hence the size range of the instrument). Positioning of individual particles within the sample volume is also a contributor.

A simple model of the instrumental asphericity broadening has been developed that shows how the observed large asphericity values could emerge by consideration of physically reasonable perturbations to a group of synthetic scattering patterns. Similar to the problem with the coincidence algorithm itself though, is the identification of the parameters that generate the required results. There are many conceivable solutions though that could result in the same output. For both tasks the use of machine learning algorithms may be required to probe for correlations between parameters that are relevant and to identify specific categories

of "event". An unsupervised hierarchical agglomerative clustering technique such as that presented by Robinson et al. (2013) for analysis of aerosol particles might be a useful method.

Manual assessment of the diameter-asphericity joint-histograms allows the identification of ice particle and liquid drop regimes. The observations of the mixed phase altocumulus clouds showed that the very top 25 m were liquid phase, or any ice particles that were present were undetectable by SID2 because they were too small, or too spherical to be distinguished from the liquid cloud drops. The identification of ice separate from liquid was possible between -50 m and -25 m from cloud top where occasional particles larger than 30 μm were present, which had asphericity values greater than 5. Particles from this category were observed to increase in number with distance below cloud top, to a maximum between -150 m and -125 m. Below here the concentrations reduced once again. The particles were observed up to the theoretical limits of asphericity for a given diameter, with the digitisation of the histograms. The two regimes could be separated by a fitted line that is a function of diameter and asphericity, but this would be arbitrary without additional information and so was not done.

Most ice particles are expected to be irregular (Korolev et al., 2000) and so will result in more complex scattering patterns in SID2 with lower asphericity values than pristine ice habits would generate. This will be especially true for any ice particles that have just formed from a freezing liquid drop. The distinction between ice and liquid is therefore blurred, but the problem is further complicated in mixed-phase clouds by the high frequency of coincidence events in only moderate concentrations of liquid particles. These coincidence events mean that the phase determination of particles that have dimensions on the same scale as the liquid cloud drops is not possible, and remains an important measurement challenge.

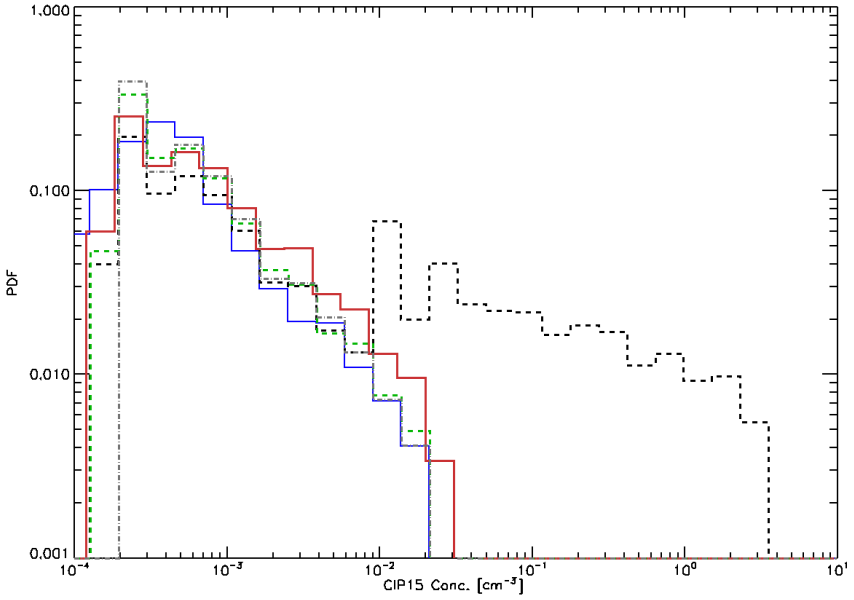

Figure 5.10: PDF of CIP15 and CIP100 concentrations. CIP15, all bins: black dashed line, CIP15 excluding smallest size bin: red line, CIP15 excluding ten smallest size bins: dashed green line, CIP15 Excluding smallest seventeen bins: grey dot-dashed line, CIP100 all data: blue solid line.

5.5 Small Ice Observations using CIP15

5.5.1 Identifying Small Ice with a Multi-Probe Approach

Another source of small ice particle information in altocumulus from 2^{nd} February 2012 is found in the OAP data which, in the case of CIP15, sampled the larger cloud drops and the population of ice particles. Observations of number concentration from CIP15 are presented as Probability Density Functions (PDFs) in Figure 5.10. Integrated concentrations from all size bins show concentrations in the range 10^{-4} cm^{-3} $\leq$ N $\leq$ 35 cm^{-3} in a bimodal distribution. The same data excluding the smallest CIP15 size channel, bin 1, (d $\geq$ 15 μm) are strikingly different and it is postulated that this is down to the impact of CIP15 responding to the largest liquid cloud drops in the smallest size channel. The second smallest CIP15 channel,

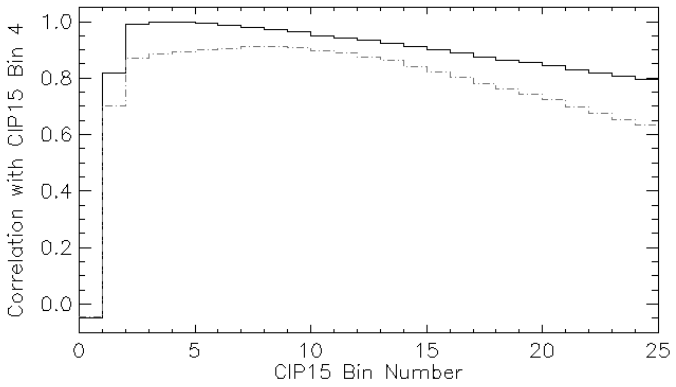

Figure 5.11: Correlations between CIP15 bin 4 concentrations and other CIP15 size channels: solid black line, and additionally, between CIP100 concentrations and CIP15 size channels: dot-dashed grey line.

bin 2 (d $\geq$ 30 μm), does not sense these particles, supported by similar shaped PDF when the lowest 10 bins are excluded and when the smallest 17 bins are excluded. Peak concentrations of these distribution are between 20 L^{-1} and 30 L^{-1}. CIP100 data follow a very similar distribution and have almost identical peak number concentrations as CIP15 data when the smallest bin sizes are excluded, as expected.

Correlations are plotted between the number concentrations from CIP15 of particles in bin 4 (60 μm) with the concentrations of particles of all sizes (Figure 5.11), from the smallest at 15 μm (bin 1) up to 375 μm (bin 25). There is no correlation between bin 1 and bin 4, which is taken to imply that the smallest bin was responding to the liquid cloud particles and bin 4 (60 μm) was not. Between bin 4 and bin 2 (30 μm) the correlation is 0.8, which is much lower than that expected if the two bins were both only responding to ice. The smaller bin responds to the liquid cloud particles some 20 % of the time. A new regime is apparent once particles are larger than 45 μm (bin 3) where the correlation approaches unity, at 0.989, and correlations are strong, $>$ 0.90, between bin 4 and larger bins, up to

bin 13 ($\approx$ 200 μm). These correlations confirm that for sizes larger than 45 μm the CIP15 probe was only responding to ice particles. Up to bin 43 (a particle size of 660 μm), the correlation is still greater than 0.5.

A similar structure was observed when the CIP100 concentration was used in place of the CIP15 bin 4 concentration as shown in Figure 5.11. In all cases the CIP100 was assumed to respond to only ice particles in these clouds. No correlation is observed with the CIP15 liquid contaminated bin 1 and similar correlation is observed with bin 2, confirming liquid contamination. The peak of the correlation, with a magnitude of 0.91 is observed to be with CIP15 bin 8 (120 μm). The comparison is not between identical parameters because the CIP100 value is total concentration and so this value represents excellent agreement.

Ice production rate observations, which varied little across the size range 30 μm $\leq$ D $_i$ $<$ 300 μm, lends support to the hypothesis that CIP15 only senses ice particles above the lower size bound since the narrow spread in computed values of P_0 indicates that those data are not contaminated by liquid particles. Following this logic, the CIP15 observations, above the smallest two size bins ($\geq$ 45 μm), are able to report the number concentration of small ice particles at 1 Hz, by exclusion of other particles known to be liquid.

5.5.2 Ice Particles Cloud Structures

Structures within the cloud were explored by looking at autocorrelations and cross-correlations between concentrations in different CIP15 bin combinations. Figure 5.12 shows the autocorrelation functions, for CIP15 number concentration parameters, for time-lag in the range -20 s $\leq$ t_{lag} $\leq$ 20 s . There are significant correlations greater than 50% at t_{lag} = $\pm$ 15 s for the integrated number concen-

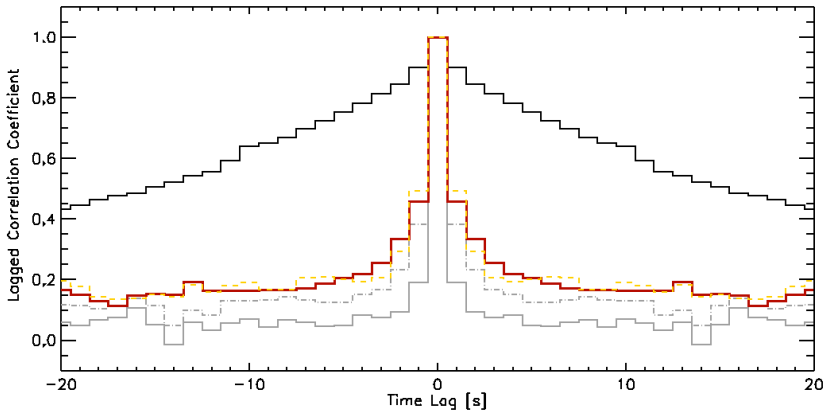

Figure 5.12: Autocorrelation as a function of time-lag, t_{lag}, for CIP15 concentrations with different bin combinations. CIP15 All bins: solid black line, CIP15 (ex. bin 1): dark red line, CIP15 (ex. bin 1-10, d $\geq$ 150 μm): dashed yellow line, CIP15 (ex. bin 1-30, d $\geq$ 450 μm): dot-dashed grey line, CIP15 (ex. bin 1-40, d $\geq$ 0.6 mm): solid grey line.

trations from all bins, which corresponds to a length scale of-the-order 2 km, and this structure is interpreted as relating to physical length scales in the liquid cloud environment.

A series of autocorrelations were calculated for concentrations of particles larger than a certain minimum size, starting with particles larger than 15 μm, where correlations were greater than 0.45 at $\pm$ 1 s, indicative of frequent similarity of number concentration on length scales up to $\approx$ 400 m. Similar correlations are observed on a similar length scale for 150 μm particles, reducing slightly for 450 μm particles where correlations of 0.35 persist at $t_{lag} = \pm$ 1 s. For particles with d $\geq$ 0.6 mm the correlations at $\pm$ 1 s are lower than 0.2. The information contained in these correlations relates to the width of these (the ice-virga) regions of similar sized ice particles, and it is noted that the width of regions decreases with increasing particle size. The scale of these observed ice virga structures in the cloud system have similar scale as and agree qualitatively with the notion of

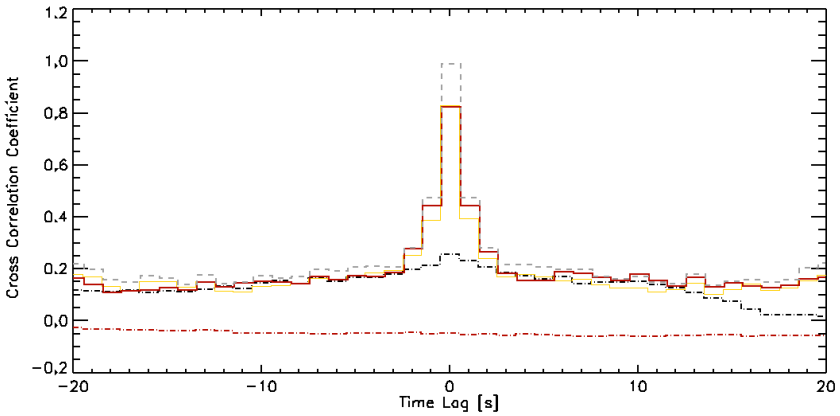

Figure 5.13: Cross-correlation functions between CIP15 channel concentrations. N_{all}, and $N_{d\geq 15}$: dot-dashed black line, N_{all}, and $N_{d\geq 30}$: dark-red dot-dashed line, $N_{d\geq 30}$ and $N_{d\geq 45}$: yellow thin solid line, $N_{d\geq 45}$ and $N_{d\geq 60}$: grey dashed line, $N_{d\geq 30}$ and $N_{d\geq 300}$: dark red solid thick line.

narrow strong downdraughts where air tends to be sub-saturated w.r.t. liquid and super-saturated w.r.t. ice.

Smaller particles are found in wider ice virga sections, and larger particles are found in regions with reduced horizontal extent. The cross-correlation between $N_{d\geq 30}$ and $N_{d\geq 45}$ is strong (Figure 5.13), greater than 0.8 for a time-lag of 0 s, and similar between $N_{d\geq 45}$ and $N_{d\geq 60}$. The cross-correlation between $N_{d\geq 45}$ and $N_{d\geq 60}$ is more than 0.4 at $t_{lag} = \pm$ 1 s. These correlation structures in ice particle concentrations are observed up to larger particle sizes, as evidenced by the correlation between $N_{d\geq 30}$ and $N_{d\geq 300}$, showing that ice virga were often present up to 500 m wide, and up to 800 m wide in decreasing frequency, and that they contain particle sizes that range from 30 μm up to at least 300 μm.

Analysis of this type would benefit greatly from higher temporal resolution, or particle-by-particle data, which would allow for finer spatial resolution than with the 1 Hz ($\approx$ 140 m) shown here. The flight strategy was not intended to make a non-biased sample of these properties and so the details are not to be relied upon,

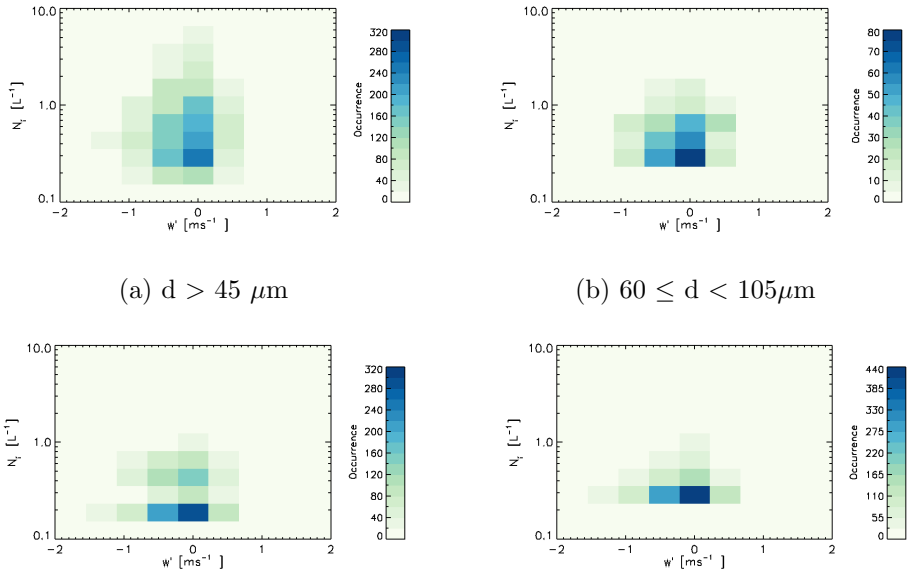

(a) d $>$ 45 μm

(b) 60 $\leq$ d $<$ 105μm

(c) 75 $\leq$ d $<$ 210μm

(d) 225 $\leq$ d $<$ 405μm

Figure 5.14: Joint-histograms of w$'$ and CIP15 ice particle number concentrations for different ice particle size ranges. Note: number scale varies between panels.

although the subjective picture is trusted.

Cross-correlation functions between concentrations of N_{all}, and $N_{d\geq 15}$ confirm the findings of Section 5.5.1 that the two parameters were not strongly related, with coefficients less than 0.25 for all time-lags (Figure 5.13), this moderate value being controlled mainly by the presence of the many small liquid cloud particles in the lowest bin, and a non-zero but small number in the second smallest bin. Weaker still was the cross-correlation between N_{all}, and $N_{d\geq 30}$, effectively this was zero.

5.5.3 Ice Particle Properties in Updraught and Downdraught Regions

Downdraughts and updraughts both act to modify any existing cloud and ice PSD by acting as either a source or sink of moisture available for condensation. The Butterworth 9 km filtered time series of vertical wind fluctuations were used to generate regimes of similar vertical velocity fluctuations in the range -2 $ms^{-1} \leq w' \leq +2$ ms^{-1} in 0.4 ms^{-1} increments at 1 Hz for comparison with CIP15 data. The length scale at this temporal frequency is $\approx$ 140 m. Ice particle concentrations were considered on a logarithmic scale.

Figure 5.14 shows 2-dimensional joint-histograms of variation in vertical velocity fluctuation, w', and CIP15 ice particle number concentrations in four different ice particle size ranges. The top-left panel shows data for all ice particles, larger than $\geq$ 45 μm (excluding bins 1 and 2). Predominantly the ice particles were found at $w' = \pm$ 0.2 ms^{-1} in concentrations of between 0.15 L^{-1} and 8 L^{-1}. Significant occurrence of ice was found in moderate downdraughts where -0.4 $ms^{-1} \leq w' <$ -0.2 ms^{-1} in a lower occurrence of higher concentrations. The incidence of ice particles found in updraughts was low. The top-right panel shows the distribution from ice particles within the size range 60 μm $\leq d <$ 105 μm. There were very few occasions where the number concentrations were greater than 1 L^{-1} and the distribution as a function of vertical velocity fluctuation is broadly similar, with the majority of events found close to zero or slightly negative values. The two lower panels show the distributions for larger ice particles within the range 75 μm $\leq d <$ 210 μm (left) and 225 μm $\leq d <$ 405 μm (right). These larger particles were found most often in lower concentrations, and, again at zero or slightly negative vertical velocity, below $\approx$ 0.7 L^{-1} and $\approx$ 0.5 L^{-1} respectively.

The occurrences are absolute values: they are not scaled to the frequency of occurrence of a particular magnitude of vertical velocity fluctuation and reference is made to the prior observations that showed skewness to the vertical velocity distribution, especially at levels below the liquid cloud, where the ice particle number and size is greatest (Section 3.1.3). However, the ice particles are certainly found predominantly in quiescent regions and in downdraughts with no sorting by particle size apparent. The strongest signal is for the highest concentrations of ice particles at low values of vertical velocity fluctuation. Low magnitudes of w' are typically found close to cloud top, at the inversion where the downdraughts are generated and updraughts terminate. Significant but lower concentrations are found in downdraughts which is taken to imply that there is no evidence for enhanced number concentrations of small ice particles within the updraught regions in these clouds, unlike observations reported by Ansmann et al. (2009). The very small mean value for the vertical velocity fluctuations (Section 2.3.3) gives good confidence that the errors are at worst a few cm s^{-1} and so there is low expectation that the results would alter significantly due to uncertainty in w'.

A simple calculation can help understand where the ice particles were formed. An ice particle with a compact hexagonal habit with d = 60 μm may have a maximum fall speed $v_{max} = 0.07$ ms^{-1} (Westbrook, 2008). Taking this fall speed to be a mean value for a particle growing from negligible size to d = 100 μm and the laboratory derived growth rate at these temperatures of 0.5 μm s^{-1} (Bailey and Hallett, 2012), the quiescent-air fall-distance from the nucleation site will be $z_{fall} \approx 14$ m. This small vertical displacement means that any particles smaller than 100 μm were effectively formed at the observation location, since the resolution in the vertical is lower than the maximum fall distance. Unless there is significant lateral mixing it seems unlikely that the "first-ice" particles were nucleated in the updraughts.

5.6 Observations of the Progressive Glaciation of a Mixed-Phase Altocumulus Cloud

A series of slant profiles were extracted from saw-tooth ascents and descents that were flown through the depth of the mixed-phase cloud system over the course of one hour. They were not chronological repeat passages through the same cloud.

Observations are presented from those profiles, plotted against Relative Altitude ($Dz_{(CTH)}$), that show liquid cloud in various stages of glaciation. The first stage, Figure 5.15, shows a well developed adiabatic LWC structure, with Figures 5.16, 5.17 and 5.18 showing stages in the progressive glaciation of the liquid layer. Supplementary figures in Appendix E show other profiles through this cloud system during the same time period, of intermediate-stage glaciation, to show the similarities between multiple cloud passes.

Each figure is composed of four panels. The vertical velocity fluctuations, w′, from Butterworth 9 km filtered time series at 32 Hz are shown in the left most pane; e.g. Figure 5.15a. Relative humidity is plotted on the upper axis, with respect to liquid, and with respect to ice. The vertical profile was saturated with respect to water in Figure 5.15a above -200 m, and with respect to ice, for the full depth of this profile, to -300 m. Vertical velocities ranged between $\pm$ 2.0 ms^{-1} below -100 m, with stronger negative values than positive. The magnitude of the positive and negative excursions increased with depth below cloud top. The range was smaller above -100 m, with $w' = \pm$ 1.0 ms^{-1}. Negative excursions were geometrically shallower ($\approx$ 15 m) than positive ones ($\approx$ 40 m) corresponding to horizontal distances of 750 m and 2000 m respectively.

Figure 5.15b shows LWC from the Nevzorov LWC probe, on a linear scale. CIP15

and CIP100 CWC values are plotted against the log scale (upper, marked "IWC") and use the IWC formulation given by Brown and Francis (1995). Integrated CIP15 measurements do not necessarily correspond to IWC.

LWC increased towards cloud top reaching a peak of 0.07 gm^{-3}. Condensed Water Content from CIP15 is shown on the log-scale and had a maximum value close to 0.03 gm^{-3} at cloud top. There was some contribution to the total CIP15 mass from both LWC and IWC. The integrated CWC mass from the CIP15 from channels above bin 1 (> 15 μm) decreases closer to cloud top, and is lower than CIP15 CWC for all bins when in liquid cloud above -150 m. Below -150 m in-cloud, and also below cloud, the values from both estimates were similar, centred on 10 mg m^{-3} and ranging between 1 mg m^{-3} and 50 mg m^{-3}. The second estimate of CWC is from CIP15 above bin 2 (> 30 μm), and this value was generally the same as for the CIP15 above bin 1 (> 15 μm) estimate in almost all cases. CIP100 mass estimate is assumed to be IWC since there were no liquid particles close to the size range that this probe can detect, with values close to 0.5 mg m^{-3} at 50 m below cloud top, but increasing to 10 mg m^{-3} in the lower part of the cloud layer ($Dz_{(CTH)}$ = -150 m) and below. The CIP15 bin 1 and bin 2 CWC measurements had similar structure to the CIP100 IWC values and this, coupled with the correlations presented in the section above, shows that CIP15 bins 1 and 2 parameters are responding to IWC. No ice was observed within 20 m of cloud top.

Liquid and ice particle number concentrations are shown in Figure 5.15c. Number concentrations of cloud drops from SID2 were relatively constant with altitude, at $N_d \approx 30$ cm^{-3}, very similar to the number concentration of SID2 particles with asphericity less than 2.0. In the interest of clarity, CDP data are not shown, but agreed well in all cases. SID2 coincidence rates are also not shown for clarity, but

correlated very closely with cloud drop number concentration, typically 10 %, as shown above. The CIP15 number concentration for all particles increased towards cloud top from 20 L^{-1} in the sub-liquid layer to 2 cm^{-3} at 20 m below cloud top. The number is a composite of the ice particles and the very largest cloud drops, follows what looks to be an adiabatic-type gradient, up through cloud.

The data from the CIP15 bins 1 and 2 (d > 15 μm and d > 30 μm) summations show that the number concentrations of ice particles varied between 0.3 L^{-1} and 10 L^{-1} with variability within the liquid cloud layer but no distinct trend. CIP100 ice number concentrations were lower at cloud top, N_i = 0.5 L^{-1}, and closer to 1.0 L^{-1} at cloud base. No particles were observed within 20 m of cloud top by either CIP probe. Coincidence rate in the SID2 data is orders of magnitude larger than these observed ice concentrations.

SID2 categories of large or aspherical particle observations are interpolated to 15 m vertical resolution and are presented to assess their usefulness as a proxy for ice concentration in this cloud. Number concentrations of particles reported by SID2 that were larger than 20 μm, and larger than 25 μm, were observed to be reasonably constant from cloud top to 150 m below cloud top. There were some observations of concentrations between 50 L^{-1} and 100 L^{-1} below -80 m, to cloud base at -300 m, and below. The concentrations of particles with asphericity greater than 10 is shown in filled blue stars, with values of 1 L^{-1} at cloud top and up to 100 L^{-1} below -170 m.

The vertically resolved asphericity distribution from SID2 is presented as a joint-histogram in Figure 5.15d with the pseudo-logarithmic scale given below the figure. The range is over three orders of magnitude, and shows that the vast majority of particles within the cloud layer had asphericity less than 2.0. Number concentrations of particles with asphericity greater than 10 showed a steady

increase with increasing distance below cloud top from 1 L^{-1} to 100 L^{-1}. The particles are likely to be small evaporating cloud drops and not small growing ice particles, but asphericity alone is not sufficient to make this distinction. The smallest "first-ice" particles are not expected to have developed large asphericity values. There is no strong correlation between the vertical velocity fluctuations and asphericity, just the observation of larger excursions of vertical velocity low in the cloud system and also increased concentrations of particles with large asphericity values.

The set of profiles in Figure 5.16 are intended to show the initial stages in a glaciation process that erodes away LWC. Vertical velocity fluctuations showed fewer large magnitude excursions which might support LWC, especially below -150 m, which was below water saturation. The LWC did generally increase with height as in Figure 5.15b and the droplet number was again, also reasonably constant with altitude. Above -150 m the layer was saturated w.r.t. liquid, but there were notable intrusions in shallow layers, between 10 m and 20 m deep, where LWC and cloud drop number were reduced especially at altitudes above -100 m. At the intrusion levels the asphericity distribution showed an increase to more than A = 4, suggesting an increase in either evaporating cloud drops (non-spherical aerosol residuals), or ice particles. The large particle (d $\geq$ 20 μm and d $\geq$ 25 μm) number concentrations from SID2 were very similar in this cloud passage to those from the CIP15 bins 1 and 2 concentrations, and numbers of particles with A $\geq$ 10 also looked similar, with number concentrations of the order 10 L^{-1}. Concentrations from CIP100 were an order of magnitude lower than this, between 0.1 L^{-1} at cloud top and increasing to 1 L^{-1} at cloud base.

There were similar magnitudes of condensed water mass, assumed to be IWC, reported by both the CIP100, probe and CIP15 larger than bins 1, and 2, implying

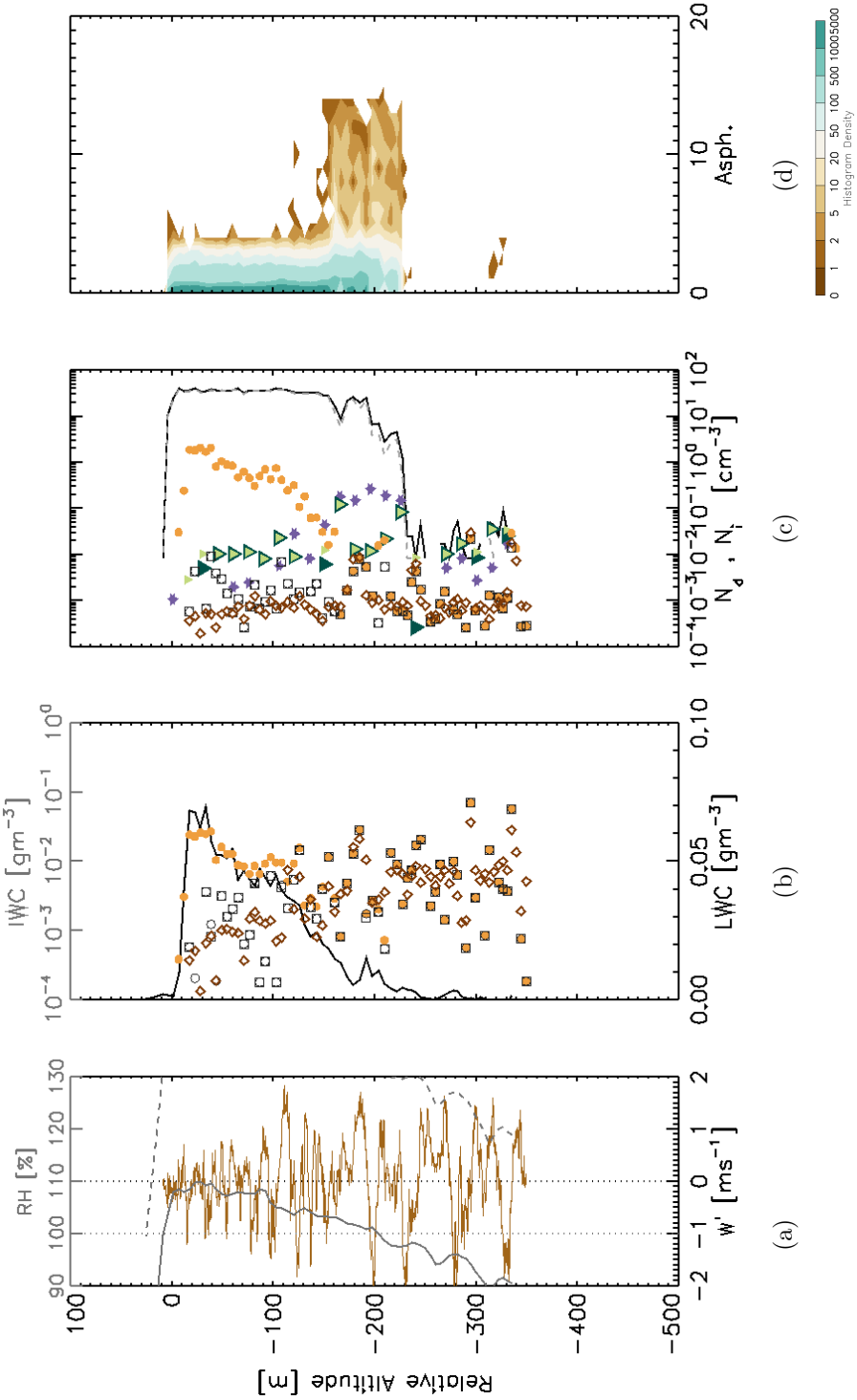

Figure 5.15: Profile (i) through altocumulus with (a) w′: brown, (zero: black dotted line), and RH_l: grey, RH_i: dashed grey (zero: grey dotted line) (b) Nevzorov LWC: black line (lower scale). Upper Scale (IWC): CWC_{CIP15}: filled-orange circles, $CWC_{CIP15>Bin\ 1}$: black empty-circles, $CWC_{CIP15>Bin\ 2}$: black empty-squares, IWC_{CIP100} red diamonds. (c) CIP15 and CIP100 as *(b)*. SID2: N_{all}: black line, $N_{A\leq 2}$: dashed grey line, $N_{D\geq 20}$: light-green filled triangle, $N_{D\geq 25}$: dark-green filled triangle, $N_{A\geq 10}$: blue-filled star. (d) Asphericity PDF, with colour scale below.

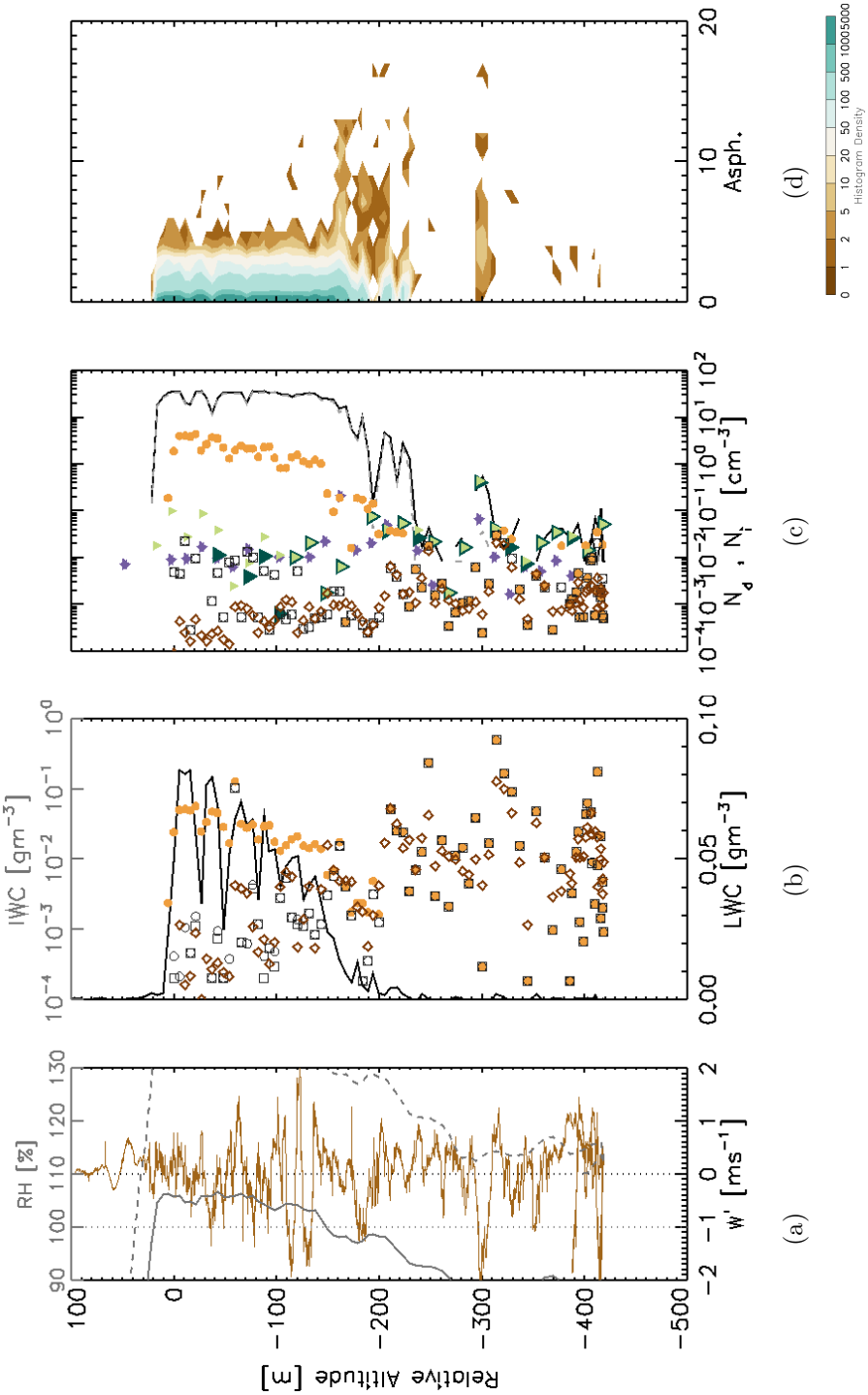

Figure 5.16: Profile (ii) through altocumulus as Figure 5.15.

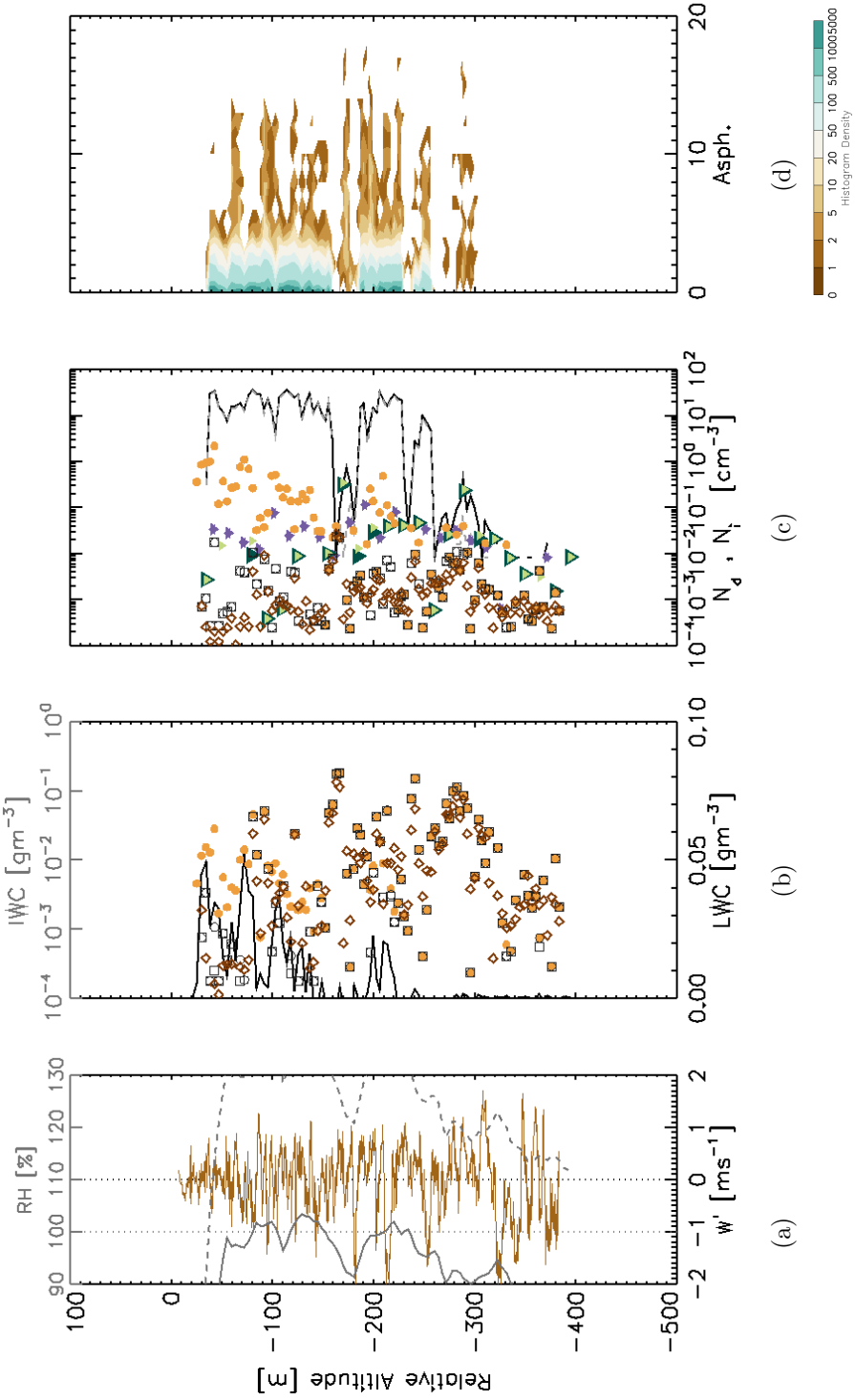

Figure 5.17: Profile (iii) through altocumulus as Figure 5.15.

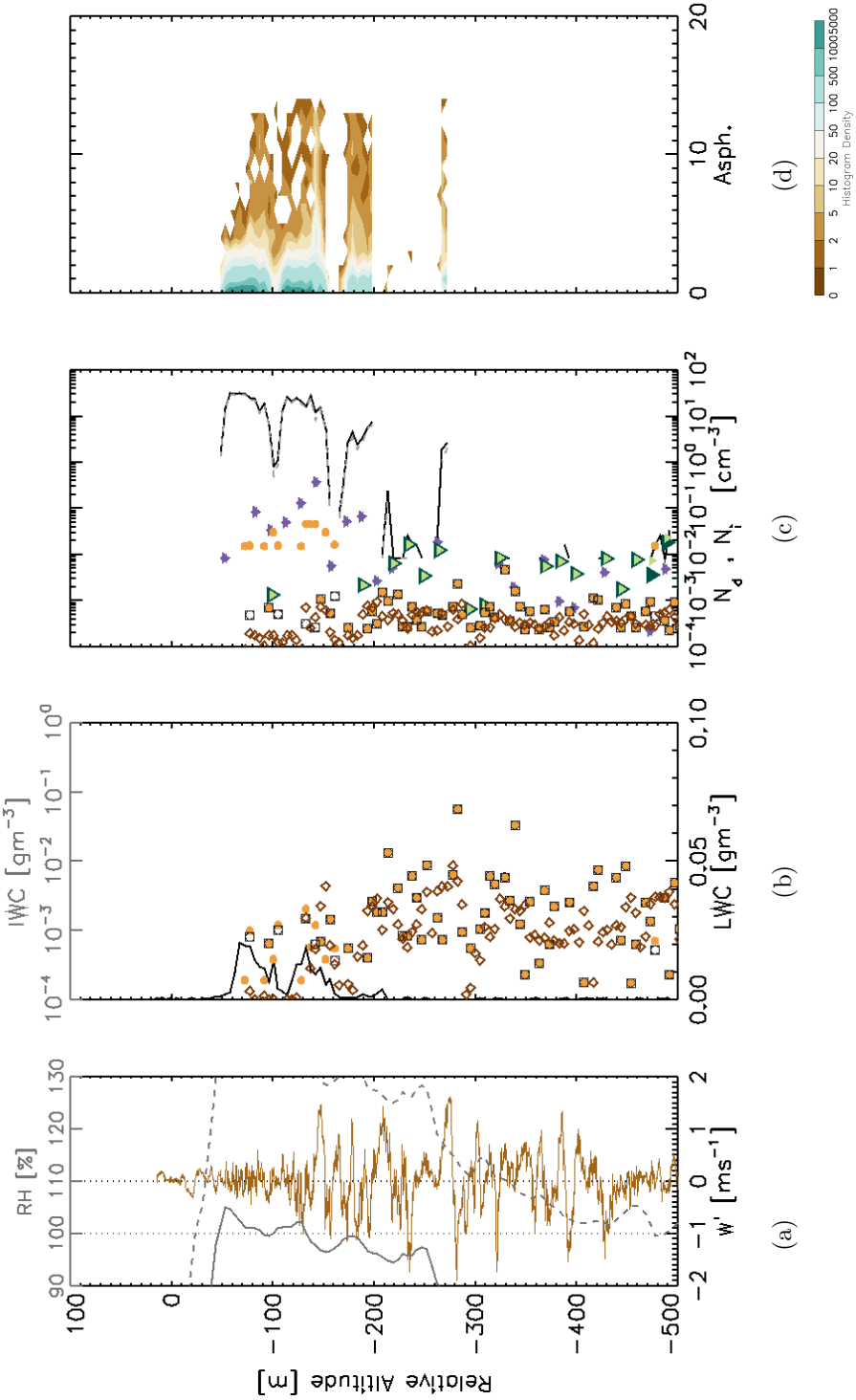

Figure 5.18: Profile (iv) through altocumulus as Figure 5.15.

that most of the mass was contained in particles larger than 100 μm. The magnitudes were in the range 0.1 mg m^{-3} to 1 mg m^{-3} in the top 50 m of cloud, on both probes, and up to 10 mg m^{-3} at cloud base.

These observations show that glaciation occurred in discrete regions. The glaciation-regions were often only 10 m deep, which corresponds to a horizontal range of 400 m. The depth of the remaining liquid layers was at least double (20 m), giving a horizontal scale of 800 m. The length scale of the ice sections corresponds to the correlated ice particle concentrations from CIP15, nearly 50 % of the time (Figure 5.12). The vertical velocity fluctuations, both for this profile and others suggest that the peak negative excursions existed on a similar depth scale, 10 m to 15 m in the vertical suggesting a link between the turbulence and ice properties. The regions where these downdraughts occurred did not, however, directly correspond to the regions where enhanced ice particle number concentrations, or IWC values were found. This suggests a temporal offset or time lag in the process. Since the downdraughts were created by LWRC, the implication appears to be that even if the ice was created, or grew within the downdraughts, it did not necessarily remain where it formed.

The progressive glaciation of mixed-phase layer cloud is further demonstrated by the profiles in Figure 5.17 that show a drastic reduction in the LWC profile as compared to the more triangular (adiabatic) LWC profiles in Figure 5.15b and even Figure 5.16b, implying that moisture was being removed through a diabatic precipitation process. The asphericity histogram shows large increases in numbers of particles with asphericities greater than 10 at all levels throughout the cloud depth. Observations show that the magnitude of IWC as measured by both CIP probes was greatest in this profile, greater than 0.1 g m^{-3} in places. Both CIP probes reported similar quantities, and so the mass was contained in particles

larger than the CIP100 lower limit of 100 μm, and smaller than the 1 mm limit of the CIP15 probe. Number concentrations followed a similar pattern to those from the previous profiles, with CIP100 concentrations increasing with depth down through the cloud. CIP15 concentrations excluding the smallest bin were similar and comparable with the SID2 concentrations of large particles. Asphericity greater than 10 does not look to be a good indicator of ice particles in this profile since at times it agrees, and, at other times is similar to the number concentrations from *all* CIP15 channels indicating sensitivity to the liquid drop population. Three additional sets of profiles are presented in Figures E.1, E.2 and E.3 in Appendix E to provide additional observations of this intermediate glaciation stage.

More fully developed glaciation is observed in Figure 5.18 which shows a shallow layer some 120@m deep with $\text{LWC}^{Peak} \leq 0.02$ g m^{-3}. IWC magnitude from CIP15 was typically between 1 mg m^{-3} and 10 mg m^{-3}, occasionally close to 100 mg m^{-3}. CIP100 IWC magnitudes were in agreement with CIP15 data above -400 m, but below the CIP15 had greater magnitude. Number concentrations were similar from CIP15 and CIP100. Particle with small asphericity (≤ 2) were observed by SID2 as low as $\text{Dz}_{(CTH)}$ = -180m. These particles were assumed to be small, as the CWC from all CIP15 parameters are in agreement which means this mass was contained in particles larger than 45 μm above -400 m. Below this level there was a shift to mass being contained in smaller particles. SID2 large particle number concentrations are 0.1 L^{-1} which is an order of magnitude greater than either CIP probe which reported number concentrations between 0.01 L^{-1} and 1 L^{-1}.

5.7 Ice Formation Discussion

Altocumulus clouds require the formation of the liquid phase before any ice is observed at all, which often has been taken to mean that an immersion freezing mechanism is required (Westbrook and Illingworth, 2013). Large drops are often observed prior to the initiation of the ice phase (Rangno and Hobbs, 2001). Large drops could be responsible for larger LWP (assuming constant number concentration) and when cloud is driven through LWRC (Smith et al., 2009), this implies greater turbulence. The actual ice nucleation mechanism may be a combination of freezing during evaporation in downdraughts, and deposition nucleation originally from clear-sky conditions in the resultant upwards air motions which cause ice supersaturation prior to liquid supersaturation such as observed by Ansmann et al. (2009).

There are two possible explanations for the nature of ice nucleation in this cloud, either:

- ice formed in regions sub-saturated w.r.t. liquid through some evaporative process (Fridlind et al., 2007) or CNIO (Durrant and Shaw, 2005) or through deposition in ice super-saturated updraughts (Ansmann et al., 2009),

or

- ice nucleation proceeded via immersion freezing and was distributed throughout liquid saturated regions.

If evaporative freezing was important (Fridlind et al., 2007) then cloud would predominantly glaciate upwards from cloud base. There may be some freezing events that take place at cloud top due to entrainment mixing dryer air from aloft.

Recent work (Ansmann et al., 2009), using ground based remote sensing, identified

that ice nucleation occurred below liquid cloud based within updraughts that were a response to LWRC initiated downdraughts. Because this occurred below water saturation, this implies a deposition nucleation mechanism process that could also be happening in addition to evaporative freezing in this cloud. There is no strong evidence for this mechanism as ice particles are distributed through cloud, but not found in updraughts regions, so they were not formed at cloud base and then lofted into the liquid layer.

Alternatively, there could be a process of ice nucleation occurring at either cloud top or distributed throughout the cloud in water saturated regions. The particles would then begin to grow and sediment at an increasing rate. At cloud top, the particles may not yet exhibit large asphericity values initially, and so be undetectable by SID2, until they have had chance to grow and develop into more spatial particles, or be large enough to be detected by CIP15.

Korolev (2007a) showed that in situations where vertical velocity is only moderate (a few cm s^{-1} to a few m s^{-1}) that the ice and liquid can both co-exist, and grow, and that the growth rate of ice will be slower than in the WBF case. Example values are presented for moderately supercooled (t = -10° C), low level (800 hPa) clouds and have been reproduced in Table 5.2. For low concentrations of small ice only very light updraughts of a few cm s^{-1} will result in co-existence of growing ice and liquid. Ice will grow in downdraughts at the expense of liquid (WBF process) when downdraughts are very light, of the order 10 cm s^{-1}. Stronger than this and both liquid and ice will evaporate. The processes may be slowed once some of the drops have already evaporated and the others reduced in size, as seen for the final row of the table. Further evaporation of liquid would only occur for a downdraught stronger than -0.7 m s^{-1}.

For this cloud with peak concentrations n_d = 30 cm^{-3}, and a mode radius

N_i [L^{-1}]	$\overline{r}_i$ [μm]	u_z^*	Notes
10	10	> 0.5 cm s^{-1}	ice and liquid grow
10	100	> 4 cm s^{-1}	ice and liquid grow
100	10	> 4 cm s^{-1}	ice and liquid grow
100	100	> 0.5 m s^{-1}	ice and liquid grow
N_d [cm^{-3}]	$\overline{r}_d$ [μm]	u_z^0	Notes
30	15	$<$ -0.09 m s^{-1}	ice and liquid evaporate
30	10	$<$ -0.1 m s^{-1}	ice and liquid evaporate
10	8	$<$ -0.7 m s^{-1}	ice and liquid evaporate

Table 5.2: Impact of updraughts on evolution of liquid and ice phase particles. Limits are given that represent the boundary between WBF and other regimes (Korolev, 2007a). The top half of the table give threshold updraughts for the growth of liquid and ice. The liquid particle observations are from data in Figure 3.18. Ice observations are taken from Figure 3.19 for high concentrations regions, assuming 'first ice" at 10 μm and growing ice at 100 μm.

close to 10 μm the vertical velocity, required to short-cut the WBF process is $1.0 \leq u_z^* < 1.5$ ms^{-1}. These conditions did occur in these altocumulus clouds and so the updraught regions would develop both IWC and LWC simultaneously. The observations suggest though, that the occurrence of ice in the updraught regions was low.

5.8 Conclusions

The largest cloud drops in these altocumulus clouds were up to ≈ 25 μm in diameter. Ice was positively-identified, even in liquid bearing regions, when d ≥ 45 μm on CIP15, and when d ≥ 25 μm on SID2, and although these SID2 diameters were not as reliable as those reported by CIP15, the number concentrations should be. This step forward in terms of in situ mixed phase cloud observations was possible by combining the data from multiple cloud physics probes, two OPCs: CDP, SID2; a Nevzerov LWC hot-wire probe, and OAPs. Perhaps in some cases the CIP15

can identify ice particles in a bin diameter lower (30 μm), but with the additional caveat that a rogue large liquid particle could be present.

The frequency of occurrence of positively identified ice particles close to the cloud top was lower than when deeper in the cloud layer. Ice particles were observed in narrow discrete layers some 10 m to 15 m deep although the nature of the slant profile data means that horizontal scale is between 400 m and 600 m. Highest concentrations of ice particles were observed in quiescent cloud conditions, with the next most common dynamic environment being moderate downdraughts. Very few ice particles were observed in the updraughts.

Constant ice particle number concentration from cloud base to a few hundred metres below is evidence that the ice particles originated within the vicinity of the liquid cloud layer and then sedimented out. At the very lowest levels, there was a reduction in number concentration of ice particles, and relative asphericity shifted to lower values indicating evaporation or aggregation or both.

Ice particles within the liquid cloud might have been smaller than 25 μm and have lower asphericities, and then grow and become more aspherical as they fall through the cloud.

SID2 has particular characteristics that make observations of small ice within liquid cloud complicated. Limitations of SID2 were explored in detail and with changes to probe operation and some design modifications could be vastly improved upon. Coincidence was identified in SID2 scattering patterns and the properties of the rejected patterns explored. Sources of asphericity-broadening in SID2 were modelled and the magnitudes of the impacts investigated. Asphericity alone from SID2 cannot identify ice.

Chapter 6

Conclusions

6.1 Summary

Detailed measurements were made of isolated highly-supercooled single-layer mid-latitude mixed-phase altocumulus clouds which, with a cloud top temperature of -30° C, were some of the coldest expected and were typical of clouds in such an environment.

The key outcomes of this research are

- improved observations of small ice with d $\geq$ 45 μm, in mixed-phase layer clouds, by exploiting a multi-probe approach to allow improved measurements of small ice particles from the CIP15 probe, when in mixed phase conditions,
- an assessment of the primary ice production rate in supercooled altocumulus,
- detailed observations of the turbulence structure and thermodynamic properties of an altocumulus cloud system, and
- a new characterisation of the SID2 probe in terms of diameter, asphericity

and coincidence in mixed phase clouds.

By carefully measuring the properties of both the liquid and ice particles simultaneously it was possible to observe ice particles as small as 45 μm within mixed-phase altocumulus clouds for the first time. An estimate of the variation of cloud top height over the duration of an airborne research flight allowed these measurements to be analysed in a new derived vertical coordinate system. Turbulence within the cloud and the surrounding environment was assessed at high vertical resolution, using a Butterworth filtering technique which was transferred from previous boundary layer studies to the mid-troposphere. Ice particles were found to be concentrated within quiescent air and downdraughts and this indicated cloud top nucleation or nucleation throughout the cloud depth. Primary ice production rate was measured using airborne observations and presented for the first time for supercooled altocumulus clouds. The ice nucleating particle budget was calculated using published parametrisations from measured aerosol size distributions within the mid-troposphere. This required that cloud free conditions be successfully identified using the background variability on a hot-wire bulk water probe. The effective mixed-phase cloud fraction on scales relevant to numerical weather prediction was determined.

6.2 Altocumulus Cloud Observations

The altocumulus was found to be topped by a weak temperature inversion. Because cloud top sloped along an isentrope a new coordinate system was defined by estimating the cloud top height and inversion altitude throughout the sampling period. This allowed for analysis of cloud and thermodynamic properties against a new vertical coordinate with vertical resolution as low as 15 m, once data were

composited.

The thermodynamics were analysed against the derived inversion altitude time series. Vertically-resolved mean properties and the variability of thermodynamic and cloud properties were presented and these observations can be used to inform numerical models.

Butterworth filtering, a technique borrowed from boundary layer studies in stable layers (Lenschow et al., 1988; Mahrt, 1985; Brooks et al., 2003), was used to condition the wind components into mean-values and high-frequency turbulent fluctuations. The technique has been applied to data from a turbulent altocumulus layer for the first time and in situ measurements of the vertical velocity fluctuations and turbulence kinetic energy structure are presented at high vertical resolution, of $\approx$ 15 m. The magnitude and structure that was found in the altocumulus clouds is analogous to that of stratocumulus driven by long-wave radiative cooling from cloud top, with a negative skewness to the vertical velocity fluctuations distribution (Nicholls, 1989; Hogan et al., 2003a). Vertically resolved PDFs of the vertical velocity fluctuations were presented and showed that skewness was greatest below the liquid cloud within the ice virga layer. A more symmetrical vertical velocity distribution was found within the liquid layer cloud itself, where only weak skewness was observed.

Cloud properties were measured with modern cloud microphysics probes, and those measurements used to calculate the in cloud ice production rate. Observations of ice particles at sizes as small as 45 μm from CIP15 was made possible by combination of data from multiple probes, sampling different size ranges and using different techniques: forward scattering (CDP); shadow imaging (OAPs) and detection of the full scattering pattern in the forward direction (SID2). Minimum discernible ice particle size is case dependent and in the altocumulus clouds here,

the minimum size was found to be between 30 μm and 45 μm.

LWC was greater at cloud top and calculations using theoretical adiabatic ascents showed that in-cloud variability was related to non-uniform cloud bases, a finding supported by the ground based observations of altocumulus clouds by Schmidt et al. (2014) and the in situ turbulence observations. Mean LWC was 0.05 gm^{-3} and the largest drops were smaller than 25 μm and total number concentrations were ≈ 30 cm^{-3}. No drizzle was observed. IWC was greatest just below cloud base, a feature which has been observed by others (Carey et al., 2008), the maximum magnitude was 0.08 g m^{-3}.

Multiple profiles through glaciating altocumulus cloud show that the liquid, which initially had a pseudo-adiabatic profile with height, decayed through conversion to ice precipitation in discrete regions. Ice particles were only observed in low concentrations close to cloud top, typically 0.5 L^{-1} to 1 L^{-1}, and increased towards a maximum at liquid cloud base, where concentrations of 10 L^{-1} were common. Number concentrations of ice particles larger than 100 μm were 1 L^{-1}. Smaller ice particles were more common, with a maximum value of 10's L^{-1}.

Ice particle concentrations from CIP15 were generally much greater in quiescent cloud with significant concentrations observed in downdraughts and little ice in updraughts, at a temporal frequency of 1 Hz ($\approx$ 140 m). Observations of ice particles from the smallest distinguishable at 45 μm, to at least 400 μm, followed the same pattern. Consequently, it seems more likely that the ice formation and growth took place in quiescent regions of cloud, close to cloud top, where vertical velocity fluctuations reduce to zero, and growth continues taking place in downdraughts in this cloud.

An effective cloud fraction was determined for the mixed phase regions based on a

scale assessment for numerical modelling applications. The areal cloud fraction in the altocumulus cloud system was generated from observations of the ice particle and liquid drop number concentrations. True liquid cloud fraction was ≈ 0.8 in a layer 200 m deep and ice cloud fraction was closer to 0.1 in a region ≥ 600 m deep. These data were found to give an effective volume cloud fraction in the 600 m deep cloud system of $cf_{liq} \approx 0.25$ and $cf_{ice} \approx 0.10$. The depth here, of 600 m, corresponding to a typical numerical weather prediction grid box in the mid-troposphere. By assuming that the numerical model would be able to fix the areal coverage of the liquid cloud at 0.8 in the upper part of this grid box, a new effective mixed-phase cloud fraction could be calculated, assuming the maximum possible overlap. The result was a maximum mixed-phase cloud fraction of 0.06 on a scale relevant to a numerical weather prediction grid box in the mid-troposphere. This information is expected to be useful for numerical modelling studies.

Mean values and distributions of the thermodynamic variables were presented along with complimentary observations of cumulus and stratocumulus clouds for comparison. The observations presented could be used to test the output of numerical models.

6.2.1 In-cloud Ice Production Rate, P_0, and Ice Nucleating Particles

The technique of calculating in-cloud ice production rate, P_0, used by Harris-Hobbs and Cooper (1987) has been applied to altocumulus clouds for the first time. In the cloud sampled on 2^{nd} February 2012, observations were used to show that the primary ice production rate was, $P_0 = 0.65 \pm 0.04$ m^{-3}s^{-1}. Cloud top temperature in this cloud was 243 K. The rate could be compared with numerical

model simulations. In comparison, observations of secondary-ice production via rime-splintering in a cumulus cloud on 24^{th} November 2013 (Hallett and Mossop, 1974) were found to be several orders of magnitude greater: $P_0 = 11.9 \pm 2.4\ m^{-3}s^{-1}$ at 268 K and $P_0 = 31.4 \pm 4.0\ m^{-3}s^{-1}$ at 265 K. It is clear that temperature was not responsible for the difference in ice production rates between the cumulus and altocumulus clouds.

The Ice Nucleating Particle (INP) budget was determined from the measurement of aerosol particles. Cloud-free data points were identified using a technique that assessed the variance of the Nevzorov TWC probe and distinguished between cloudy and cloud-free points. Clear-sky data points were used to extract observations from PCASP and CDP of large ($> 0.5\ \mu$m) aerosol particles, for use in INP concentration parametrisations. A series of fitted log-normal curves demonstrated that the large aerosol mode was distinct and the observed number concentration of large aerosol was used as input to the schemes of DeMott et al. (2015) and Tobo et al. (2013). Accounting for correction factors the INP concentrations were found to be between 0.1 L^{-1} and 3 L^{-1} at 243 K. Simple cloud glaciation-time calculations (Korolev and Isaac, 2003) suggested that the clouds may not simply be controlled by the INP budget, but also by the transfer of moisture between phases.

6.3 SID Characterisation and Importance for Mixed-Phase Clouds

6.3.1 Coincidence in SID2

A scheme was developed to identify coincidence events in SID2 by interrogation of the returned scattering patterns. The tests were based on anecdotal observations that coincidence events results in particular features in those scattering patterns. Once identified the coincidence events were determined to occur in the range $4\ \mu\text{m} \leq \text{d} < 20\ \mu\text{m}$, most being found close to the modal diameter at $\text{d} \approx 8\ \mu\text{m}$, with a range of asphericities of $0.8 \leq \text{A} < 12$. These events were more common at the top of the cloud, reducing in frequency with depth in cloud. It is recognised that any algorithm such as this is likely to be statistically biased to the most common particles, but that this is also the physical reality. Frequency of identified coincidence was a nearly a factor of two larger than that predicted by statistical considerations using Poisson statistics (Johnson et al., 2014). Some off-axis, or otherwise, spurious scattering patterns may have been wrongly identified as coincidence. It is not clear how many of the real coincidence events have been identified, and how many are false positives.

6.3.2 Determination of the Phase Space of SID2

There is currently no *a priori* way of determining the phase of a particle from the information contained in a SID2 scattering pattern. Neither asphericity, or the large particle number concentrations are able to objectively identify ice without supplementary information. Calculations were performed that show the limits of asphericity as a function of diameter, given the optics and detector arrangement,

that it is possible for SID2 to measure, in all cases. The maximum possible asphericity value is $A_{SID2} = 63.9$ and this reduces greatly once particles have spherical equivalent $d \geq 26$ μm. Values as large as these would not be attained in reality as the requirement of some blank detectors would result in application of the scattering pattern rejection criteria. Previous work by Cotton et al. (2010) defined the asphericity on a scale $0 \leq k < 100$ that was independent of the number of detector elements. The scaling factor, k, is unable to account for the physical operation of the detection system in the presence of real particles. Many combinations of diameter and asphericity are physically impossible. A new scaling parameter could be included to account for this feature but it is not done here because traceability with previous measurements would be lost. Previous measurement should be reassessed in light of this new understanding.

6.3.3 Asphericity Broadening

A model is developed that replicates some sources of artificial asphericity-broadening, including off-axis sampling, detector digitisation and realistic noise levels. It is shown that the large asphericity values obtained in warm clouds are easily replicated using this simple model. A statistically robust assessment whereby full treatment of the sources of asphericity are modelled for real clouds is deemed unnecessary, in part because the features have been demonstrated successfully. The complexity of understanding the true nature of the impact of off-axis sampling and out-of-focus particles near the edge of the sample volume would require detailed laboratory work to better understand the sample volume and extended sample volume and is beyond the scope of this work.

Chapter 7

Further Work

7.1 Cluster Analysis

7.1.1 Cluster Analysis of SID2 Scattering Patterns

The diameter, asphericity and individual detector element response data from SID2 could be used for interrogation by machine-learning algorithms, in particular, the hierarchical clustering technique employed by Robinson et al. (2013). The technique is able to resolve populations that have similar properties even when the number of members of each of the categories is vastly unequal; as is the case for liquid and ice concentrations in altocumulus. It is highly probable that this technique can be used to identify key properties of coincidence events and other instrumental artefacts so that objective categorisation algorithms can be designed.

7.1.2 Multi-Instrument Clustering: "Cloudy Clusters"

There is no reason to limit the cluster analysis to just one microphysics probe. The inclusion of CIP15 data, CPI habit resolved concentrations, as well as the underlying thermodynamics, and properties of bulk condensed water contents could prove to be useful when trying to determine the phase composition of cloudy parcels. Such a method could be used to identify parcels where ice nucleation is occurring by virtue of the fact that those parcels contain different distribution of cloud and ice particles than more mature mixed-phase regions, or even ice-free regions.

7.2 SID2 Operation In Mixed-Phase Clouds

Coincidence and asphericity-broadening are two critical limitations of the SID2 probe. The instrument has been designed to observe particles with 1 μm $\leq$ d $<$ 100 μm. It is recommended that for mixed-phase cloud observations that the gain is increased so that the maximum particle dimension is reduced to $\approx$ 50 μm. This will allow for reduction in noise on the smaller particles, and thus reduce the instrumental asphericity-broadening.

Additionally, the trigger threshold of SID2 can be tuned to only respond to larger sizes of particles. Raising this above the expected mode diameter would reduce coincidence sampling frequency. The narrower range of operation, if correctly specified, will allow better observations at the cross-over size range between the liquid cloud population, and the growing first-ice particles. Laboratory tests could determine the best settings and calibration of the new response of the SID2 probe should be undertaken before, before collecting in situ data.

Newer OAP probes including CIP15 and 2DS now have a resolution that permits the observation of particles in the 50 μm to 100 μm particle range and so it is no longer necessary to use SID probes to measure in this size range.

7.3 Additional In Situ Data

Sampling within the liquid cloud layer for extended periods would help to provide additional data to make more statistically robust measurements of size-resolved ice number concentrations found in updraught and downdraught situations, which may help identify the ice nucleation mechanisms. This is complicated by the fact that extended periods in supercooled liquid cloud increase the likelihood of icing affecting the instrumentation.

Drizzle was not found in these clouds, and it will be interesting to know in which clouds, if any, drizzle occurs prior to ice formation. Similar instruments will be able to provide useful additional information even given the limitations.

Sampling similar altocumulus clouds at different temperatures, and in different aerosol loading situations might help understand the phase space of controls on these clouds and in particular provide insight into the ice nucleation process and ice production rate.

7.4 Instrumentation

7.4.1 Holographic Techniques

Holographic techniques have been employed in the past (Brown, 1989). A new holographic instrument (HALO-HOLO (Spuler and Fugal, 2011)) has recently

been fitted to the FAAM BAe146 research aircraft and has produced interesting observations in cirrus cloud (O'Shea et al., 2016). Data from HALO-HOLO at ice particle sizes smaller than 50 μm showed a general reduction in concentration with a decrease in particle size, in contrast to the observations from 2DS in the same size range. This throws the observations of existing instrumentation into some doubt. Whilst their measurements were made in pure ice cloud, the simultaneous recovery of the size distribution of both liquid and small ice in a co-located volume could revolutionise understanding of mixed-phase clouds and the ice nucleation process. The HALO-HOLO instrument has great potential for making observations of particles in mixed-phase clouds with phase discrimination and should be flown through altocumulus clouds where possible.

7.4.2 Using SID3 to Redesign a High-Resolution SID2

The scattering patterns recorded by SID3 (Vochezer et al., 2016) show an improved level of detail over and above that of the SID2. The limitation of this probe is the speed of readout of the CCD device, similar to that of CPI, which prohibits use in making statistically robust estimates of particle size distributions in mixed-phase cloud systems. SID3 scattering patterns could be used to help understand the minimum level of detail required to make the distinction between liquid, ice and coincidence events, and lead to an improved SID2 detector, that might have more sectors, or a different geometric arrangement, specifically designed to exploit differences in the expected scattering patterns of the various categories of particles in mixed phase conditions.

7.5 Large Eddy Simulation (LES) Study of Observed Altocumulus

To fully explore the details of the evolution and phase changes in this cloud would require a detailed cloud resolving model such as a Large Eddy Simulation (LEM) model. The calculated ice production rate and INP budget observations can be used as input to the numerical model. Some example topics are

- Do INP concentrations have an impact? Observations suggest 0.1 L^{-1} to 1 L^{-1} in this cloud. Were there more at the start of glaciation?
- How does LWC affect TKE and hence evolution of the ice phase?
- Is ice production rate a steady continuous process, or does it happen in discrete bursts, then glaciation proceeds, then elsewhere, or at a different time, the ice production begins again? One unknown is where in cloud the ice nucleation takes place.

Appendix A

Optical Particle Counter Bin Dimensions

	Bin Diameter [μm]		
bin #	Min.	Mid.	Max.
1	0.117	0.119	0.120
2	0.120	0.123	0.125
3	0.125	0.128	0.131
4	0.131	0.137	0.143
5	0.143	0.147	0.152
6	0.152	0.156	0.161
7	0.161	0.165	0.170
8	0.170	0.179	0.188
9	0.188	0.197	0.206
10	0.206	0.216	0.225
11	0.225	0.235	0.245
12	0.245	0.256	0.266
13	0.266	0.306	0.345
14	0.345	0.399	0.453
15	0.453	0.490	0.527
16	0.527	0.654	0.781
17	0.781	0.858	0.935
18	0.935	1.012	1.088
19	1.121	1.304	1.487
20	1.454	1.546	1.638
21	1.665	1.776	1.887
22	1.841	1.928	2.014
23	1.959	2.028	2.097
24	2.171	2.255	2.339
25	2.351	2.458	2.565
26	2.559	2.667	2.774
27	2.768	2.873	2.979

Table A.1: PCASP Bin Dimensions at Native Resolution (gain-stage-crossover bins (4, 16) combined (Ryder et al., 2013)).

	Bin Diameter [μm]		
bin #	Min.	Mid.	Max.
1	0.117	0.121	0.125
2	0.125	0.134	0.143
3	0.143	0.152	0.161
4	0.161	0.174	0.188
5	0.188	0.206	0.225
6	0.225	0.246	0.266
7	0.266	0.360	0.453
8	0.453	0.617	0.781
9	0.781	0.935	1.088
10	1.121	1.504	1.887
11	1.841	2.090	2.339
12	2.351	2.665	2.979

Table A.2: PCASP Bin Dimensions at Downgraded Resolution (12 Bins), (gain-stage crossover bins combined (Ryder et al., 2013)).

	Bin Diameter [μm]		
bin #	Min.	Mid.	Max.
1	n/a	n/a	n/a
2	8.15	8.50	8.84
3	8.44	8.83	9.23
4	8.82	9.33	9.83
5	9.52	10.00	10.48
6	10.18	10.61	11.05
7	10.44	10.89	11.34
8	10.54	11.01	11.48
9	11.12	11.75	12.39
10	11.86	12.66	13.45
11	12.37	13.21	14.05
12	13.42	14.58	15.75
13	13.54	16.41	19.28
14	17.07	18.81	20.55
15	18.60	19.83	21.06
16	19.70	21.86	24.01
17	21.90	24.12	26.34
18	23.98	26.31	28.63
19	26.51	28.50	30.49
20	28.74	30.38	32.01
21	30.21	31.96	33.71
22	31.64	33.99	36.34
23	34.14	36.21	38.28
24	36.46	38.25	40.03
25	38.34	39.88	41.42
26	39.76	41.41	43.06
27	41.19	43.24	45.28
28	43.38	45.31	47.24
29	45.48	47.06	48.64
30	47.08	48.50	49.92

Table A.3: CDP Bin Dimensions at Native Resolution (30 Bins).

	Bin Diameter [μm]		
bin #	Min.	Mid.	Max.
1	8.15	8.99	9.83
2	9.52	10.43	11.34
3	10.54	11.99	13.45
4	12.37	15.82	19.28
5	17.07	20.54	24.01
6	21.90	26.19	30.49
7	28.74	32.54	36.34
8	34.14	37.78	41.42
9	39.76	43.50	47.24
10	45.48	47.70	49.92

Table A.4: CDP Bin Dimensions at Downgraded Resolution (10 Bins) for Aerosol Observations.

	Bin Diameter [μm]		
bin #	Min.	Mid.	Max.
1	8.15	9.60	11.05
2	10.44	12.24	14.05
3	13.42	18.72	24.01
4	21.90	27.80	33.71
5	31.64	37.35	43.06
6	41.19	45.55	49.92

Table A.5: CDP Bin Dimensions at Downgraded Resolution (6 Bins) for Aerosol Observations.

	Bin Diameter [μm]			Bin Diameter [μm]	
bin #	Min.	Max.	bin #	Min.	Max.
1	0.51	0.61	21	7.9	10.2
2	0.61	0.68	22	10.2	10.5
3	0.68	0.75	23	12.5	15.0
4	0.75	0.82	24	15.0	20.0
5	0.82	0.89	25	20.0	25.0
6	0.89	0.96	26	25.0	30.0
7	0.96	1.03	27	30.0	35.0
8	1.03	1.10	28	35.0	40.0
9	1.10	1.17	29	40.0	45.0
10	1.17	1.25	30	45.0	50.0
11	1.25	1.5	31	50.0	55.0
12	1.5	2.0	32	55.0	60.0
13	2.0	2.5	33	60.0	65.0
14	2.5	3.0	34	65.0	70.0
15	3.0	3.5	35	70.0	75.0
16	3.5	4.0	36	75.0	80.0
17	4.0	5.0	37	80.0	85.0
18	5.0	6.5	38	85.0	90.0
19	6.5	7.2	39	90.0	95.0
20	7.2	7.9	40	95.0	100.0

Table A.6: SID2 Defined Bin Dimensions.

	Asphericity	
bin #	Minimum	Maximum
1	0	1
2	1	2
3	2	3
4	3	4
5	4	5
6	5	6
7	6	7
8	7	8
9	8	9
10	9	10
11	10	12
12	12	14
13	14	16
14	16	18
15	18	20
16	20	25
17	25	30
18	30	40
19	40	60
20	60	80
21	80	100

Table A.7: SID2 Defined Asphericity Thresholds.

Appendix B

Aerosol Data Processing

B.1 Aerosol Log-Normal Fitting

The double mode log-normal fit is generated in multiple stages by considering the PCASP data only. Initially a single mode log-normal is fitted to the 27 bin native resolution data in an accumulation mode, with 0.17 μm $\leq$ d $<$ 0.935 μm (10 bins). The output is then used to initialise a two mode log-normal fit, to two accumulation modes, in the size range 0.125 μm $\leq$ d $<$ 0.935 μm (15 bins), keeping the previous parameters held fixed. The output initialises a fit to a three mode log-normal curve for particles with 0.125 μm $\leq$ d $<$ 2.97 μm (25 bins).

The small accumulation mode is then neglected. A single mode log-normal is then fitted to the reduced resolution PCASP data in the size range 0.174 μm $\leq$ d $<$ 0.935 μm (6 bins) with start parameters for the larger accumulation mode. A final stage uses the output of this as the start parameters for a two mode log-normal fit to the reduced resolution PCASP data with 0.161 μm $\leq$ d $<$ 2.97 μm (9 bins).

The details of the fit parameters and the fitting process, are given in Table B.1

		Stage				
		S1	S2	S3	S4	S5
		Parameter Values				
Mode	Parameter	Full Res.			Low Res.	
Acc_A	N_0	-	0.022	0.022*	-	-
	σ	-	1.045	1.045*	-	-
	$\overline{d}$	-	0.134	0.134*	-	-
Acc_B	N_0	4.01	0.089*	0.089*	0.087	0.0809
	σ	1.05	1.63*	1.63*	1.625	1.568
	$\overline{d}$	0.29	0.176*	0.176*	0.191	0.199
Lar_A	N_0	-	-	0.012	-	0.00026
	σ	-	-	2.81	-	1.915
	$\overline{d}$	-	-	7.53	-	1.44

Table B.1: Fit parameters for Upper Layer Particle Size Distributions, derived for a three mode lognormal curve. The process is described in the text. A star, * indicates that the parameter is held fixed during that particular fitting stage.

for the Higher Level. In these tables there are three major rows which give the fit parameters for each mode, either one of two accumulation modes, Acc_A and Acc_B, and a larger mode, Lar_A. The three parameters for the log-normal curves for the minor rows, N_0, the number concentration, σ the standard deviation, or width of the distribution, in units of microns, and $\overline{d}$, the geometric mean of the size distribution, in units of microns. The columns under "Stage" give the fit parameters at the various stages through the fitting process.

B.2 Lower Level Aerosol

The data from the boundary layer and stable layer have very similar properties across the size range of PCASP, with slightly lower concentrations. There are greater concentrations of large particles in the boundary layer than the stable layer by almost two orders of magnitude for particles between 5 μm and 8 μm.

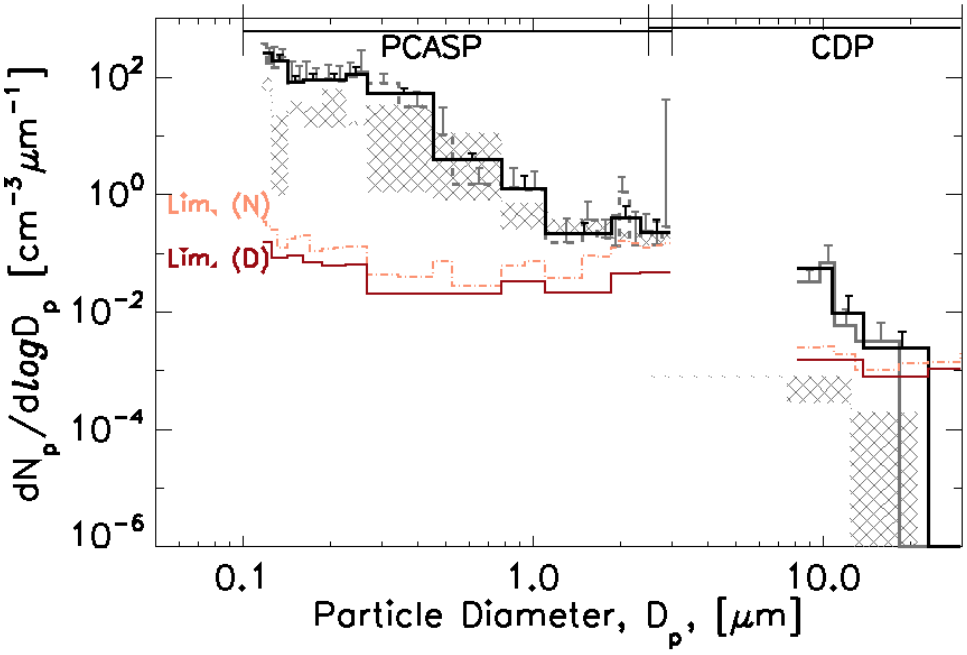

Figure B.1: Lower Level layer, composed of Boundary Layer and Stable Layer.

Appendix C

FAAM Sortie Briefs for Flights B668 and B674

The candidate undertook the drafting and execution of the two sorties presented here, B668, and B674. The sortie B816 was drafted and executed by S. Abel (Met Office). A copy is not available.

Sorties taken from documents hosted by BADC (2017).

B668, 23 January 2012: PIKMIX: super-cooled cumulus transition flight

Science objectives

There are few in-situ observations of the transition from boundary layer stratus cloud in the North to cellular convection in the South during a cold-air outbreak. Observations of the evolution of super-cooled cumulus are required for studies of mixed-phase clouds where primary ice nucleation, secondary ice multiplication and warm-rain processes are important. Boundary layer structure, which controls cloud evolution, is expected to vary as a function of latitude.

Weather and sortie location

Cold northerly airflow over a relatively warm sea. Stratiform or shallow cumulus to the north and cellular cumulus convection to the south. CTH: slope from higher values in south, 61N, 18kft to lower in north, 64N, 10kft

WayPoint: 63N 10W (after 2 hours)
ROSTI : 63N24 14W06 (end of science)
Routing: Prestwick – Stornoway - Waypoint – Rosti - Keflavik

Sortie summary

Double flight with re-fuel at Keflavik – Iceland.

Sortie 1 *t/o 0900UTC 4 hours:* Survey of boundary layer structure and cloud characteristics using Dropsondes (~4), LIDAR (CTH), ARIES (SST CTT) and aircraft RADAR and in-situ microphysical measurements: PMS probes, Total Water, Humidity.
Altitudes FL200 to Stornoway, Then stepped survey legs: i) above cloud ii) -20DegC iii) -10DegC

Sortie 2 *t/o 1430UTC 3 hours:* Survey of boundary layer structure and cloud properties using Dropsondes (~4) using LIDAR (CTH), ARIES (SST, CTT). In-situ microphysical measurements if time allows.

Sortie detail

1.1 Transit to Stornoway area at FL200. During transit while in clear air (at Mission scientist discretion) carry out Nevzorov speed self-calibrations. Run at science speed, +20knots, -20knots each for 2 minutes. Lidar to identify cloud structure and tops. **[60mins]**
1.2 Drop a Sonde – north of land
1.3 Begin northbound survey leg

i) FL200 above cloud survey leg, RADAR pointing down. **[10 mins]**
ii) Drop a sonde **[5mins]**
iii) Profile descent to minus 20 degC (in cloud ~15kft) **[5mins]**
Deviation of-track to intercept cloud is recommended.
iv) Cloud Leg Upper T=-20DegC **[10mins]**
v) Profile descent to minus 15 degC (in cloud ~10kft) **[5mins]**
vi) Cloud Leg Middle T=-15degC **[10mins]**
vii) Profile climb to FL180 **[8mins]**

1.4 Repeat the cycle heading north. The altitude of the survey leg will be lower to the north. **[45mins each]**
1.5 Additional legs at lower altitudes will be flown at mission scientist discretion if time allows
1.6 At Way Point - Head west to Rosti – continue cycle
1.7 At ROSTI – follow airway into Keflavik

2.1 Take off Keflavik
2.2 Transit to ROSTI
2.3 Cycle as 1.3. Upper level survey leg and dropsondes have priority over in-situ microphysics

Key Instrumentation

LIDAR, ARIES (SST, CTT), Aircraft RADAR – 5 degrees down above cloud, Dropsondes, 8-10
TWC, Nevzorov, JW
Cloud microphysics including SIDs, Humidity, including WVSS-II

B674, 02 February 2012: PIKMIX: MOCCA and super-cooled Alto–cumulus Version 3, 201202021058z

Science objectives
Comparison legs will be flown at the start of the sortie in conjunction with the MOCCA Cessna 421 to compare data from wind, T, RH and aerosol probes.

Water is present in cloud with tops as cold as minus 40. The production of ice in these clouds is controlled by long-wave radiative cooling leading to in cloud turbulence and subsequent modification of the droplet size spectra. Few observations of liquid cloud with tops between minus 20 and minus 30. These clouds will be sampled ahead of a cold front.

Weather and sortie location
Aerosol laden boundary layer.
Altocumulus/Altostratus layer in warm stable airflow typically in a warm sector. Cloud top in the range -10 to -30.
Way points: **55°30'N, 7°00'W, 500ft (point A)**
55°30'N, 8°00'W, 500ft (point B)
55°30'N, 8°00'W, FL100 (point C)
55°45'N, 8°00'W, FL100 (point RV)
56°00'N, 8°00'W, (point D)

Sortie summary
Comparison legs between BAe146 and MOCCA to measure boundary layer winds, aerosol, T, RH and free –troposphere winds and T, RH including formation leg at FL100.
Characterisation of a layer of altocumulus using the BAe146.

Sortie detail BAe146 5 hours
1. BAe146 to transit to **Point A** – offset to north by 0°5' [30mins]
   INTERCOMPARISON
2. fly 500ft leg in boundary layer to **point B** – offset to north by 0°5' [10mins]
3. Profile climb to **point C** heading to north-south stepped profile at 8W. to meet up, hold, and formate with MOCCA [15mins]
4. Formation leg heading west in conjunction with MOCCA [15mins]
5. Break formation
6. Profile Climb heading east to FL200 with MOCCA displaced by 0°5' [10mins]
7. MOCCA to return to Base, BAe146 to continue science
8. Move to **Point D** - Leg in clear sky between cloud layers,(~FL220) 2000ft above cloud top, ARIES looking up [10mins]
9. Sawtooth (1000ft/min) through mid-level moist layer (expected FL150-FL220) [20mins]
10. Sub cloud leg under cloud – across wind (L-pattern if time) [10mins, 25mins]
11. Levels in cloud at mission scientist discretion (L-pattern if time) [10mins, 25mins]
12. Additional sub-cloud legs as time allows (l-pattern if possible) [10mins, 25mins]
13. Above cloud leg with ARIES and LIDAR heading east on return transit (Cloud top plus 2000ft) [10mins]

Sortie detail MOCCA 3 hours
1. Transit to **Point A** [45mins]
2. Fly 500ft leg in boundary layer, to **point B** [15mins]
3. Profile climb to **point C** heading north-south at 8W and hold for BAe146 [20mins]
4. Formation leg heading west in conjunction with BAe146 [20mins]
5. Break formation
6. Profile Climb heading east to FL200 with BAe146 displaced by 0°5' [15mins]
7. Reposition to **Point D**
8. Profile descent through cloud to 2000ft below cloud base [15mins]
9. Return transit >2000ft under any mid level cloud wth LIDAR looking up.

Appendix D

SID2 Additional Figures

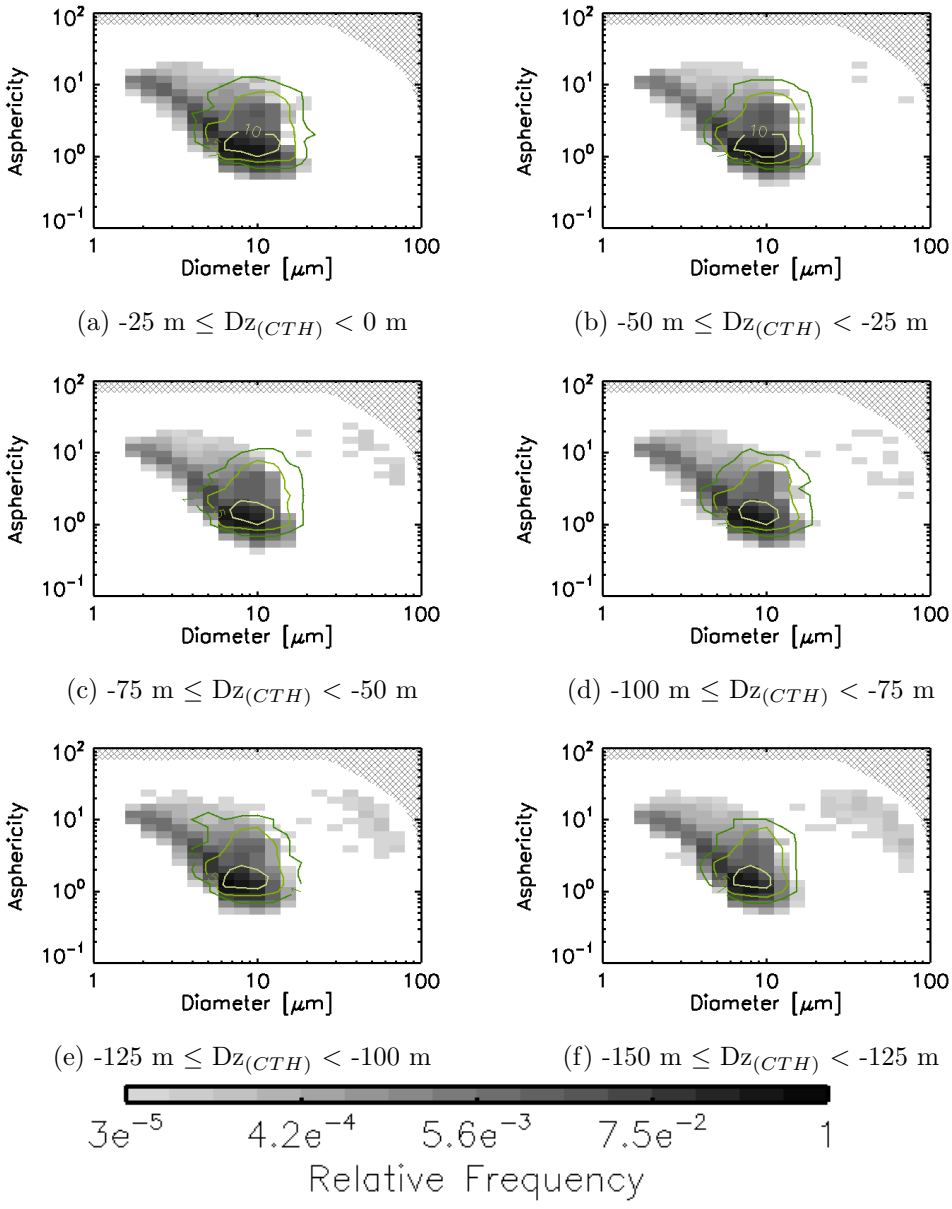

(a) -25 m ≤ $Dz_{(CTH)}$ < 0 m

(b) -50 m ≤ $Dz_{(CTH)}$ < -25 m

(c) -75 m ≤ $Dz_{(CTH)}$ < -50 m

(d) -100 m ≤ $Dz_{(CTH)}$ < -75 m

(e) -125 m ≤ $Dz_{(CTH)}$ < -100 m

(f) -150 m ≤ $Dz_{(CTH)}$ < -125 m

Figure D.1: Vertically resolved corrected diameter vs asphericity joint-histogram, for 25 m deep vertical levels between -150 m ≤ $Dz_{(CTH)}$ < 0 m, as Figure 5.7c with coincidence (as Figure 5.7b) over-plotted in green contours, and logarithmic colour scale replicated below.

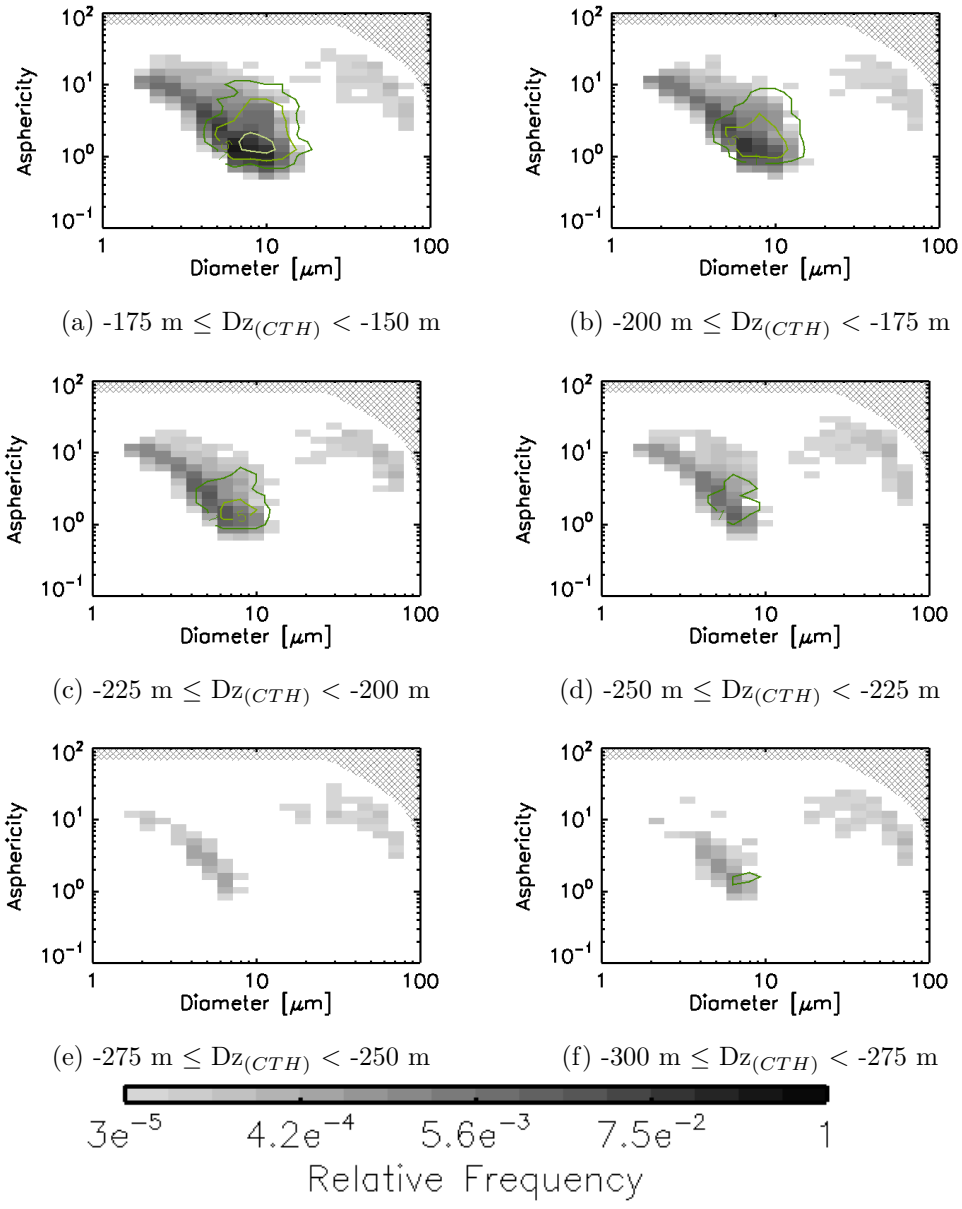

(a) -175 m ≤ $Dz_{(CTH)}$ < -150 m

(b) -200 m ≤ $Dz_{(CTH)}$ < -175 m

(c) -225 m ≤ $Dz_{(CTH)}$ < -200 m

(d) -250 m ≤ $Dz_{(CTH)}$ < -225 m

(e) -275 m ≤ $Dz_{(CTH)}$ < -250 m

(f) -300 m ≤ $Dz_{(CTH)}$ < -275 m

Figure D.2: Vertically resolved corrected diameter vs asphericity joint-histogram, for 25 m deep vertical levels between -300 m ≤ $Dz_{(CTH)}$ < -150 m, as Figure 5.7c with coincidence (as Figure 5.7b) over-plotted in green contours, and logarithmic colour scale replicated below.

Appendix E

Microphysics Profiles, 2^{nd} February 2016

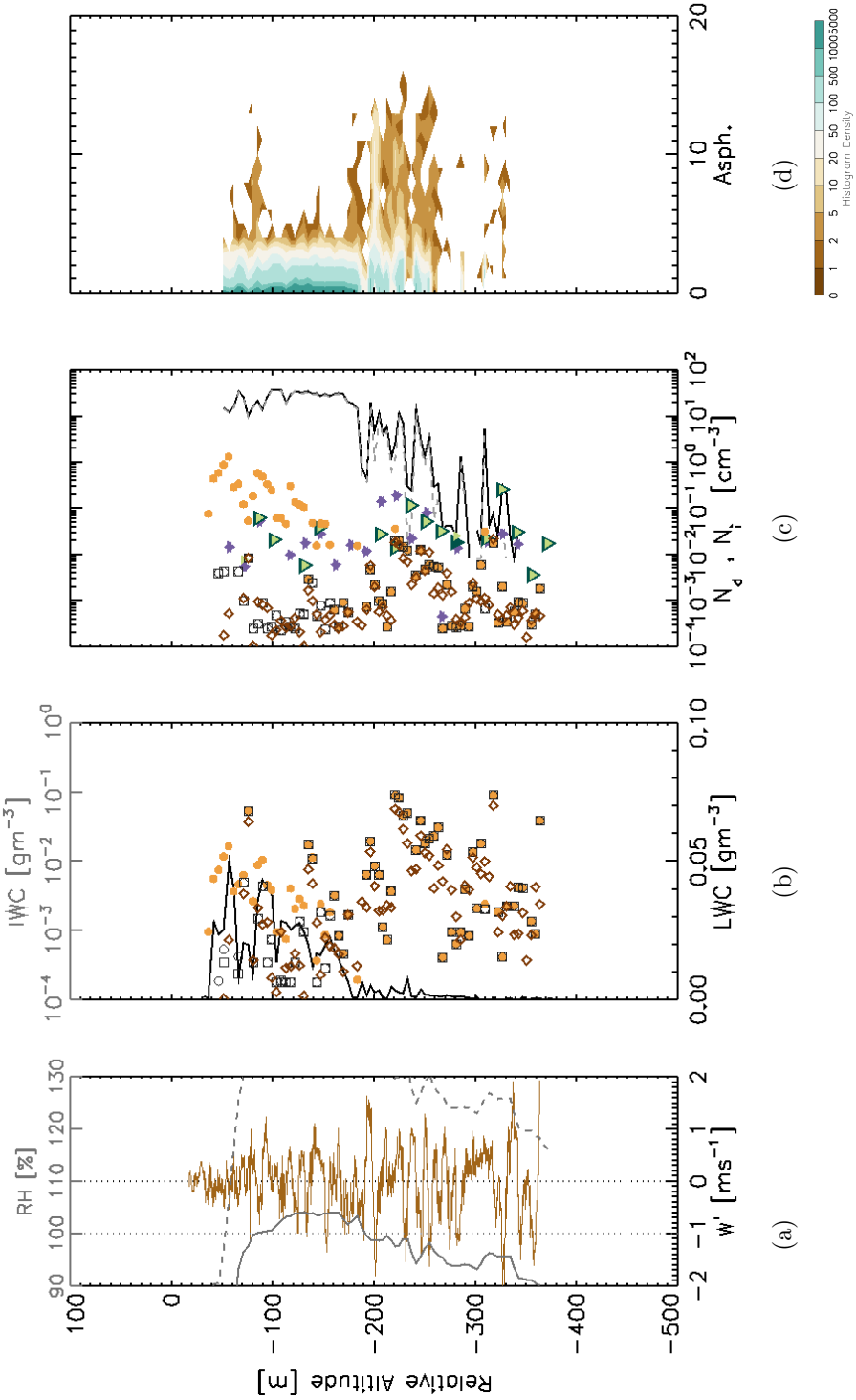

Figure E.1: Profile (v) through altocumulus as Figure 5.15.

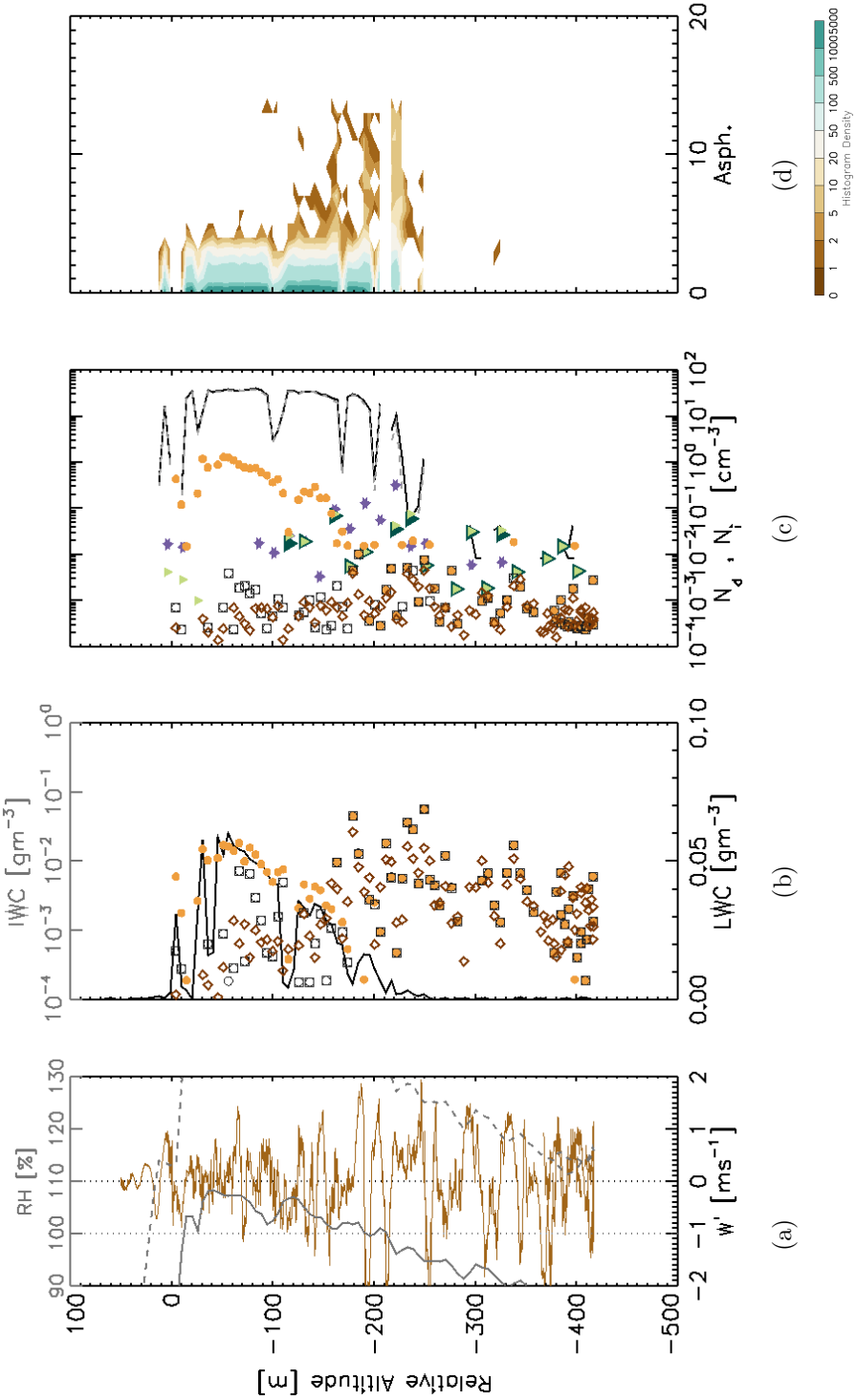

Figure E.2: Profile (vi) through altocumulus as Figure 5.15.

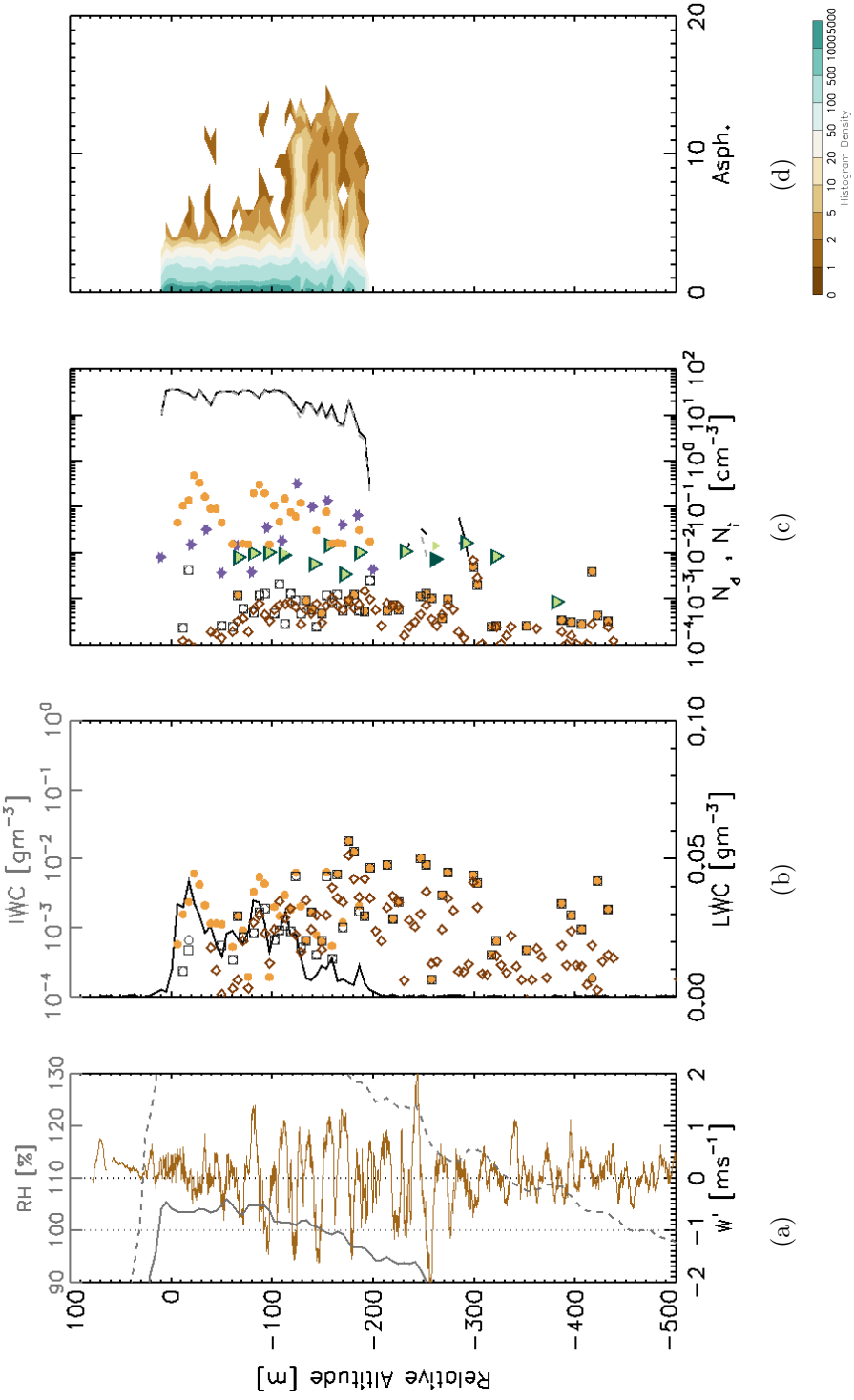

Figure E.3: Profile (vii) through altocumulus as Figure 5.15.

Bibliography

Abel, S., R. Cotton, P. Barrett, and A. Vance, 2014: A comparison of ice water content measurement techniques on the FAAM BAe-146 aircraft. *Atmos. Meas. Tech.*, **7**, 3007–30022, doi:10.5194/amt-7-3007-2014.

Abel, S. J., I. A. Boutle, K. Waite, S. Fox, P. R. Brown, R. Cotton, G. Lloyd, T. Chourlarton, and K. N. Bower, 2017: The role of precipitation in controlling the transition from stratocumulus to cumulus clouds in a northern hemisphere cold-air outbreak. *J. Atmos. Sci*, **in press**, doi:10.1175/JAS-D-16-0362.1.

Allen, G., S. Illingworth, S. O. S. Newman, A. Vance, S. Bauguitte, F. Marenco, J. Kent, K. Bower, M. Gallagher, J. Muller, C. Percival, C. Harlow, J. Lee, and J. Taylor, 2014: Atmospheric composition and thermodynamic retrievals from the ARIES airborne TIR-FTS system - Part 2: Validation and results from aircraft campaigns. *Atmos. Meas. Tech.*, **7**, 4401–4416, doi:10.5194/amt-7-4401-2014.

Ansmann, A., M. Tesche, P. Seifert, D. Althausen, R. Englemann, J. Fruntke, U. Wandinger, I. Mattis, and D. Müller, 2009: Evolution of the ice phase in tropical altocumulus: SAMUM lidar observations over Cape Verde. *J. Geophys. Res.*, **114**, 1–20, doi:10.1029/2008JD011658.

BADC, 2017: http://catalogue.ceda.ac.uk/uuid/affe775e8d8890a4556aec5bc4e0b45c.

Facility for Airborne Atmospheric Measurement and Met Office and Natural Environment Research Council and M. Smith (2004).

Bailey, M. and J. Hallett, 2004: Growth Rates and Habits of Ice Crystals between -20 ° C and -70 ° C. *J. Atmos. Sci*, **61**, 514–544.

— 2009: A Comprehensive Habit Diagram for Atmospheric Ice Crystals: Confirmation from the Laboratory, AIRS II and Other Field Studies. *J. Atmos. Sci*, **66**, 2888–2899.

— 2012: Ice Crystal Linear Growth Rates from -20° to -70° C: Confirmation from Wave Cloud Studies. *J. Atmos. Sci*, **69**, 390–402.

Bansemar, A., 2016: SODA2. http://ncar.ucar.edu/.

Bodas-Salcedo, A., M. Webb, M. Brooks, M. Ringer, K. Williams, S. Milton, and D. Wilson, 2008: Evaluating cloud systems in the Met Office global forecast model using simulated CloudSat radar reflectivities. *J. Atmos. Sci*, **113**, D00A13.

Bodas-Salcedo, A., K. Williams, P. Field, and A. Lock, 2012: The Surface Downwelling Solar Radiation Surplus over the Southern Ocean in the Met Office Model: The Role of Midlatitude Cyclone Clouds. *J. Climate*, **25**, 7467–7486.

Bodas-Salcedo, A., K. Williams, M. Ringer, I. Beau, J. Cole, J.-L. Dufresne, T. Koshiro, B. Stevens, Z. Wang, and T. Yokohata, 2014: Origins of the Solar Radiation Biases over the Southern Ocean in CFMIP2 Models. *Journal of Climate*, **27**, 41–56, doi:10.1175/JCLI-D-13-00169.1.

Bohlender, D., P. Dowler, and D. Durand, eds., 2009: *Non-Linear Least Squares Fitting in IDL with MPFIT*, volume 411 of *ASP Conference Series*, Astronomical Society of the Pacific: San Francisco, Quebec, Canada.

Bolton, D., 1980: The Computation of Equivalent Potential Temperature. *Mon. Weather Rev*, **108**, 1046–1053.

Broadley, S., B. Murray, R. Herbert, J. Atkinson, S. Dobbie, T. Malkin, E. Condliffe, and L. Neve, 2012: Immersion mode heterogeneous ice nucleation by an illite rich powder representative of atmospheric mineral dust. *Atmos. Chem. Phys.*, **12**, 287–307.

Brooks, I. M., S. Søderberg, and M. Tjernstrøm, 2003: THE TURBULENCE STRUCTURE OF THE STABLE ATMOSPHERIC BOUNDARY LAYER AROUND A COASTAL HEADLAND: AIRCRAFT OBSERVATIONS AND MODELLING RESULTS. *Boundary-Layer Meteorology*, **2003**, 531–559.

Brown, E., C. Friehe, and D. Lenschow, 1983: The use of pressure fluctuations on the nose of an aircraft for measuring air motion. *J. Appl. Meteorol. Clim.*, **22**, 171–180.

Brown, P., 2009: Turbulence Probe: Flow Angle and TAS Calibration. Technical report, FAAM, http://www.faam.ac.uk/index.php/science-instruments/turbulence/117-turbulence-probe.

Brown, P. R., 1989: Use of holography for airborne cloud physics measurements. *J. Atmos. Oceanic Technol.*, **6**, 293–306.

Brown, P. R. and P. N. Francis, 1995: Improved measurements of the ice water content in cirrus using a total-water probe. *J. Atmos. Oceanic Technol.*, **12**, 410–414.

Bühl, J., P. Seifert, A. Myagkov, and A. Ansmann, 2016: Measuring ice- and liquid-water properties in mixed-phase cloud layers at the Leipzig Cloudnet station. *Atmos. Chem. Phys.*, **16**, 10609 – 10620.

Cantrell, W. and A. Heymsfield, 2005: Production of ice in tropospheric clouds. *Bull. Amer. Meteorol. Soc.*, **86**, 795–807.

Carey, L., J. Niu, P. Yang, J. Kankiewicz, V. Larson, and T. H. Vonder Haar, 2008: The Vertical Profile of Liquid and Ice Water Content in Midlatitude Mixed-Phase Altocumulus Clouds. *J. Appl. Meteorol. Clim.*, **47**, 2487–2495.

Chen, G., P. Yang, G. W. Kattawar, and M. I. Mishchenko, 2006: Scattering phase functions of horizontally oriented hexagonal ice crystals. *J. Quant. Rad. Spec. Trans.*, **100**, 91–102.

Connolly, P. J., M. J. Flynn, Z. Ulanowski, T. Choularton, M. Gallagher, and K. Bower, 2007: Calibration of the Cloud Particle Imager Probes Using Calibration Beads and Ice Crystal Analogues: The Depth of Field. *J. Atmos. Oceanic Technol.*, **24**, 1860–1879.

Cotton, R., P. Field, Z. Ulanowski, P. Kaye, E. Hirst, R. Greenaway, I. Crawford, J. Crosier, and J. Dorsey, 2013: The effective density of small ice particles obtained from *in situ* aircraft observations of mid-latitude cirrus. *Quart. J. Roy. Met. Soc.*, **139**, 1923–1934.

Cotton, R., S. Osborne, Z. Ulanowski, E. Hirst, P. Kaye, and P. Greenaway, 2010: The ability of the Small Ice Detector SID-2 to characterise cloud particle and aerosol morphologies obtained during flights of the FAAM BAe146 research aircraft. *J. Atmos. Oceanic Technol.*, **27**, 290–303.

Crosier, J., K. Bower, T. Choularton, C. Westbrook, P. Connolly, Z. Cui, I. Crawford, G. Capes, H.Coe, J. Dorsey, P. Williams, A. Illingworth, M. Gallagher, and A. Blyth, 2011: Observations of ice multiplication in a weakly convective cell embedded in supercooled mid-level stratus. *Atmos. Chem. Phys.*, **11**, 257–273.

Crosier, J., T. Choularton, C. Westbrook, A. Blyth, K. Bower, P. Connolly, C. Dearden, M. G. Z. Cui, and J. Nicol, 2014: Microphysical properties of cold frontal rainbands. *Quart. J. Roy. Met. Soc.*, **140**, 1257–1268.

de Boer, G., T. Hashino, and G. Tripoli, 2010: Ice nulceation through immersion freezing in mixed-phase stratiform clouds: Theory and numerical simulations. *Atmos. Res.*, **96**, 315–324.

DeMott, P., A. Prenni, G. McMeeking, R. Sullivan, M. Petters, Y. Tobo, M. N. O. Møhler, J. Snider, Z. Wang, and S. Kreidenweis, 2015: Integrating laboratory and field data to quantify the immersion freezing ice nucleation activity of mineral dust particles. *Atmos. Chem. Phys.*, **15**, 393–409.

DMT, 2016: www.droplet-measurement.com. Droplet Measurement Technologies, 2545 Central Avenue, Boulder, CO 08301, USA.

Durrant, A. J. and R. A. Shaw, 2005: Evaporation freezing by contact nucleation inside-out. *Geophys. Res. Lett.*, **32**, L20814, doi:10.1029/2005GL024175.

Erfani, E. and D. L. Mitchell, 2017: Growth of ice particle mass and projected area during riming. *Atmos. Chem. Phys.*, **17**, 1241–1257, doi:10.5194/acp-17-1241-2017.

ETH Zurich, 2016: IMCA. Technical report, Insitut Für Atmosphäre und Klima, Eva Brigitte Choffat, CHN O 12.3, Universitätstrasse 16, 8092 Zürich, Switzerland, www.iac.ethz.ch/group/atmosperic-physics/research/ice-nucleation/imca.html.

FAAM, 2017: http://www.faam.ac.uk. Accessed: 24 January 2017.

Fanning, D. W., 2017: Coyote Library. http://github.com/davidwfanning/idl-coyote.

Field, P., A. Heymsfield, and A. Bansemer, 2006: Shattering and particle interarrival times measured by optical array probes in ice clouds. *J. Atmos. Oceanic Technol.*, **23**, 1357–1371.

Field, P., R. Wood, P. Brown, P. Kaye, E. Hirst, R. Greenway, and J. Smith, 2003: Ice particle interarrival times measured with a fast FSSP. *J. Atmos. Oceanic Technol.*, **20**, 249–261.

Fleishauer, R., V. Larson, and T. Vonder Haar, 2002: Observed microphysical structure of midlevel, mixed-phase clouds. *J. Atmos. Sci*, **59**, 1779–1804.

French, J. R., W. M. Drennan, J. A. Zhang, and P. G. Black, 2007: Turbulent Fluxes in the Hurricane Boundary Layer. Part I: Momentum Flux. *J. Atmos. Sci*, **64**, 1089–1102, doi:10.1175/JAS3887.1.

Fridlind, A., A. Ackerman, G. McFarquhar, G. Zhang, M. Poellot, P. DeMott, A. Prenni, and A. Heymsfield, 2007: Ice properties of a single-layer stratocumulus during the Mixed-Phase Arctic Cloud Experiment: 2. Model results. *Geophys. Res. Lett.*, **112**, D24202, doi:10/1029/2007JD008646.

Gardiner, B. and J. Hallet, 1985: Degradation of in-cloud forward scattering spectrometer probe measurements in the presence of ice particles. *J. Atmos. Oceanic Technol.*, **2**, 171–180.

Garimella, S., D. A. Rothenberg, M. J. Wolf, R. O. David, Z. A. Kanji, C. Wang, and D. J. Cziczo, 2017: Uncertainty in counting ice nucleating particles with continuous diffusion flow chambers. *Atmos. Chem. Phys. Discuss.*, 1–28.

Gayet, J.-F. and G. Febvre, 1996: The reliability of the PMS FSSP in the presence of small ice crystals. *J. Atmos. Oceanic Technol.*, **13**, 1300–1310.

Ghate, V. P., B. A. Albrecht, M. A. Miller, A. Brewer, and C. W. Fairall, 2014:

Turbulence and Radiation in Stratocumulus-Topped Marine Boundary Layers: A Case Study from VOCALS-REx. *J. Appl. Meteorol. Clim.*, **53**, 117–135, doi:10.1175/JAMC-D-12-0225.1.

Goff, J. and S. Gratch, 1946: Low-pressure properties of water from -160 to 212 f (presented at the 52nd Meeting of the American Society of Heating and Ventilating Engineers, New York). *Trans. Am. Soc Heating Air-Cond. Eng.*, **52**, 95–122.

Hallett, J. and S. Mossop, 1974: Production of secondary ice particles during the riming process. *Nature*, **249**, 26–28.

Hamann, U., A. Walther, B. Baum, R. Bennartz, L.Bugliaro, M. Derrien, P. Francis, A. Heidinger, S. Joro, A. Kniffka, H. Le Gléau, M. Lockhoff, H. Lutz, J. Meirink, P. Minnis, R. Palikonda, R. Roebeling, A. Thoss, S. Platnick, P. Watts, and G. Wind, 2014: Remote sensing of cloud top pressure/height from SEVIRI: analysis of ten current retrieval algorithms. *Atmos. Meas. Tech.*, **7**, 2839–2867, doi:doi:10.5194/amt-7-2839-2014.

Harris-Hobbs, R. L. and W. A. Cooper, 1987: Field Evidence Supporting Quantitative Predictions of Secondary Ice Production Rates. *J. Atmos. Sci*, **44**, 1071–1082.

Herbert, R. J., B. J. Murray, S. J. Dobbie, and T. Koop, 2015: Sensitivity of liquid clouds to homogeneous freezing parameterizations. *Geophys. Res. Lett.*, **42**, 1599–1605.

Heymsfield, A., L. Miloshevich, A. Slingo, K. Sassen, and D. Starr, 1991: An observational and theoretical study of highly supercooled altocumulus. *J. Atmos. Sci*, **48**, 923–945.

Heymsfield, A. J. and J. L. Parrish, 1978: A Computational Technique for Increasing the Effective Sampling Volume of the PMS[1] Two-Dimensional Particle Size Spectrometer. *J. Appl. Meteorol.*, **17**, 1566–1571.

Hobbs, P. and A. Rangno, 1985: Ice particle concentrations in clouds. *J. Atmos. Sci*, **42**, 2523–2549.

— 1998: Microstructures of low and middle-level clouds over the Beaufort Sea. *Quart. J. Roy. Met. Soc.*, **124**, 2035–2071.

Hogan, R., P. Francis, H. Flentje, A. Illingworth, M. Quante, and J. Pelon, 2003a: Characteristics of mixed-phase clouds. I: Lidar, radar and aircraft observations from CLARE'98. *Quart. J. Roy. Met. Soc.*, **129**, 2089 – 2116, doi:10.1256/qj.01.208.

Hogan, R., A. L. Grant, A. J. Illingworth, G. N. Pearson, and E. J. O'Conner, 2009: Vertical velocity variance and skewness in clear and cloud-topped boundary layers as revealed by Doppler lidar. *Quart. J. Roy. Met. Soc.*, **135**, 635–643, doi:10.1002/qj.413.

Hogan, R., A. Illingworth, E. O'Conner, and J. P. Baptista, 2003b: Characteristics of mixed-phase clouds. II: A climatology from ground-based lidar. *Quart. J. Roy. Met. Soc.*, **129**, 2117–2134, doi:10.1256/qj.01.209.

Illingworth, A., R. Hogan, E. O'Connor, D. Bouniol, J. Delanoe, J. Pelon, A. Protat, M. Brooks, N. Gaussiat, D. Wilson, D. Donovan, H. Klein Baltink, G. van Zadelhoff, J. Eastment, J. Goddard, C. Wrench, M. Haeffelin, O. Krasnov, H. Russchenberg, J. Piriou, F. Vinit, A. Seifert, A. Tompkins, and U. Willen, 2007: CLOUDNET continuous evaluation of cloud profiles in seven operational models using ground-based observations. *Bull. Amer. Meteorol. Soc.*, **88**, 883–898.

JAR, 2007: Joint Airworthiness Regulations JAR-25. www.jaa.nl, Joint Avaition Authorities, PO BOX 3000, 2130 KA Hoofddorp, The Netherlands.

Johnson, A., S. Lasher-Trapp, A. Bansemer, Z. Ulanowski, and A. J. Heymsfield, 2014: Difficulties in early ice detection with the Small Ice Detector-s HIAPER (SID-2H) in maritime cumuli. *J. Atmos. Oceanic Technol.*, **31**, 1263–1275.

Jones, A., D. Thomson, M. Hort, and B. Devenish, 2007: The U.K. Met Office's next-generation atmospheric dispersion model, NAME III. *Proceedings of the 27th NATO/CCMS International Technical Meeting on Air Pollution Modelling and its Application*, 580–589.

Knollenberg, R. G., 1970: The Optical Array: An Alternative to Scattering or Extinction for Airborne Particle Size Determination. *J. Appl. Meteorol.*, **9**, 86–103.

Korolev, A., 2007a: Limitations of the Weneger-Bergeron-Findeison Mechanism in the Evolution of Mixed-Phase Clouds. *J. Atmos. Sci*, **64**, 3372–3375.

— 2007b: Reconstruction of the Sizes of Spherical Particles from Their Shadow Images. Part 1: Theoretical Considerations. *J. Atmos. Oceanic Technol.*, **24**, 376–389.

Korolev, A., E. Emery, J. Strapp, S. Cober, G. Isaac, M. Wasey, and D. Marcotte, 2011: Small Ice Particles in Tropospheric Clouds: Fact or Artifact? Airborne Icing Instrumentation Evaluation Experiment. *Bull. Amer. Meteorol. Soc.*, **92**, 967–973.

Korolev, A. and P. Field, 2008: The effect of dynamics on mixed phase clouds: Theoretical considerations. *J. Atmos. Sci*, **65**, 66–86.

Korolev, A. and G. Isaac, 2003: Phase transformation in mixed-phase clouds. *Quart. J. Roy. Met. Soc.*, **129**, 19–38.

Korolev, A., G. Isaac, and J. Hallett, 2000: Ice particle habits in stratiform clouds. *Quart. J. Roy. Met. Soc.*, **126**, 2873–2902.

Korolev, A., G. Isaac, J. Strapp, S. Cober, and H. Barker, 2007: *In Situ* measurements of liquid water content profiles in midlatitude stratiform clouds. *Quart. J. Roy. Met. Soc.*, **133**, 1693–1699.

Korolev, A., J. Strapp, G. Isaac, and E. Emery, 2008: Improved airborne hot-wire measurements of ice water content in clouds. *15th Intl. Conf. on Cloud and Precipitation*, **ICCP**, Cancun, Mexico.

Korolev, A., J. Strapp, G. Isaac, and A. Nevzorov, 1998a: The Nevzorov Airborne Hot-Wire LWC-TWC Probe: Principle of Operation and Performance Characteristics. *J. Atmos. Oceanic Technol.*, **15**, 1495–1510.

Korolev, A. V., S. Kuznetsov, Y. E. Marakov, and V. Novikov, 1991: Evaluation of Measurements of Particle Size and Sample Area from Optical Array Probes. *J. Atmos. Oceanic Technol.*, **8**, 514–522.

Korolev, A. V., J. Strapp, and G. Isaac, 1998b: Evaluation of the Accuracy of PMS Optical Array Probes. *J. Atmos. Oceanic Technol.*, **15**, 708–720.

Krämer, M., C. Schiller, A. Afchine, R. Bauer, I. Gensch, A. Mangold, S. Schlicht, N. Spelten, N. Sitnikov, S. Borrmann, M. de Reus, and P. Spichtinger, 2009: Ice supersaturations and cirrus cloud crystal numbers. *Atmos. Chem. Phys.*, **9**, 863505–3522.

Ladino, L., O. Stetzer, and U. Lohmann, 2013: Contact freezing: a review of

experimental studies. *Atmos. Chem. Phys.*, **13**, 9745–9769, doi:10.5194/acp-13-9745-2013.

Lance, S., C. A. Brock, D. Rogers, and J. Gordon, 2010: Water droplet calibration of the cloud droplet probe CDP and in-flight performance in liquid, ice and mixed-phase clouds during ARCPAC. *Atmos. Meas. Tech.*, **3**, 1683–1706.

Larson, V., A. Smith, M. Falk, K. Kotenberg, and J. Golaz, 2006: What determines altocumulus dissipation time. *J. Geophys. Res.*, **111**, D19207.

Lawson, R. P., D. O'Connor, P. Zmarzly, K. Waever, B. Baker, Q. Mo, and H. Jonsson, 2006: The 2D-S (Stereo) Probe: Design and Preliminary Tests of a New Airborne, High-Speed High-Resolution Particle Imaging Probe. *J. Atmos. Oceanic Technol.*, **23**, 1462–1477.

Lenschow, D. H., X. S. Li, C. J. Zhu, and B. B. Stankov, 1988: THE STABLY STRATIFIED BOUNDARY LAYER OVER THE GREAT PLAINS I. Mean and Turbulence Structure. *Boundary-Layer Meteorology*, **42**, 95–121.

Lloyd, G., T. W. Choularton, K. N. Bower, J. Crosier, H. Jones, J. R. Dorsey, M. W. Gallagher, P. Connolly, A. C. R. Kirchgaessner, and T. Lachlan-Cope, 2015: Observations and comparisons of cloud microphysical properties in spring and summertime Arctic stratocumulus clouds during the ACCACIA campaign. *Atmos. Chem. Phys.*, **15**, 3719–3737, doi:10.5194/acp-15-3719-2015.

Lock, A., A. Brown, M. Bush, G. Martin, and R. Smith, 2000: A new boundary layer mixing scheme. Part I: Scheme description and single-column model tests. *Mon. Weather Rev*, **128**, 3187–3199.

Mahrt, L., 1985: Vertical Structure and Turbulence in the Very Stable Boundary Layer. *J. Atmos. Sci*, **42**, 2333–2349.

Marenco, F., B. Johnson, K. Turnbull, S. Newman, J. Haywood, H. Webster, and H. Ricketts, 2011: Airborne lidar observations of the 2010 Eyjafjallajökull volcanic ash plume. *J. Geophys. Res.*, **116**, D00U05.

Marsham, J., S. Dobbie, and R. Hogan, 2006: Evaluation of large-eddy model simulation of a mixed-phase altocumulus cloud using microwave radiometer, lidar and Doppler radar data. *Quart. J. Roy. Met. Soc.*, **132**, 1693–1715.

Mason, S., C. Jakob, A. Protat, and J. Delanoeë, 2014: Characterizing observed midtopped cloud regimes associated with southern ocean shortwave radiation biases. *J. Climate*, **27**, 6189–6203.

McFarquhar, G., S. Ghan, J. Verlinde, A. Korolev, J. Strapp, B. Schmid, J. Tomlinson, M. Wolde, S. Brooks, D. Cziczo, M. Dubey, J. Fan, C. Flynn, I. Gultepe, J. Hubbe, M. Gilles, A. Laskin, P. Lawson, W. Leaitch, P. Liu, X. Liu, D. Lubin, C. Mazzoleni, A. Macdonald, R. Moffet, H. Morrison, M. Ovchinnikov, M. Shupe, D. Turner, S. Xie, A. Zelenyuk, K. Bae, M. Freer, and A. Glen, 2011: Indirect and Semi-Direct Aerosol Campaign. *Bull. Amer. Meteorol. Soc.*, **92**, 183–201.

Mirza, A. K., S. P. Ballard, S. L. Dance, P. Maisey, G. G. Rooney, and E. K. Stone, 2016: Comparison of aircraft-derived observations with *in situ* research aircraft measurements. *Quart. J. Roy. Met. Soc.*, **142**, 2949–2967, doi:10:1002/qj.2864.

Morrison, H., G. de Boer, G. Feingold, J. Harrington, and M. Shupe, 2012: Resilience of persistent Arctic mixed-phase clouds. *Nature Geoscience*, **5**, 11–17.

Murphy, D. and T. Koop, 2005: Review of the vapour pressure of ice and supercooled water for atmospheric applications. *Quart. J. Roy. Met. Soc.*, **131**, 1539–1656, doi:10.1256/qj.04.94.

Nicholls, S., 1987: A model of drizzle growth in warm, turbulent, stratiform clouds.

Quart. J. Roy. Met. Soc., **113**, 1141–1170.

— 1989: The structure of radiatively driven convection in stratocumulus. *Quart. J. Roy. Met. Soc.*, **115**, 487–511.

Nicholls, S., J. Leighton, and R. Barker, 1990: A new fast response instrument for measuring total water content from aircraft. *J. Atmos. Oceanic Technol.*, 706–718.

Nott, G., 2013: FAAM Core Passive Cavity Aerosol Spectrometer Probe. Technical report, FAAM, http://www.faam.ac.uk/index.php/science-instruments/aerosol/304-pcasp, accessed: 17 Jan 2017.

— 2017: FAAM Core Cloud Physics. Technical report, FAAM, http://www.faam.ac.uk/index.php/science-instruments/cloud-physics, accessed: 20 Jan 2017.

O'Shea, S., T. Choularton, G. Lloyd, J. Crosier, K. N. Bower, M. Gallagher, S.J.Abel, R. Cotton, P. Brown, J. Fugal, O. Schlenczek, S. Borrmann, and J. Pickering, 2016: Airborne observations of the microphysical structure of two contrasting cirrus clouds. *J. Geophys. Res.*, **121**, 13,510–13,536, doi:10.1002/2016JD025278.

Petersen, G. and I. Renfrew, 2009: Aircraft-based observations of air-sea interface fluxes over Denmark Strait and the Irminger Sea during high wind speed conditions. *Quart. J. Roy. Met. Soc.*, **135**, 2030–2045, doi:10.1002/qj.355.

Rangno, A. L. and P. V. Hobbs, 2001: Ice particles in stratiform clouds in the Arctic and possible mechanisms for the production of high ice concentrations. *J. Geophys. Res.*, **106**, 15065–15075.

Rauber, R. and A. Tokay, 1991: An explanation for the existence of supercooled water at the top of cold clouds. *J. Atmos. Sci*, **17**, 1048–1057.

Robinson, N., J. Allan, J. Huffman, P. Kaye, V. Foot, and M. Gallagher, 2013: Cluster analysis of WIBS single-particle bioaerosol data. *Atmos. Meas. Tech.*, **6**, 337–347.

Rogers, D. C., 1988: Development of a continuous flow thermal gradient diffusion chamber for ice nucleation studies. *Atmos. Res.*, **22**, 149–181.

Rosenberg, P., A. Dean, P. Williams, J. Dorsey, A. Minikin, M. Pickering, and A. Petzold, 2012: Particle sizing calibration with refractive index correction for light scattering optical particle counters and impacts upon PCASP and CDP data collected during the Fennec campaign. *Atmos. Meas. Tech.*, **5**, 1147–1163, doi:10.5194/amt-5-1147-2012.

Ryan, B., E. Wishart, and D. Shaw, 1976: The growth rates and densities of ice crystals between -3° C and -21° C. *J. Atmos. Sci*, **33**, 842–850.

Ryder, C., E. Highwood, P. Rosenberg, J. Trembath, J. Brooke, M. Bart, A. Dean, J. Crosier, J. Dorsey, H. Brindley, J. Banks, J. Marhsam, J. McQuaid, H. Sodemann, and R. Washington, 2013: Optical properties of Saharan dust aerosol and contribution from the coarse mode as measured during the Fennec 2011 aircraft campaign. *Atmos. Chem. Phys.*, **13**, 303–325.

Schmidt, J. M., P. J. Flatau, and R. D. Yates, 2014: Convective cells in altocumulus observed with a high-resolution radar. *J. Atmos. Sci*, **71**, 2130–2154.

Seinfeld, J. H. and S. N. Pandis, 2006: *Atmospheric Chemistry and Physics*. John Wiley and Sons, Hoboken, New Jersey, second edition.

Simmel, M., J. Bühl, A. Ansmann, and I. Tegen, 2015: Ice phase in altocumulus

clouds over Leipzig: remote sensing observations and detailed modelling. *Atmos. Chem. Phys.*, **15**, 10453–10470, doi:10.5194/acp-15-104530-2015.

Smith, A., V. Larson, J. Niu, and A. Kankiewicz, 2009: Processes that generate and deplete liquid water and snow in thin midlevel mixed-phase clouds. *J. Geophys. Res.*, **114**, D12203.

SPEC, 2017: http://www.specinc.com. Stratton Park Engineering 3022 Sterling Circle, #200, Boulder, CO 80301.

Spuler, S. M. and J. Fugal, 2011: Design of an in-line, digital holographic imaging system for airborne measurement of clouds. *Applied Optics*, **507**, 1–9.

Stein, T., D. Parker, J. Delanoë, N. Dixon, R. Hogan, P. Knippertz, R. Maidment, and J. Marsham, 2011: The vertical cloud structure of the West African Monsoon: A 4 year climatology using CloudSat and CALIPSO. *J. Geophys. Res.*, **116**, 1–13.

Stetzer, O., B. Baschek, F. Lüönd, and U. Lohmann, 2008: The Zurich Ice Nucleation Chamber (ZINC) - a new instrument to investigate atmospheric ice formation. *Aerosol. Sci. and Technol.*, **42**, 64–74, doi:10.1080/02786820701787944.

Stevens, B., D. H. Lenschow, G. Vali, H. Gerber, A. Bandy, B. Blomquist, J.-L. Brenguier, C. S. Bretherton, F. Burnet, T. Campos, S. Chai, I. Faloona, D. Friesen, S. Haimov, K. Laursen, D. K. Lilly, S. M. Loehrer, S. P. Malinowski, B. Morley, M. D. Petters, D. C. Rogers, L. Russell, V. Savic-Jovcic, J. R. Snider, D. Straub, M. J. Szumowski, H. Takagi, D. C. Thornton, M. Tschudi, C. Twohy, M. Wetzel, and M. C. van Zanten, 2003: Supplement to Dynamics and Chemistry of Marine Stratocumulus DYCOMS-II Flight Summaries. *Bull. Amer. Meteorol. Soc.*, **84**, 12–25.

Storelvmo, T., C. Hoose, and P. Eriksson, 2011: Global modelling of mixed phase clouds: The albedo and lifetime effects of aerosols. *J. Geophys. Res.*, **116**, D05207, doi:10.1029/2010JD014724.

Strapp, J. W., F. Albers, A. Reuter, A. V. Korolev, U. Maixner, E. Rashke, and Z. Vukovic, 2001: Laboratory measurements of the response of a PMS OAP-2DC. *J. Atmos. Oceanic Technol.*, **18**, 1150 – 1170.

Stull, R., 1997: *An Introduction to Boundary Layer Meteorology*. Kluwer Accademic Press, Dordrecht, The Netherlands.

— 2015: *Practical Meteorology: An Algebra-based Survey of Atmospheric Science*. Univ. of British Columbia, Vancouver, BC, Canada, https://www.eoas.ubc.ca/books/Practical_Meteorology/, https://creativecommons.org/licenses/by-nc-sa/4.0/.

Sun, Z. and K. Shine, 1995: Parameterization of ice cloud radiative properties and its application to the potential climatic importance of mixed-phase clouds. *J. Climate*, **8**, 1874–1888.

Taylor, J., T. Choularton, A. Blyth, Z. Liu, K. Bower, J. Crosier, M. Gallagher, P. Williams, J. Dorsey, M. Flynn, L. Bennet, Y. Huang, J. French, A. Korolev, and P. Brown, 2016: Observations of cloud microphysics and ice formation during COPE. *Atmos. Chem. Phys.*, **16**, 799–826.

Tobo, Y., A. J. Prenni, P. J. DeMott, J. A. Huffman, C. S. McCluskey, G. Tian, C. Pöhlker, U. Pöschl, and S. M. Kreidenweis, 2013: Biological aerosol particles as a key determinant of ice nuclei populations in a forest ecosystem. *J. Geophys. Res.*, **118**, 10100–10110.

Ulanowski, Z., 2005: SID-2 data analysis and preliminary results from AIDA ice

nucleation campaign IN5. Technical Note - DRAFT, Science and Technology Research Institute, University of Hertfordshire.

Vali, G., 2014: Interpretation of freezing nucleation experiments: singular and stochastic: sites and surfaces. *Atmos. Chem. Phys.*, **14**, 5271–5294, doi:10.5194/acp-14-5271-2014.

Vance, A., S. Abel, R. Cotton, and A. Woolley, 2014: Performance of WVSS-II hygrometers on FAAM research aircraft. *Atmos. Meas. Tech.*, **8**, 1617 – 1625.

Verlinde, J., J. Harrington, G. McFarquhar, V. Yannuzzi, A. Avramov, S. Greenberg, N. Johnson, G. Zhang, M. Poellot, D. Turner, E. Eloranta, B. Zak, A. Prenni, J. Daniel, G. Kok, D. Tobin, R. Holz, K. Sassen, D. Spangenberg, P. Minnis, T. Tooman, M. Ivey, S. Richardson, C. Bahrmann, M. Shupe, P. DeMott, A. Heymsfield, and R. Schofield, 2007: The Mixed-Phase Cloud Experiment. *Bull. Amer. Meteorol. Soc.*, **88**, 205–221.

Vochezer, P., E. Järvinen, R. Wagner, P. Kupiszewski, T. Leisner, and M. Schnaiter, 2016: In situ characterisation of mixed phase clouds using the small ice detector and the particle phase discriminator. *Atmos. Meas. Tech.*, **9**, 159–177.

Walters, D., M. Brooks, I. Boutle, T. Melvin, R. Stratton, S. Vosper, H. Wells, K. Williams, N. Wood, T. Allen, A. Bushell, D. Copsey, P. Earnshaw, J. Edwards, M. Gross, S. Hardiman, C. Harris, J. Heming, N. Klingaman, R. Levine, J. Manners, G. Martin, S. Milton, M. Mittermaier, C. Morcrette, T. Riddick, M. Roberts, C. Sanchez, P. Selwood, A. Stirling, C. Smith, D. Suri, W. Tennant, P. L. Vidale, J. Wilkinson, M. Willett, S. Woolnough, and P. Xavier, 2017: The Met Office Unified Model Global Atmosphere 6.0/6.1 and JULES Global Land 6.0/6.1 Configurations. *Geoscientific Model Development*, **10**, 1487–1520, doi:10.5194/gmd-10-1487-2017.

Wang, Z., J. French, G. Vali, P. Wechsler, S. Haimov, A. Rodi, M. Deng, D. Leon, J. Snider, L. Peng, and A. L. Pazmany, 2012: Single aircraft integration of remote sensing and in situ sampling for the study of cloud microphysics and dynamics. *Bull. Amer. Meteorol. Soc.*, **93**, 653–668, doi:10.1175/BAMS-D-11-00044.1.

Warren, S., C. Hahn, J. London, R. Chervin, and R. Jenne, 1988: Global distribution of total cloud cover and cloud type amounts over the ocean. Technical report, National Centre for Atmospheric Research, http://nldr.library.ucar.edu/repository/collections/TECH-NOTE-000-000-000-467.

Watson, N., 1967: Some measurements of turbulence in altocumulus clouds. *Quart. J. Roy. Met. Soc.*, **93**, 227–236.

Westbrook, C., 2008: The fall speeds of sub-100 μm ice crystals. *Quart. J. Roy. Met. Soc.*, **134**, 1243–1251, doi:10.1002/qj.290.

Westbrook, C. and A. Illingworth, 2011: Evidence that ice forms primarily in supercooled liquid clouds at temperatures $\geq$ -29° C. *Geophys. Res. Lett.*, **38**, L14808.

— 2013: The formation of ice in a long-lived supercooled layer cloud. *Q.J.R. Meteorol. Soc.*, **139**, 2209–2221, doi:10:1002/qj.2096.

Wexler, R. H. A., 1983: Formulations for the thermodynamic properties of the saturated phase of H_20 from 173.15 k to 473.15 k. *ASHRAE Trans.*, **89**, 500–519.

Woolley, A., 2009a: GIN Project. Technical report, FAAM, http://www.faam.ac.uk/index.php/science-instruments/primary-systems/103-gin.

— 2009b: Temperature Instrumentation. Technical report, FAAM,

http://www.faam.ac.uk/index.php/science-instruments/temperature/102-rosemount-total-air-temperature.

— 2017: Aircraft Horizontal Wind. Technical report, FAAM, http://www.faam.ac.uk/index.php/science-instruments/turbulence/446-aircraft-horizontal-wind.

World Meteorological Organisation, 2008: WMO guide to meteorological instruments and methods of observation. WMO-No. 8 (Seventh Edition) Part 1, W.M.O., Chapter 15 Observation of Clouds.

Yang, F., M. Ovchinnikov, and R. J. Shaw, 2013: Minimalist model of ice microphysics in mixed-phase stratiform clouds. *Geophys. Res. Lett.*, **40**, 3756–3760, doi:10.1002/grl.50700.

Zhang, D., Z. Wang, and D. Liu, 2010: A global view of midlevel liquid-layer topped stratiform cloud distribution and phase partition from CALIPSO and CloudSat measurements. *J. Atmos. Sci*, **115**, DOOH13.